Phyllosilicate-bearing fault zones: the mechanical role of fluids, lithology and temperature.

Thesis submitted in accordance with the requirements of the University of Liverpool for the degree of Doctor in Philosophy by

Isabel Rose Ashman

April 2023.

Abstract

Large earthquakes nucleate on crustal faults that have accumulated significant slip displacement and field observations show that these mature fault cores are comprised of extremely fine, low permeability, phyllosilicate-bearing gouges. Phyllosilicate minerals have layered anisotropic structures that are thought to impart an anomalously weak mechanical behaviour to the deformation of fault rocks and shear zones. An area of interest in rock mechanics research is the discrepancy between observed natural fault behaviour and the data collected from rock deformation experiments. Phyllosilicate-bearing materials in rock mechanics experiments consistently exhibit weak, stable sliding deformation behaviour, whereas clay-bearing, crustal-scale faults in nature can rupture via aseismic creep, slow slip or fast earthquakes. This thesis aims to investigate and quantify the controls on the deformation of phyllosilicate-bearing fault rocks including the dilatancy of granular fault materials, the effect of temperature on fault slip and the deformation of heterogeneous fault zones.

Granular fault materials are known to dilate in response to increases in sliding velocity, resulting in significant pore pressure drops that can suppress instability, known as dilation hardening. Dilation hardening is a mechanism proposed to govern slow slip earthquakes. A suite of triaxial deformation experiments revealed that, upon a 10-fold velocity increase, gouges of systematically varied clay-quartz contents displayed measurable dilatancy. Peak dilation did not occur in the pure quartz gouges, but rather in gouges containing 10 to 20 wt% clay. A transition occurred at ~40 wt% clay content from strong, unstably sliding quartz-dominated gouges to weak but stably sliding clay-dominated gouges. These results indicate that in a low permeability, clay-rich fault zone, the increases in pore volume could transiently decrease pore-fluid pressure through dilatant hardening, thus contributing to the arrest of earthquake nucleation or the promotion of sustained slow slip.

The vast majority of previous experiments that investigated the frictional stability of phyllosilicate-bearing gouges were performed at room temperatures (~20°C), but elevated temperatures are known to affect frictional behaviour. There has not, to date, been a study that systematically documents the effect of frictional stability as a function of clay content and temperature. A suite of triaxial experiments showed that gouges containing ≤ 50 wt% clay became increasingly unstable with increasing temperature so that the materials displayed conditionally unstable slip at temperatures between 100 and 180°C, whereas at room temperature the same materials hosted only stable slip. This reduction in stability with increasing temperature coincides with a greater degree of localization observed in the gouge

microstructure. This indicates that a broad compositional range of clay-bearing fault rocks can nucleate unstable slip at conditions common to the shallow brittle crust.

The Carboneras Fault Zone (CFZ) in southern Spain is a 1km wide left-lateral, strike slip fault zone that consists of high-strain fault strands of phyllosilicate-rich gouges anastomosing with lower-strain lenses of basement protolith. The mechanical strength contrasts and geometry of the fault rock domains affect the distribution of strain through a fault zone. Field work was conducted in the Rambla del Cajon site in the core of the CFZ to collect samples for microstructural, chemical and frictional analyses to study how strain transferred from localising to non-localising fault materials and to search for microstructural evidence of seismicity. The fault samples showed strain localisation across multiple scales, with fault gouge strands ~10 m wide in the field to 200 μm wide in thin section. Quantification of the mineral contents of the fault rocks by X-Ray Diffraction (XRD) techniques showed that phyllosilicate minerals (muscovite/illite, chlorite, paragonite, kaolinite and smectite) dominated the assemblages. Frictional experiments showed that all of the tested fault materials were velocity strengthening, with a relatively low frictional strength contrast between the protoliths and the fault gouges. The fault gouges included pulverised quartz clasts that contained dauphiné twins, which can form due to seismic shock. It was concluded that the phyllosilicate-rich fault materials caused deformation on the CFZ to be dominated by aseismic fault creep, and that the anastomosing structure of the CFZ arose because of the low strength contrast between the protolith and fault rocks. However, the identification of pulverised quartz clasts indicates that intermittent seismic slip on the localising materials in the CFZ should not be discounted.

Acknowledgements

I feel extremely lucky to have had Dan and Betty as my PhD supervisors – firstly because they are amazing scientists, and secondly for their kind support, constructive critique and friendship even in the toughest of times. My PhD experience has been tough but it has made me far more confident and self-aware than I was at the start, and your belief in me has been no small part in that.

Moving to an entirely new city in 2018 was very intimidating, but I've gained so many wonderful friends in the Liverpool geology department in my 5 years there. To Elliot and Louisa, my lab buddies, I love you both dearly and I would never have gotten through this without you. You both helped me laugh through lab slip-ups, tough field days, endless admin and stressful conferences. Stay chaotic Elliot. Don't forget me when you're famous Louisa.

Thank you to Gary and Mike for your patience and care in training me on how to work in a lab. I'll miss our hours-long chats around the table in the lab, it was great craic! The rock def lab community, including JB, Joe A, Joe G., Marieke, Steve, Dave, Mahesh, Wheeler, Pier, Sam, was always so much fun to be a part of. I'm glad that everyone was very willing to eat the products of my stress baking!

I really appreciated the EAO DTP community in Liverpool and Manchester – it made such a difference to have friends who understood exactly what you go through at each stage of the PhD. Thank you also to my office friends in Liverpool, Amy, Jenny, Josh, Jade, Kate, Tegan, Chloe, and Dawid for keeping me (reasonably) sane, even if we were always complaining about that office!

One of the most (surprisingly) rewarding aspects of the PhD for me was demonstrating to the undergraduate students. I am so grateful that I was able to demonstrate on field trips to Anglesey, Ireland and Spain, so thank you to Graham, Charlotte, Dave, Betty, Pete, and Dan for trusting me with teaching your students.

I'm glad that despite my move to the north-west, I was able to keep in touch with my friends in the rest of the UK. I've known Raina since we were 10 years old and she is still one of my best friends – thank you for putting up with me and supporting me for so long Raina!

I was ecstatic when I found out that my friend from sixth form, Alfie, was coming to do a PhD in Liverpool too. I am so glad that we have reconnected and I'm blown away by how supportive Alfie has been of me, especially in this last year – you are an amazing friend and a real positive force in my life!

My friends from my undergraduate geology degree, Emma, Heather, Olivia, Robyn and Yannick, have always been there for me these last 10 years and I love them all for it, whether just for listening to me gripe via text or for organising escapes for long weekends together.

Finally, the biggest thank you goes to my family for their unconditional support. It's been the toughest 5 years of my life, with a global pandemic, loss and chronic illness, but you've gotten me through it. Grandma and Poppa never doubted that I could finish the PhD. Henry and Freddie have always had my back and were happy to help me reduce my stress by joining me on fun days out. I really struggle to put into words what the support from my Mum and Dad means to me – it genuinely makes me cry every time! I love you both very much and thank you for being my parents.

Contents

List of Figures

1. **Introduction**

The importance of understanding earthquake nucleation, propagation and recurrence cannot be understated, as the resultant ground shaking poses a threat to property, infrastructure and life. The recent M_w 7.8 and M_w 7.6 earthquakes in southern Turkey on the 6th February 2023, which led to the deaths of more than 50,000 people and over US$100 billion in damages (Zilio & Ampuero, 2023), are a stark reminder of the devastating power of earthquakes. Many hazard assessments and earthquake planning models are informed by seismic modelling that simulates the expected slip behaviours of an idealised fault or fault network (Dal Zilio et al., 2020; Lambert et al., 2021; Lapusta et al., 2000). Such seismic models are largely grounded in physical and microphysical laws or relationships observed from natural faults, earthquakes and from rock mechanics experiments.

An area of interest in rock mechanics research is the apparent discrepancy that occurs between natural fault behaviour and the data collected from rock deformation experiments. In particular, clay-bearing materials in rock deformation experiments consistently exhibit velocity-strengthening, stable creep behaviour, whereas clay-bearing, crustal-scale faults in nature have ruptured in high magnitude (M_w > 7) earthquakes. This exposes the limitations of applying results from rock deformation experiments to nature, in that it is not possible to recreate the conditions of natural fault deformation perfectly on the length and time scales that are available in a laboratory.

Many existing measurements of the frictional properties of phyllosilicate-rich fault gouges used unconfined shear apparatus, so that the experiments were conducted without any pore fluid pressure (Giorgetti et al., 2015; Ikari et al., 2007; J. M. Logan & Rauenzahn, 1987; Lupini et al., 1981; Meike, 1989; Saffer & Marone, 2003; Zhang et al., 2020). Another parameter that is often omitted from laboratory friction tests is that of temperature, which increases with increasing depth in the Earth's crust. Temperature is known to affect the frictional properties of rock, yet there are few studies that have measured this relationship systematically (Blanpied et al., 1995; Boulton et al., 2014; Den Hartog & Spiers, 2013; Mariani et al., 2006; Okamoto et al., 2019; Verberne et al., 2010). With the relatively recent recognition that natural fault slip encompasses a spectrum of slip behaviours ranging from aseismic creep, to slow slip and earthquake ruptures (Ikari, 2019; Ikari et al., 2020; Leeman et al., 2018; Obara & Kato, 2016; Peng & Gomberg, 2010), this thesis aims to investigate and quantify key mechanical processes and environmental conditions that control the frictional behaviour of clay-bearing fault materials to improve our physical models of fault slip.

1.1. Scientific Background:

The following section introduces the theory for frictional sliding, the spectrum of fault slip behaviours and details the properties of phyllosilicate minerals to provide context for the aims of this thesis, given in Section 1.2.

Faults and Friction:

A fault is a discontinuity in a volume of rock across which measurable displacement has been accommodated. Earthquakes usually occur on pre-existing faults, meaning that frictional processes (the resistance to motion of a body sliding tangentially on a surface) govern earthquake behaviour. Normal stress (σ_n) is supported by the adhesion of asperities on the fault planes or in the fault rock material, and for fault slip to initiate, the shear stress (τ) needs to exceed the shear strength of the asperities. This static friction (μ) relationship is given by:

$$\mu = \frac{\tau}{\sigma_n} \qquad \text{(Eq. 1.1)}$$

Byerlee (1978) conducted frictional experiments on a wide range of lithological materials and developed an empirical relationship demonstrating that the frictional strength of geological materials ranged from $0.6 \leq \mu \leq 0.85$. Borehole stress measurements suggest that Byerlee friction is applicable to natural faults (Byerlee, 1978; Sibson, 1994). Faults that appear anomalously weak may contain weak materials (e.g. phyllosilicates) or may be affected by high pore fluid pressures – the effective pressure law describes the role of pore fluid pressure in determining fault shear resistance:

$$\tau = \mu(\sigma_n - p) \qquad \text{(Eq. 1.2)}$$

where p is pore pressure (von Terzhagi, 1936). Hence, by increasing the pore pressure the apparent strength of a brittle fault will decrease, or vice-versa (Ougier-Simonin & Zhu, 2013).

Dynamic friction is the relationship between the shear stress and the normal stress that is required to maintain slip on an already sliding surface. If there is any variation in frictional resistance during sliding, a dynamic frictional instability can occur that causes sudden slip with an associated stress drop. The instability is usually followed by a period of no slip as the stress is recharged. This repeated stick-slip behaviour can be modelled using a simple spring loading model, as shown in Figure 1.1. In the model, the frictional resistance (F) to slip has a maximum value that decreases with further slip (u) along the slope of the spring stiffness (K). At point 1 in Figure 1.1, F decreases faster with increasing u than the slope (K), which causes acceleration to unstable slip due to the force imbalance in the system. At point 2, F becomes greater than the force in the spring so that the slip decelerates to a stop by point 3 in Figure 1.1. The condition for instability is:

$$\left|\frac{\partial F}{\partial u}\right| > K \qquad \text{Eq. 1.3}$$

These repeated stick-slip instabilities bear a close resemblance to natural earthquake behaviour, albeit in an over-simplified system – faults also cycle between periods of unstable slip in the form of earthquakes and 'locked' periods of no slip displacement as the stress recharges.

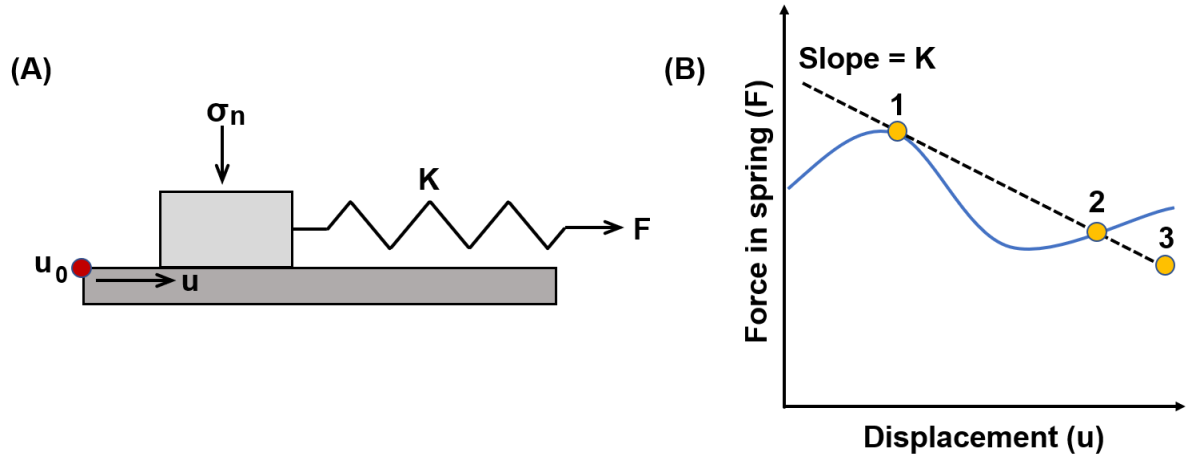

Figure 1.1: Schematic diagram showing (A) a simple spring and block model and (B) a theoretical graph of force (F) against displacement (u) where the frictional resistance falls with displacement at a rate faster than the system can respond (modified after Scholz, 2019). Point 1: acceleration phase of unstable slip. Point 2: deceleration phase of unstable slip. Point 3: deceleration of slip to zero.

Laboratory observations of the dynamic frictional response to imposed step changes in sliding velocity led to the development of the empirical rate and state frictional (RSF) laws (Dieterich, 1979). At sub-seismic slip rates (<1 m/s), fault strength is dependent on both the slip velocity (V) and the slip history of the fault (θ):

$$\mu = \mu_0 + a \ln\left(\frac{V}{V_0}\right) + b \ln\left(\frac{V_0 \theta}{D_C}\right) \qquad \text{Eq. 1.4}$$

Where μ_0 is the initial steady state friction coefficient at an initial slip velocity V_0 (m/s), a is the direct effect, b is the evolution effect, and D_C is the slip weakening distance (Dieterich 1979). The direct effect a is linked to the breaking of atomic bonds, whereas the evolution effect b results from the evolution of contact area or the evolving strength of the contact area (Dieterich, 1979; Ikari et al., 2009a; Li et al., 2011). A combined parameter of (a-b) is used to describe the dependence of friction on the velocity of fault slip (Figure 1.2) – a material with a positive (a-b) is velocity strengthening, but a material with a negative (a-b) is velocity weakening. Velocity strengthening materials are stronger at greater slip velocities, hence they are unlikely to host unstable slip and deform via stable creep. Velocity weakening materials can host unstable slip due to the weakening that accompanies the acceleration of slip. The

state variable θ in Eq. 1.4 has units of time and can be defined using one of two empirical laws:

$$\frac{d\theta}{dt} = 1 - \frac{V\theta}{D_C} \qquad \text{Eq. 1.5 (Aging Law)}$$

$$\frac{d\theta}{dt} = -\frac{V\theta}{D_C}\ln\left(\frac{V\theta}{D_C}\right) \qquad \text{Eq. 1.6 (Slip Law)}$$

The aging law predicts the evolution of the state variable even at $V = 0$ m/s, whereas the state variable in the slip law requires fault slip ($V \neq 0$ m/s). The application of these two state variables to rate and state friction modelling is contentious, as neither law fully describes the range of frictional behaviours observed in rock deformation experiments (Aharonov & Scholz, 2018; Ampuero & Rubin, 2008; Bhattacharya et al., 2017; Dieterich, 1979, 1992; Rathbun & Marone, 2013; Ruina, 1983; Segall & Rice, 1995; van den Ende et al., 2018). Several composite rate and state friction frameworks have been proposed to account for stick-slip behaviour, conditionally stable slow fault slip, dilatancy, and temperature effects (Aharonov & Scholz, 2018; F. M. Chester & Higgs, 1992; N. Kato & Tullis, 2001; Niemeijer & Spiers, 2007; Rubin, 2008; Samuelson et al., 2009; Segall et al., 2010; Segall & Rice, 1995; van den Ende et al., 2018).

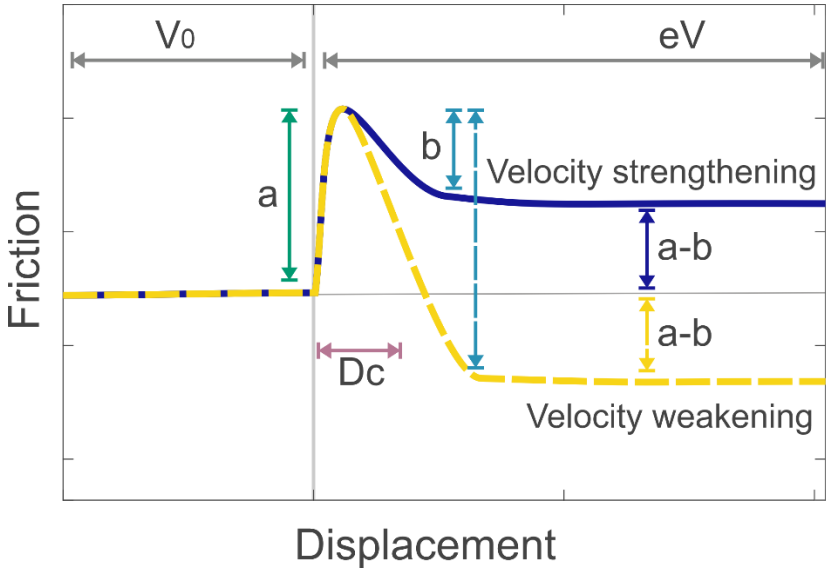

Figure 1.2: Schematic graph showing the rate and state frictional response to e-fold changes in sliding velocity in velocity strengthening (blue solid line) and velocity weakening (yellow dashed line) materials (modified after Dieterich, 1979).

The incorporation of temperature into the rate and state frictional framework has been based around the application of Arrhenius-type laws to asperity contacts or indentation hardness (Aharonov & Scholz, 2018; Blanpied et al., 1998; F. M. Chester & Higgs, 1992; van den Ende et al., 2018). Arrhenius laws predict the temperature dependence of reaction rates:

$$k = Ae^{\frac{-Q}{RT}}$$ Eq. 1.7 (modified after Arrhenius, 1889)

Where *k* is a rate constant, *A* is a pre-exponential factor, *Q* is the activation energy, *R* is the universal gas constant (8.3145 J/mol K) and *T* is temperature in Kelvin. An example of the formulation of this temperature-dependent rate and state friction is in Chester and Higgs (1992). By assuming that the thermally activated slip mechanisms can be described using an Arrhenius relationship, the rate and state constitutive equations (Eq. 1.4 to 1.6) can be altered to:

$$\mu = \mu_0 + a\left(\ln\frac{V}{V_0} + \frac{Q_a}{RT}\right) + b\theta$$ Eq. 1.8

$$\frac{d\theta}{dt} = -\left(\frac{V}{D_C}\right)\left(\theta + \ln\frac{V}{V_0}\right) + \frac{Q_b}{RT}$$ Eq. 1.9

Where Q_a is the activation energy in the direct effect and Q_b is the activation energy in the evolution effect, which assumes that the two effects are governed by different mechanisms. Thus, the steady state friction equation in Eq. 1.4 can be rewritten as:

$$\mu = \mu_0 + (a-b)\ln\frac{V}{V_0} + (aQ_a - bQ_b)/RT$$ Eq. 1.10

The drawbacks of the temperature-dependent rate and state friction laws are that they were formulated based on the deformation of quartz powders (F. M. Chester & Higgs, 1992), granite powders (Blanpied et al., 1998) or were based on computational modelling (Aharonov & Scholz, 2018; van den Ende et al., 2018). The general lack of experimental data that systematically varies temperature in friction experiments on minerals other than quartz (Boulton et al., 2014; Den Hartog & Spiers, 2013; Verberne et al., 2010) limits our understanding of the activation energies of frictional deformation mechanisms in natural, clay-rich fault gouges.

Slow Slip Earthquakes:

Previously, it was thought that elastic stress accrued by active faults was released either by aseismic fault creep or through rapid (~1 m/s) earthquake ruptures. With the ongoing improvement of geodetic monitoring and the coverage of seismic monitoring networks, our understanding of the seismic cycle developed to include a spectrum of fault slip behaviour between these end members (Figure 1.3). Slow slip earthquakes or events (SSE) release accrued elastic stress via discrete fault slip events, as with traditional earthquakes, but the duration of SSE can last from days to years (Dal Zilio et al., 2020; Ide et al., 2007; Ikari et al., 2015, 2020; Im et al., 2020; Leeman et al., 2016; Michel et al., 2019; Peng & Gomberg, 2010; Voss et al., 2018; Wallace et al., 2017). SSE are usually detected using geodesy techniques that track the offset of the Earth's surface as SSE slip at rates from just above plate velocity

to 100 times the plate motion rates (Dal Zilio et al., 2020; Ide et al., 2007). Some types of SSE register on seismographs, such as: tremors, which are continuous vibrations that have durations on the scale of minutes (Figure 1.3A); Very Low Frequency Earthquakes (VLFE Figure 1.3B) that last for 10s of seconds; and Low Frequency Earthquakes (LFE, Figure 1.3C) that have durations on the order of less than a second (Dal Zilio et al., 2020; Leeman et al., 2016; Peng & Gomberg, 2010). Whilst 'traditional' fast earthquakes obey a cubic relationship between moment magnitude (M: the integral of slip over the rupture area multiplied by the shear modulus) and duration (T), SSE appear to have an apparent scaling that is linear ($M \propto T$) (Figure 1.4). This view is currently under debate, as individual sets of observations in this broader picture appear to show cubic scaling ($M \propto T^3$) (Dal Zilio et al., 2020; Frank & Brodsky, 2019; Michel et al., 2019; Takagi et al., 2019). Fast earthquakes are modelled using a circular-crack model, in which a circular rupture experiences a constant stress drop that expands at a constant rate (Kanamori & Anderson, 1975). If the geodetically detected SSE do have a linear moment magnitude-duration relationship, this could be explained by the elongated rupture areas that propagate along the full width of the seismogenic fault (Dal Zilio et al., 2020; Frank & Brodsky, 2019; Michel et al., 2019; Takagi et al., 2019).

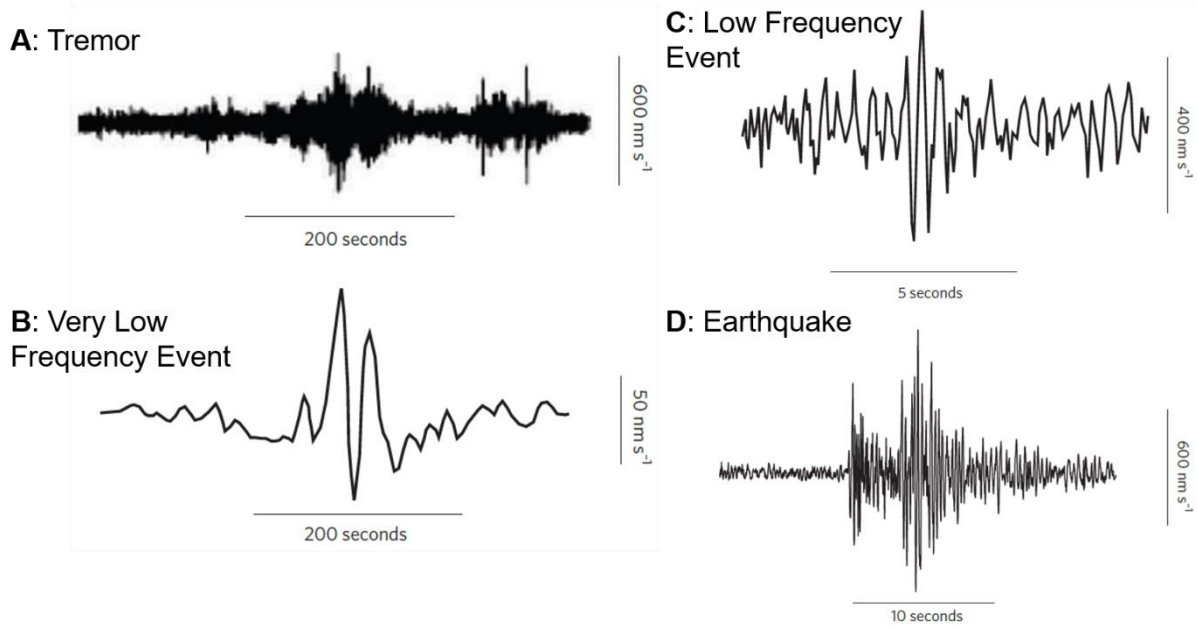

Figure 1.3: Illustrative examples of seismic wave signals from various earthquake phenomena including: (A) tremors, (B) Very Low Frequency Events (VLFE), (C) Low Frequency Events (LFE) and (D) 'traditional' fast earthquakes (Adapted from Peng & Gomberg (2010)).

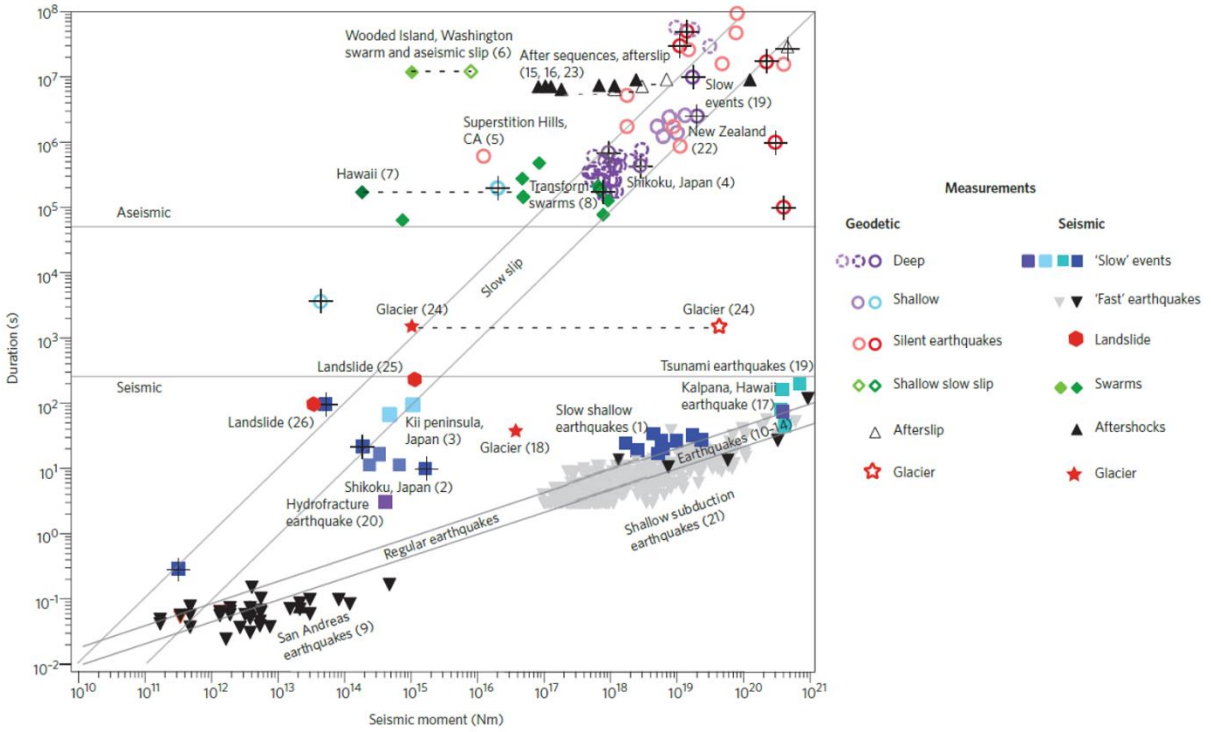

Figure 1.4: Duration (s) against the seismic moment (N_m) of fault slip events from fault zones across the globe (labelled) – discrete fault slip events show relationships of moment magnitude to duration ranging between linear and cubic (Peng & Gomberg, 2010 and references therein).

SSE are of interest to the earthquake science community because of the potential to release or load stress across a fault network, which could avert or trigger seismic slip (Ikari et al., 2013, 2020; Peng & Gomberg, 2010; Voss et al., 2018). Fast earthquakes can trigger SSE (Wallace et al., 2017) or arrest SSE (Wallace et al., 2014), and SSE may load locked fault patches to failure (Ito et al., 2013; A. Kato & Nakagawa, 2014; Miyazaki et al., 2011). The driving mechanisms that cause SSE to accelerate beyond plate motion rates, but that prevent the run-away acceleration to fast earthquake slip rates are not fully constrained (Ikari, 2019; Ikari et al., 2020). SSE occur in regions of high pore fluid pressures and low effective normal stresses, such as on the subduction interface, due to the dehydration of hydrous minerals (Peng & Gomberg, 2010; Wallace et al., 2017). The low effective normal stresses make the faults highly sensitive to pressure fluctuations, such as from propagating seismic waves or transient pore fluid pressures. Dilatant hardening has been suggested as a mechanism to prevent the acceleration of slow slip to fast earthquake slip rates, as a drop in pore fluid pressure due to dilation of the fault increases the apparent fault strength, thus preventing run away slip acceleration (Ougier-Simonin & Zhu, 2013; Rathbun & Marone, 2013; Samuelson et al., 2009; Segall et al., 2010; Wallace et al., 2017).

Phyllosilicate Minerals in Fault Rocks:

The frictional behaviour of phyllosilicates is of interest to rock mechanics as these unusually structured sheet silicates are simultaneously systematically weaker than other silicate

minerals and of common occurrence in crustal-scale fault and shear zones (Byerlee, 1978; Crawford et al., 2008; Giorgetti et al., 2015; Ikari et al., 2007, 2009a; J. M. Logan & Rauenzahn, 1987; Lupini et al., 1981; Mariani et al., 2006; Meike, 1989; Ruggieri et al., 2021; Saffer & Marone, 2003; Takahashi et al., 2007; Tembe et al., 2010a; Zhang et al., 2020). Phyllosilicate minerals are common components of fault rocks because of the cataclasis and comminution during fault slip and the circulation of pore fluids through fault and fracture networks. Faults can act as fluid pathways as the permeability in the direction parallel to the fault surfaces can be several magnitudes higher than the permeability of the host rock and the direction perpendicular to the fault plane (Faulkner et al., 2003, 2010). The reduction of grain size and the opening of fluid pathways through a fault increases the rock surface area that is available for hydrothermal alteration to form phyllosilicate minerals.

Multiple drilling projects through crustal-scale faults have revealed active principal slip zones (PSZ) that are rich in phyllosilicate minerals, such as the San Andreas Fault in USA, the Nankai Trough near Japan, and the Alpine Fault Zone in New Zealand. Parkfield in California was chosen as the site of the San Andreas Fault Observatory at Depth (SAFOD) to target the transition between the creeping and locked sections of the SAF (Solum et al., 2006; Zoback et al., 2011). The Parkfield segment of the SAF ruptures on various timescales including repeating microearthquakes of M_w ~2.0 with recurrence periods of months to years, M_w 6.0 earthquakes that occur on 20-40-year cycles such as in 2004, and the estimated 150-year cycle of earthquake slip in the locked patches of the SAF, such as in 1906 (Ben-Zion et al., 1993; F. M. Chester & Logan, 1987; J. Murray & Langbein, 2006). The drilling at SAFOD has revealed various fault cores within the SAF with clay contents between 1 and 69 wt% (Schleicher et al., 2010; Solum et al., 2006).

Following the M_w 9.0 Tohoku-Oki earthquake and resulting tsunami on the 11th March 2011, the International Ocean Drilling Project (IODP) targeted the Nankai Trough off the south coast of Japan (F. M. Chester, Mori, et al., 2013). As part of the Japan Trench Fast Drilling Project (JFAST) and IODP expedition 343, the fault decollement was successfully drilled and cored at 820 mbsf (F. M. Chester, Rowe, et al., 2013; Fulton et al., 2013; Ujiie et al., 2013). The recovered PSZ and damage zone were <10 m thick and included a 4.68 m thick ‘brown scaly’ clay (F. M. Chester, Mori, et al., 2013; F. M. Chester, Rowe, et al., 2013; Ujiie et al., 2013). Smectite, illite and kaolinite formed 77 wt% of the fault material in the PSZ (Fulton et al., 2013; Remitti et al., 2015). Kilometres of slip displacement had been accommodated within such a narrow (<10 m) zone because the clay-rich material was significantly weaker than the host rocks, which led to long term slip localisation (F. M. Chester, Rowe, et al., 2013; Ujiie et al., 2013). The Tohoku-Oki earthquake was so unusual because it ruptured by a 50 m offset along

the fault all the way to the trench axis and this caused a nearly total stress drop (F. M. Chester, Rowe, et al., 2013).

A final example of a phyllosilicate-bearing, crustal-scale fault is the right-lateral, transpressional Alpine Fault Zone (AFZ), which separates the Pacific and Australian tectonic plates. In the central AFZ in the South Island of New Zealand, the Deep Fault Drilling Project (DFDP-1) recovered cores from a PSZ of the 'blue' and 'brown' fault gouges, which contained 16 % and 31 % clay, respectively (Boulton et al., 2014; Toy et al., 2015). The significant seismic hazard posed by the AFZ is due to the episodic ruptures of M_w 8 earthquakes at ~300-year intervals. The previous surface-rupturing earthquake along the AFZ occurred in 1717 (Berryman et al., 2012; Boulton et al., 2014), which implies that another M_w 8 earthquake will rupture the AFZ within a few decades.

Phyllosilicate Mineral Properties:

Phyllosilicate minerals are composite structures formed of layers of silicate tetrahedral and octahedral layers (Aslin et al., 2019; Behnsen & Faulkner, 2012; Bergaya et al., 2011; Brindley & Bradley, 1951; G. Brown, 1982; Deer et al., 2013; Hendricks, 1942; Hey, 1954; H. H. Murray, 2006; J. V Smith & Yoder, 1956). A cation (Si^{4+}, Al^{3+} or Fe^{3+}) is joined to 4 O atoms and the tetrahedra are linked by sharing 3 corners, to form a continuous hexagonal mesh (T, Figure 1.5A) along the *a* and *b* crystallographic directions (Aslin et al., 2019; Bergaya et al., 2011; Brigatti et al., 2006; G. Brown, 1982; Hendricks, 1942; H. H. Murray, 2006). The octahedral sheets (M, Figure 1.5B) can contain a wide range of cations (e.g. Al^{3+}, Fe^{3+}, Fe^{2+}, Mg^{2+}) and connect by sharing edges in a hexagonal or pseudo-hexagonal symmetry (Aslin et al., 2019; Bergaya et al., 2011; Brigatti et al., 2006; G. Brown, 1982; Hendricks, 1942; H. H. Murray, 2006). A perfect basal cleavage between the layers is a defining characteristic of the atomic structure of phyllosilicates. The atomic layers can be bound by charge-balancing interlayer cations, Van der Waals forces or hydrogen bonding, depending on the electrical charge of the layer (Bergaya et al., 2011; H. H. Murray, 2006).

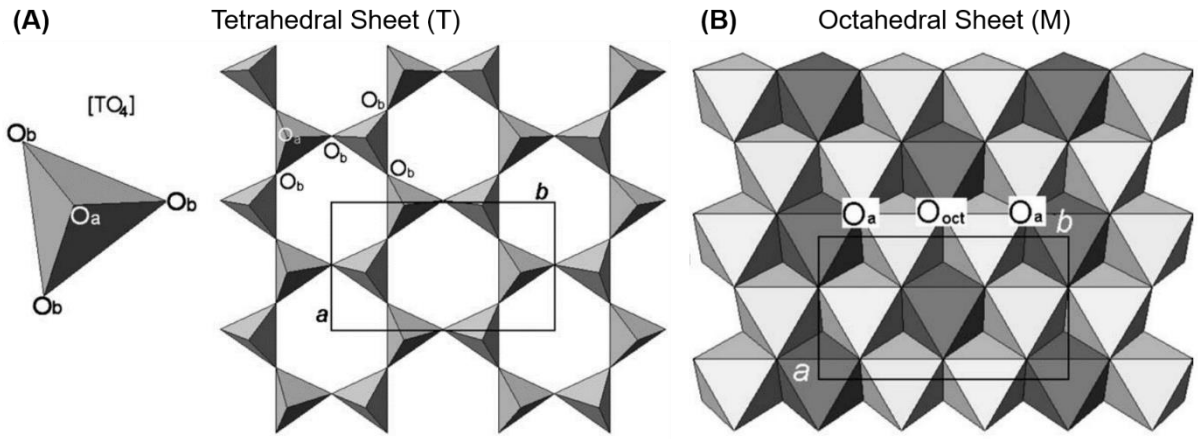

Figure 1.5: Schematic diagrams of the structure of (A) the tetrahedral sheets and (B) the octahedral sheets in phyllosilicate minerals (adapted from Brigatti et al., 2006). O_a is an apical oxygen atom, O_b is a basal oxygen atom and a and b refer to the unit cell parameters.

Phyllosilicate minerals are categorised by the structure of the octahedral layer, the sequence of atomic layers and the composition of the cations in the octahedral layer (Table 1.1). In a brucite-type octahedral layer, all of the cation sites are filled and the cations have a charge of 2+ (e.g. Fe^{2+}, Mg^{2+}), but in a gibbsite-type octahedral layer the cations have a charge of 3+ (e.g. Al^{3+}) and not all of the cation sites are filled. This gives rise to dioctahedral or trioctahedral phyllosilicates, depending on the number of atomic bonds on the O or OH ions (2 trivalent or 3 divalent cations, respectively). Groups of phyllosilicates can be further subdivided through the ratio of tetrahedral (T) to octahedral (M) atomic layers (Table 1.1). Two major groups of phyllosilicate minerals are the micas and clays. Mica minerals can be generated in igneous bodies, as weathering products in sedimentary lithologies, or as secondary metamorphic minerals. Clay minerals are generated through hydrothermal alteration or weathering of silicate minerals. Certain swelling-type clays have variable layer separation distances due to intercalation of water in the atomic structure – the substitution of cations into the atomic structure creates a negative charge on the crystal surface, which results in hydrogen bonding between the crystal surface and water molecules. Clay minerals often contain both structural water within the crystal lattice and surface-bonded water. When clay minerals are exposed to elevated temperatures, the clay minerals first lose the surface-bonded adsorbed water and then the structural water in the atomic lattice at higher temperatures (Brady et al., 1996; Y. Han et al., 2020; Horváth et al., 2003).

	Phyllosilicate Group:	Minerals	T to M ratio	Inter-layers	Formation
Mica Groups	Dioctahedral mica	Muscovite, paragonite	2:1	K^+ cations	Crystallisation of igneous lithologies, metamorphism, alteration of alumino-silicates
	Trioctahedral mica	Phlogopite, biotite, lepidolite	2:1	K^+ cations	Crystallisation of igneous lithologies, metamorphism,
	Chlorite	Chlorite	2:1:1	Brucite layer	Metamorphism, hydrothermal alteration
	Serpentine	Lizardite, antigorite, chrysotile	1:1	-	Hydrous alteration of Mg-silicates – enstatite, forsterite
Clay Groups	Kaolinite	Kaolinite, dickite, halloysite	1:1	-	Alteration of alumino-silicates – Feldspars
	Illite	Illite, phengite	2:1	K^+ cations	Alteration of muscovite, feldspars
	Smectite	Montmorillonite, talc, vermiculite, hectorite, saponite	2:1	H_2O, alkali cations	Alteration of igneous lithologies – basalt, gabbro, volcanic deposits

Table 1.1: Summary table of the major phyllosilicate mineral groups, showing the different layer structures and the formation methods.

Strong framework silicate minerals in granular fault materials deform via cataclastic mechanisms, such as fracturing, grain rolling and dilation. The weak interlayer bonds in phyllosilicate minerals allow slip or ripples along the basal plane, which, due to the weakness of Van der Waals forces and hydrogen bonding, can occur at far lower applied stresses than cataclastic deformation mechanisms (Aslin et al., 2019; Kushima et al., 2015). The platy shape of phyllosilicate minerals causes the grains to be susceptible to compaction, as the grains will preferentially align the basal planes. As the phyllosilicate minerals are significantly weaker than other silicate minerals, it is generally accepted that, at shallow depths, strain is preferentially accommodated in phyllosilicate-rich regions of fault rocks.

Heterogeneous Fault Zones:

Unusual fault slip phenomena, such as SSE, often occur in faults that consist of heterogeneous materials or have complex fault geometries (Collettini et al., 2011; Dieterich & Smith, 2009; Fagereng & Sibson, 2010; Goebel et al., 2017; Tesei et al., 2014; Thomas, Avouac, Gratier, et al., 2014). A simple fault model (Figure 1.6A) includes the localisation of strain onto a single fault core surrounded by a damage zone of off-fault fracturing (F. M. Chester & Logan, 1986; Faulkner et al., 2003, 2010). Observations of mature, plate-bounding faults (Collettini et al., 2011; Fagereng & Sibson, 2010; Faulkner et al., 2003; Rutter et al., 2012; Tarling et al., 2019) have shown that faults can have broad (up to ~1 km wide) core structures that incorporate blocks or lenses of low strain protolith between anastomosing, high-strain fault strands. This led to the development of a more complex fault model (Figure 1.6B)

that can accommodate shear via elastic strain on discrete fault planes within or on the boundaries of competent fault blocks, in addition to distributed shear in the non-competent matrix (Collettini et al., 2011; Fagereng & Sibson, 2010; Faulkner et al., 2003; Rutter et al., 2012; Tarling et al., 2019; Tesei et al., 2014). Commonly, the anastomosing fault strands are rich in phyllosilicate minerals and are strongly foliated (Collettini et al., 2011; Faulkner et al., 2003; Tarling et al., 2019). The geometry of the fault rock domains and the mechanical strength contrasts between the fault rock lithologies can affect the propagation of seismic ruptures through the fault zone (Ben-Zion & Shi, 2005; Tesei et al., 2014; Thomas, Avouac, Gratier, et al., 2014) and would trigger different dynamic weakening mechanisms in response to accelerated fault slip (Collettini et al., 2011; Rice, 2006).

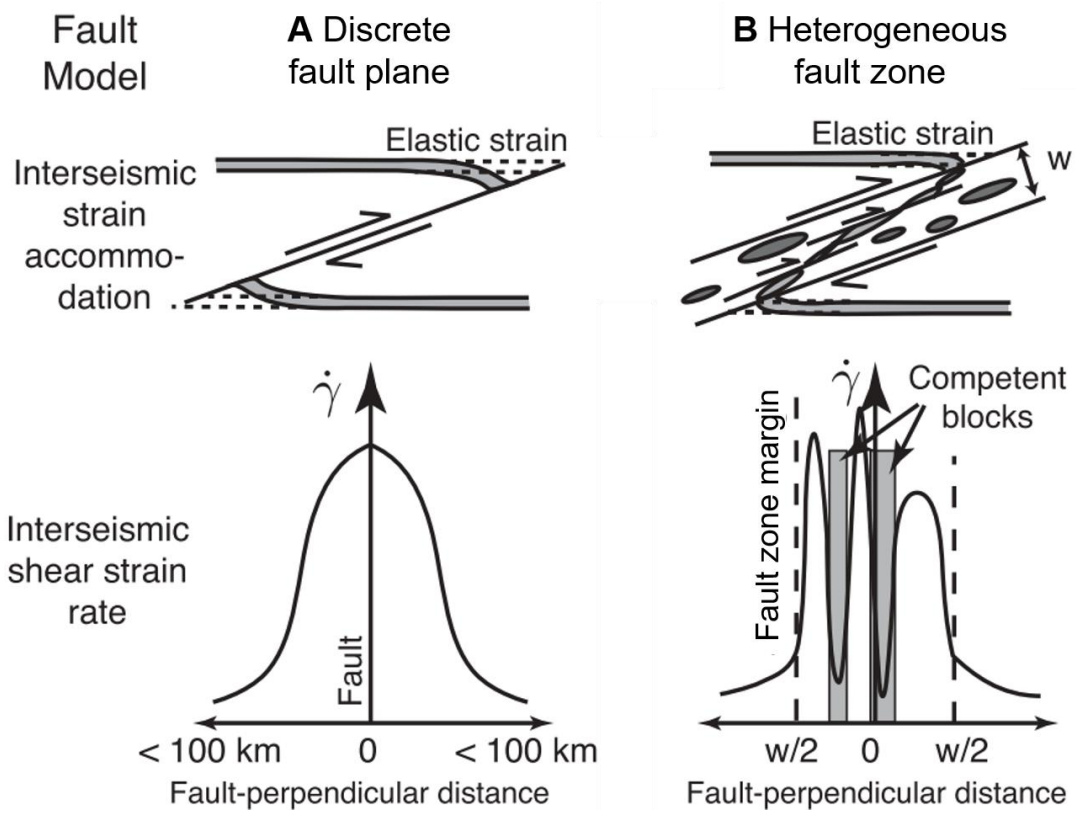

Figure 1.6. Schematic fault models that accumulate fault slip across: (A) a single high strain fault core of infinitesimal thickness; (B) a heterogeneous fault zone of width (w) undergoing mixed localised and distributed deformation (modified after Fagereng & Sibson, 2010). In model A, inter-seismic strain ($\dot{\gamma}$) is accommodated by elastic deformation of the rigid wall rock, whereas in model B the shear strain rate is highly variable as shear is accommodated by both aseismic creep in the non-competent matrix and by rapid seismic ruptures in the competent fault blocks.

A fault zone's geometric and structural heterogeneity, and the subsequent stress distributions, influence the expected magnitudes of fault ruptures (Candela et al., 2012; Dieterich & Smith, 2009; Goebel et al., 2017; Gutenberg & Richter, 1944; King, 1983; Manighetti et al., 2007). The relative proportion of small- to large-magnitude earthquakes is described using the Gutenberg & Richter (1944) relationship:

$$\log_{10} N = a - bM \qquad \text{Eq. 1.11 (Gutenberg \& Richter, 1944)}$$

Where *N* is the number of earthquake events, *a* is productivity, *b* or the *b-value* is the exponent that describes the potential for seismic events to grow to large magnitudes (*M*). Following this relationship, the number of earthquake events exponentially decreases with increases in the event magnitude, as observed in natural faults and in the laboratory (Goebel et al., 2013, 2017; Gutenberg & Richter, 1944). Potential controls on the *b-value* include stress levels (Scholz, 1968), and fault geometry (e.g. bends, discontinuities, segmentation, transfer zones) or fault 'roughness' (King, 1983). 'Rough' (high *b-value*) faults have smaller effective contact areas, which generates localised high stresses at the contact asperities (M. Chester & Chester, 2000; Dieterich & Kilgore, 1996; Dieterich & Smith, 2009; Fang & Dunham, 2013; Goebel et al., 2013). The local stress heterogeneities lead to small-magnitude, highly localised ruptures so that seismicity is distributed across the fault zone (Dieterich & Kilgore, 1996; Dieterich & Smith, 2009; Fang & Dunham, 2013; Goebel et al., 2013, 2017). Rough faults are normally immature, as they have accommodated offset of less than 10 – 100 m (Candela et al., 2012; Dieterich & Kilgore, 1996; Fang & Dunham, 2013; Goebel et al., 2013). As slip accumulates on a fault, the permanent damage from the yielding of asperities decreases the fault roughness to produce a 'smooth' (low *b-value*) fault with a more homogeneous stress field, which is less likely to release elastic strain in small magnitude events (Candela et al., 2012; M. Chester & Chester, 2000; Dieterich & Kilgore, 1996; Dieterich & Smith, 2009; Fang & Dunham, 2013; Goebel et al., 2017). Fault roughness and lithological heterogeneities can explain the variation in seismic coupling (from locked to aseismic creeping) along fault strike or with increasing depth (Goebel et al., 2013; Lambert et al., 2021; Lapusta et al., 2000; Thomas, Avouac, Gratier, et al., 2014).

1.2. Thesis Aims:

The overall aim of this thesis is to investigate and quantify the mechanical processes that control the frictional behaviour of phyllosilicate-bearing fault materials, so as to improve the data available for micromechanical- and seismic modelling. To expand on this, the specific aims of this thesis are:

- To develop new rock deformation experimental equipment and techniques with the aim of bridging the gap between laboratory and natural conditions.
- To measure, in quantifiable terms, the changes in the frictional behaviour of fault materials due to clay content by producing simulated fault gouges that systematically vary the clay content between 0% and 100%.
- To investigate the effect of the deformation variables on the frictional behaviour of clay-bearing fault gouges, including effective normal stress and temperature.

- To investigate the potential mechanisms that could drive slow slip earthquakes, such as dilatant hardening, high pore fluid pressure conditions, and heterogeneous fault structures and lithologies.
- To evaluate the evidence for mixed-mode seismicity in a natural fault zone by investigating the accommodation of strain across heterogeneous fault structures and lithologies.

1.3. Thesis Structure and Status of Manuscripts:

Chapter 2 describes the equipment, techniques and methods that were utilised throughout this research, including the rock deformation apparatus, scanning electron microscopy, field techniques and chemical analyses.

Chapter 3: The effect of clay content on the dilatancy and frictional properties of fault gouge. This chapter presents experimental data that investigate the effect that changing clay content has on the frictional strength, stability and pore volume dilatancy in fault gouges.

Submitted to Journal of Geophysical Research: Solid Earth.

Manuscript submission: 27th October 2022

Major revisions received: 2nd December 2023

Manuscript 1st resubmission: 14th February 2023

Minor revisions received: 23rd February 2023

Manuscript 2nd resubmission: 23rd March 2023

Manuscript accepted: 25th March 2023

Manuscript published: 11th April 2023

Author contributions:

- I.R. Ashman: main author, methodology development, data acquisition, data analysis, visualisation, discussion;
- D.R. Faulkner: conceptualisation, funding acquirement, training, methodology development, supervision, discussion, manuscript review.

Chapter 4: Clay-rich gouges become unstable at higher temperatures. This chapter presents experimental data measuring the effect of increasing temperatures on the frictional stability of kaolinite-quartz simulated fault gouges.

Manuscript complete, to be submitted to Nature Geoscience.

Author contributions:

- I.R. Ashman: main author, conceptualisation, methodology development, data acquisition, data analysis, visualisation, discussion;
- D.R. Faulkner: conceptualisation, funding acquirement, methodology development, supervision, discussion, manuscript review;
- E. Mariani: conceptualisation, funding acquirement, training, supervision, discussion, manuscript review.

Chapter 5: Strain accommodation in heterogeneous shear zones: the Carboneras Fault Zone. This chapter presents observations from field work in the Carboneras Fault Zone in the region of Almeria in southeast Spain. Microstructural, chemical and rock deformation experimental analysis techniques were used to investigate the mechanisms of deformation in a heterogeneous fault zone.

Manuscript to be drafted for Geology.

A manuscript detailing the microstructures of the potentially pulverised quartz clasts in the fault rocks of the Carboneras Fault Zone, with a specific focus on EBSD experiments that will build on the work in Chapter 5, will be drafted for submission to The Geological Society of America journal '*Geology*'. This is in response to the manuscript published in '*Geology*' by Rodríguez-Escudero et al., (2020) that observed similar quartz clasts from the Alhama de Murcia fault, which is located 80 km to the north of the Carboneras Fault Zone.

Chapter 6 summarises the findings of the individual research projects, evaluates the success of the thesis aims, and suggests avenues for further research.

1.4. Funding Information:

In 2018, I.R. Ashman was awarded a NERC Earth Atmosphere & Oceans (EAO) Doctoral Training Studentship with the NERC grant reference number: NE/L002469/1 at the University of Liverpool. Due to the impact of the Covid-19 pandemic from March 2020 to March 2022, including national lockdown, laboratory closures and restricted access to the Rock Deformation Laboratory, the NERC funded studentship was extended by 6 months. The unfunded submission pending phase of the studentship was extended by an additional 6 months by the University of Liverpool.

2. Methods

All of the deformation experiments in this project were conducted on a high-pressure triaxial deformation apparatus designed by D.R. Faulkner in the Rock Deformation Laboratory at the Department of Earth, Ocean and Ecological Sciences at the University of Liverpool. Electron microscopy analyses in this project were conducted in the Scanning Electron Microscopy Shared Research Facility (SEM SRF) at the University of Liverpool. This chapter describes the development and implementation of the bespoke experimental apparatus as well as the qualitative and quantitative microscopy and chemical analysis techniques used to complete this project, including the methods, software and work strategies adopted.

2.1 Experimental Apparatus:

The high-pressure triaxial deformation apparatus was first described in Faulkner & Armitage (2013) and it can be used for hydrostatic pressure tests, permeability measurements and axisymmetric compressional and extensional tests (Figure 2.1). The maximum working pressures for the triaxial apparatus are 250 MPa for confining pressure and 200 MPa for pore pressure, so that the apparatus is capable of maintaining conditions equivalent to ~10 km depth in the Earth's crust. All of the deformation experiments undertaken in this project were axisymmetric compression tests. In these experiments, the maximum principal stress (σ_1) is applied by the axial loading column and the intermediate and minimum principal stresses (σ_2 and σ_3) are applied equally by the confining medium:

$$\sigma_1 > \sigma_2 = \sigma_3 \quad \text{(Eq. 2.1)}$$

2.1.1. Sample Assembly:

The sample assembly (Figure 2.2) houses the connections between the sample within the pressure vessel and the control systems of the triaxial apparatus (Figure 2.3). In the sample assembly, a cylindrical rock core or a fault gouge sample contained in direct shear sliders is held between an upper and a lower block. To fit the sample assembly platens, both sample types have diameters of 20 mm and maximum lengths of 60 mm for a rock core and 100mm for the assembled direct shear sliders. The upper sample assembly block houses an inlet that connects the interior of the pressure vessel to the confining pressure control system. Two thin bore high-pressure pipes (of internal diameter 0.5 mm), which are sealed to the upper block by high-pressure glands, connect the top (upstream) and base (downstream) of the sample to the pore pressure control system. The upstream inlet is housed within the upper assembly block, whereas the downstream inlet passes through the upper block to the lower block and the base of the sample via another thin bore pipe, which spirals around the sample. A support ring attaches the upper and lower blocks of the sample assembly to protect the coiled downstream pore pipe from damage.

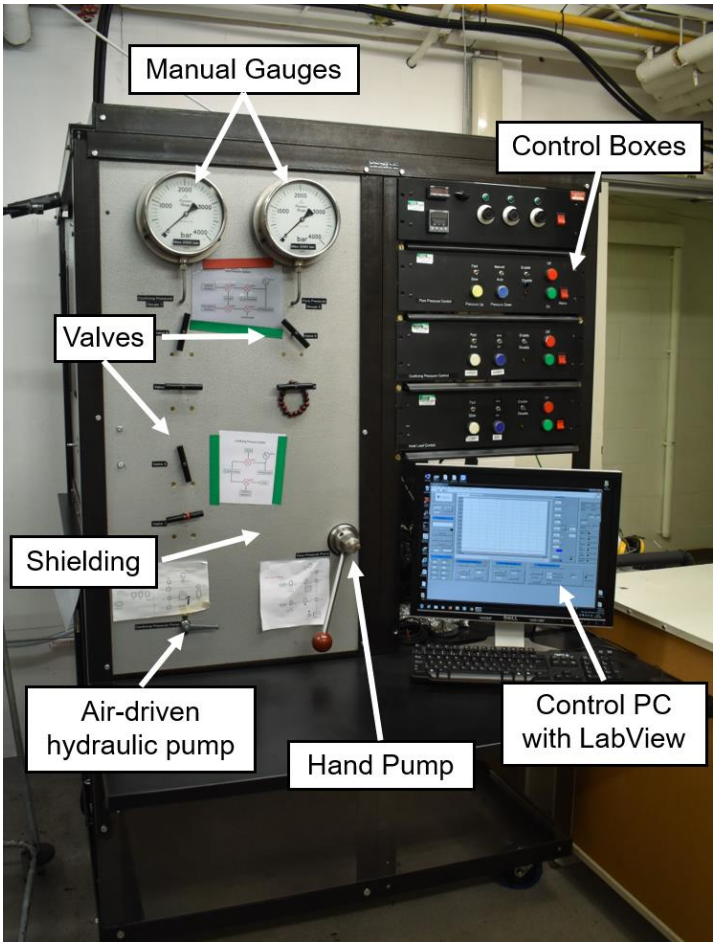

Figure 2.1: Triaxial Deformation Apparatus 2 (TR2) in the Liverpool Rock Deformation Laboratory.

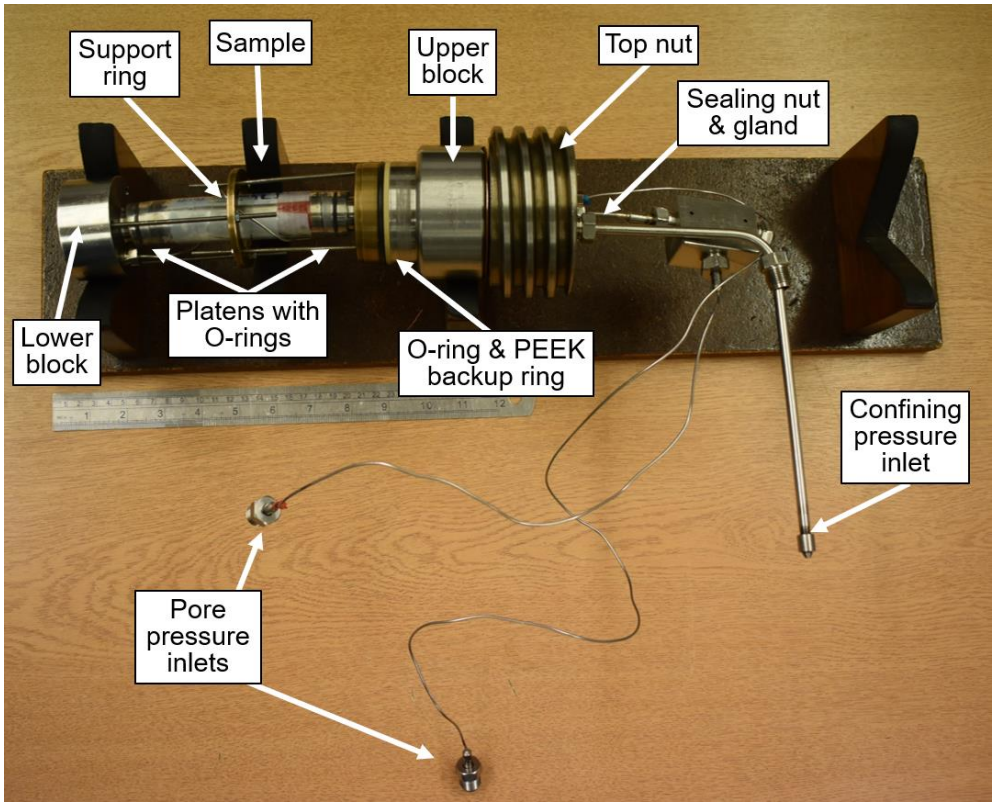

Figure 2.2: The sample assembly containing an assembled direct shear slider sample.

2.1.2. Confining Pressure System:

The pressure vessel is located at the top of the loading column and is attached by the bottom nut to the force gauge column. The hot work tool steel (Jessop Saville H.50 AISI H13) has an outer diameter of 180 mm and an internal bore of 60mm diameter, in which the sample assembly is accommodated (Figure 2.4). The sample assembly is secured in the pressure vessel by a threaded top nut and an O-ring acts as the pressure seal with a PEEK (polyether ether ketone) backup ring that prevents extrusion of the O-ring into the vessel. Silicon oil (10 cSt viscosity) is used as the confining medium in tests conducted at room temperature. In accordance with the High-Pressure Safety Code, the pressure vessel has been tested to pressures 1.5 times the maximum working pressure (375 MPa for a maximum of 250 MPa confining pressure).

Confining pressure is controlled and monitored by a network of pumps, valves and transducers (Figure 2.3). Initial loading of confining pressure is done through an air-driven SC hydraulic pump, while a second servo-controlled pump is used to maintain the working pressure during tests. The servo-controlled Nova-Swiss 10 cc pump is set to control a maximum volume range of 6500 mm^3 that can adjust for 20-30 MPa pressure change. The main reason for changes in confining pressure during a test is from driving the axial piston, which changes the volume within the pressure vessel. A manual gauge and a RDP TJE differential pressure transducer with 0.007 MPa resolution are both used to monitor the confining pressure within the vessel. A Linear Variable Differential Transducer (LVDT) measures the position of the control pump and acts as a volumometer for the confining medium.

2.1.3. Pore Pressure System:

The pore pressure can be applied to a maximum pressure of 200 MPa using a medium of either liquids or inert gases such as argon. For tests using a medium that is liquid at room temperature (e.g. brine, deionised water), pore pressure is primed through a Nova Swiss hand pump. When using a gas medium, pore pressure is primed using a gas booster (Haskel AGT-32/152H) that can reach a maximum of 120 MPa. A series of valves can isolate the upstream and downstream ends of the sample from the priming and control pumps. By closing the valve to one end of the assembly, the permeability of the sample can be measured using either the pulse transient decay method or the pore pressure oscillation technique (see Section 2.3). Pore pressure is measured by two RDP transducers located on the upstream and downstream sides of the sample. Once at the target pore pressure, a Nova-Swiss 5 cc pump is used to control the pore pressure during a test (Figure 2.4).

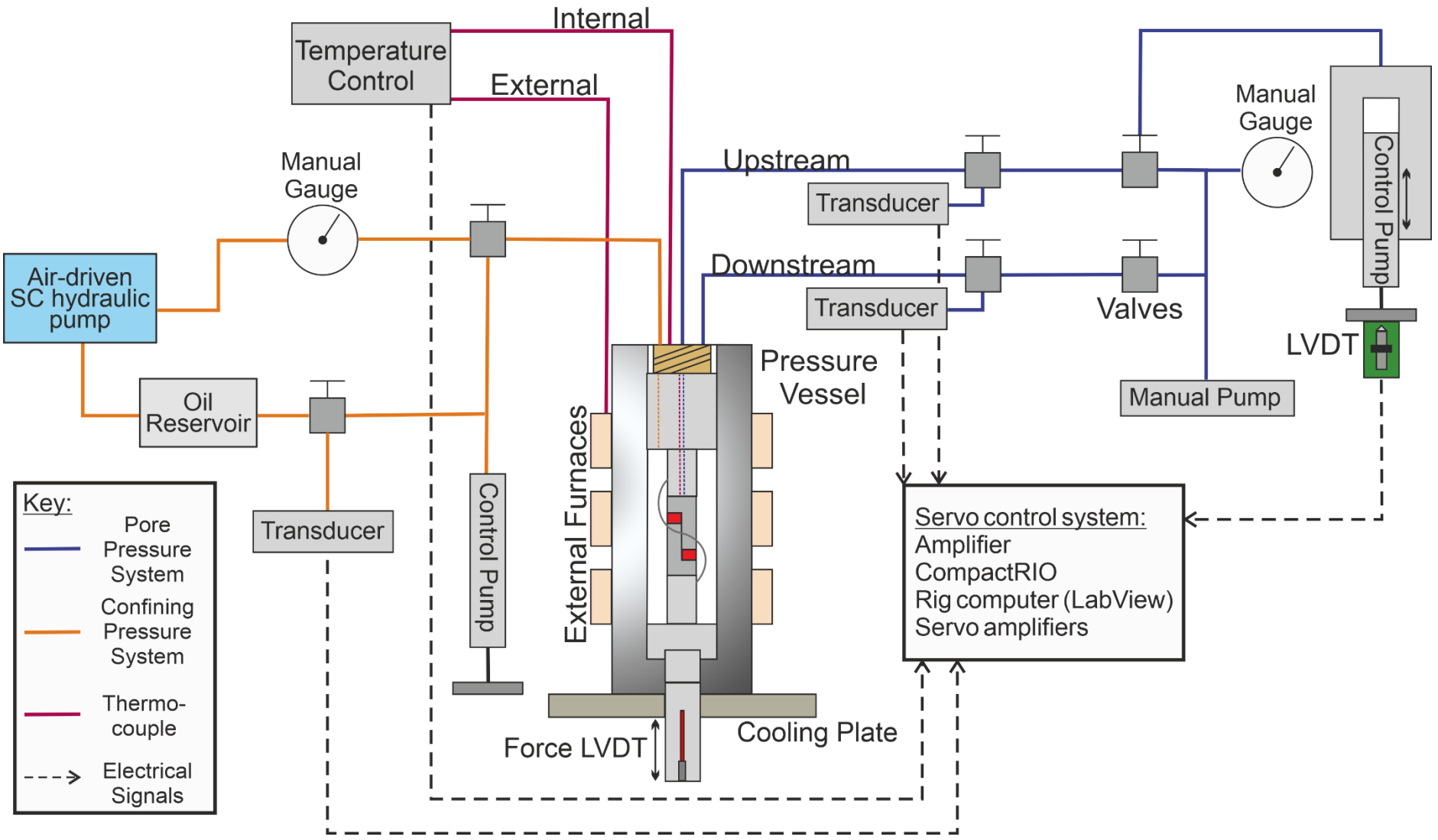

Figure 2.3: A schematic diagram of the pore pressure, confining pressure and temperature control systems on the triaxial deformation apparatus.

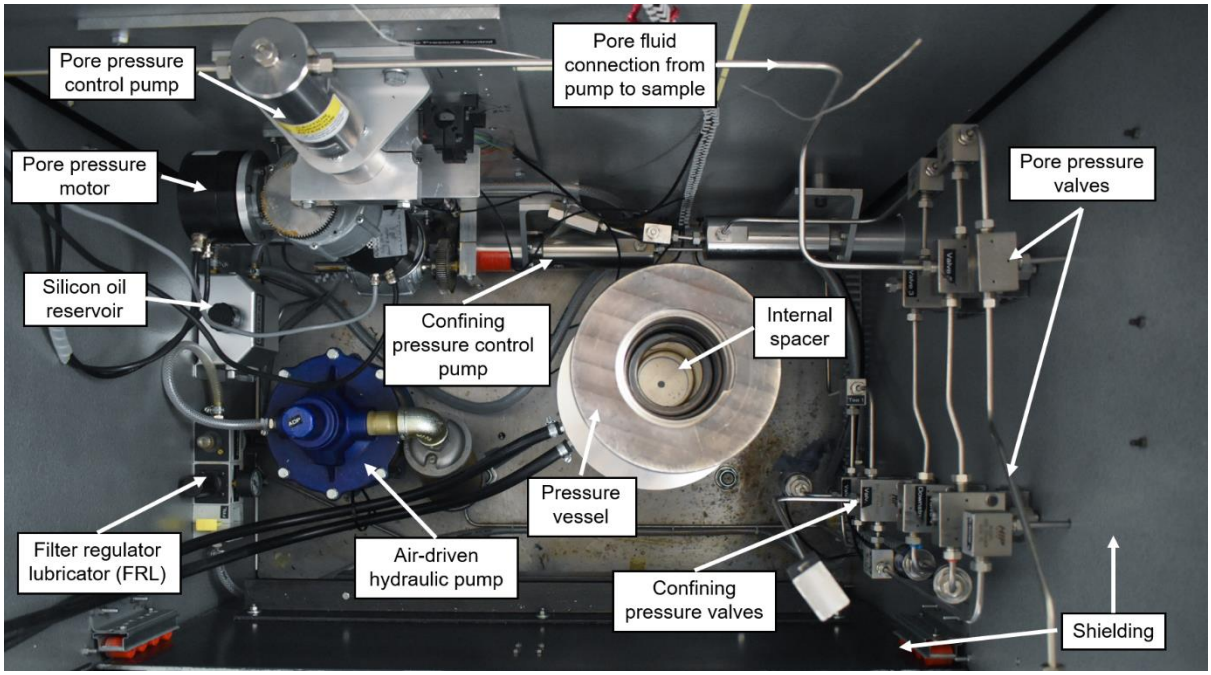

Figure 2.4: The top-down view into the interior of TR2.

The maximum servo-controllable volume of pore fluid within the control pump is 4000 mm^3 and the volume change in the pump relates directly to pore volume changes within the sample. A LVDT is used to monitor the position of the pump within its stroke and, as the area of the piston is known, the LVDT acts as a volumometer. Trigger switches act as hardware limits for the piston strokes of both the pore pressure and confining pressure control systems (Figure 2.5).

As a target of the experiments in this project includes small scale (<1 mm^3) transient volume changes, an upgrade to the existing pore volume monitoring system had to be applied. A RDP D6/01000A – L10 LVDT with a linear range of ±1 mm was added to monitor the pore pressure control pump. The limited range of the D6 LVDT means that it cannot monitor the full stroke of the pump. Hence, the LVDT was mounted on an adjustable platform that can be moved along a runner into position for the start of an experiment (Figure 2.5). The high resolution of the D6 LVDT revealed a periodicity in the movement of the pore pressure pump that was not previously evident (Figure 2.6). To stiffen the displacement measuring assembly connected to the main piston, all parts were replaced with steel counterparts and the LVDT was mounted to be <2 cm from the piston connection to the steel plate. Previously a perspex plate was used to measure the displacement of the piston. As shown in Figure 2.6, the changes to the pore pressure control pump eliminated the periodicity in the signal. When calibrated, the D6 LVDT has a resolution of 0.01 mm^3 and a range of 210 mm^3, which is sufficient for a direct shear experiment with load point displacements of up to 8.5 mm. Total sample volume reduction was always less than 200 mm^3 for velocity step tests on fault gouge materials.

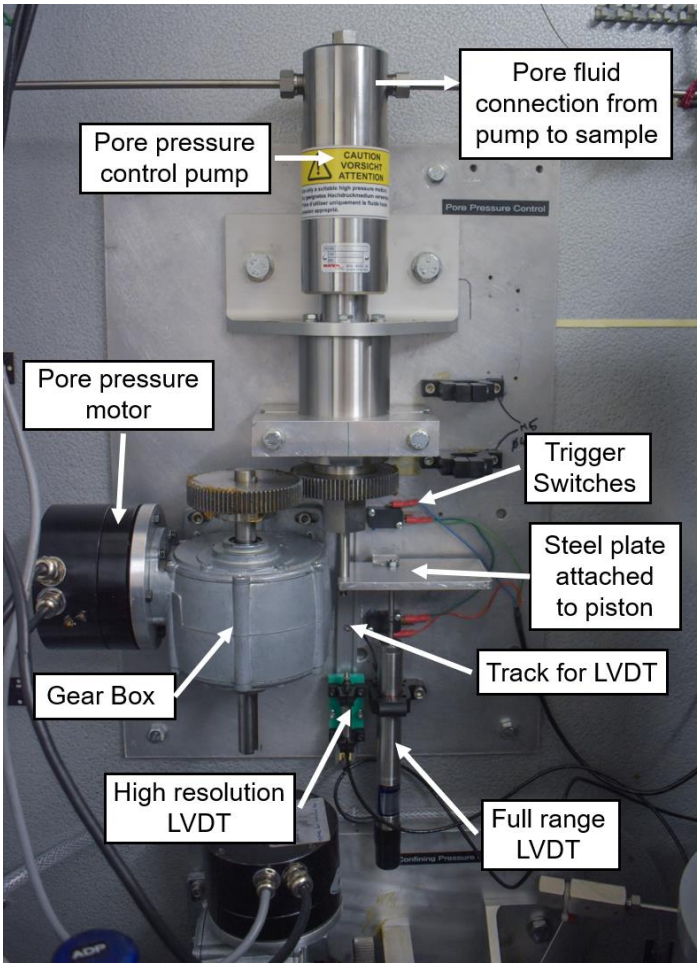

Figure 2.5: The pore pressure control system on TR2.

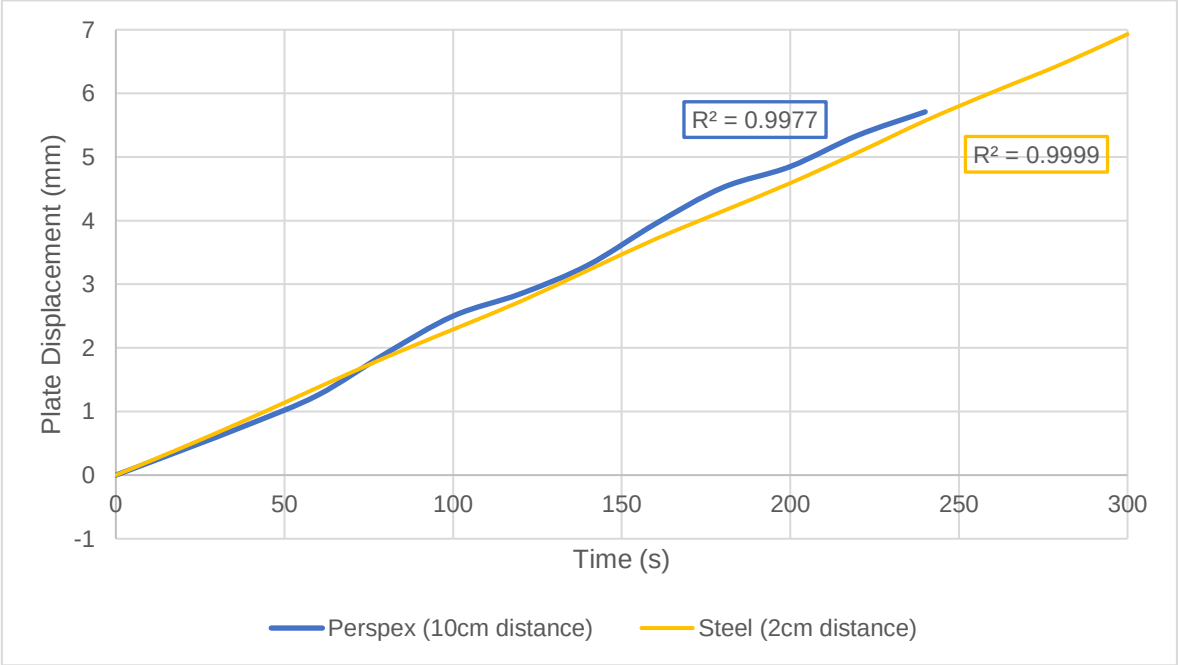

Figure 2.6: A graph showing the displacement of the plate attached to the pore pressure control pump before adjustments (perspex plate) and after adjustments (steel plate).

2.1.4. Axial Loading System:

Below the pressure vessel is the axial loading column, comprising the driving motor, gear box, axial piston and the force gauge column. The base of the axial loading system is attached to the underside of the apparatus baseplate by 8 M16 high tensile bolts (8.8 grade). The system is driven by a Printed Motor Works GM12 pancake-type servo motor that connects into a gear train of 3 gearboxes with a total gear ratio of 20700:1. A Parvalux gearbox with a gear ratio of 115:1 is attached to a Hydro-mec worm gearbox at 36:1 and the final connection is to a drive gear at 5:1. This system drives a BXR ball screw that can withstand a maximum load of 500 kN. An anti-rotation THK ball spline with a hemispherical base connects to the ball screw and ensures that the load from the ball screw is applied concentrically.

Above the ball spline is the force gauge assembly that houses an LVDT used to measure the force acting on a sample during an experiment by monitoring the elastic distortion of the force gauge casing. The force gauge assembly extends into the pressure vessel, and the casing is made of maraging steel (M300) with a yield strength of ~2 GPa. The pressure vessel seals to the force gauge assembly through a dynamic Variseal (nano-PTFE flouroelastomer) with 2 PEEK back-up rings to prevent extrusion into the vessel. A LVDT with a spring-loaded long armature is housed within the force gauge extension above the level of the dynamic seal. This avoids the need for a seal friction correction. To produce a force measurement, the LVDT measures the elastic distortion of the force gauge column to a resolution of <0.03 kN. A correction is applied to the force gauge measurement to account for the effect of increasing confining pressure on the measured force value. The displacement of the ball screw is measured by a LVDT at the base of the axial loading system. This load point displacement is used as a reference for sample displacement because after the sample yields, the force on the sample does not vary very much and, for the velocity steps, the stiffness of the apparatus is accounted for in the processing. The maximum vertical displacement of the system is 16 mm. The driving speeds that can be maintained by the drive train range from 0.01 μm/s to ~20 μm/s.

2.1.5. Temperature System:

In experiments that are conducted at elevated temperatures, an external furnace is added to the triaxial deformation apparatus (see Figure 2.3). Three Chromalox knuckle band heaters encircle the pressure vessel and the heat is conducted through the vessel to the sample. Although the maximum temperature of the knuckle band heaters is 870˚C, the experiments at elevated temperatures are limited by other components of the triaxial deformation apparatus. The hot-work tool steel of the pressure vessel has maximum service temperatures of ~400˚C. The direct shear sliders and silicon spacers further limit temperatures to below 200˚C, due to the risk of bending the shear sliders and fluidising the silicon spacers used in the friction

assembly (see Section 2.2.3). At operating temperatures above 100˚C, the sample is contained in a Viton jacket in place of a PVC jacket because the PVC becomes unstable and fails at these temperatures. The individually controllable knuckle band heaters are spaced along the height of the pressure vessel to control and minimise any temperature gradient across the sample. Previous calibration tests have shown the temperature gradient across the length of the sample to be <2˚C (Leclère et al., 2016).

One challenge in running friction experiments at elevated temperatures are the readings collected from the force gauge. The temperature produces an offset on the force gauge due to temperature effects on the electronics, which is accounted for in the calibration applied through LabView to the raw voltage data from the force gauge. As the temperature increases, the elastic properties of the loading column will change, thus affecting the measurement of elastic distortion of the loading column used in the force measurement (Section 2.1.4). At experimental conditions of 200°C, the reduction in tensile strength of the loading column would introduce an error of ~7% into the force gauge readings (Nickel Development Institute, 2015). To minimise the conduction of heat through the sample assembly to the force gauge column, a bespoke cooling plate sits between the base of the pressure vessel and the loading column. A TAE EVO Chiller (now ICS Cool Energy's i-Chiller Compact) pumps water chilled to 15˚C through the cooling plate, which reduces heat conduction to the force gauge assembly. Hence, the maximum error in the force gauge measurement is ~7% at the highest operating temperature used, but it is likely far lower.

During the operation of an elevated temperature test, two thermocouples are used to monitor the temperatures of the knuckle band heaters and the sample within the pressure vessel. Both the internal and external thermocouples are K-type (nickel-chromium/nickel-aluminium) surface temperature and immersion thermocouples. The internal thermocouple is run through the top block of the sample assembly through the pore pressure pipework to contact the top of the direct shear slider assembly. The range of the thermocouple measurements is -200 to 1100˚C with a sensitivity of 41 μV/˚C. The external furnace system is controlled through a West P6100+ unit using solid state relays to provide power to the knuckle band heaters. A target temperature is set in LabView (Section 2.1.6) and is referenced to the temperature recorded by the internal thermocouple. A West N2300 monitor records and displays the temperature of the external knuckle band heaters.

2.1.6. Control Systems:

The control systems on the deformation apparatus use a PC and a Compact Rio (NI9024) that work in tandem to measure and adjust the conditions throughout the experiment. On the PC, the LabView software written by D.R. Faulkner allows the user to input working set points

(WSP) for the control of confining pressure, pore pressure, temperature and load point displacement. The LabView software has procedures for different experiments in the program that allow the user to run velocity step tests, pore pressure oscillations and constant force or displacement tests. A series of software limits (Table 2.1) are imposed on the deformation apparatus to prevent the program from running the systems beyond safe limits and so protects the hardware from damage. This is an additional safety feature on top of hardware limits.

LabView Software Limits	Maximum	Minimum
Force (kN)	200	-1
Displacement (mm)	17	1
Confining Pressure Pump (mm^3)	6500	0
Pore Pressure Pump (mm^3)	4000	0

Table 2.1: The software limits used in the LabView program on the triaxial deformation apparatus.

The transducers that measure conditions within the pressure vessel send a millivolt (mV) signal to an amplifier so that it can be read by the ±10 V NI-cRIO. The amplified signals are received by 4 channel, 16-Bit analogue input modules contained within the casing of the NI-cRIO. A servo loop compares the signals received from the transducers and the WSP in LabView. Any mismatch causes the RIO to send a signal out through a 4 channel, 16-Bit analogue output module to the corresponding control box. The magnitude of the signal is adjusted by the proportional gain, integral gain and derivative gain (PID) settings (see Table 2.2). A servo-amplifier in the control boxes amplifies the signal to drive the actuators that connect to the control pumps. The control boxes can also operate independent of the LabView software by using a set of manual controls for the actuators.

PID Gain Settings	Proportional Gain	Integral Gain	Derivative Gain
Confining Pressure (holding)	75	0.3	0
Pore Pressure (holding)	10	0	0
Displacement	250	0	0
Temperature	4	15	5.5

Table 2.2 Example PID settings used in LabView to control the signal sent from the RIO to the apparatus control boxes.

The LabView software applies calibrations to the raw voltage data to produce the correct units of pressure, volume or force. To calibrate the ±10 V transducers, the voltage output is compared to external pressure gauges and a load cell. The voltage is plotted against the output of the gauges and the gradient of the best fit line and the calculated intercept are applied to produce the calibrated data. The force gauge has additional calibrations for the applied

confining pressure and the temperature. The calibration values are checked and updated regularly for all of the deformation apparatus.

2.2. Sample Preparation:

Consistent sample preparation is vital in deformation experiments, especially when using a synthesised material as an analogue for natural materials. The research in this project required the development of a clear methodology for the mixing and building of the fault gouge samples.

2.2.1. Simulated Gouge Preparation:

The benefit of using simulated gouges in deformation experiments is that the properties of the gouge are controlled, so that the effect of only one changing variable can be tested. For the experiments in Chapters 3 and 4, a set of simulated gouges with incremental changes in clay composition were produced. The clay chosen for testing was kaolinite, on account of its non-swelling properties when wet, its common occurrence in fault rocks and its stability up to temperatures of 450˚C (Brady et al., 1996; Chakraborty, 2014; Y. Han et al., 2020; Horváth et al., 2003). A kaolinite powder (KGa-1B) from the Clay Mineral Society was chosen for its purity at >99 % with minimal TiO_2 impurities (Vogt et al., 2002). KGa-1B is sourced from the Tuscaloosa Formation in Georgia, USA, and has a very fine grain size with 57 wt% at <2 μm (Pruett & Webb, 1993; Vogt et al., 2002). A quartz powder from the US Silica Company was chosen as the second gouge component because the quartz powder Min-U-Sil 15 is widely used in rock deformation experiments and is well characterised (Bedford & Faulkner, 2021). Min-U-Sil 15 is sourced from the St. Peters Formation in Missouri, USA. It also has a purity of >99 % and is sieved to grain sizes of <15 μm. To verify the grain size distributions in the chosen materials, a Beckman-Coulter LS Particle Size Analyser was used to measure the grain diameter distributions for KGa-1B and Min-U-Sil 15. The laser diffraction of aqueous suspended samples returned average grain sizes of 3.7 μm for Min-U-Sil 15 and 4.7 μm for KGa-1B – the distribution of grain diameters are shown in Figure 2.7. It is expected that the KGa-1B data was affected by partial flocculation of the kaolinite grains in the aqueous solution, despite the addition of an anti-flocculation agent.

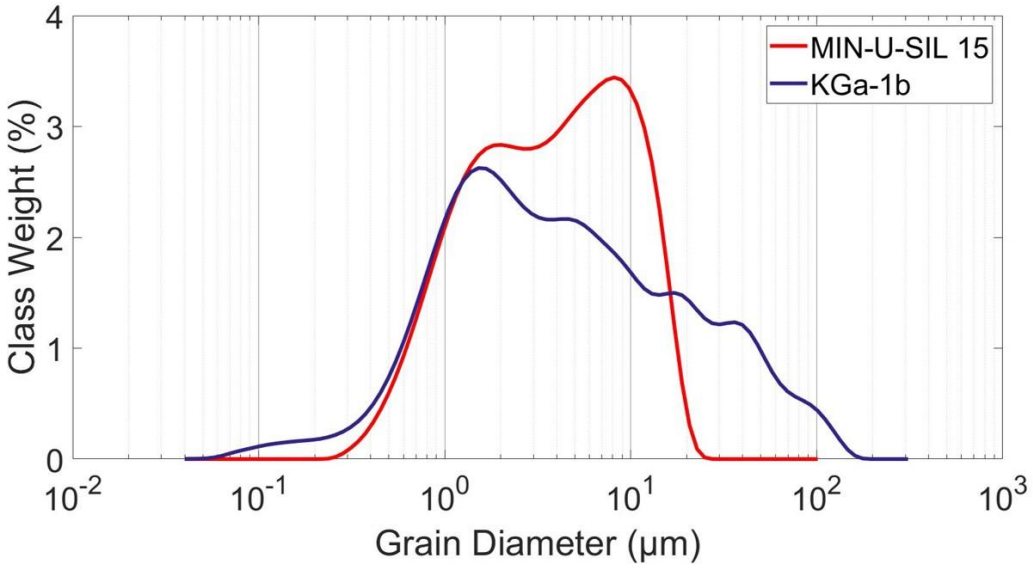

Figure 2.7: The grain size distribution of KGa-1B and Min-U-Sil 15 measured using a laser diffraction particle size analyser.

As both the quartz and kaolinite powders have densities of 2.65 g/cm^3, the simulated gouges were mixed by weight rather than by volume. Both mixing in suspension and dry tumbling methods were tested, but the dry tumbling was considered sufficient to produce a random mixture as the similar densities of the two materials promote mixing over segregation (Williams, 1968). Also, the mixing in suspension introduced several problems, such as the slow settling out of fine material from suspension and the need to break up the dried product. A 2 lb Pro Evans Stone Tumbler was used to turn the 20 g powder samples for a 3-hour period at 68 rpm in a 575 cm^3 plastic container. The mixing was halted every hour to check that the materials were still mixing freely. Initially, the mixing process was compromised by the build-up of static electricity between the tumbler and the plastic container. This caused the powders to both adhere to the walls of the container and to clump into monomineralic balls, both of which produced heterogeneous powders. Consequently, a grounding wire and plug were attached to the plastic container, so that the plastic container would not retain a static charge during the 3-hour tumbling period. This effectively prevented the build-up of static electricity in the quartz and kaolinite powders and produced more homogeneous simulated fault gouge powders.

2.2.2. Field Sample Preparation for Frictional Experiments:

In addition to the microstructural and chemical techniques used in the field study (Section 2.4), six samples of fault gouge and rock were tested in the triaxial deformation apparatus to ascertain the frictional strength and rate and state frictional (RSF) behaviour of the natural fault materials. The samples that had been selected for frictional analysis had to be crushed to powders for use in the direct shear sliders to allow direct comparisons between non-cohesive fault gouges and cohesive rock samples. The material was crushed in a disc mill

Nickel Tema crusher for 10 seconds and then sieved to grain sizes of <125 μm for use in the direct shear slider assembly (Section 2.2.3). It was necessary to grind any remaining material coarser than 125 μm for another 10 seconds in the disc mill, so as to avoid any fractionation of minerals by grain size or competency.

2.2.3. Direct Shear Sliders

To conduct friction experiments on fault gouge samples, the sample requires an arrangement where a layer of gouge is contained by a jacket. One such configuration uses two rock cores with 30˚ or 45˚ sawcut surfaces that act as the fault walls. This sawcut setup poses a problem for the control of normal stress on the inclined fault surfaces during axial loading. Application of an axial load will increase both shear and normal stress on an inclined sample, so that the deformation apparatus must constantly adjust the confining pressures to maintain the desired normal stress. Also, the properties of the bounding rocks (e.g. permeability) will affect the outcome of the experiments.

The direct shear slider assembly was developed by D.R. Faulkner based on equipment used in the High Pressure and Temperature (HPT) lab in Utrecht to minimise these issues for fault gouge friction experiments. In this configuration, the axially applied load directly increases the shear stress on the sample, which means that normal stress will not be affected by axially loading the sample. A direct shear assembly set includes two identical 17 – 4 stainless steel sliders that sandwich the gouge sample. The steel has been heat treated to a hardness of Rockwell C45 to give the sliders a yield strength of 1350 MPa. All the sliders have a diameter of 20 mm when assembled so as to fit the platens of the sample assembly. There are three different sizes of direct shear sliders with sample lengths that range from 25 mm to 50 mm (see Table 2.3).

Sliders	Length (mm)	Area (mm^2)	Sample Weight (g)	Uniaxial pre-compaction at 50 MPa (tonnes)	Max. Displacement (mm)
Short	25	500	1.4	2	3.5
Medium	36	720	1.6	3.6	5.5
Long	50	1000	2.2	5	8.5

Table 2.3: Parameters for sample preparation in the three direct shear slider configurations.

A central borehole drilled through the sliders connects the sample to the pore pressure control system of the deformation apparatus. Two to three stainless steel porous disks (SIKA-R AX) with permeabilities of 10^{-12} m^2 fit within 8- or 10-mm diameter seats in the sample area of the sliders. The porous disks prevent the extrusion of fine gouge particles into the pore pressure pipework and increase the area of pore fluid exchange, which reduces the generation of pore pressure gradients within the sample. Thus, permeability can be measured across the

thickness of a fault gouge sample using techniques such as pore pressure oscillation or pulse transients. In the early tests of the direct shear slider design, it was found that failure of the sample occurred along the interface of the gouge and the slider. To improve the cohesion between the slider and the gouge, the slider surface area was machined with grooves of 0.5 mm depth that were oriented perpendicular to the direction of shear. The microstructures of samples sheared in the sliders with the machined grooves show that failure is contained fully within the gouge.

An important component in the design of the direct shear sliders is the material that compresses during shear to allow the movement of the sliders relative to each other. A weak elastic material is ideal because: it shows no strain rate dependence in velocity step tests; it poses little resistance to gouge deformation; and it does not undergo permanent deformation. The chosen silicon-based gasket material (Vital Red RTV) meets these requirements, as its strength is barely resolvable in the deformation apparatus and it shows no jumps in strength in response to velocity changes. The silicon spacers are prepared in the laboratory to three different lengths to fit the different slider lengths. The silicon-based gasket material is designed for high temperature (343°C) applications but at temperatures >200°C the risk of fluidising the silicon spacers becomes unacceptable, as it would extrude into the sample and the pore pressure pipework. Hence, elevated temperature experiments were limited to maximum temperatures of 180°C (Chapter 4).

The process of preparing a sample for a deformation experiment in the direct shear sliders is shown in Figure 2.8. Gouge thickness in the direct shear sliders is designed to be ~1 mm, so the weight of gouge used in the sample depends on the size of the sliders. For the simulated quartz-kaolinite gouges used in Chapters 3 and 4, the weight of gouge to a unit of area to produce ~1 mm thickness was calculated at 2.2 kg/m^2 (0.0022 g/mm^2). The correct weight of gouge for the slider, given in Table 2.3, is poured over one of the pair of sliders that is held within a bespoke jig (Figure 2.8.B). After the gouge is planed out, the jig is placed in a Sealey floor-type uniaxial hydraulic press (max load 20 tonnes) and put under a load specific to the sample area (Table 2.3) to compact the gouge. This pre-compaction improves the cohesion of the gouge for the construction of the sample.

After the sample has been compacted, the slider is removed from the jig and married with the other slider. A PTFE sleeve is taped to the sliders to act as a low friction barrier between the sliders and the PVC or Viton jacket (Figure 2.8.G). The PTFE sleeve is necessary to allow free movement of the sliders and to prevent mild stick-slip behaviour between the sliders and the jacket, which was observed in early friction tests using the direct shear sliders. The two types of jacket used, PVC or Viton, are heated in an oven set at 60˚C until it is more malleable,

at which point it is placed in an attachment to a vacuum pump (Figure 2.8.H). An O-ring and a hollow steel wedge are used to seal the PVC or Viton tube when the vacuum pump is turned on (Figure 2.8.I). Under vacuum, the jacket material is enlarged so that the assembled direct shear sliders can pass through the wedge into the jacket. Once the sliders are in place, the vacuum is released and the jacket collapses around the sliders (Figure 2.8.J). A final circle of PTFE is added to one end of the sample to prevent coupling between the sliders and the platens of the sample assembly and to allow compaction of the sample. The PVC or Viton jacket extends over the O-rings on the sample assembly platens and isolates the sample from the silicon confining oil when the confining pressure exceeds the pore pressure.

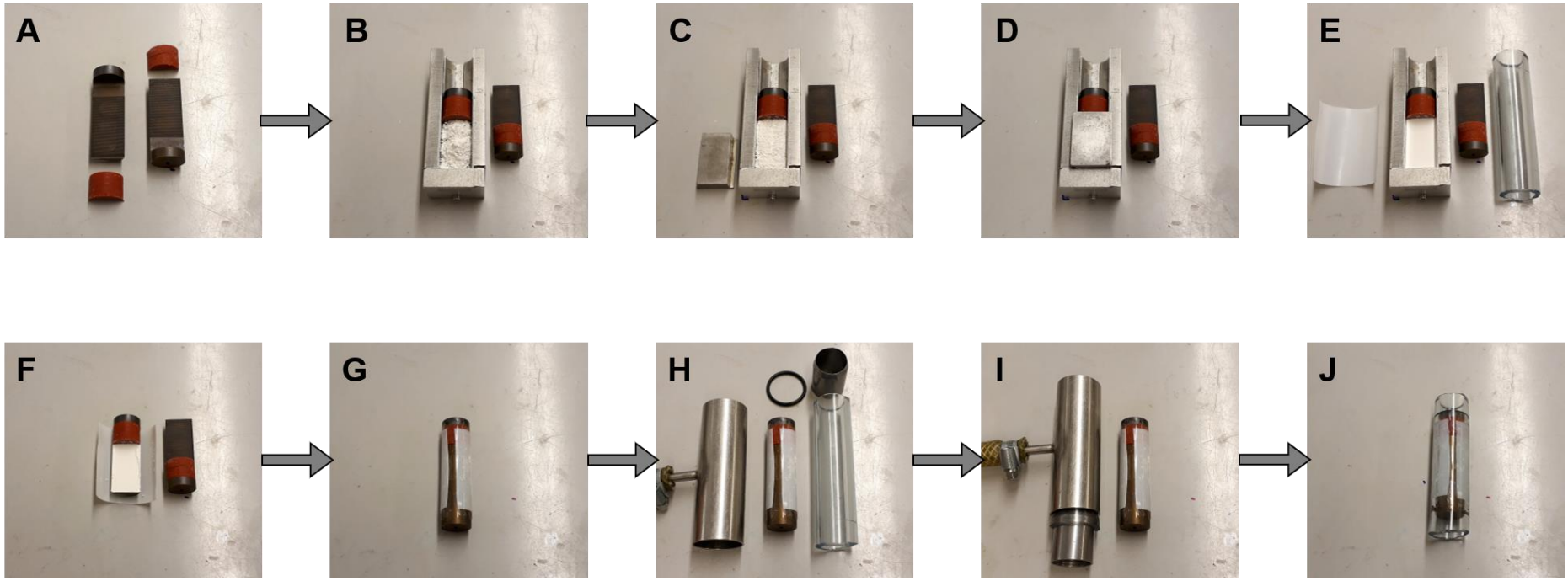

Figure 2.8 The preparation of an experimental sample in the direct shear configuration (A to J). Panels A through D show the pre-compaction of the gouge in the bespoke jig. Panels E through G show the joining of the two sliders and the addition of the PTFE sleeve. Panels H to J show the placement of the sliders in the PVC jacket using a vacuum pump.

2.3 Permeability Processing:

For permeability measurements of experimental samples, the pore pressure oscillation technique was used (Fischer & Paterson, 1992; Kranz et al., 1990). This method uses the attenuation and phase shift of a forced sinusoidal pressure wave as it is transmitted through a sample. This allows for continuous monitoring throughout an experiment to measure changes in permeability during deformation.

2.3.1. Downstream Storage Capacity:

The storage capacity (units Pa^{-1}) is defined as the increase in volume of pore fluid stored per unit increase in pore fluid pressure at a given fluid density (Fischer & Paterson, 1992). The downstream storage capacity (units m^3/Pa) describes the additional volume of fluid the downstream reservoir can store per unit rise in pressure. For the pore pressure oscillation technique of permeability measurements, the downstream storage capacity of the triaxial deformation apparatus had to be measured at the pressure conditions used in the experimental work. The measurements were taken with a metal blank in the direct shear slider assembly to separate the upstream and downstream reservoirs. The volume changes due to small changes in pressure were calculated by measuring the linear displacement of the piston in the upstream reservoir pump that has a known area. Measurements of the volume change were initially taken with the valve to the downstream reservoir open, then the procedure was repeated with the valve closed. By comparing the results of the upstream and downstream reservoirs together against the upstream reservoir alone, the storage capacity of the downstream reservoir was calculated. This method assumes that any volume changes in the downstream pore fluid pipes due to pressure changes with the valve shut are vanishingly small.

2.3.2. Pore Pressure Oscillation Measurements:

During permeability measurements, the valve between the pore pressure control pump and the downstream end of the sample is closed. Control software in LabView is used to impose a sinusoidal pressure signal to the upstream end of the sample. The signal received at the downstream transducer results from fluid flow through the sample, perpendicular to the direction of shear (see Figure 2.9). Due to the placement of the porous disks in the direct shear slider assembly, the permeability parallel to the shear direction cannot be measured. The optimum period and amplitude of the pore pressure oscillations applied to a sample depends on the sample size and permeability. To minimise the errors on the measured amplitude ratio (α) and phase shift (θ), an estimate of the expected permeability of the sample is needed.

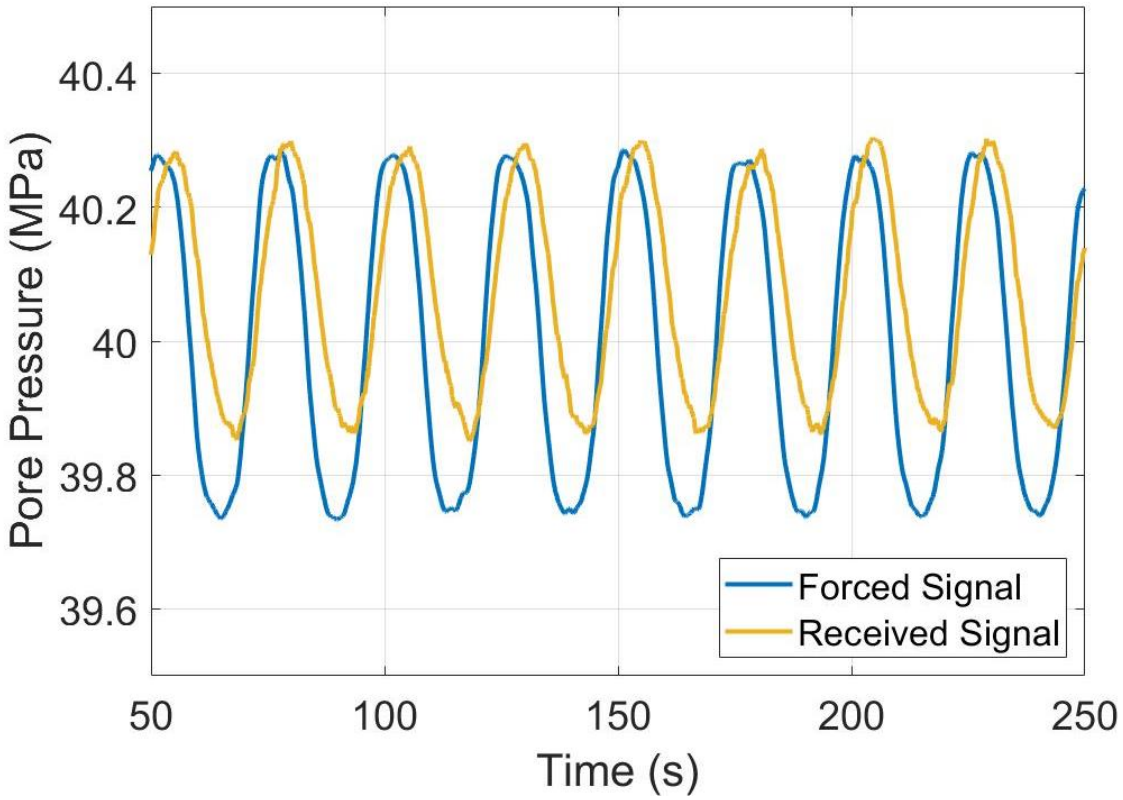

Figure 2.9: A graph of the forced (upstream) and received (downstream) pore pressure signals generated during a pore pressure oscillation permeability measurement.

2.3.3. Permeability Calculation:

The method used to calculate the permeability using pore pressure oscillation is based on the techniques of Fischer & Paterson (1992) and Faulkner & Rutter (2000). The values of the experimental amplitude ratio (α) and phase shift (θ) were resolved using fast Fourier transforms on the measured imposed and received pore pressure signals.

α	Amplitude ratio (dimensionless)	θ	Phase shift (radians)
L	Sample length (m)	η	Fluid viscosity (Pa s)
B_C	Storage capacity of the porous medium (Pa^{-1})	B_d	Downstream storage capacity (m^3/Pa)
A	Sample cross-sectional area (m^2)	T	Period of pressure oscillation (s)
k	Permeability (m^2)	ψ	$L(\pi\eta\beta_C/Tk)$ (dimensionless)
γ	Storage capacity of the downstream reservoir/storage capacity of the specimen (dimensionless) (≥0)	X_D	$\cosh\psi\cos\psi+\gamma\psi(\sinh\psi\cos\psi-\cosh\psi\sin\psi)$
Y_D	$\sinh\psi\sin\psi+\gamma\psi(\cosh\psi\sin\psi+\sinh\psi\cos\psi)$	A	$X_D^2+Y_D^2$
P	$\cosh\psi\cos\psi$	Q	$\psi(\sinh\psi\cos\psi-\cosh\psi\sin\psi)$
R	$\sinh\psi\sin\psi$	S	$\psi(\cosh\psi\sin\psi+\sinh\psi\cos\psi)$

Table 2.4: Summary table of all of the mathematical terms used in the processing of permeability data.

The measured amplitude ratio and phase shift are expressed using the two dimensionless parameters of ψ and γ:

$$\alpha = \sqrt{(X_D/A)^2 + (-Y_D/A)^2} \quad \text{(Eq. 2.2)}$$

$$\theta = \tan^{-1}(-Y_D/X_D) \quad \text{(Eq. 2.3)}$$

These equations need to be expressed in terms of only ψ and θ – as θ is an experimentally measured value, the dimensionless parameter ψ becomes the only unknown. The parameter ψ is solved iteratively, and subsequently, γ can be calculated from ψ. There may be more than one solution for ψ, therefore the value of γ is used to back-calculate θ, which can be compared to the experimentally-derived phase shift. All of the terms in X_D and Y_D that contain ψ are rearranged into 4 variables that are defined in Table 2.4:

$$X_D = P + \gamma Q \quad \text{(Eq. 2.4)}$$

$$Y_D = R + \gamma S \quad \text{(Eq. 2.5)}$$

By substituting the equations with the new variables into Eq. 2.3, γ can be defined as:

$$\gamma = \frac{R + P\tan\theta}{S + Q\tan\theta} \quad \text{(Eq. 2.6)}$$

From this, the amplitude ratio can also be expressed only in terms of ψ and θ by substituting the value for γ into Eq. 2.2:

$$\alpha = \{(P + \gamma Q)^2 + (R + \gamma S)^2\}^{-0.5} \quad \text{(Eq. 2.7)}$$

Using the value of γ from the measured θ, Eq. 2.7 can be resolved by iterating ψ to fit the measured α. With the best fitting values of ψ and γ, the permeability and storage capacity can be resolved using:

$$k = \frac{\pi\eta B_D L}{TA\psi^2\gamma} \quad \text{(Eq. 2.8)}$$

$$\beta_C = \frac{B_D}{LA\gamma} \quad \text{(Eq. 2.9)}$$

The application of this method is contained within a LabView program that was written by D.R. Faulkner. In addition to the pore pressure oscillation data, the program requires the user to input the fluid viscosity, the length scale of the fluid flow (~1.2 mm in the direct shear sliders) and the downstream storage capacity of the apparatus at the effective pressure conditions of the experiment.

2.4 Field Oriented Sample Collection:

As a target for sampling, fault gouges present many challenges to researchers, due mainly to their extreme fragility. The chosen method of sample collection was based upon the work of Faulkner & Rutter (1998), in that the fault gouge samples were collected in 22 mm internal diameter copper tubing (Figure 2.10). To collect fault gouge samples, firstly the weathered top soil had to be removed from the targeted area (Figure 2.10). Often, the volume of material that needed to be removed was on the order of 0.3 m^3 before fresh fault gouge material was exposed.

Figure 2.10: Two copper tubes that were used to collect oriented samples of fault gouge from an area cleared of weathered top soil. Compass clinometer for scale.

The copper tubes were gently hammered into the fault gouges in two sets of orientations – either a vertical or horizontal orientation (Figure 2.11). The aim was to produce thin sections that represent a surface perpendicular to the targeted, localised fault plane but parallel to the direction of shear. In some cases, the copper tubes were bent or broken by more resistant clasts within the fault gouge. In several instances, the copper tubes became stuck in the fault gouge and had to be carefully dug out, without damaging either the sample or the copper jacket. Once collected, the copper jacketed samples were sealed with a rapid-setting superglue to prevent the movement of the fragile sample inside, which would destroy the

microstructures that were of interest to this research. The collection of cohesive rock samples from dolomite and mica schist exposures in the field area was relatively straight forward – the rock samples were labelled with their orientation and sample code (e.g. CFIA23) using permanent markers and were separated from the exposures using a geological hammer and chisel.

The gouge sample collection method was effective in the field because it protected the delicate structures within the sample, it provided robust surfaces for orientation markers and it allowed a tight grouping of multiple samples to be taken from a small area. The drawbacks of this method were that it was labour-intensive, the samples could fail to be sealed within the copper tube and that, once in the laboratory, the jackets became a barrier to accessing the fault gouge within the copper tubes.

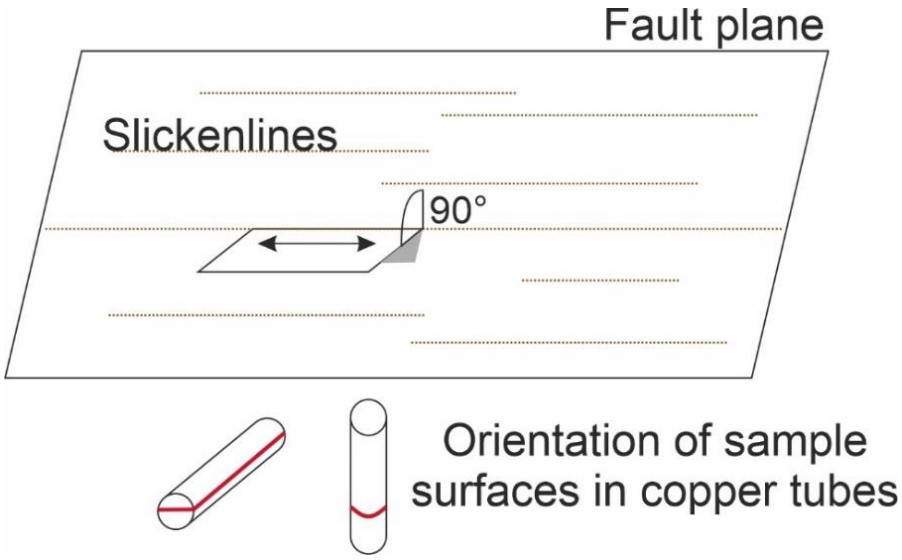

Figure 2.11: A schematic diagram showing the orientation of fault gouge samples taken in the field relative to the fault plane. The target surfaces for microstructural analysis from samples in copper tubes are shown relative to both the copper tubes and the fault plane.

2.5 Chemical Analysis Techniques:

X-Ray Fluorescence (XRF) is a non-destructive analytical technique in which the chemistry of a sample is determined by exciting a sample with a primary X-ray. When the incident X-Ray exceeds the energy of an inner electron shell (e.g. K, L), an electron is emitted. To prevent a charge imbalance, the resulting vacancy must be filled by an outer shell (e.g. M) electron. XRF measures the fluorescent X-ray that is released by the higher energy, outer shell electron as it substitutes for the emitted electron. Each element emits characteristic fluorescent X-rays, which correspond to the energy difference between the vacant electron site and the substituting electron. The emitted X-Rays allow the elemental components of a sample to be quantified.

X-Ray Diffraction (XRD) is another non-destructive analytical technique that identifies the mineralogy of a sample through the diffraction of incident X-rays through a crystal lattice (Starkey et al., 1984). In an XRD instrument, a detector is moved relative to the target sample to change the diffraction angle (2θ). Each mineral structure has unique spacings between the planes of its constituent atoms, which creates characteristic diffraction peaks (Chung, 1974; Hillier, 2000; Starkey et al., 1984). The analytical techniques of XRD and XRF required multiple stages of sample crushing, mixing or curing.

2.5.1. Sample Preparation for Chemical Analysis:

Chemical analyses by XRD and XRF were conducted on both fault gouge samples and cohesive rock samples. Prior to crushing, the cohesive rock samples were cut into centimetre-scale chips using a diamond-edged circular saw, in order to fit the samples in the crushing equipment. Also, the fault gouge samples needed to be extracted from their copper jackets, with minimal material loss or contamination from either the superglue sealant or the copper jacket. The sealed base of the copper jacket was removed using the diamond-edged circular saw. The samples were then inspected to determine if there were sufficient amounts of fault gouge necessary for the analytical techniques (>40 g) – only one sample had to be discounted at this stage. The sample copper jackets were cut open using a hand saw and once the sample was more easily accessible, the material was chiselled out of the jacket and into a sample pot. The copper contamination of the fault gouge samples, measured as CuO via XRF, varied from 0.04 to 0.59 mass%. All samples chosen for chemical analysis were initially ground to a powder in a disc mill Nickel Tema crusher. Samples were ground in this first stage for 10 seconds in the disc mill.

2.5.2. X-Ray Fluorescence (XRF) Sample Preparation and Analysis:

In XRF sample preparation, the powder was dry crushed in an agate (SiO_2) ball mill pot in a planetary motion mill. For samples from cohesive rocks, the crushing time lasted for 20 minutes at 400 rpm, whereas samples from fault gouges were crushed for 10 minutes at 400 rpm due to the pre-existing fine grain sizes and relatively weak mineralogy of the fault gouges. The XRF measurements were conducted on geo-pellets of the field samples because this allowed for analysis under vacuum conditions, which removed atmospheric interference from the measurements. A ratio of sample powder to wax binder of 6 g: 1.5 g was used to make the geo-pellets. This composite powder was mixed using a Fine Vortex mixer for a period of 1 minute 30 seconds and the resultant mixture was pressed into a pellet in a uniaxial press at a load of 10 tonnes (~98 kN) for 3 minutes. The countertop XRF machine (*Rigaku SuperMini-200, WD-XRF*) is calibrated to exclude the chemical signature of the wax binder.

2.5.3. X-Ray Diffraction (XRD) Sample Preparation and Analysis:

The XRD technique requires the crystallinity of the material to be preserved following crushing. The samples were therefore ground in the presence of water in a McCrone Mill via the oscillation movement of cylindrical agate beads. The mixing time was set at 10 minutes, after which the suspended samples were left to dry for at least 24 hours in an oven set at 60°C. An agate pestle and mortar were used to grind the oven dried wafers to a powder. The bulk powder XRD analysis, which used a *Panalytical X'Pert Pro MPD*, measured the samples as random powders held in cavity holders. A Cu X-ray tube was used, with a Ni filter to select for Cu *k-α* radiation. The scans covered the 2*θ* range of 4-70°. Operation of the XRD equipment and software was done by James Utley, using the HighScore Plus analysis software (Figure 2.12). The quantification of the measured diffraction peaks used the Relative Intensity Ratio (RIR) method (Chung, 1974; Hillier, 2000; Starkey et al., 1984). The reference crystallographic diffraction patterns were obtained from the International Centre for Diffraction Data, Powder Diffraction File-4+ Release 2022.

The bulk powder XRD analysis identified that a significant portion of the natural fault rock samples were rich in clay and mica minerals (>50 %, Figure 2.12). Hence, additional clay-separate XRD techniques were applied to 11 of the samples as this improved the identification and quantification of the clay-sized particles. A 1 g sample of the material was suspended in 300 ml of tap water and agitated in an ultrasonic bath for 4 periods of 5 minutes. The solution was mixed by hand between each 5-minute period and following the full 20 minutes in the ultrasonic bath. Following this, the solutions were rested for at least 37 minutes and 30 seconds to allow the gravity settling of any particles >5 μm in size. The solution containing the clay-sized suspended particles was then separated from the settled material into a new container. Between 4 ml and 6 ml of the clay suspension solutions were then filtered through a silver filter disc to leave the clay-sized particles on the filter. The filters were left to dry for at least 24 hours before analysis. To improve the XRD instruments ability to detect swelling clays (e.g. smectite), the powdered samples were saturated with ethylene glycol using the vapour pressure method at 60 °C for 24 hours, and were then rescanned (Figure 2.12).

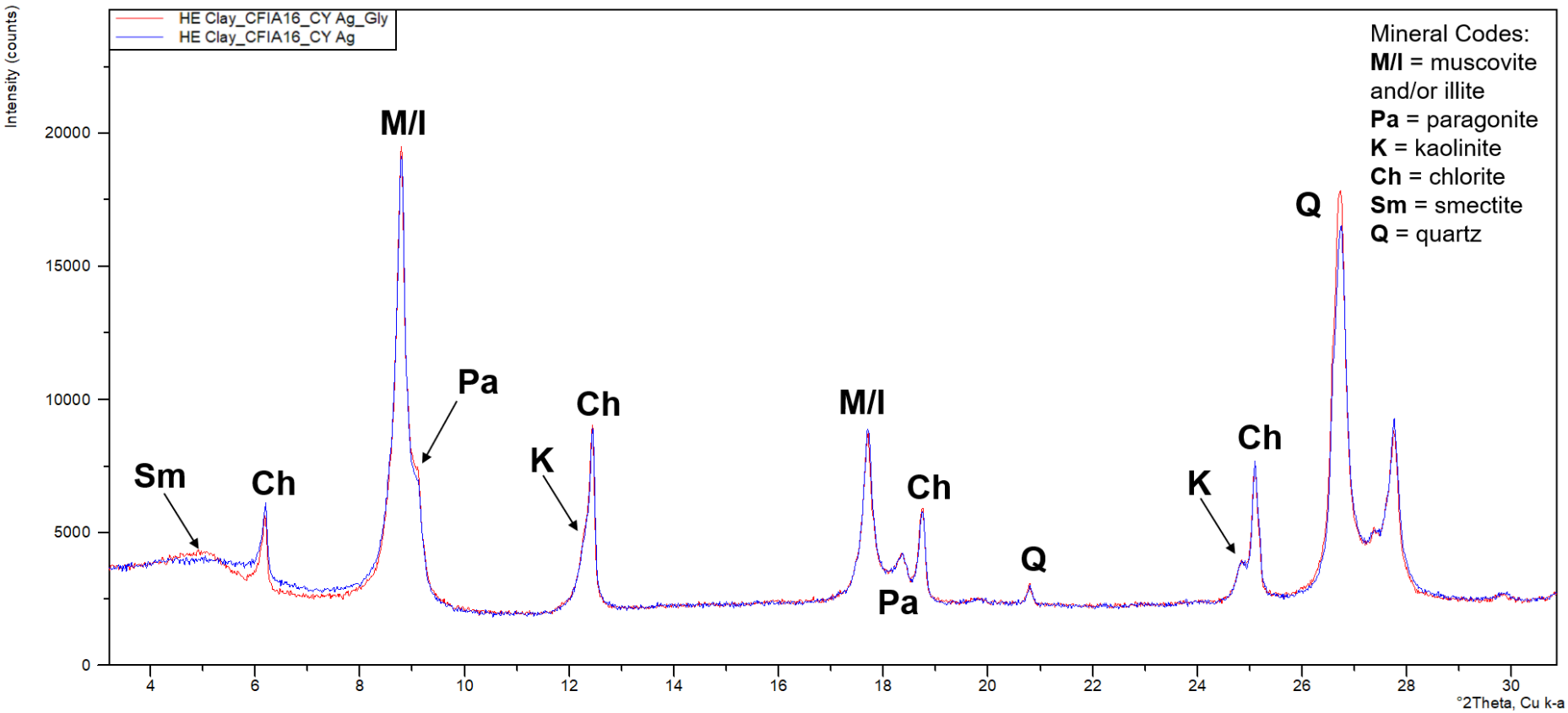

Figure 2.12: An example XRD diffractogram for sample CFIA16 from Chapter 5 showing the intensity count against the diffraction angle (°2θ) range of 4-30° using a copper X-Ray tube. Bulk powder analysis – blue line. Clay separate glycolate analysis – red line.

2.6 Microscopy:

Field observations and experimental data need to be coupled with qualitative and quantitative microstructural observations as these provide physical evidence for the deformation processes that may be active during the deformation of a sample. Hence, microstructural observations of samples are included in all of the chapters of this thesis. Due to the fine grain sizes of the samples studied in this thesis, microscopy analyses were conducted using a scanning electron microscope (SEM). SEMs are capable of analysing large sample areas (up to centimetre-scale), while also providing access to nanometre-scale sample features. These instruments also offer quantitative chemistry and crystallography measurements. Thanks to their flexibility, high-resolution imaging and multiscale quantitative analyses, SEMs are the most used instruments in the Earth Sciences. All of the microstructural work in this thesis was undertaken in the Scanning Electron Microscopy Shared Research Facility (SEM-SRF) at the University of Liverpool.

2.6.1. Scanning Electron Microscopes:

The Zeiss GeminiSEM 450 in the SEM-SRF was the state-of-the-art instrument used to analyse both the laboratory and natural rock samples in this thesis. The Zeiss GeminiSEM 450 is an ultra-high resolution FEG (Field Emission Gun) SEM that produces a finer and more stable electron beam than a tungsten filament SEM. The operating parameters of the Zeiss Gemini can be adjusted between 0.02 kV to 30 kV for the accelerating voltage, and between 3 pA to 40 nA for the beam current. An example of the operating parameters used for imaging the laboratory samples (Chapter 3 and 4) are 10 kV and 1 nA for the accelerating voltage and beam current, respectively. These settings were used to obtain high-resolution images of the polished sample surfaces.

More generally, the best operating conditions must be chosen based on the research goals and on the type of sample being analysed. The four major parameters that shape an electron beam in a SEM are the accelerating voltage, the convergence angle, the beam current and the spot size (Figure 2.13). These all change the physical characteristics of the electron beam – thus, it is important to identify the optimum balance between the operating values to enable the acquisition of the best possible results. Optimal operating parameters vary with the different techniques that are applied to samples in an SEM, as is described in the following sections.

The most prominent change associated with decreasing the accelerating voltage is a corresponding decrease in the interaction volume below the sample surface (Figure 2.13). A small interaction volume reduces the flurry of electrons and provides sharper details of features near or at the sample surface (Dusevich et al., 2010), which highlights microfractures, cleavages and grain boundaries.

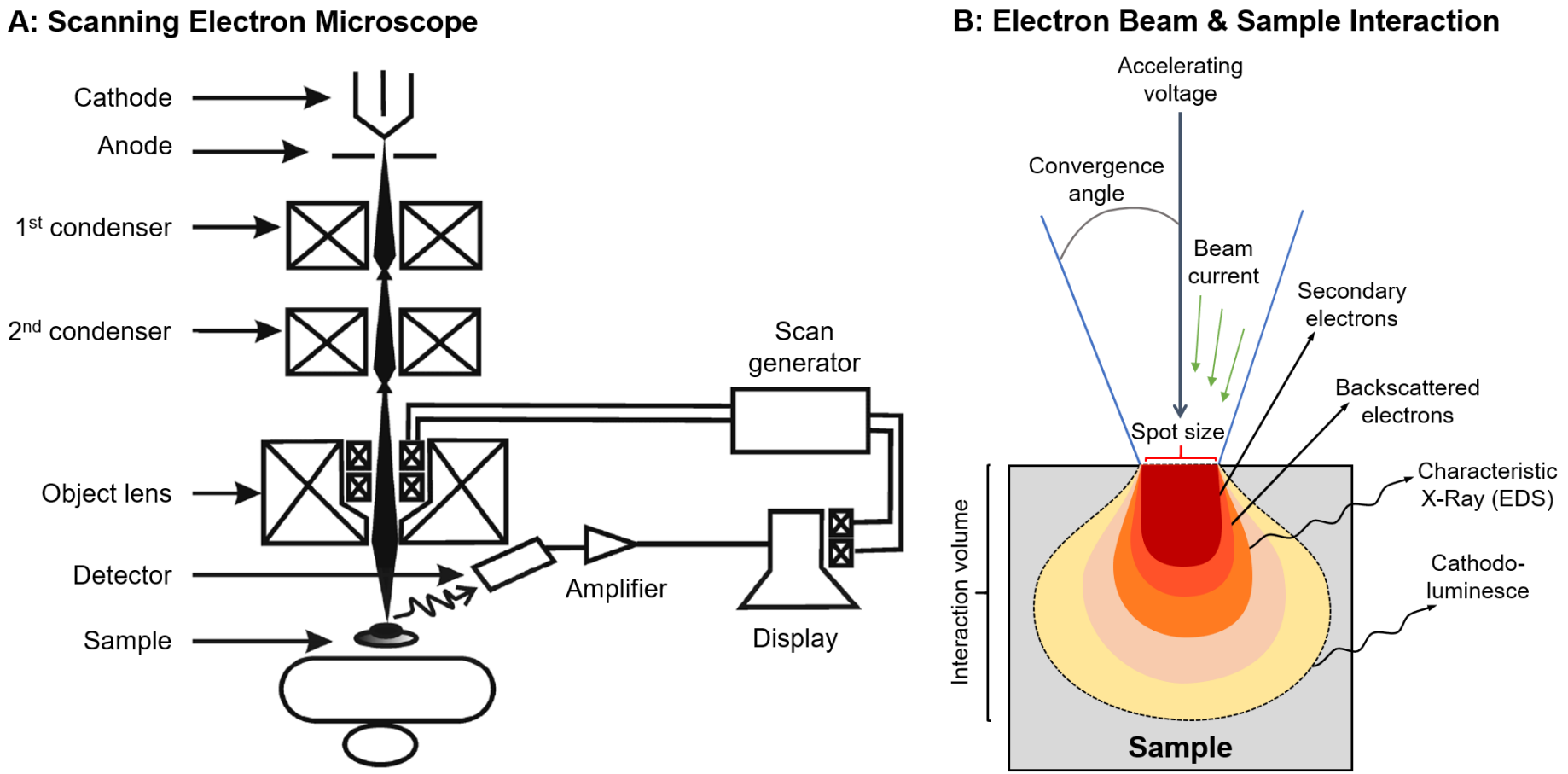

Figure 2.13: Schematic diagrams of: (A) a generalised scanning electron microscope system – the entire column is held under a high vacuum to achieve a highly focused electron beam for high resolution imaging; and (B) the interaction volume from the incident electron beam with the sample surface (modified from Chen et al., 2015).

The spot size of the electron beam has the same effect of reducing the interaction volume. To obtain high-resolution images, the beam spot size must be small so that nanometre-scale details can be imaged. However, a small spot size generates a low beam current, so that the electron signal that reaches the detector is weak. A compromise has to be made that uses a sufficient signal to noise ratio to achieve the best quality image.

To avoid electron charging issues, the Zeiss GeminiSEM 450 offers a Variable Pressure (VP) capability, where the chamber vacuum can be decreased and electron charges are driven away by positively charged particles in the chamber. Using a dedicated VP detector, an image resolution of 1 nanometre is attainable. The Zeiss GeminiSEM 450 is equipped with a number of detectors, including:

- In-lens and in-chamber Secondary Electron (SE) and Backscatter Electron (BE) detectors;
- A Variable Pressure Backscatter Electron (VPBSD) detector;
- A panchromatic cathodoluminescence (CL) detector;
- A high-speed Symmetry S2 Electron Backscatter Diffraction (EBSD) detector (Oxford Instruments);
- An X-Max 50 mm^2 Energy Dispersive X-ray (EDX or EDS) detector (Oxford Instruments).

AZtec 6.0 software was used for the acquisition of EBSD and EDS datasets on the Zeiss GeminiSEM 450. These datasets were subsequently analysed using AZtec Crystal.

2.6.2. Microscopy Analysis Techniques:

A number of different SEM techniques were used for the microstructural analysis of experimental and field samples. These techniques include: Backscatter Electron (BSE) imaging; Secondary Electron (SE) imaging; Energy Dispersive Spectroscopy (EDS); and Electron Backscatter Diffraction (EBSD). In BSE imaging, a significant proportion of the incident beam electrons undergo scattering in the target sample. The electrons reverse their initial trajectory and exit the sample. The number of backscattered electrons exiting the sample increases as a function of the atomic number (Z) and/or an increase in the tilt angle of the sample relative to the incident beam (L. Chen et al., 2015; Lloyd, 1987). BSE imaging can therefore convey information on both the composition and the topography of the sample. However, it is used predominantly to image flat, polished surfaces where the chemical information carried by the BSE signal is optimised. Secondary electrons are generated through inelastic scattering, when the incident beam electrons cause excitation in the sample interaction volume, resulting in the ejection of weakly bound valence electrons or conduction band electrons in metals (Bleloch et al., 1989; L. Chen et al., 2015). This effect is quantified (δ) through the ratio of secondary electrons (N_{SE}) emitted from the sample to the number of incident beam electrons (N_E, so that $\delta = N_{SE}/N_E$). Secondary electrons are low energy electrons and only those that are close to the sample surface can be ejected, then attracted

to and detected by the SE detector. For this reason, the secondary electrons carry detailed information on the sample topography and are the best type of signal for the 3D image reconstruction of uneven sample surfaces (Bleloch et al., 1989; Ciston et al., 2015).

In an SEM, EDS is used to identify the chemical elements present in a sample (L. Chen et al., 2015; S. Han et al., 2022; Schulz et al., 2020). The photoelectric absorption of an X-ray photon in a semiconductor detector, such as silicon, causes the entire energy of the photon to be transferred to a bound inner shell atomic electron. This is then ejected with the kinetic energy equal to the photon energy minus the atomic shell ionisation energy. The photoelectron undergoes inelastic scattering in the semiconductor and migrates to the conduction band of the semiconductor, which leaves positively charged 'holes' in the valence bands. The charged photoelectrons drift to the electrode at the rear of the semiconductor and generate a charge. A histogram is generated with a series of energy bins and the number of photons that fall within those energy ranges. Elements have been indexed to their characteristic energy peaks so that the measured energy peaks in EDS can show the elemental composition of a sample (L. Chen et al., 2015; S. Han et al., 2022; Schulz et al., 2020). The limitations of EDS analysis include the broadening and subsequent mutual interfering of energy peaks. Also, coincident peaks can be created by the measurement of more than one photon at a time. The system must be correctly indexed to minimise false results from broad or coincident energy peaks. EDS data can be obtained in the form of maps and point analyses (Schulz et al., 2020). Maps generally give qualitative information on the type and distribution of mineral phases present in a sample. A spectrum obtained from a point analysis can be fitted, using pre-existing standards, to provide the quantitative elemental composition of a mineral phase. In this thesis, EDS maps were used in Chapters 4 and 5.

EBSD is a fully quantitative technique that measures the absolute crystallographic orientation of any crystalline material (L. Chen et al., 2015; Mariani et al., 2009; Prior et al., 1999, 2009; Wallis et al., 2019). It can be used to determine:

- The crystallographic preferred orientation (CPO), often referred to as *fabric* in geosciences and as *texture* in materials science, of a polycrystalline rock;
- Intracrystalline distortions in grains, from which inferences on slip system types can be made;
- Grain size and roundness;
- Grain boundary type, abundance and orientation.

EBSD can also measure more sophisticated properties such as dislocation densities (Wheeler et al., 2012), crystal chirality (Winkelmann & Nolze, 2015), and residual stresses and strains using high angular resolution (HR-) EBSD (Wallis et al., 2019). These techniques have been important achievements in the development of EBSD in the last 20 years.

In the SEM, EBSD is achieved by illuminating a highly tilted (70° to the horizontal) sample with a stationary electron beam. The incident electrons interact with the sample at shallow depths. Due to the glancing incident angle, statistically significant electron scattering is produced and the conditions for Bragg's diffraction within the crystalline planes of the sample are satisfied (Kacher et al., 2009; Prior et al., 1999). Backscattered electrons that escape the sample surface form Kikuchi patterns or Electron Backscatter Patterns (EBSP) that are visualised on the phosphor screen positioned at the front of the EBSD detector. Images of Kikuchi patterns are collected using a CMOS technology camera and transferred to the AZtec software, where these patterns are automatically indexed using available crystal structure databases. The angles between Kikuchi bands, the angles between zone axes and the band intensity are specific for a given crystal structure (L. Chen et al., 2015; Prior et al., 1999). Thus, each Kikuchi pattern can be matched with its best fit in the database. Using this method, the absolute orientation of each individual point on a map can be determined and grains can be reconstructed (Humphreys, 2004; Prior et al., 1999, 2009; Schulz et al., 2020).

EBSD requires that the sample surfaces that are targeted for analysis are flat and highly polished – any amorphous layers on the sample surface must be removed so that the crystal planes that cause electron diffraction are well exposed to the electron beam. While the technique works well on most crystalline materials, phyllosilicates are difficult to polish to high quality and so cannot be studied using EBSD. In this thesis, EBSD was used to analyse the microstructure of deformed quartz grains that commonly occur in the gouges from the Carboneras Fault Zone (Chapter 5).

2.6.3. Friction Experiment Sample Preparation for Microstructural Analyses:

Following a friction experiment, the deformed sample was carefully removed from the direct shear slider assembly and allowed to dry in an open container for at least 48 hours. The samples were dried on top of a warm (60°C) oven to encourage the evaporation of any remaining pore fluid contained in the sample. A low viscosity epoxy (EpoFix Resin and Hardener) was used to impregnate and thus stabilise the sample. EpoFix epoxy is especially effective at penetrating low permeability samples under vacuum, so the samples were held under a vacuum for the first 30 minutes of epoxy impregnation. The vacuum forced the air out of the pore spaces in the samples and allowed the resin to fill the pore spaces. The epoxy resin was left to cure at room temperature for a minimum of 24 hours. The disks of epoxy resin were then cut using a diamond-edged saw to produce a cross-sectional view of the sample parallel to the direction of shear. As this type of sample mount would have been unstable on a SEM stage, and as the samples were fragile, the sample mounts were impregnated and cured in the epoxy resin under a vacuum for a second time, oriented with the target surface on the base of the epoxy disk. The target surfaces of the samples were polished using a series

of silicon carbide and aluminium oxide grits down to the 0.3μm grit size, to produce a highly polished surface suitable for SEM analysis. Before mounting the polished samples in the SEM, each sample was carbon coated and fixed on a mount using copper tape. This was to prevent the build-up of static charge on the surface of the sample from the electron beam in the SEM. The conductive carbon coat and copper tape allow the static charge of the sample surface to dissipate.

2.6.4. Rock Chip Preparation for Thin Sectioning:

Microstructural analysis of samples taken from the field site was conducted only on fragile fault gouge samples. Time restrictions on data collection led to the prioritisation of the fault gouges over the cohesive rock samples. Once in a laboratory setting, the collection of samples in copper jackets presented many obstacles to thin section preparation. Copper does not cut cleanly, but rather tears. Early attempts to cut the copper jackets produced sample surfaces with an unacceptable amount of copper dust incorporated into the fault gouge and a significant proportion of the surface was covered with the bent copper casing. Also, the sealing of the samples with superglue, while necessary to protect the samples during transit, did prevent the impregnation of the samples with epoxy resin. Two workflows for sample preparation were developed for the vertically and horizontally oriented samples in response to these setbacks.

The 'vertical' copper jacket samples were collected with the long axis of the copper tube parallel to the dip angle and dip direction of the secondary faults in the study area (Figure 2.11). Hence, the target planes for microstructural analysis were the cross-section perpendicular to the long axis of the copper jacket (Figure 2.11). Prior to sample cutting, the fault gouges had to be stabilised by epoxy resin. The bases of the copper jackets with the sealing superglue were removed using a diamond-edged disc saw. The EpoFix low-viscosity Resin and Hardener was poured into the newly exposed fault gouges within the 30-minute period after the epoxy resin was prepared. In order to reduce the contamination of the samples by copper fragments, the thicknesses of the copper jackets were reduced using a Colchester lathe. The lathe reduced the thickness of the copper jacket walls by 1-1.5 mm along the target plane, so that when the samples were again cut by the diamond-edged circular saw, far fewer copper fines were produced (Figure 2.14A). Due to the low permeability of the fault gouges (10^{-17} to 10^{-22} m^2 as measured by Faulkner & Rutter (2000)), all of the vertically oriented samples underwent a second stage of epoxy impregnation to ensure the preservation of the microstructures. Epoxy was applied to the samples in this second stage using a 20-gauge syringe, in order to avoid flooding the samples with too much resin.

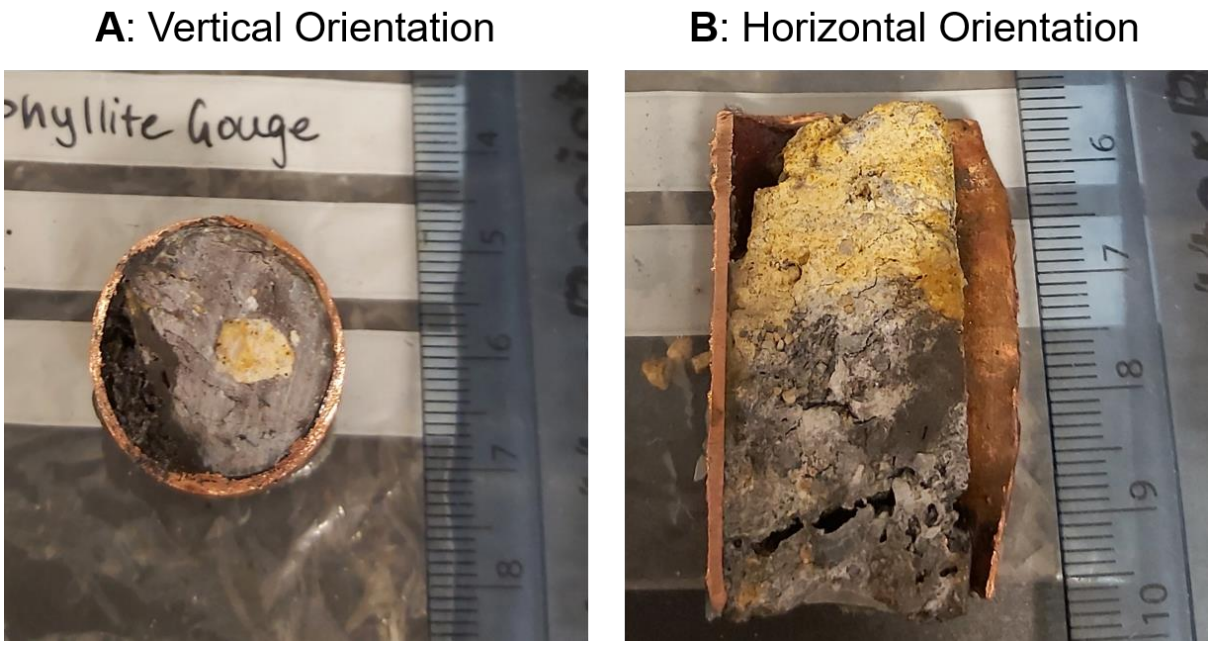

Figure 2.14. Photos of the two orientations of fault gouge samples: vertical (A) and horizontal (B).

The ‘horizontal’ copper jacket samples were collected with the long axis of the copper tube perpendicular to the dip angle and direction of the secondary faults (Figure 2.14B). The target plane of the sample was therefore parallel to the long axis of the copper jacket (Figure 2.14B). It was not possible to remove the thickness of the copper jacket using a lathe, as with the vertically oriented samples, because the lathe could not remove material in straight lines along the edge of a cylinder. Copper material along the length of the jackets had to be removed using a hand graver tool. Following this, the copper jacket walls were cut with a hand saw and carefully bent outwards to expose the cylinder of fault gouge within. Epoxy resin was then injected into the samples using 20-gauge syringes, in order to stabilise the fragile fault gouges before cutting. After a curing-period of at least 24 hours, the stabilised fault gouge samples were cut along the target plane using the diamond-edged disc saw. A second stage of epoxy impregnation was not deemed necessary for these samples, because the epoxy had infilled the fractures within the samples and stabilised the fault gouges.

A total of 11 copper jacketed fault gouge samples were prepared for thin section preparation. Uncovered thin sections were made by Paul Hands at Hands on Thin Sections Ltd, Birmingham.

3. The effect of clay content on the dilatancy and frictional properties of fault gouge.

I. R. Ashman[1] and D. R. Faulkner[1]

[1]Department of Earth, Ocean, and Ecological Sciences, University of Liverpool, Liverpool, UK

Corresponding author: Isabel Ashman (isabel.ashman@liverpool.ac.uk)

Published 11th April 2023 in the Journal of Geophysical Research: Solid Earth.

Key Points:

- Dilatancy with increasing slip velocity is seen for fault gouges ranging from 100 wt% quartz to 100 wt% clay.
- Dilatancy is at a maximum in the quartz-rich, clay-poor gouges, rather than in the end member compositions.
- Increasing clay content systematically decreases the gouge frictional strength and promotes velocity strengthening behaviour.

Abstract

Mature fault cores are comprised of extremely fine, low permeability, clay-bearing gouges. Saturated granular fault materials are known to dilate in response to increases in sliding velocity, resulting in significant pore pressure drops that can suppress instability. Up to now, dilatancy has been measured predominantly in clay-poor gouges. Clay minerals have low frictional strengths and, in previous experiments, even small proportions of clay minerals were shown to affect the frictional properties of a fault. It is important, therefore, to document in detail the impact of the proportion of clay on the frictional behaviour and dilatancy of fault rocks. In this work, a suite of triaxial deformation experiments elucidated the frictional behaviour of saturated, synthetic quartz-clay (kaolinite) fault gouges at effective normal stresses of 60 MPa, 25 MPa and 10 MPa. Upon a 10-fold velocity increase, gouges of all clay-quartz contents displayed measurable dilatancy with clay-poor samples yielding comparable changes to previous studies. Peak dilation did not occur in the pure quartz gouges, but rather in gouges containing 10 to 40 wt% clay. The clay content of the simulated gouges was found to control the gouge frictional strength and the stability of slip. A transition occurred at ~40 wt% clay from strong, unstably sliding quartz-dominated gouges to weak but stably sliding clay-dominated gouges. These results indicate that in a low permeability, clay-rich fault zone, the increases in pore volume could generate pore-fluid pressure transients, contributing to the arrest of earthquake nucleation or potentially the promotion of sustained slow slip.

Plain Language Summary

The strength of faults is dependent on the fluid pressure contained within the pore space of fine-grained fault rocks on which fault slip events such as earthquakes occur. When slip velocity increases at the start of an earthquake, the fault rocks dilate, thereby reducing the fluid pressure and consequently strengthening the fault. If this strengthening is sufficient, an earthquake may arrest. Clay minerals are commonly present within faults, but previous measurements of fault volume changes have focused on clay-poor materials. In this study, a series of experiments simulated the conditions within a tectonic fault in the Earth's crust. The experiments focused on the effect of changing the proportion of clay on the strength, slip behaviour and volume changes of the fault material. All of the experiment materials experienced measurable volume changes that would change the pressure, and therefore the strength, of the fault. Fault composition was found to control both the strength and slip behaviour of the fault. Clay-poor materials were stronger and more likely to initiate earthquake slip, whereas the clay-rich materials were weaker and slip via steady creep. This study provides essential insight and data towards understanding the slip behaviour of faults, from slow fault creep to earthquakes.

3.1. Introduction:

Field observations have shown that mature fault zone cores contain a significant proportion of clay minerals, such as the Median Tectonic Line in Japan (Jefferies et al., 2006; Wibberley & Shimamoto, 2003b), the San Andreas Fault including the Punchbowl Fault in USA (F. M. Chester & Logan, 1987; French & Chester, 2018), and the Alpine Fault Zone in New Zealand (Toy et al., 2015). The presence of clay minerals has the potential to influence the seismic cycle, and earthquake nucleation in particular, through the frictional strength and stability of the gouge, and pore fluid pressure changes resulting from dilation or compaction during slip velocity transients (Byerlee 1978; Segall and Rice 1995; Faulkner et al. 2018). While the effect of clay content on the bulk frictional strength and permeability of fault gouges is relatively well documented (K. M. Brown et al., 2003; Crawford et al., 2008; Giorgetti et al., 2015; Ikari et al., 2007; J. M. Logan & Rauenzahn, 1987; Lupini et al., 1981; Moore & Lockner, 2011a; Ruggieri et al., 2021; Takahashi et al., 2007; Tembe et al., 2010a; Zhang et al., 2020), the effect of dilatancy induced by increasing slip velocity on frictional stability, particularly in clay-rich gouges, is poorly documented.

The role of pore fluid pressure in determining fault shear resistance (τ) is described using the effective pressure law:

$$\tau = \mu(\sigma_n - p) \qquad \text{(Eq. 3.1)}$$

where μ is the coefficient of friction, σ_n is normal stress and p is pore pressure (von Terzhagi, 1936). Thus, by increasing the pore pressure, the apparent strength of a brittle fault decreases (Ougier-Simonin & Zhu, 2013), or vice-versa. Given the low compressibility of aqueous fluid, even small changes in the pore volume of a shearing fault gouge during changes in slip velocity will produce large fluid pressure variations (Morrow & Byerlee, 1989; Rudnicki & Chen, 1988). The dilation and compaction of granular materials is accredited to changes in the packing arrangement of the grains (Mead, 1925; Reynolds, 1885). Slip velocity increases are accompanied by dilation of the sample material and a pore pressure drop, whereas slip velocity decreases show compaction of material and pore pressure increases (Brantut, 2020; Carpenter et al., 2016; Lockner and Byerlee, 1994; Morrow and Byerlee, 1989; Proctor et al., 2020; Rathbun and Marone, 2013; Samuelson et al., 2009). The timescale of pore pressure changes due to dilatancy or compaction depends on the competition between the changes in pore pressure and the drainage of pore fluid away from sites of excess pressure (Faulkner et al., 2018).

Previous friction experiments focused on dilatancy have typically used quartz-rich sands and powders (Lockner & Byerlee, 1994; Rathbun & Marone, 2013; Samuelson et al., 2009) or studied the initiation of a shear fracture in intact material and subsequent slip (Brantut, 2020;

Proctor et al., 2020). In contrast, mature fault cores consist of extremely fine-grained fault gouges that are typically rich in clay minerals and have very low permeabilities, from 10^{-18} m^2 to 10^{-24} m^2 (Behnsen & Faulkner, 2011; Chester et al., 1993; Crawford et al., 2008; Faulkner et al., 2003; Faulkner and Rutter, 2000; Ikari et al., 2009; Morrow et al., 1984). Low permeabilities in clay-rich fault materials increases the timescales of the pore pressure changes and their significance in terms of fault shear strength and behaviour.

Dilation of fault material could arrest a nucleating rupture due to a drop in pore pressure, which would increase the apparent shear strength of the fault. Dilatancy in response to slip velocity changes could also suppress fully dynamic behaviour leading to the propagation of slow slip earthquakes (SSE), which can last periods of days to weeks (Frank et al., 2015; Liu, 2013; Rubin, 2008; Segall et al., 2010). SSE are inferred to occur in regions of elevated pore pressures at close to lithostatic conditions, including plate boundary settings such as the subduction interface or transform faults (e.g. Audet et al., 2009; Frank et al., 2015; Kodaira et al., 2004; Peng and Gomberg, 2010; Saffer and Wallace, 2015). Hence, fault networks that host SSE could be highly sensitive to pressure fluctuations and stable fault slip may be promoted on otherwise unstable faults (Obara & Kato, 2016; Ougier-Simonin & Zhu, 2013; Peng & Gomberg, 2010). SSE-hosting fault rocks are often rich in clay minerals (e.g. Audet et al., 2009; Frank et al., 2015; Ikari, 2019; Ikari et al., 2015), thus measuring dilatancy in clay-rich gouges is vital to understand whether pore pressure fluctuations will impact fault seismicity.

While the focus in this work is on dilatancy, intrinsic changes in the frictional strength with changes in slip velocity, such as in earthquake nucleation or propagation, are also investigated. Rate and state friction describes the response to slip velocity variations and is quantified by the constitutive law:

$$\mu = \mu_0 + a \ln\left(\frac{V}{V_0}\right) + b \ln\left(\frac{V_0 \theta}{D_c}\right) \qquad \text{(Eq. 3.2)}$$

Where μ_0 is the initial steady state friction coefficient at slip velocity V_0 (ms^{-1}), the velocity after the step change is V (ms^{-1}), a is the direct effect, b is the evolution effect, D_C is the slip weakening distance and θ is the state variable with units of time (Dieterich, 1979). If the friction stability parameter (a-b) is greater than zero in response to a velocity step increase, the material is designated as velocity strengthening. Velocity strengthening materials cannot nucleate seismic slip because with accelerating slip the material strengthens and so prevents instability. Conversely, a friction stability parameter of less than zero indicates that the material is velocity weakening. Velocity weakening is a prerequisite for unstable slip due to the material's overall weakening response to slip acceleration. Previous measurements of the

stability of clay minerals (Giorgetti et al., 2015; Ikari et al., 2009a; J. M. Logan & Rauenzahn, 1987; Ruggieri et al., 2021; Saffer & Marone, 2003; Tembe et al., 2010a; Zhang et al., 2020) have shown them to be velocity strengthening, although there is a paucity of systematic measurements of how clay content affects stability compared to measurements of the bulk strength. The compilation by Ikari et al. (2011) indicates that there is broad correlation between clay content and higher *(a-b)* values. In contrast, more recent measurements by Ikari (2019) show that natural, clay-bearing fault gouges host SSE at slip rates simulating tectonic driving rates (cm/yr). Hence, it is important to document the effect of gouge composition on the friction parameter *(a-b)*, alongside the dilatancy, in order to understand the relative contributions of intrinsic material effects and pore fluid pressure changes on shear resistance.

In this work, the materials and methods used to perform the experiments are first described. A series of synthetic quartz-kaolinite gouges were produced that cover kaolinite contents from 0 wt% to 100 wt% and the synthetic gouges were sheared in a conventional triaxial deformation apparatus. The experimental results first describe the pore volume changes that occur in the synthetic fault gouges as a function of the controlled clay content, both during a bulk compaction phase and also in response to steps in the sliding velocity. The changes in the bulk strength and variation of the friction parameter *(a-b)* as a function of clay content are then reported. In the discussion, all the results are compared to existing data from the literature and the controls on dilatancy, gouge strength and stability are considered. Finally, the implications of the dilatancy for natural fault slip for the range of fault materials tested are discussed.

3.2. Materials and Methods:

The materials used for the quartz-kaolinite synthetic fault gouges were Min-U-Sil 15 silica powder from the US Silica Company and KGa-1B kaolinite source clay from the Clay Minerals Society. Kaolinite was the chosen clay mineral for this study as it is a non-swelling clay and it is frictionally weaker than framework silicates in a similar way to other clay species (Behnsen & Faulkner, 2012; Moore & Lockner, 2004). Behnsen & Faulkner (2012) found that the water-saturated shear stress at yield for kaolinite was similar to chlorite, illite and lizardite. Hence, kaolinite acts as a useful proxy in this study for other species of non-swelling phyllosilicates that are common to fault gouges. Kaolinite is of common occurrence in fault rocks – examples of kaolinite-bearing faults that host both aseismic creep and seismic slip include the Median Tectonic Line in Japan, the Longitudinal Valley Fault and the Chelungpu Fault in Taiwan, at up to 19% (Anko section), 10-12% and 10-20% kaolinite respectively (Den Hartog et al., 2021; Ishikawa et al., 2014; Kuo et al., 2009).

Min-U-Sil 15 was chosen for its high purity at >99% silica and the fine grain size sieved to <15 µm. KGa-1B also has a purity of >99% (Vogt et al., 2002) and was sieved during manufacturing to <44 µm to produce extremely fine grain sizes, with 57 wt% at <2 µm (Pruett & Webb, 1993; Vogt et al., 2002). Thus, the grain sizes in the quartz-kaolinite mixtures was comparable with fault gouges that have grain sizes down to the sub-micron scale. As quartz and kaolinite have very similar densities (2.65 g/cm^3), the synthetic fault gouges were mixed by weight, which was also representative of the relative volumes. Kaolinite composition was varied by 10 wt% increments to produce 11 samples from 0 wt% to 100 wt% kaolinite. With the aim of producing a well-mixed starting material, 20g of the samples were tumbled as dry powders for a 3-hour period at 68 rpm in a 575 cm^3 volume container. Dry tumbling was chosen because the similar grain sizes and densities of the kaolinite and quartz powders promotes mixing over segregation (Williams, 1968). Microstructural observations of pre-shear gouge samples show a good degree of mixing, with only minor clumping of clay due to a build-up of static charge in intermediate mixtures.

All deformation experiments were conducted using a direct shear configuration in a triaxial deformation apparatus (Figure 3.1). Using servo-controlled pumps, the apparatus can apply and maintain confining pressures up to 250 MPa and pore fluid pressures up to 200 MPa to an accuracy of 0.007 MPa. The confining and pore fluids used in the experiments were silicon oil and deionised water, respectively. An internal force gauge measures the axial force at a resolution better than 0.05 kN (Mitchell & Faulkner, 2008).

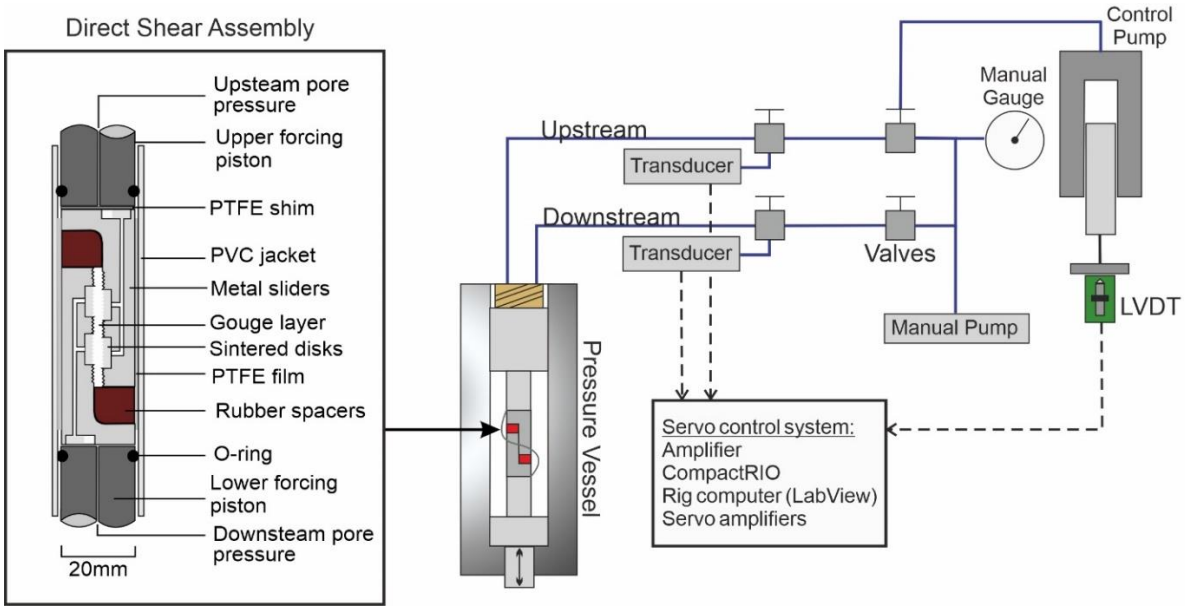

Figure 3.1: Schematic diagram of the servo-controlled pore pressure control system on the triaxial deformation apparatus (adapted from Mitchell & Faulkner, 2008).

In the experiments, samples of fault gouge were deformed in direct shear sliders (Faulkner et al., 2018; Sánchez-Roa et al., 2016) shown in Figure 3.1. The dimensions of the direct shear sliders created a sample area of 720 mm^2 and two rubber spacers allowed a maximum load point displacement of 6 mm. Air dry synthetic gouge samples of 1.6 g were pre-compacted by loading using a uniaxial press oriented perpendicular to the layer at 10 MPa for the 10-25 MPa effective normal stress tests, or at 50 MPa for the 60 MPa effective normal stress tests. This produced samples with initial thicknesses of ~1.3 mm before pressurisation, improved sample cohesion for assembly, and reduced the initial porosity of the gouge. Porous stainless-steel disks with permeabilities of 10^{-13} m^2 in the direct shear sliders allowed transfer of pore fluid between the sample and the servo-controlled pore pressure pump (Figure 3.1).

The synthetic gouge samples were sheared in velocity-step tests at pore pressures held at 40 MPa and effective normal stresses (σ_n^{eff}) of 60 MPa, 25 MPa and 10 MPa to represent increasingly overpressured conditions. Samples were initially run at an axial loading rate of 0.3 µm/s for a displacement of 2 mm to bring the sample past yield, where the shear strength of the sample reached steady state. Following the initial yield phase, the sliding velocity was stepped between 0.3 µm/s and 3.0 µm/s every 0.5 mm of load point displacement to a maximum of 5.5 mm. The displacement on the friction curves has not been corrected for machine compliance, which was 75 kN/mm. Permeabilities of the gouge samples were measured at the end of shearing using the pore pressure oscillation technique (Bernabé et al., 2006; Faulkner & Rutter, 2000; Kranz et al., 1990), which returned final permeabilities of 10^{-17} m^2 for quartz-rich gouges to 10^{-20} m^2 for kaolinite-rich gouges. This concurs with previous permeability measurements of phyllosilicate powders, including muscovite, pyrophyllite, biotite, phlogopite, illite and talc (Behnsen & Faulkner, 2011), and natural fault gouges (Faulkner et al., 2003, 2018; Faulkner & Rutter, 2000; Wibberley & Shimamoto, 2003a; W. J. Wu et al., 2020), which show ranges in permeabilities from 10^{-17} to 10^{-24} m^2. The permeability was not monitored throughout the test as this reduced the capacity to monitor very small changes in pore volume during velocity steps, the technique for which is described next.

Pore volume changes during a test were monitored using the pore pressure control system, shown in Figure 3.1. The servo-controlled 5000 mm^3 pump adjusted the volume of fluid in the system to maintain the pressure at 40 MPa from measurements in the sample; a pore pressure increase required pore fluid to be extracted into the pump, whereas a pressure decrease required pore fluid to be added to the sample. By monitoring the displacement of the piston in the pore fluid control pump using a high-resolution linear variable differential transformer (LVDT), the equivalent changes in pore volume in the sample were measured (Figure 3.2). The maximum volume change that the LVDT could measure with one stroke was 200 mm^3 and the measurements were resolvable to 0.01 mm^3. This pore volume monitoring technique

(volumometery) included a time-dependent component because the control pump could only respond to pore pressure changes that had diffused out of the gouge sample. In order to assess the potential effect of these transients, the characteristic time (*t*) for equilibration of pore pressure across the sample was calculated using the thickness of the sample (*l*) and the hydraulic diffusivity (*κ*, see Supporting Info for calculations):

$$t = \frac{l^2}{\kappa} \qquad \text{(Eq. 3.3)}$$

This returned characteristic times across the range of gouge compositions of 10^{-3} to 1 sec. The synthetic gouges therefore had sufficiently high permeabilities for any pore pressure transients to equilibrate rapidly with the control pump, and thus gave reliable measurements of pore volume changes produced during the velocity steps (180 secs to 1800 secs).

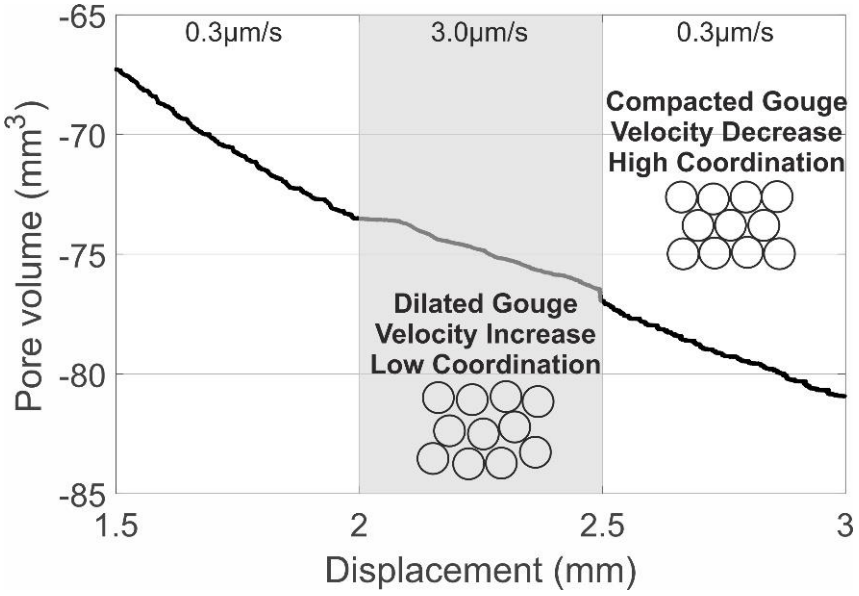

Figure 3.2: Measured pore volume changes in response to velocity step changes due to changes in packing of a granular material.

To determine the volume changes in response to velocity steps in a reproducible way, the volume curve for an individual velocity step was incrementally adjusted to produce a least-squares fit to the overall compaction trend (see Figure 3.2 and Supporting Info for calculations). In addition to reporting the measured volume changes, a dimensionless dilatancy parameter ***ε*** is reported for comparison between literature dilatancy data (Samuelson et al., 2009; Segall et al., 2010). ***ε*** normalises the measured volume change (*Δvol*) to both the total sample volume (*vol*) and the step change from initial slip velocity (V_0) to the increased slip velocity (*V*):

$$\varepsilon = \left({}^{\Delta vol}/_{vol}\right)/\log {}^{V}/_{V_0} \qquad \text{(Eq. 3.4)}$$

This removes the effects of sample volume and the scale of velocity step change from ε and allows direct comparison between published datasets.

Rate and state frictional parameters of the gouges were determined using the program RSFit3000 (Skarbek & Savage, 2019) that uses a non-linear least squares routine (Reinen & Weeks, 1993) to fit the experimental data to obtain the direct effect *a*, evolution effect *b,* and the slip weakening distance D_c from imposed velocity step changes. The stiffness (*k*) of the apparatus is also a fitting parameter (Noda & Shimamoto, 2009). In RSFit3000, the state evolution was described using the aging law (Ruina, 1983):

$$\frac{d\theta}{dt} = 1 - \frac{V\theta}{D_c} \qquad \text{(Eq. 3.5)}$$

This experimental framework that measures the gouge frictional strength, stability and dilatancy has been developed so that it can be applied to a wider range of fault gouge compositions.

3.3. Results:

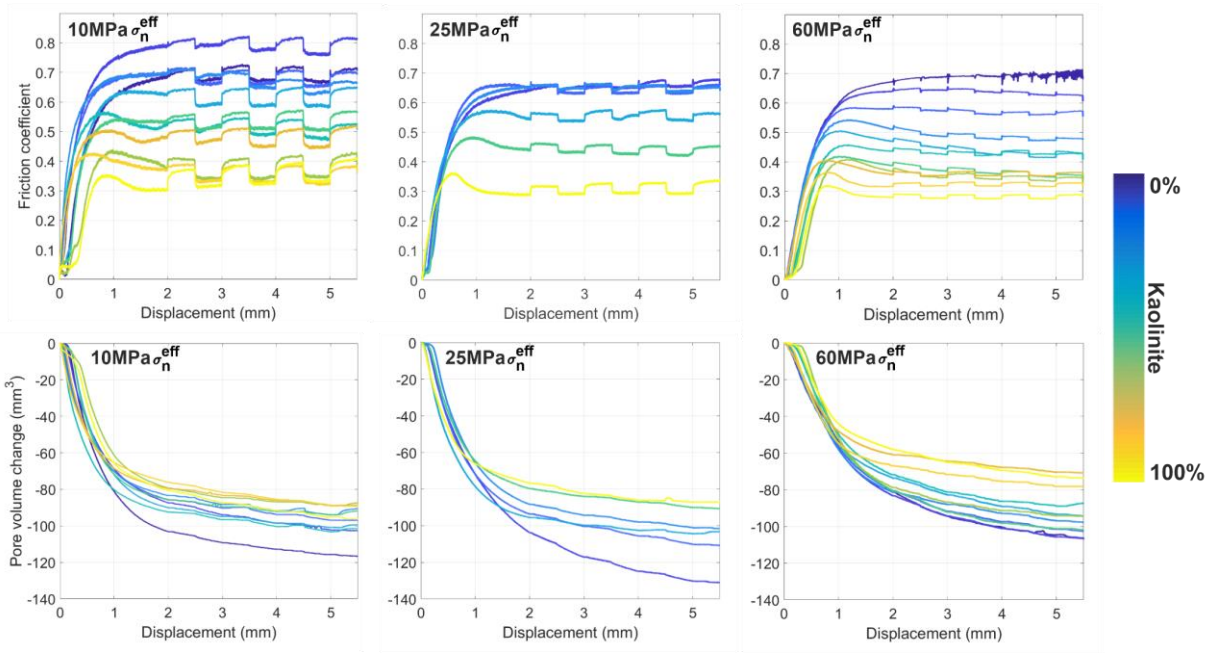

Figure 3.3: Summary of friction results (top) and volume change results (bottom) for velocity step test experiments at 10MPa, 25MPa and 60MPa effective normal stresses with incremental changes in gouge kaolinite content.

Prior to the onset of sliding, the samples were pressurized, which resulted in them compacting hydrostatically. Upon commencement of sliding, a phase of shear enhanced compaction occurred (Figure 3.3). The majority of shear enhanced compaction occurred prior to the yield phase of the tests. The kaolinite-rich gouges saw less compaction prior to the yield phase than the kaolinite-poor gouges, which is in line with previous studies that showed that more pre-

shear hydrostatic compaction occurred in the clay-rich gouges (e.g. Crawford et al. 2008). All gouges continued to compact after yield, although at a slower rate. The total amount of compaction, shown in Figure 3.4, was sensitive to the kaolinite content of the gouge. Increasing the kaolinite content led to a decrease in overall compaction, such as at 60 MPa σ_n^{eff} the 0 wt% kaolinite gouge experienced 106 mm^3 of compaction compared to 79 mm^3 of compaction for the 100 wt% kaolinite gouge. Increasing σ_n^{eff} decreased the overall shear enhanced compaction only in the clay-rich samples. The 100 wt% kaolinite gouge underwent 96 mm^3, 87 mm^3 and 40 to 70 mm^3 pore volume reduction across the increasing effective normal stresses (Figure 3.4).

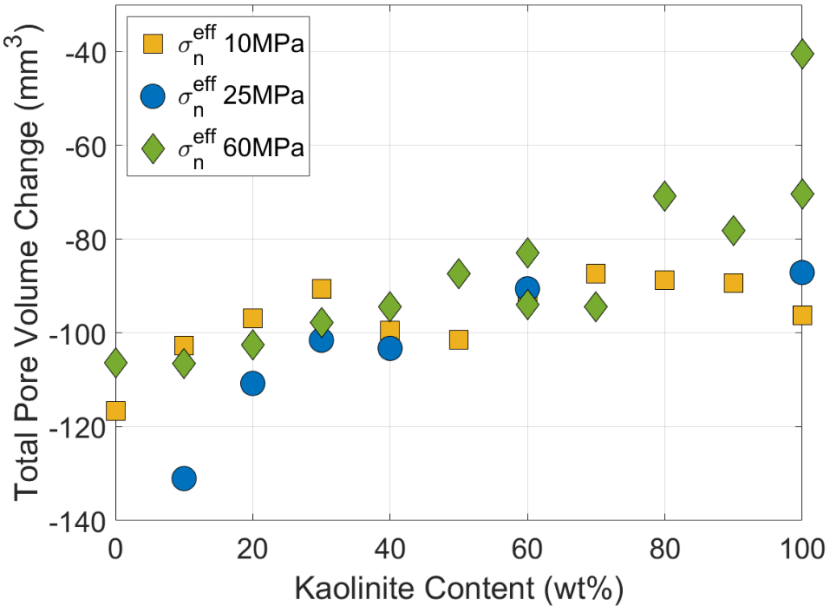

Figure 3.4: Experimental shear-enhanced compaction of synthetic fault gouges at 5.5mm displacement.

Dilation and compaction in response to velocity step changes that deviated from the overall compaction trend were observed in all the quartz-kaolinite gouges (Figure 3.5). Dilation always followed an increase in slip velocity and compaction always followed a decrease in slip velocity. The compaction following a velocity decrease was greatest in the 30 wt% kaolinite (70 wt% quartz) gouge at 10 MPa σ_n^{eff}, but compaction was fairly consistent across the gouge compositions. The dilation was greatest at kaolinite contents of 10-40 wt% with a decreasing trend towards the two end-member gouge compositions. Unlike the shear enhanced compaction results, there was no effect from varying the σ_n^{eff} on the dilatancy behaviour. The dilatancy was asymmetric as pore volume increases after velocity upsteps were always greater than pore volume decreases following velocity downsteps. For example, at 25 MPa σ_n^{eff} the 10 wt% kaolinite had a mean dilation of 0.88 mm^3 and a mean compaction of 0.25 mm^3.

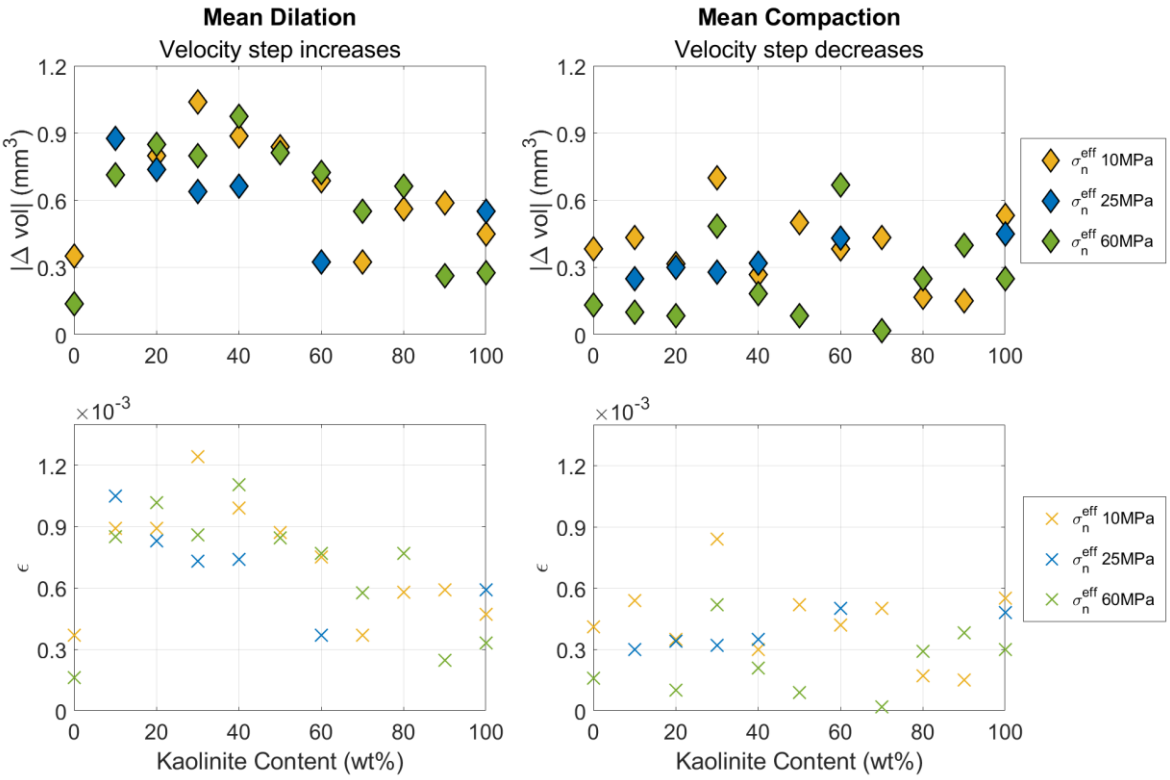

Figure 3.5: Measured (top) and normalised (bottom) experimental dilation and compaction in response to velocity-step changes in synthetic fault gouges.

All of the synthetic gouges reached a steady state yield strength following the initial 2 mm of load point displacement (Figure 3.3). The frictional strength of the synthetic gouges showed a strong dependence on the kaolinite content (Figure 3.6). The frictional strength of the gouges at the end of the tests, as shown in Figure 3.6, decreased with increasing kaolinite content from 0.689 for 0 wt% kaolinite to 0.275 for 100 wt% kaolinite at 60 MPa σ_n^{eff}. This negative trend was non-linear – at 60 MPa σ_n^{eff} frictional strength decreased steeply to 40wt% kaolinite, beyond which the decreasing trend shallows. At the lower σ_n^{eff} conditions, the transition from a shallowly decreasing trend to a steeper decreasing trend in frictional strength occurs at ~30 wt% kaolinite.

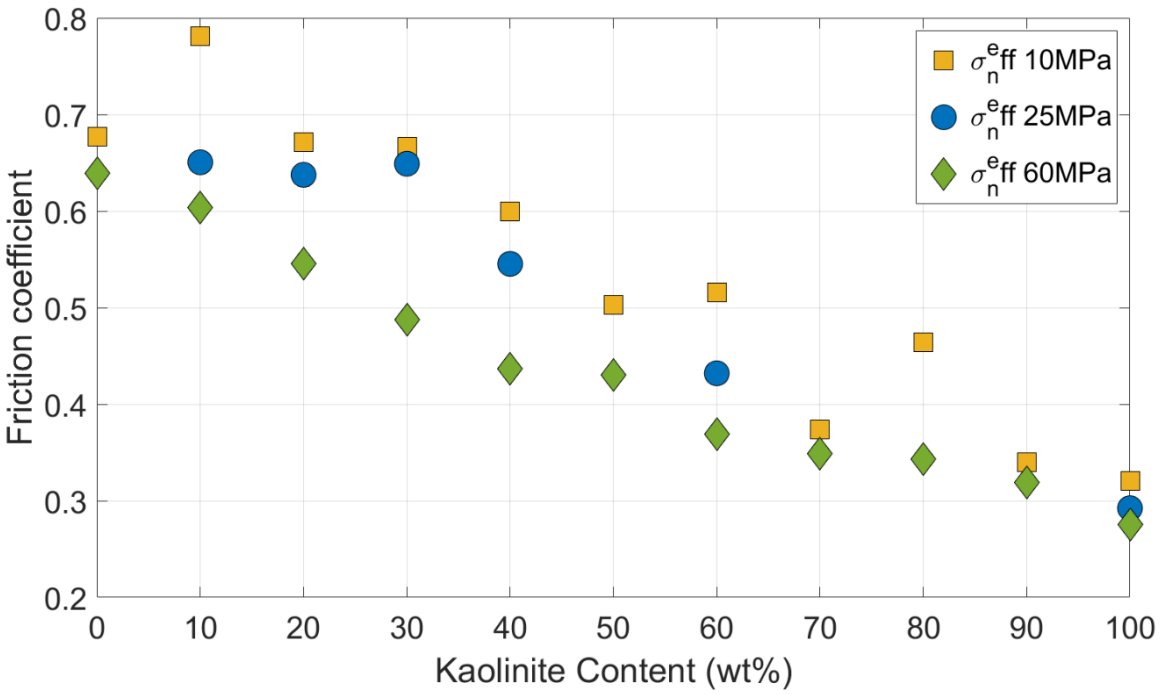

Figure 3.6: Average experimental frictional strength of synthetic quartz-kaolinite fault gouges.

The frictional parameter *(a-b)* was also strongly dependent on the kaolinite content (see Figure 3.7). Only gouges with 0 wt% kaolinite displayed velocity weakening behaviour in response to velocity steps, with the test at the highest effective normal stress (60 MPa) producing stick-slip instabilities at the end of the test (Figure 3.3). All gouges that contained any amount of kaolinite showed velocity strengthening behaviour. As with the gouge strength, the *(a-b)* results showed a change in sensitivity to gouge clay content. Below 40 wt% kaolinite, *(a-b)* increased with increasing kaolinite content but beyond 40 wt% kaolinite *(a-b)* was less dependent on the kaolinite content. The stability of the synthetic gouges was also strongly affected by the effective normal stress, as shown in Figure 3.7. Decreasing σ_n^{eff} decreased *b* to negative values, leading to larger *(a-b)* values and greater stability of sliding in the gouges. For example, in the 100 wt% kaolinite gouge *(a-b)* increased from 0.003 at 60 MPa σ_n^{eff} to 0.025 at 10 MPa σ_n^{eff}.

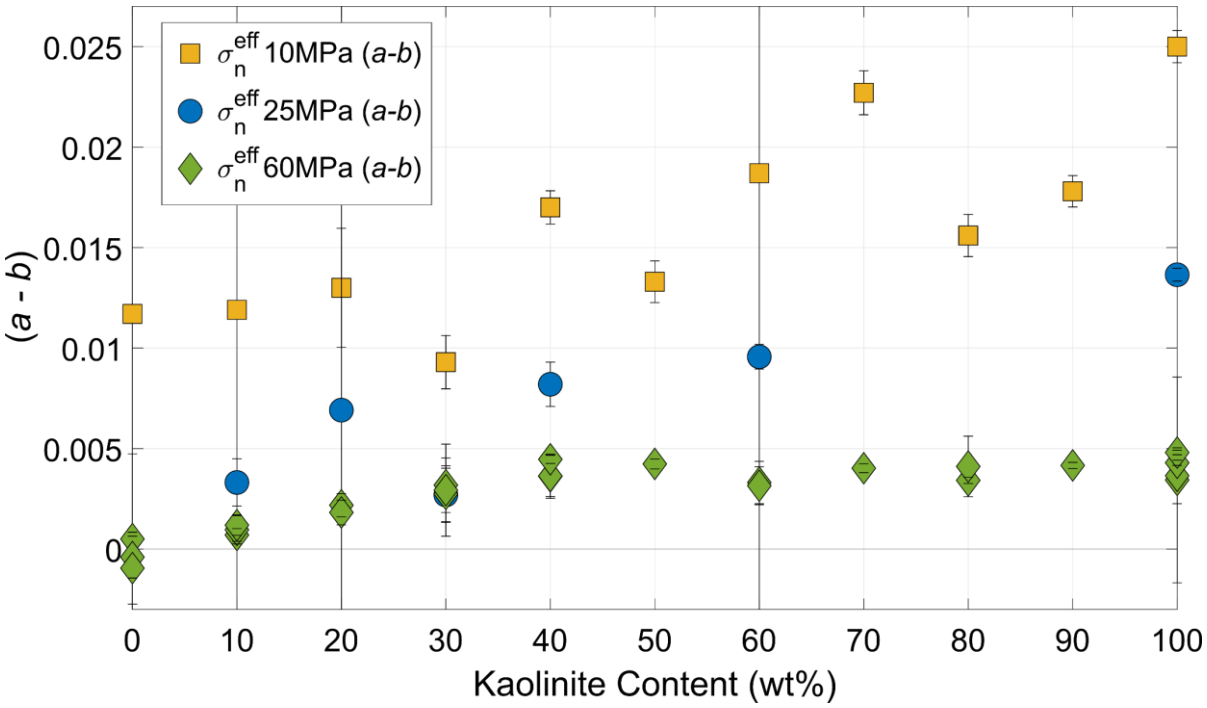

Figure 3.7: Average experimental rate and state stability of synthetic fault gouges from a velocity step increase. A material is velocity weakening when (a-b)<0 or velocity strengthening when (a-b)>0.

Samples of the synthetic gouges were recovered post-shearing for observations of the microstructures using a scanning electron microscope (Figure 3.8). The gouge microstructures showed a change with increasing kaolinite content from localised shear zones to more diffuse deformation across the gouge layer. Fractures were classified as shear fractures only if grain size reduction via cataclasis could be identified. In the clay-poor (0-10 wt% kaolinite) gouge samples, there was evidence of grain comminution and cracking in localised shear zones, as shown by the significant decrease in quartz grain size (Figure 3.8, a & b). Shear across the layer had been accommodated by a series of R_1 Riedel and shear-direction parallel Y-shears. The Y-shears were located on the periphery of the gouge layer, close to the interface with the direct shear slider surface (sometimes called boundary or B shears). As the kaolinite content increased, the quartz grains became increasingly more isolated and the microstructure changed from a clast-supported to a matrix-supported framework. From intermediate kaolinite contents (>30 wt%), Riedel shears and evidence of grain comminution became increasingly rare. The lack of a throughgoing Y-shear was shown by the 80 wt% kaolinite sample in Figure 3.8 (g), as the sawtooth interface between the shear slider and the gouge had been preserved.

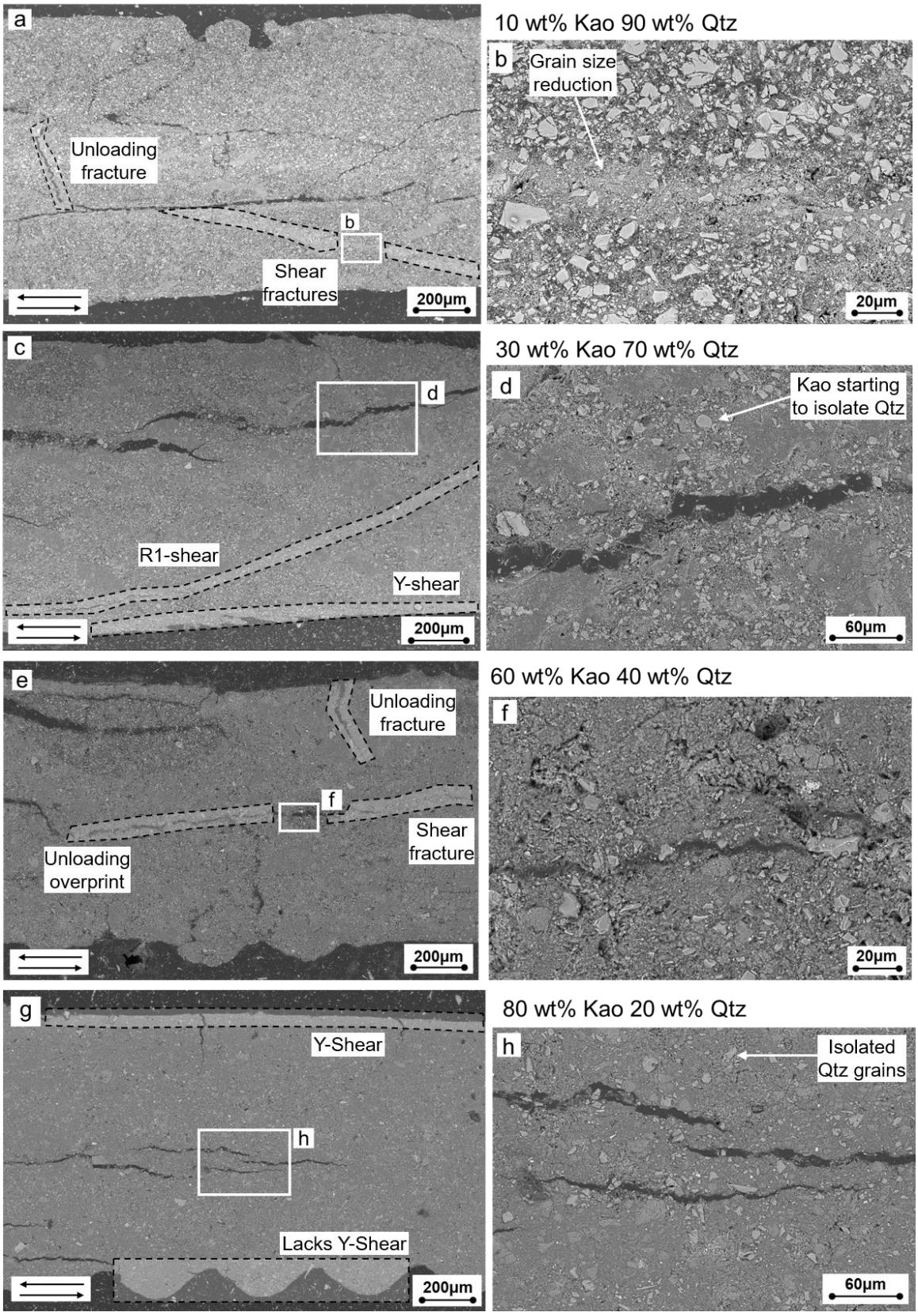

Figure 3.8: Back scatter SEM images of sheared samples of synthetic kaolinite-quartz gouges. The kaolinite content of the examples increases from 10 wt% (a,b) to 30 wt% (c,d), 60 wt% (e,f) and 80 wt% (g,h).

3.4. Discussion:

Controls on Dilatancy:

Previous measurements of dilatancy in granular materials have focused on quartz-rich materials. The dataset presented in this work greatly expands the compositional range of measurements to include clay-rich and clay-only materials (Figure 3.9). The results in Figure 3.9 show that gouge composition is a factor on the magnitude of dilatancy. Figure 3.9 also shows that maximum ε occurs not in the quartz-only gouges, but in the quartz-clay mixtures with 10-40 wt% clay. Changes in composition of a gouge incorporates multiple factors that may affect the scale of dilatancy, such as grain size, grain shape (aspect ratio) and roughness, although the scale of dilatancy in this study is comparable to measurements by Zhang et al. (2020) on smectite-quartz mixtures. The dilatancy of the very fine-grained (<2 μm) clay material was very similar or exceeded the dilatancy in the coarser-grained quartz. The maximum dilatancy at intermediate clay proportions likely results from changes in the mechanisms that accommodate shear, as compared to the end member gouges. Firstly, the smearing of a weak phase along grain contacts reduces the shear strength of a granular material, even at small proportions (5 wt%) of the weak phase (Rutter et al., 2013). The addition of very fine-grained clay may act to disrupt quartz-quartz contacts through grain sliding on the clays. The mechanisms of grain rolling and dilation would be promoted over cracking of the quartz grains. Secondly, Rathbun & Marone (2010) proposed dilatancy increases with the width of the zone of active shear. The proportion of kaolinite to quartz increases the width of the active shear zone. The Min-U-Sil quartz powder forms highly localised R_1 Riedel shears in triaxial deformation experiments (e.g. Bedford and Faulkner, 2021), however, with increasing kaolinite content, the gouges deform in broader, less localised shear zones and localized shears become rare (Figure 3.8). Dilatancy may be greater in the kaolinite-rich gouge mixtures due to the more distributed shear that occurs across the gouge layer in comparison to the quartz-only gouge.

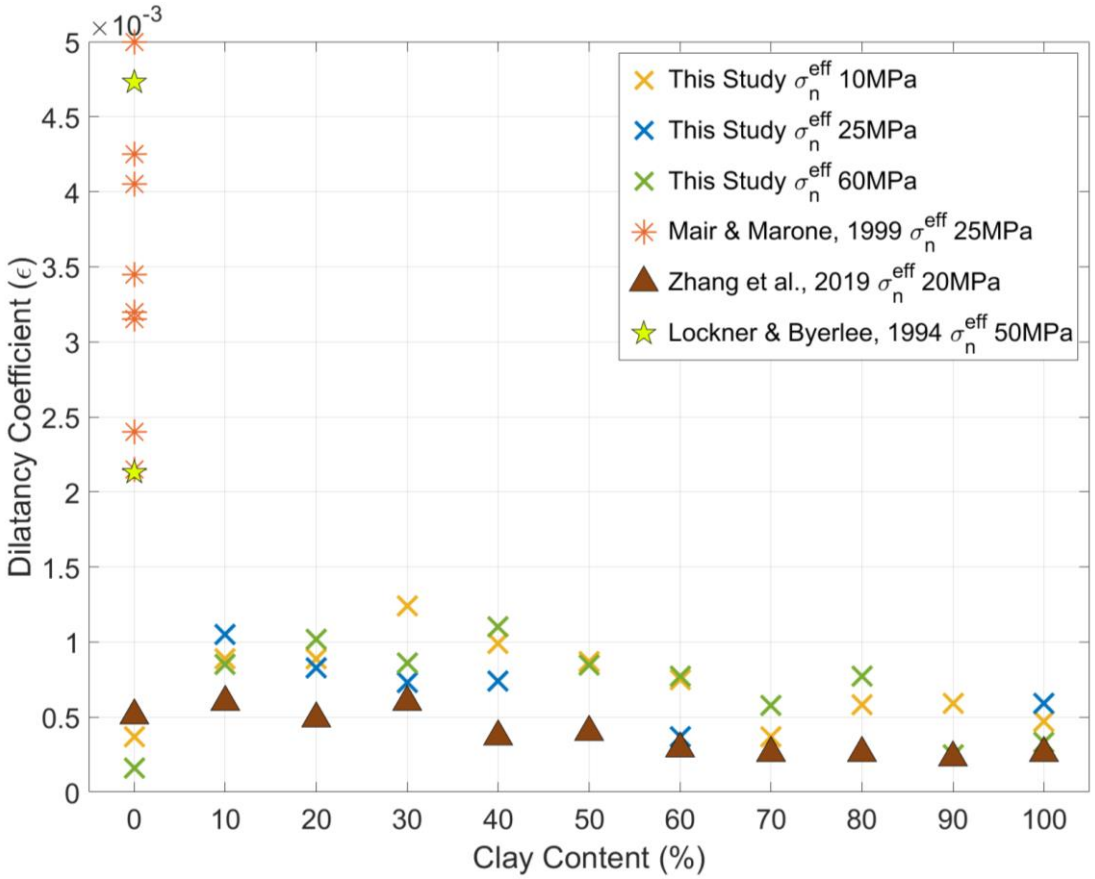

Figure 3.9: Pore volume increase (dilation) of experimental fault gouges normalised to sample volume and velocity step change (ε).

The dilatancy results also showed a distinct asymmetry between the scale of dilation and compaction for velocity up-steps versus down-steps (Figure 3.5). The quartz-only gouges showed equivalent compaction and dilation in response to velocity step changes, whereas all kaolinite-bearing gouges showed greater dilation than compaction. The asymmetry in the dilatancy results suggests that the strain rate history of the gouge affects the overall pore volume change in a sample. A velocity-stepping experiment produced less overall compaction than a constant velocity experiment, due to this asymmetry. In the measurements by Rathbun & Marone (2013) on quartz powders and clay-bearing glacial tills, both symmetry and asymmetry in the frictional curves and volume changes were observed. The asymmetry in their data is the opposite to that seen in this study, with compaction greater than dilation. Rathbun & Marone (2013) posit that dilation occurs only in the active slip zone and requires both shear strain and interparticle slip, but compaction occurs across the whole layer and only requires a change in stress to occur. The broad and diffuse microstructures in the kaolinite-bearing gouges of this study (Figure 3.8) may incorporate a higher proportion of the sample that dilates at a slip velocity step increase. The inversion of the asymmetry may result from the higher clay content and different grain size ranges in the gouges of this study, as this

subsequently created differences in the gouge microstructures to the experiments done by Rathbun & Marone (2013).

Controls on Frictional Behaviour:

Previous experimental investigations have already established clay content as a primary control on the frictional strength of fault gouges, as summarised in Figure 3.10 (K. M. Brown et al., 2003; Crawford et al., 2008; Ikari et al., 2009a; J. M. Logan & Rauenzahn, 1987; Moore & Lockner, 2011a; Takahashi et al., 2007; Tembe et al., 2010a). The data produced in this investigation adds measurements of rate and state friction parameters in greater detail across the compositional range of kaolinite-bearing fault gouges (e.g. Crawford et al., 2008) by controlling kaolinite-quartz content in 10 wt% increments between the two end member compositions. The non-linear decreasing trend of frictional strength with kaolinite content concurs with other deformation experiments using kaolinite (Crawford et al., 2008) and other clays, including: smectites (Ikari et al., 2007; J. M. Logan & Rauenzahn, 1987; Takahashi et al., 2007; Tembe et al., 2010a; Zhang et al., 2020), illite (K. M. Brown et al., 2003), and talc (Moore & Lockner, 2011a). Kaolinite-quartz mixtures display a 2-phase decrease in frictional strength with a transition at ~30-40 wt% (see Figure 3.10).

Grain packing models (e.g. Lupini et al., 1981; Marion et al., 1992; Takahashi et al., 2007) can be used to understand the changes in frictional strength of a gouge due to the gouge's composition. For gouges with low clay contents, an interconnected framework of quartz grains supports the applied stresses and governs the gouge deformation (Ikari et al., 2007; J. M. Logan & Rauenzahn, 1987; Takahashi et al., 2007). With increasing clay content, the available pore space within the quartz grain-supported framework will be filled by the finer-grained clay (see Figure 3.8). Under zero pressure the porosity of the quartz is ~40 % and the clay ~70 %. Hence at ~40 wt% clay, the clay grains fill the available pore space and the gouge strength cannot be supported by quartz grain contacts alone (Takahashi et al., 2007). At clay contents of >40 wt%, quartz-quartz contacts become rare and the applied stresses are supported by an interconnected clay matrix (see Figure 3.8). When pressure is applied both end members compact, so that the porosity minimum migrates from 40 wt% clay to lower values (Crawford et al. 2008). A 3 phase decrease in frictional strength observed for smectite mixtures was explained using a transitional regime between the quartz- and clay-dominated regimes, which was not observed here (Lupini et al., 1981; Tembe et al., 2010a). However, the porosity measurements by Marion et al. (1992) show that porosity is at a minimum between 20 wt% to 40 wt% clay in a quartz sand-kaolinite mixture at effective stresses of 10 MPa to 50 MPa. This broadly fits with the transition in the frictional data from the grain-supported framework of quartz to the matrix-supported framework of clay at ~30-40 wt% clay in this study.

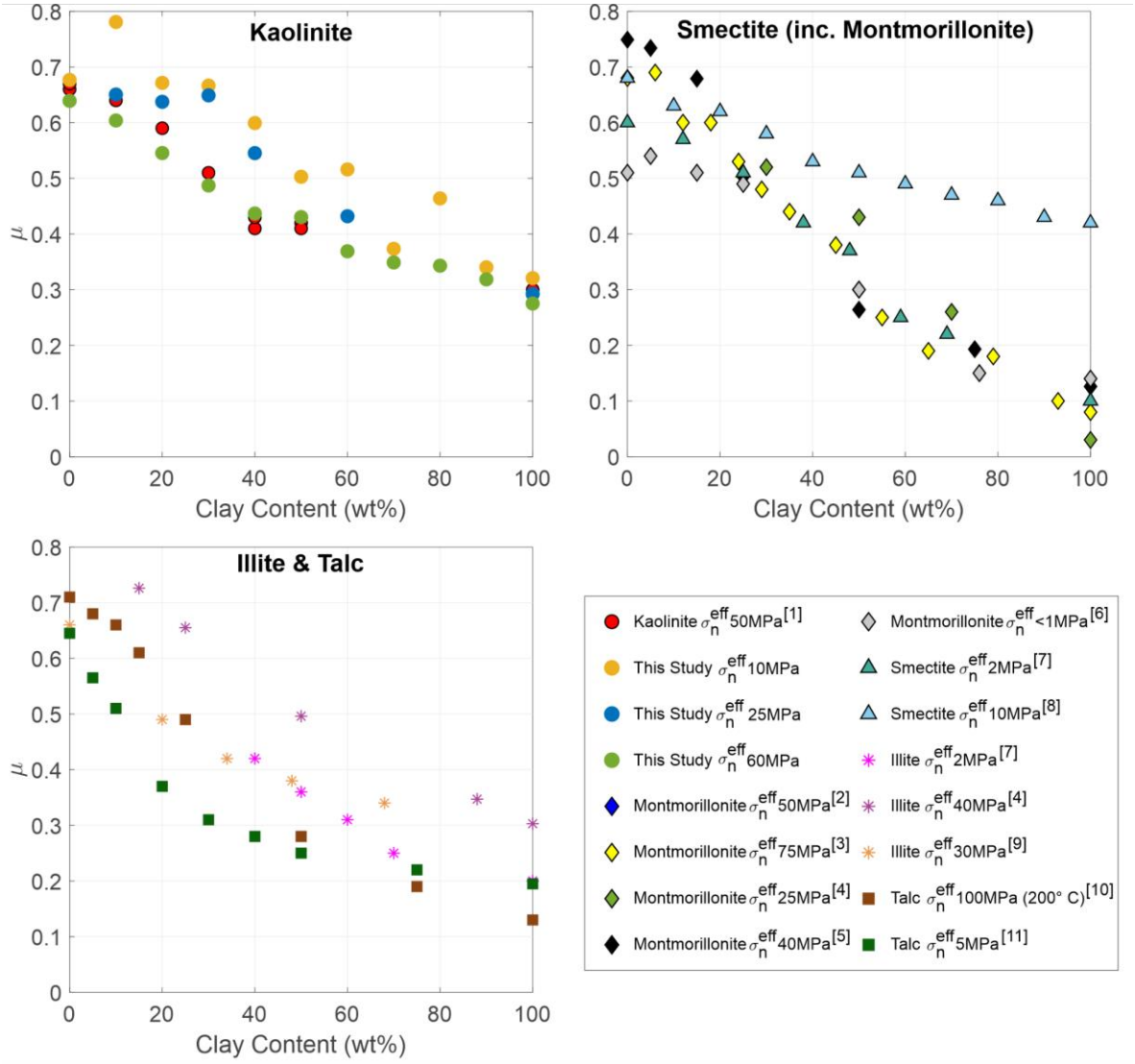

Figure 3.10: Experimental frictional strengths of quartz-clay gouges. Literature sources: [1] Crawford et al., 2008; [2] Logan & Rauenzahn, 1987; [3] Takahashi et al., 2007; [4] Ikari et al., 2007; [5] Tembe et al., 2010; [6] Lupini et al., 1981; [7] Brown et al., 2003; [8] Zhang et al., 2020; [9] Ruggieri et al., 2021; [10] Moore & Lockner, 2011; [11] Giorgetti et al., 2015.

Across various literature sources, apparatus and experimental parameters, there is consensus that clay minerals typically display velocity strengthening behaviour (Figure 3.11). The consistency of the (*a*-*b*) parameter beyond ~40 wt% kaolinite indicates that the frictional response to a velocity-step change is strongly influenced by the kaolinite (Figure 3.7) and is supported by the microstructural transition from a localized quartz-dominated fabric to a distributed clay-dominated fabric (Figure 3.8). Quartz is a typically velocity weakening material but the addition of only 10 wt% kaolinite, a typically velocity strengthening material, is enough to change the gouge to velocity strengthening behaviour. In contrast to the frictional strength results, the (*a*-*b*) parameter shows not only a strong positive dependence on kaolinite proportion but also on σ_n^{eff}. Bedford and Faulkner (2021) report a similar dependence of (*a*-*b*) on σ_n^{eff} in quartz powders as is observed in this study. As σ_n^{eff} increases, the friction

parameters become more velocity weakening and stick slip behaviour becomes prevalent, although this is not consistent across all reported data. Saffer & Marone (2003) and Zhang et al. (2020) observed negative correlation of (*a*-*b*) with σ_n^{eff} in smectite-quartz mixtures (but not in illite-quartz mixtures), although these tests were conducted at room humidity without pore pressure. The change in phyllosilicate behaviour between dry and wet conditions, which is significant in kaolinite, lizardite and chlorite, has been well documented and may account for this opposing trend (Behnsen & Faulkner, 2012; Han, et al., 2020; Moore & Lockner, 2004; Saffer & Marone, 2003).

In this study, the direct effect *(a)* remained constant at ~0.005 at clay proportions >40 wt% across all σ_n^{eff}. The increased *(a-b)* parameter at lower σ_n^{eff} was due to changes in the evolution effect *(b)*, which decreased to strongly negative values, with a minimum of -0.011. Negative *b* values do not conform to the interpretation of the evolution effect deriving from changes in the contact area (Dieterich, 1979; Li et al., 2011). If the evolution effect is a result of changes in the contact area, contact saturation would occur at $b = 0$ so that a negative *b* value would imply that the contact area of the grains exceeds saturation (Ikari et al., 2009a). Negative *b* values therefore lend weight to the argument that the frictional aging of grain contacts, through processes such as chemical bonding, controls the friction evolution effect in clay-rich gouges (Li et al., 2011). Mineral surfaces of phyllosilicates commonly have a high surface charge, and so can produce grain contacts with variations in strength dependent on the presence or absence of absorbed water (Y. Han et al., 2020).

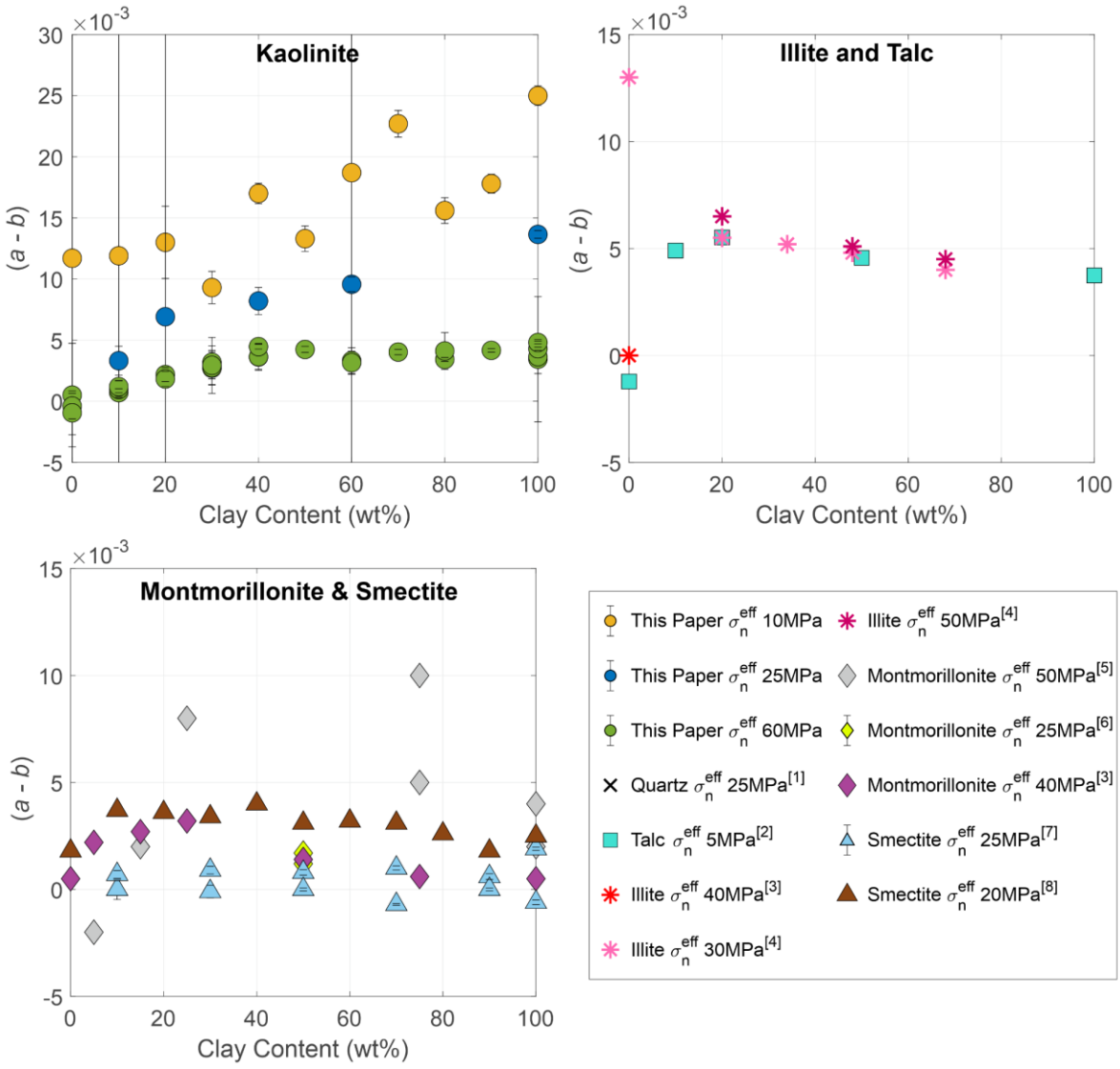

Figure 3.11: Experimental frictional stability parameters (a-b) from velocity step tests reported from literature sources: [1] Mair & Marone, 1999; [2] Giorgetti et al., 2015; [3] Tembe et al., 2010; [4] Ruggieri et al., 2021; [5] Logan & Rauenzahn, 1987; [6] Ikari et al., 2009; [7] Saffer & Marone, 2003;[8] Zhang et al., 2020.

Implications of gouge dilatancy:

Several studies have incorporated dilatancy into models for earthquake nucleation and propagation (e.g. Dal Zilio et al., 2020; Liu, 2013) and rate and state friction frameworks (Ferdowsi & Rubin, 2020; Heimisson et al., 2021; Rathbun & Marone, 2013; Segall & Rice, 1995). In the results presented here, only the quartz gouges showed velocity-weakening behaviour and could therefore nucleate earthquakes. Consequently, for earthquake nucleation, the pore pressure changes in clay-poor (quartz-rich) gouges are more significant. The dilation in response to acceleration of slip would cause a pore pressure drop and any potential instability would be damped. Dilatancy in clay-rich gouges would lead to more prolonged pore pressure changes than in clay-poor gouges, because low permeabilities in

clay-rich gouges tend towards undrained conditions. However, the weak, velocity strengthening clay-rich gouges will not nucleate instabilities. Instead, dilatancy increases the capacity of more clay-rich regions of faults to arrest growing slip patches during nucleation and earthquake propagation. Current models of fault seismicity have incorporated dilatancy parameters on the order of 10^{-4} to investigate the role of dilatancy in the seismic cycle (Dal Zilio et al., 2020; Heimisson et al., 2021; Liu, 2013; Segall et al., 2010). This study has measured dilatancy in the range of $2x10^{-4}$ to $1.2x10^{-3}$ across the full compositional range of quartz to clay content.

In previous investigations (Rathbun & Marone, 2013; Segall & Rice, 1995), attempts have been made to describe the stability of fault slip using both the rate and state friction parameters and the dilatancy parameter. An example from Segall & Rice (1995) defines the stability parameter (*E*):

$$E = \frac{\mu\varepsilon}{\beta b(\sigma - p)} \qquad \text{(Eq. 3.6)}$$

Where β is the compressibility of the material. If $E < 1 - a/b$ it indicates that, under the set conditions, the fault has the potential to host an earthquake, whereas a value of $E > 1 - a/b$ indicates that quasi-static slip behaviour would occur (Segall & Rice, 1995). An alternative method to calculate the effect of dilatancy on fault slip behaviour is to relate the change of steady state shear stress (τ_{ss}) with the natural log of slip velocity (v) to the steady state frictional strength of the material (μ_{ss}) (Segall & Rice, 1995):

$$\frac{\partial \tau_{ss}}{\partial \ln v} = \frac{\mu_{ss}\varepsilon}{(\sigma - p)\beta} \qquad \text{(Eq. 3.7)}$$

In order to produce instability, this parameter would need to be negative and bring the curve below a critical stiffness criterion (k_{crit}) that is defined for an undrained system as:

$$k_{crit} = \frac{1}{D_C}\left[(\sigma - p)(b - a) - \frac{\varepsilon\mu_{ss}}{\beta}\right] \quad . \qquad \text{(Eq. 3.8)}$$

Use of these parameters is based on the assumption of velocity weakening materials. Hence the approach has limited applicability for the majority of this data set, which is dominated by velocity strengthening characteristics. However, the velocity strengthening behaviour and lack of unstable slip may be, in part, an effect of the low temperature conditions of the tests. The aseismic creep observed for clay-bearing material in rock deformation experiments is at odds with the observations that most mature (and hence likely clay-bearing) fault zones are also seismogenic (e.g. Chester et al., 1993; Jefferies et al., 2006; Chester and Logan, 1987; Toy et al., 2015; Wibberley and Shimamoto, 2003). A limited quantity of experimental data indicate

that clay-bearing gouges become less stable with increasing temperature (Boulton et al., 2014; den Hartog et al., 2013; Verbene et al., 2010).

The potential effect of compaction weakening is not considered in most stability analyses. Faulkner et al. (2018) showed that compaction of gouge in experiments can produce pore pressure transients that affect the gouge mechanical strength and also the determination of the rate and state parameters. In nature, if porosity is 'reset' due to fluidization in earthquakes, there is potential for compaction to occur with fault slip during earthquake nucleation. The dilatancy effects described in this work, produced by slip velocity changes, would be superimposed on these slip-dependent porosity changes. Consequently, the interplay of compaction and dilatancy has the potential to produce quite complex pore pressure development during accelerating fault slip.

3.5. Conclusions:

A series of velocity-step deformation experiments were conducted on synthetic quartz-kaolinite fault gouges to investigate the controls on pore volume changes in fault gouges. The kaolinite content in the gouges was controlled at 10 wt% increments to test the effect of composition on the frictional strength, stability and dilatancy of the gouges. The pressure conditions were set at 60 MPa, 25 MPa and 10 MPa σ_n^{eff} to simulate a fault system at hydrostatic to overpressured conditions. The experimental results include that:

- All of the quartz-kaolinite gouges experienced dilation in response to an increase in slip velocity and compaction in response to a decrease in slip velocity.
- The scale of dilatancy in response to velocity-step changes was affected by the gouge kaolinite content but not by the effective stress conditions.
- Increasing kaolinite content in the synthetic gouges decreased the gouge frictional strength and increased (*a*-*b*) to promote stable sliding rather than unstable, earthquake slip.
- Increasing effective normal stress increased the likelihood of nucleation of unstable slip by decreasing the rate and state friction parameter (*a*-*b*).

Acknowledgments:

We acknowledge financial support from a Natural Environment Research Council grant NE/V011804/1 to DRF and the NERC EAO DTP studentship to IRA at the University of Liverpool. Gary Coughlan and Michael Allen provided essential technical support in the maintenance and construction of the experimental apparatus. We gratefully acknowledge the Albert Crewe Centre for Electron Microscopy SEM Shared Research Facility for their technical support, training & assistance in this research. We are grateful to M. Ikari and Y. Bernabe as

editors, B. Carpenter and an anonymous reviewer for their time, effort and insightful comments on our manuscript.

Open Research:

Experimental data files and the code and functions used for dilatancy volumometry analysis are available in the BGS National Geoscience Data Centre (NGDC) under the Open Government Licence (ID 176345).

3.6. Supporting Information:

Contents of this section:

Introduction:

The information included in this document details the method of calculating dilatancy from pore volumometry measurements. In addition to Figure 3.12, the MatLab functions that were formulated to process the pore volumometry measurements for dilatancy are available at https://github.com/izzyashman/rock-friction-dilatancy.git under a GNU General Public License v3.0.

In the velocity step tests, an initial shear enhanced compaction phase drastically reduces the sample pore volume until the sample yields. After the sample yields, the pore volume continues to decrease but at a lower rate of decrease. The imposed velocity steps cause compaction or dilation of the sample material that is superimposed on this overall compaction trend. Pore pressure is held at a set point (40 MPa) in all tests and any volume changes in the control system are assumed to correspond directly to changes in pore volume in the sample. The method here is aimed at producing quantitative, reproducible values for dilatancy from experimental data. This code could easily be used to process dilatancy data that is recovered from measurements of changes in shear zone width in biaxial apparatus (e.g. Carpenter et al., 2016; Mair & Marone, 1999; Rathbun & Marone, 2013; Zhang et al., 2020).

The script fits a polynomial function to all the volume data to give the overall trend of the shear enhanced compaction. The data position of the start of the velocity step of interest is entered manually into the function. When dilatancy occurs on a step change in velocity, this is not immediately recorded using volumometry, as the permeability of the sample will produce a transient response as pore fluid pressure equilibrates between the sample and the pore fluid pressure system. In order to discount this effect, every velocity step was processed with a

'*time_dep*' phase for the first 100 μm of displacement after the imposed velocity step change. For our samples, the characteristic time for fluid diffusion was well within the time represented by 100 μm of displacement, so we were confident that any pore pressure transients had dissipated by this point in the test.

This method relies on the transmission of fluid between the pore pressure control pump and the sample, which introduces a time-dependency to the method. Hence, the characteristic time (*t*) for equilibration of pore pressure across the sample was calculated using the thickness of the sample (*l*) and the hydraulic diffusivity (*κ*) to test the advocacy of the method. Hydraulic diffusivity was calculated using: the measured sample permeability; the fluid compressibility (*βf*), which was calculated from the volume changes that resulted from cycling the pressure (Eq. S3); and the viscosity of the fluid at the given conditions, as taken from the NIST Chemistry WebBook (https://webbook.nist.gov/chemistry/fluid/).

$\kappa = k / \beta c\, \eta$ where k = permeability, βc = compressibility, and η = viscosity of fluid. (Eq. 3.9)

$\beta c = \beta f * \varphi$ where βf = fluid compressibility and φ=porosity. (Eq. 3.10)

$\beta f = -1/V * \delta V/\delta P$ where V=volume, and P=pressure. (Eq. 3.11)

Using the values for '*vel_step*' and '*time_dep*', the volumometry data are split into separate matrices incorporating time and volume preceding and following the velocity step change. A linear regression model fits a polynomial curve to the pore volumometry data and returns the coefficient of determination (R^2) for the fit of the model. The shear enhanced compaction phase prior to yield is included in the fit but it excludes the time-dependent data in '*time_dep*'. The code then incrementally adds the value entered for '*step*' to the data in the velocity step of interest. This '*step*' value will be a positive or negative value depending on whether the imposed velocity has increased or decreased, respectively. A new linear regression model is then fitted to the whole dataset and if the R^2 value has increased, the code will continue to loop to add the value of 'step' to the pore volume data following the velocity step of interest. The loop concludes when the R^2 value reaches a peak and begins to decrease, as the fit of the linear regression model to the overall compaction trend is no longer improving. We assume at this point that the effect of the dilatancy due to the velocity step has been removed, and the cumulative sum of the '*step*' values is equivalent to the dilatancy. As the loop goes one iteration past the optimum R^2 value, the code reverts to the previous set of values with the best R^2 value. The final stage of the code is to plot the uncorrected and corrected data as a visual cue to the user of the offset identified.

In experiments with multiple velocity step changes, the code needs to retain the previous corrections of the data as the deviation from the overall compaction trend will then impact the model for subsequent velocity step changes. The function '*pf_correct*' is used to correct the velocity steps that have been previously processed. The values for '*vel_step'*, '*time_dep*' and the returned value of '*offset*' need to be given in the inputs for '*pf_correct'*.

The rate and state friction (RSF) data in this study was analysed using the MatLab software RSFit3000 (Skarbek and Savage, 2019). Figure 3.13 shows examples of the model fits to the experimental data in the RSFit3000 GUI. The program is able to apply both the aging law (Ruina, 1983) and the slip law (Dieterich, 1979) in the data processing. Both methods returned identical or very similar values of the RSF parameters (*a*-*b*), *dc* and *k* and the coefficient of determination (R^2) for the experimental data.

A summary table of the friction and dilatancy results is also included for transparency (Table 3.1). The full range of experimental conditions and quartz-clay compositions of gouge have been included. The sample volume, total shear enhanced compaction, averaged measured dilation and the returned value of ε have been included to allow this dilatancy method to be tested for reproducibility.

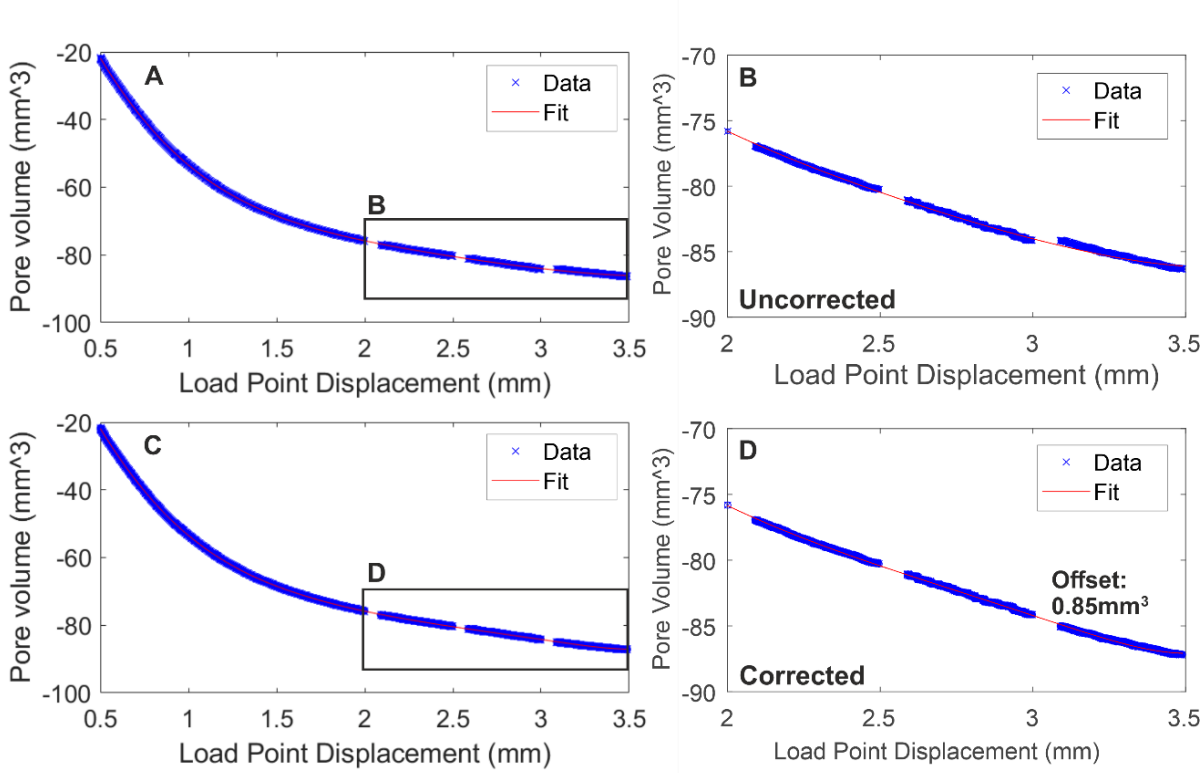

Figure 3.12: An example of the method that is used to calculate the dilation and compaction of the simulated fault gouges in response to a change in slip velocity from the measured pore volume data. The targeted velocity step in the example shown here is from a quartz-kaolinite fault gouge of 80 wt% quartz to 20 wt% kaolinite. Panels A and B show the pore volumometry data that has not been adjusted for the velocity step change at 3 mm of load point displacement from 0.3 to 3.0 µm/s. Panels C and D show the pore volumometry data with the calculated offset of 0.85 mm^3 removed from the velocity step at 3 mm load point displacement.

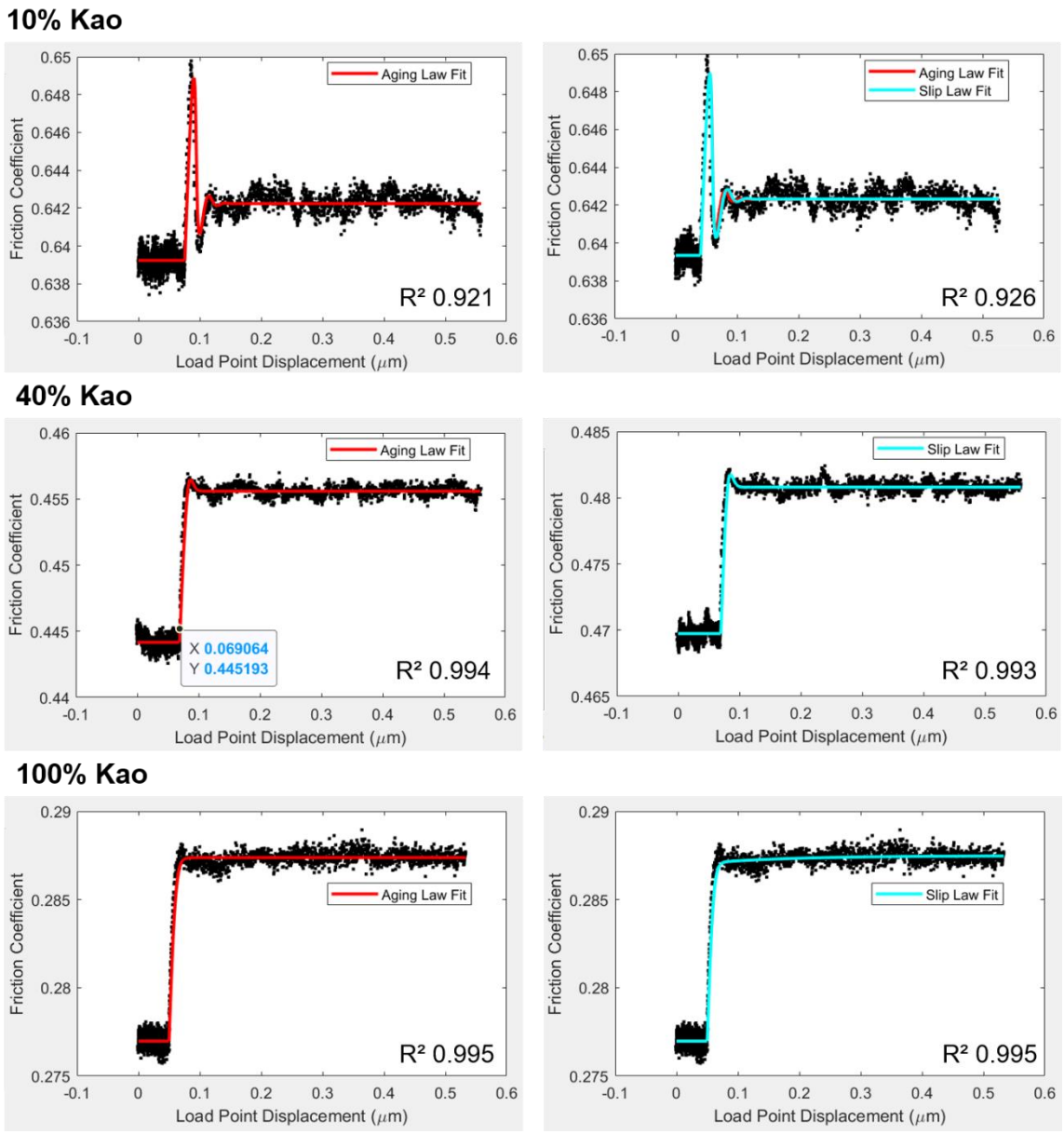

Figure 3.13: Examples of the rate and state friction (RSF) analysis from the MATLAB software RSFit3000 (Skarbek and Savage, 2019) of velocity step increases imposed on quartz-kaolinite fault gouges, which used both the aging law in red (Ruina, 1983) and, for comparison, the slip law in blue (Dieterich, 1979). All of the example tests shown here were taken from experiments conducted at 60 MPa effective stress.

Code	Clay content (wt%)	σ_n^{eff}	Slip velocity (μ/ms)	Sample Volume (mm^3)	Total shear enhanced compaction (mm^3)	μ (aver-age)	[a-b] (aver-age)	2SD error [a-b]	Measured average dilation (mm^3)	ε
10KAO0	0	10	0.3-3	935.28	116.65	0.6768	0.0117	0.0541	0.35	0.00037
10KAO10	10	10	0.3-3	798.48	102.65	0.7808	0.0119	0.0382	0.7125	0.00089
10KAO20	20	10	0.3-3	895.68	96.95	0.6715	0.013	0.0029	0.8	0.00089
10KAO30	30	10	0.3-3	837.36	90.62	0.6665	0.0093	0.0013	1.0375	0.00124
10KAO40	40	10	0.3-3	896.4	99.46	0.5993	0.017	0.0008	0.8875	0.00099
10KAO50	50	10	0.3-3	958.32	101.48	0.5028	0.0133	0.001	0.8375	0.00087
10KAO60	60	10	0.3-3	920.88	91.88	0.516	0.0187	0.0386	0.6875	0.00075
10KAO70	70	10	0.3-3	872.64	87.43	0.3735	0.0227	0.0011	0.325	0.00037
10KAO80	80	10	0.3-3	964.8	88.69	0.4640	0.0156	0.001	0.56255	0.00058
10KAO90	90	10	0.3-3	995.042	89.35	0.3403	0.0178	0.0008	0.5875	0.00059
10KAO100	100	10	0.3-3	966.96	96.22	0.3208	0.025	0.0008	0.45	0.00047
25KAO10	10	25	0.3-3	833.76	131.05	0.6505	0.0033	0.0012	0.875	0.00105
25KAO20	20	25	0.3-3	891.36	110.77	0.6375	0.0069	0.0600	0.7375	0.00083
25KAO30	30	25	0.3-3	874.08	101.56	0.649	0.0027	0.0013	0.6375	0.00073
25KAO40	40	25	0.3-3	900	103.29	0.5453	0.0082	0.0011	0.6625	0.00074
25KAO60	60	25	0.3-3	871.92	90.6	0.432	0.0096	0.0006	0.325	0.00037
25KAO100	100	25	0.3-3	936	87.12	0.2923	0.0136	0.0003	0.55	0.00059
60KAO0	0	60	0.3-3	833.76	106.4	0.69	-0.0004	1.042E-03	0.135	1.62E-04
60KAO10	10	60	0.3-3	835.2	106.5	0.626	0.00096	7.043E-04	0.7125	8.53E-04
60KAO20	20	60	0.3-3	836.64	102.6	0.562	0.00218	5.834E-04	0.85	1.02E-03
60KAO30	30	60	0.3-3	929.52	97.8	0.476	0.00293	2.291E-03	0.8	8.61E-04
60KAO40	40	60	0.3-3	884.16	94.4	0.416	0.00364	1.030E-03	0.975	1.10E-03

Code	Clay content (wt%)	σ_n^{eff}	Slip velocity (μ/ms)	Sample Volume (mm^3)	Total shear enhanced compaction (mm^3)	μ (aver-age)	[a-b] (aver-age)	2SD error [a-b]	Measured average dilation (mm^3)	ε
60KAO50	50	60	0.3-3	961.2	87.3	0.428	0.004236	2.482E-04	0.8125	8.45E-04
60KAO60	60	60	0.3-3	936	82.9	0.365	0.00315	9.447E-04	0.725	7.75E-04
60KAO70	70	60	0.3-3	955.44	93.4	0.336	0.004022	2.185E-04	0.55	5.76E-04
60KAO80	80	60	0.3-3	859.32	70.8	0.352	0.00411	1.506E-03	0.6625	7.71E-04
60KAO90	90	60	0.3-3	1061.28	78.2	0.318	0.004162	1.492E-04	0.2625	2.47E-04
60KAO100	100	60	0.3-3	840.6	70.4	0.275	0.004294	1.315E-04	0.275	3.27E-04

Table 3.1: A summary table of the experimental results of the measured frictional strength, rate and state friction values, and volume changes in simulated quartz-kaolinite gouges with compositions from 0 wt% to 100 wt% kaolinite.

4. Clay-rich fault gouges become frictionally unstable at elevated temperatures

Isabel Ashman[1], Daniel Faulkner[1] & Elisabetta Mariani[1]

[1]School of Environmental Sciences, University of Liverpool, UK

Formatted for submission to Nature Geoscience.

Abstract:

Large earthquakes nucleate on crustal faults that have accumulated significant slip displacement and field observations show that these faults are ubiquitously clay-rich. Earthquake nucleation requires a reduction in shear resistance for instabilities to develop. Previous laboratory friction measurements indicate almost exclusively that only stable fault creep should occur in clay-rich faults; a result apparently at odds with observations of widespread earthquake behaviour on mature clay-rich faults in nature.

Here we show that the frictional stability of clay-bearing fault gouges decreases systematically with elevated temperatures commensurate with those found at typical earthquake depths. In materials containing ≤ 50 % clay, the stability of slip decreased with increasing temperature so that the materials displayed unstable slip at temperatures between 100 and 180°C, whereas at room temperature the same materials hosted only stable slip. This reduction in stability with increasing temperature coincides with a greater degree of localization observed in the gouge microstructure.

Our results indicate that a much broader compositional range of clay-bearing fault rocks, and therefore mature faults, can nucleate unstable slip at conditions common to the clay-bearing brittle crust; a result that resolves the apparent paradox that mature clay-bearing faults in nature can nucleate and propagate earthquakes.

There is a fundamental discrepancy concerning clay-rich fault rocks between the typical frictionally stable slip produced in rock deformation experiments and observations of unstable seismic slip on natural, mature faults. Seismogenic, mature faults, from surface observations and from drilling, typically contain significant proportions of clay and would not be expected to nucleate earthquakes based on laboratory measurements. For earthquake nucleation, the strength of the fault material must decrease with increased slip velocity to produce run-away unstable slip. In the laboratory, clay-bearing materials almost exclusively strengthen with increasing slip velocity (Giorgetti et al., 2015; Ikari et al., 2009b; J. Logan & Rauenzahn, 1987; Saffer & Marone, 2003; Tembe et al., 2010b; Zhang et al., 2020) and so deform via stable creep, which precludes the possibility of seismic slip.

In contrast, earthquakes of all magnitudes commonly occur on mature faults, in addition to a spectrum of stable and unstable slip behaviours including aseismic creep and slow slip earthquakes (Den Hartog et al., 2021; Lee et al., 1998; Thomas, Avouac, Gratier, et al., 2014; Y. M. Wu et al., 2006). Examples of such mature, multi-slip-mode fault zones include the Longitudinal Valley Fault (LVF) in Taiwan with several 10s of kilometres displacement, the Alpine Fault Zone (AFZ) in New Zealand with an estimated 475 km displacement, and the Median Tectonic Line (MTL) in Japan, with estimates of displacement between 200 and 1000 km (Figure 4.1). Observations suggest that the fault core on all these structures, and other similar structures, contains abundant clay minerals.

The LVF constitutes a series of locked and creeping fault segments (Den Hartog et al., 2021; Lee et al., 1998; Thomas, Avouac, Champenois, et al., 2014) with fault rock clay contents from both fault segment types ranging from 20 to 57 wt% (Den Hartog et al., 2021). Even in low proportions of the bulk material (<10 %), a weak phase has a disproportionate control on the bulk deformation behaviour (Moore & Lockner, 2011b; Rutter et al., 2013; Tembe et al., 2010b). Hence, seismic slip at such clay proportions should be highly improbable, but the LVF has ruptured in earthquakes of M_w 6.8 in 2003 (Y. M. Wu et al., 2006) and twelve M_w > 6.0 earthquakes in 1951 (K. H. Chen et al., 2009; Y. M. Wu et al., 2006). In the central AFZ (Figure 4.1c & d), the Deep Fault Drilling Project (DFDP-1) recovered cores from a principal fault slip zone of the 'blue' and 'brown' fault gouges, which contained 16 % and 31 % clay, respectively (Boulton et al., 2014). This contrasts with the significant seismic hazard posed by the AFZ due to the episodic ruptures of M_w 8 earthquakes at ~300-year intervals, such as the previous surface-rupturing earthquake in 1717 (± 5) (Berryman et al., 2012; Boulton et al., 2014). A final example of a clay-rich mature fault zone is the MTL in southwestern Japan, which last ruptured in seismic slip in the 1500s (Patria et al., 2022; Sugiyama, 1992). Clay contents within the Anko section of the MTL range from 22 to 56 wt% (Ishikawa et al., 2014) in gouges derived from the Ryoke and Sambagawa metamorphic belts (Figure 4.1a & b).

The vast majority of previous experiments that investigated the frictional stability of clay minerals were performed at room temperatures (~20°C). The seismogenic portion of tectonic faults are subject to elevated temperatures dependent on the local geothermal gradient (e.g. 25°C/km in stable continental regions gives ~120°C at ~4 km depth). Elevated temperatures have been shown to affect the frictional behaviour of gouges, but these studies have focused on a limited range of fault gouge compositions (Blanpied et al., 1995; Boulton et al., 2014; Den Hartog & Spiers, 2013; Okamoto et al., 2019; Verberne et al., 2010). Boulton et al. (2014) and den Hartog & Spiers (2013) observed decreases in the frictional stability of three compositions of clay-bearing (muscovite/illite, smectite & chlorite) fault gouges at temperatures up to 300°C (10 to14 km depth). While these studies provide key evidence that clay-rich gouges alter their stability at elevated temperature there has not, to date, been a study that systematically documents the effect of frictional stability as a function of clay content. Hence, the aim of this study is to investigate the effect of increasing temperature on frictional stability across the full range of clay proportions (0 to 100 wt%) in fault gouges.

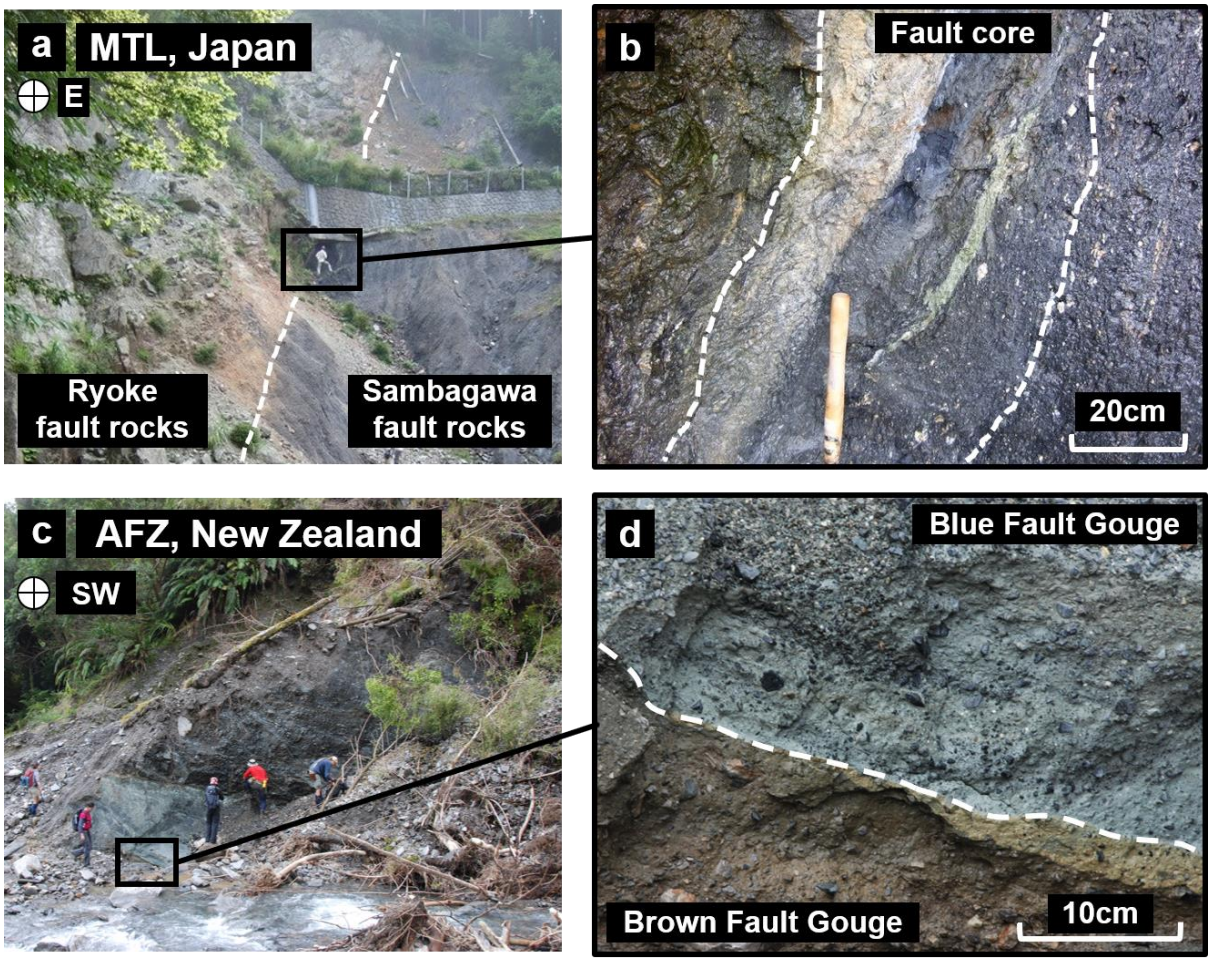

Figure 4.1: Examples representing exposures of clay-rich, mature tectonic faults. Photos a & b: Median Tectonic Line, Japan; Example clay contents of 35 – 73 wt% Anko Section (Ishikawa et al., 2014). Photos c & d: Alpine Fault Zone (Stony Creek); clay contents in 'brown' and 'blue' gouges are between 16 and 31 wt% (Boulton et al., 2014).

4.1. Velocity-step experiments:

Kaolinite was the chosen clay for this investigation as it commonly occurs in mature fault zones (Den Hartog et al., 2021; Ikari et al., 2020) and it has frictional characteristics that are similar to other clays (Behnsen & Faulkner, 2012). Kaolinite is a non-swelling clay with a dioctohedral structure and it is chemically stable to temperatures >450°C (Brady et al., 1996; Y. Han et al., 2020). These properties identify it as a clay mineral that does not have the complications of ultra-low permeability and the variable frictional stability characteristics of a swelling clay, such as montmorillonite (Morrow et al., 2017; Saffer & Marone, 2003) – hence, kaolinite broadly represents a wide range of non-swelling clay types. The proportion of kaolinite (<2 μm grain size, >99% purity) to a pure quartz powder (< 15μm grain size, >99% purity; see Section 4.5) was stepped in 25 wt% increments to produce five synthetic fault gouge mixtures. The velocity-step experiments were conducted in a triaxial deformation apparatus in a direct shear slider assembly (see Section 4.5). In addition to room temperature experiments (~23°C), the temperature was controlled at 60°C, 100°C, 140°C and 180°C (+/- 0.4°C) using external band heaters. A confining pressure of 150 MPa and a pore fluid pressure (using deionized water as the pore fluid) of 60 MPa mimicked the conditions typical of the seismogenic continental crust at approximately 6-7 km depth with a hydrostatic pressure gradient (λ = pore pressure/overburden = 0.4).The experiments included an initial 'yield phase' involving 2 mm of displacement at a velocity of 0.3 μm/s, during which the samples were loaded to failure (Figure 4.2). Subsequently, in the 'velocity step phase' the slip velocity was stepped between 3.0 μm/s and 0.3 μm/s every 0.5 mm of slip until the maximum displacement of 5.5 mm was reached.

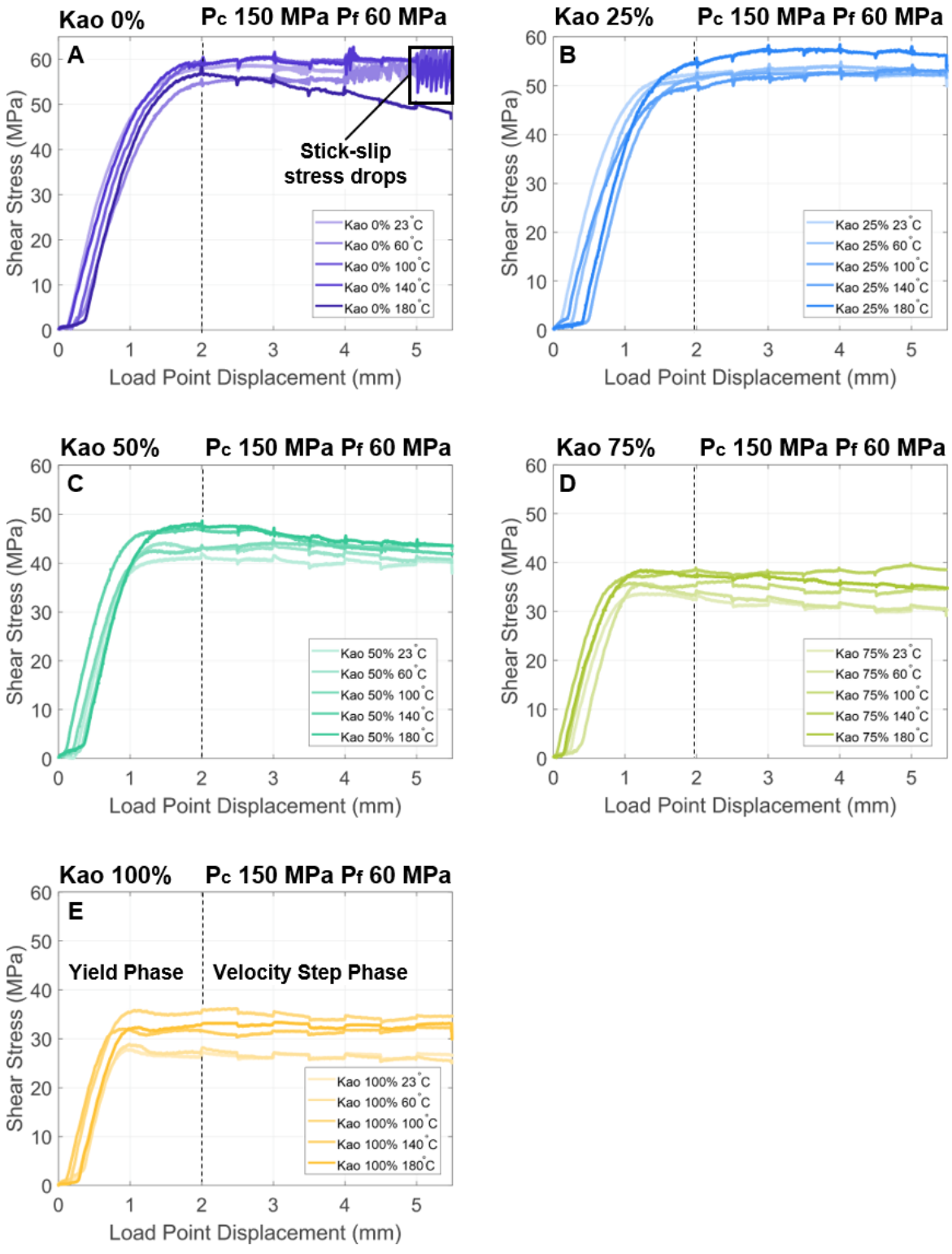

Figure 4.2: Shear stress curves against load point displacement for all 5 gouge compositions at 5 experimental conditions (25 total tests – A to E). Conditions in all experiments were 150 MPa total normal stress and a pore fluid pressure (deionized water) of 60 MPa.

Rate and state friction (RSF) laws are used to describe the frictional response to such changes in slip velocity and to identify the frictional stability. The rate- and state-dependent constitutive law (Dieterich, 1979) describes the direct effect (*a*) and evolution effect (*b*) on the initial friction coefficient of a material (μ_0) due to a change from an initial slip velocity (V_0) to a new velocity (V) over a critical slip distance (D_C). The RSF parameter of *(a–b)* is used to assess the stability of fault slip in a material (Figure 4.3 inset). A material that has negative (*a–b)* values is velocity weakening, so that it weakens progressively with increasing slip velocity. Hence, negative (*a–b*) values are considered a prerequisite for seismic slip, although instability still depends on the stiffness of the loading system. In contrast, a material that has positive (*a–b*) values is velocity strengthening, so that it strengthens with increasing slip velocity, leading to the arrest of seismic slip and stable sliding.

$$\mu = \mu_0 + a \ln\left(\frac{V}{V_0}\right) + b \ln\left(\frac{V_0 \theta}{D_c}\right) \qquad \text{(Eq. 4.1)}$$

The state parameter θ has units of time and can be described using the aging law (Ruina, 1983) or the slip law (Dieterich, 1979). In this study the data were fitted using the aging law:

$$\frac{d\theta}{dt} = 1 - \frac{V\theta}{D_c} \qquad \text{(Eq. 4.2)}$$

A notable result from the experiments is the consistent negative trend of the averaged stability parameter $(a-\bar{b})$ derived from velocity step increases with increasing temperature in all of the clay-bearing fault gouges tested (Figure 4.3). In the 25 wt% and 50 wt% kaolinite gouges, $(a-\bar{b})$ decreases from velocity strengthening values at room temperature to become velocity weakening at temperatures ≥ 100°C. The gouges with higher proportions of kaolinite (75 and 100 wt%) show the same negative trend with increasing temperature, but $(a-\bar{b})$ does not decrease below 0. The minimum values of $(a-\bar{b})$ for all of the clay-bearing fault gouges occurs at 140°C, which is then followed by a slight increase as temperature is increased to 180°C. The only material that does not follow this pattern is the 100 wt% quartz (clay absent) gouge, which shows an opposite positive trend of $(a-\bar{b})$ values with increasing temperature. The quartz $(a-\bar{b})$ values increase with temperature and transition from velocity weakening at room temperature to velocity strengthening at temperatures > 60°C.

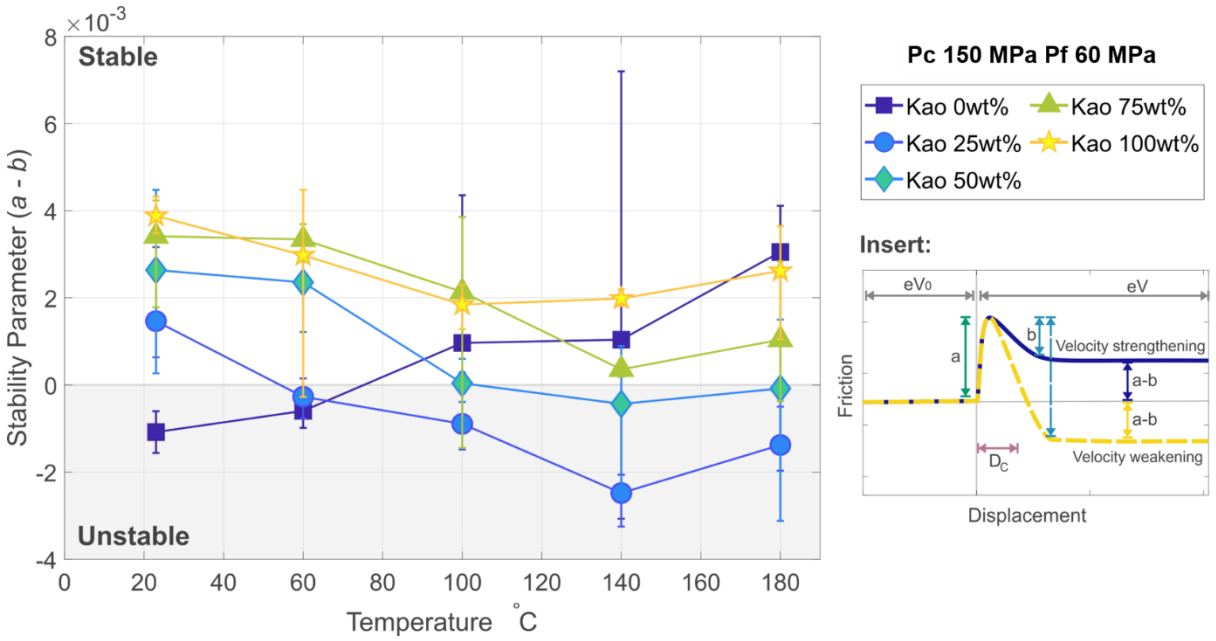

Figure 4.3: Stability parameter ($a-\bar{b}$) for velocity step increases in all synthetic fault gouges across the increasing temperature conditions. Symbols mark the average ($a-\bar{b}$) value and the bars represent the data range. The insert summarises the typical rate and state friction behaviour for both a velocity strengthening material and a velocity weakening material.

The changes in the measured stability parameters are reflected in changes in the mode of slip. At room temperatures, all of the clay-bearing fault gouges slip by stable sliding, but as the temperature increases and ($a-\bar{b}$) decreases, unstable slip becomes more common in the clay-bearing gouges. At 140°C, the 25 and 50 wt% clay gouges sometimes experience stick-slip, with significant stress drops occurring immediately following velocity step increases. This unstable slip rapidly transitions to stable slip within the displacement of the velocity step (Figure 4.2B & C). This behaviour is expected and can be modelled as a system that is on the boundary of unstable slip given the combination of RSF parameters and apparatus stiffness (Ikari et al., 2020; Lambert et al., 2021; Lapusta et al., 2000). The 100 wt% quartz (clay absent) gouge shows the opposite trend by becoming more stable at higher temperatures. At room temperatures, a velocity step increase leads to repeated stress drops that occur over less than 0.1 second (our data logging rate) and repeat throughout the entire displacement range of the velocity step. At elevated temperatures, the 100 wt% quartz (clay absent) gouge undergoes a single, audible stress drop upon a velocity step increase, but the behaviour transitions towards stable sliding.

The frictional strength shows a weak positive trend with increasing temperature that is consistent across all of the tested clay-bearing fault gouges (Figure 4.2). The positive trend of frictional strength with increasing temperature is most evident in the gouges with higher proportions of kaolinite, as the 25 wt% kaolinite gouge increases by 0.04 whereas the 100 wt% kaolinite gouge increases by 0.07 across the temperature range. The only tested material

that does not follow this trend is the 100 wt% quartz (clay absent) gouge, which shows no significant trend with increasing temperature.

4.2. Microstructures:

Following the deformation experiments, samples of fault gouge were recovered from the apparatus, dried, and impregnated with epoxy resin. The samples were cut perpendicular to the shear zone boundary, parallel to the slip displacement and polished for analyses using the Zeiss GeminiSEM 450 in the Scanning Electron Microscopy Shared Research Facility (SEM SRF) at the University of Liverpool. High resolution images across a wide range of scales were collected in backscattered electron mode. Localised failure in granular materials is characterised by a high strain gradient within a narrow area, which includes such microstructures as grain comminution, shear or compaction bands, and preferred alignment of clasts (Rutter et al., 1986). Strain was accommodated in the gouges through shear arrays including shear-parallel Y-shears and low-angle R_1 Riedel shears (Rutter et al., 1986) (Figure 4.4) that were associated with grain size reduction and were typically less than 50μm thick. The most prominent features in the micrographs are stress-relief (unloading) fractures that opened up during the sample preparation. These commonly occur along the site of shear localization that is marked by grain size reduction. Hence, these fractures were classified as shear fractures only if grain size reduction of quartz via cataclasis could be identified along their boundaries. The number and lengths of localized shears was quantified using FracPaQ (Healy et al., 2017) (Figure 4.4).

Fault gouges deformed at room temperature had a greater number of shear localization features and a small average shear localization length normalised to sample area (around $1.14x10^{-2}$ mm^{-1} in the 25 wt% kaolinite gouge sample). At elevated temperatures, the strain was accommodated in fewer but longer R_1 Riedel and Y shears, as the localized shear length by sample area in the 25 wt% kaolinite gouge increased to $2.5x10^{-2}$ mm^{-1} at 140°C (Figure 4.4). This indicates that localisation of deformation increases with increasing temperature in clay-bearing fault gouges. The total amount of shear-enhanced compaction of the bulk fault gouge in the velocity step tests also increased with increasing temperature across the 5 different fault gouge compositions, such as the 25 wt% kaolinite gouge that, by the end of the experiments, had compacted relative to the initial volume by 7.6% (71 mm^3) at 23°C and 11.8% (123 mm^3) at 180°C. Energy dispersive X-ray spectroscopy (EDS) chemical mapping of the gouge samples in the SEM showed a minor concentration of quartz over kaolinite in the localised shear zones, perhaps due to the EDS resolution limit of 1 μm.

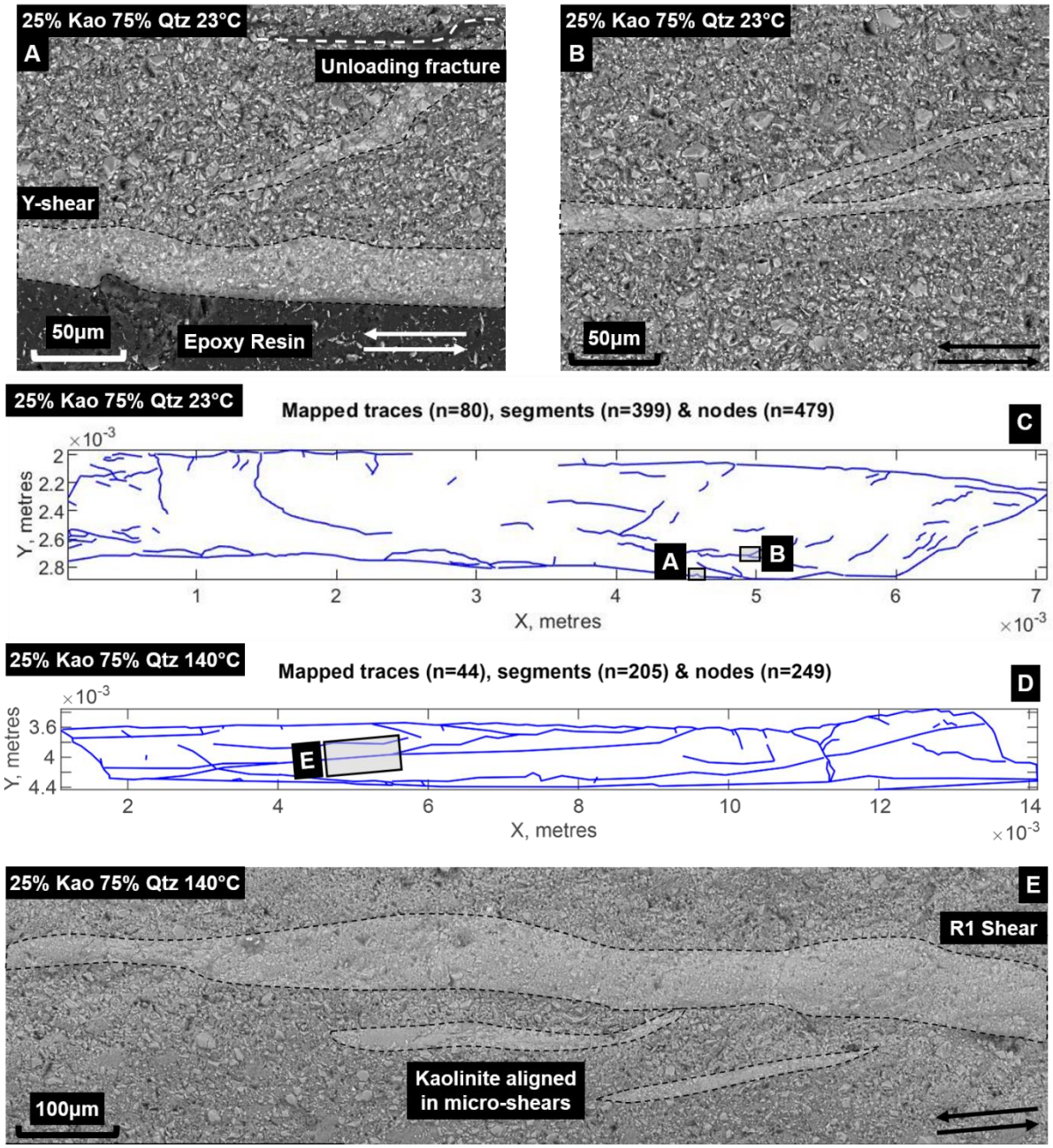

Figure 4.4: (A) and (B) Backscatter electron (BSE) images of 25 wt% kaolinite gouge deformed at room temperature with shears highlighted; (C) fracture trace map of the 25 wt% kaolinite sample deformed at room temperature as the input for the FracPaQ analysis software; (D) fracture trace map of the 25 wt% kaolinite sample deformed at 140°C as the input for the FracPaQ analysis software; (E) BSE image montage of 25 wt% kaolinite gouge deformed at 140°C with shears highlighted. All images have top to the right sense of shear.

4.3. Discussion:

The issue of the disparity between field observations and laboratory stability data impacts physics-based modelling of earthquake sequences (Lambert et al., 2021), that represent a key link between laboratory measurements and nature, so it is vital that these models are based on laboratory data that reflect observations in nature. Many models involve rate and state friction laws (Hillers et al., 2006; Lambert et al., 2021; Lapusta et al., 2000; Y. Wu &

Chen, 2014) and the parameters from rock friction studies conducted at room temperature. Due to a lack of friction data at elevated temperature, few models incorporate a temperature (or depth) dependence of (*a-b*) (Hillers et al., 2006) – the relationships that are used are commonly based upon materials such as granite gouge (Blanpied et al., 1995) that do not reflect natural fault lithologies present in mature faults. The results of this study show that ≤50 wt% clay fault gouges can host unstable slip at elevated temperatures typical of depths up to ~7km (Figure 4.5). This indicates that the difference in temperature conditions can account for the wide variety of fault slip behaviours seen in nature including the prominence of seismogenic slip on many major faults, which otherwise would have been difficult to explain. Segments of the example faults including the LVF in Taiwan and the MTL in Japan have measured clay proportions of 1-69 wt% clay (Den Hartog et al., 2021; Ishikawa et al., 2014), which covers the range of gouge clay proportions tested in this study, and that acted as conditionally-unstable at elevated temperatures. The shear in the experiments was sometimes accommodated via stable creep until a velocity step increase was imposed, which induced unstable slip – a scenario that may be similar to a propagating slip patch impinging on a clay-rich fault segment in nature. If earthquake models discount the potential for seismic slip on clay-bearing fault segments, the seismic hazard could be underestimated.

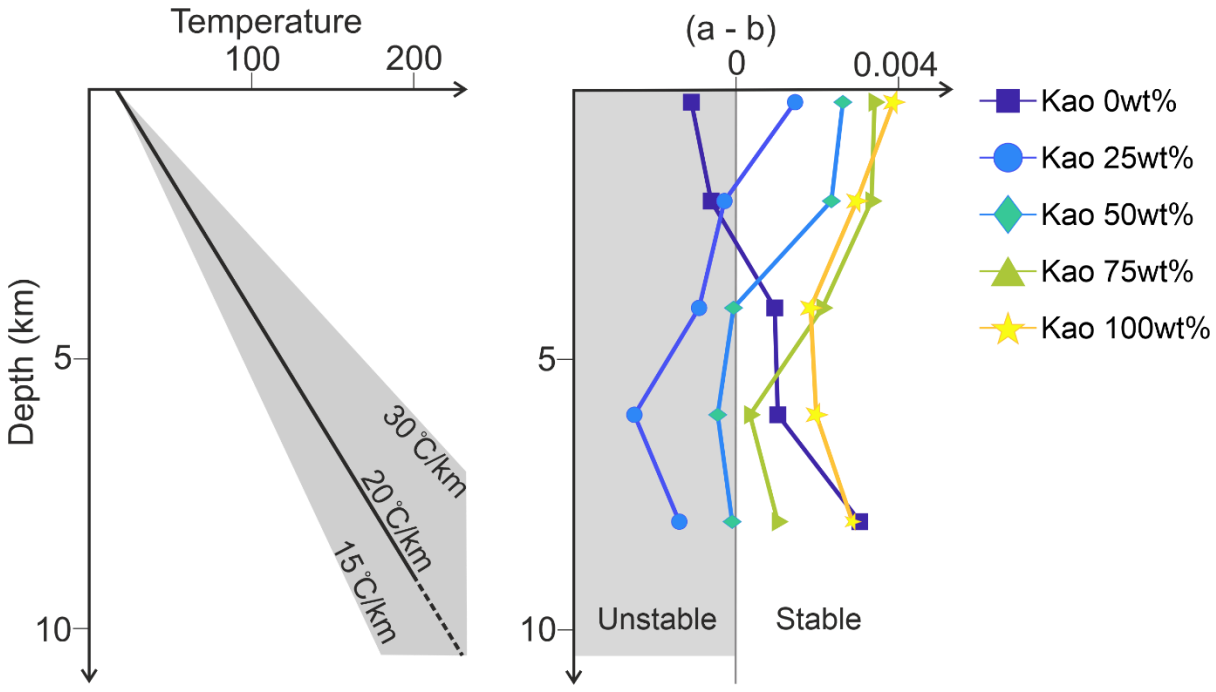

Figure 4.5: Summary diagram of the conditions within a tectonic fault, showing the change in temperature with depth and the change in (a-b) with depth.

The observed dependence of experimental rate and state friction on temperature (Blanpied et al., 1995; Boulton et al., 2014; F. M. Chester & Higgs, 1992; Den Hartog & Spiers, 2013; Okamoto et al., 2019; Verberne et al., 2010) has led to several attempts at incorporating the

effect of temperature into a microphysical rate and state friction framework (Aharonov & Scholz, 2018; F. M. Chester & Higgs, 1992; Niemeijer & Spiers, 2007; van den Ende et al., 2018). Arrhenius-type relationships for pressure solution (Aharonov & Scholz, 2018; F. M. Chester & Higgs, 1992; van den Ende et al., 2018) have been used to describe two slip-mechanism-driven regimes: cataclastic flow and dilation at low temperatures (100-300°C for quartz) and solution-precipitation-aided cataclastic flow at higher (>300°C) temperatures (Den Hartog & Spiers, 2013; Niemeijer & Spiers, 2007). Den Hartog et al. (2013) observed an increase in frictional strength and reduction in (*a*-*b*) with increasing temperature (at σ_n^{eff} = 170 MPa), and attributed the cause to the formation of a denser microstructure due to compaction via stress corrosion cracking or pressure solution. In this study, the high strain rates (~$2x10^{-4}$ to $2x10^{-3}$ s^{-1}) relative to nature and the weakening responses to velocity step changes do not favour pressure solution as the dominant deformation mechanism. While the bulk pore volume decreased, as compaction progressed with increasing temperature (Hüpers & Kopf, 2009), no evidence of pressure solution facilitating cataclasis was observed in this study, such as grain boundary truncation, indentation or mineral overgrowths.

An alternative deformation mechanism that should be considered is the propagation of crystal defects in phyllosilicates, namely ripplocations (Aslin et al., 2019; Kushima et al., 2015). These extremely weak defects behave as waves in the phyllosilicate structure, by stretching or breaking the bonds (hydrogen bonds or van der Waals forces) between mineral layers (Aslin et al., 2019; Kushima et al., 2015). Hence, ripplocations can explain layer-normal strain in phyllosilicates that are unable to accommodate viscous deformation such as dislocation creep. Ripplocations may act as an efficient process for fluid transport in phyllosilicate-rich rocks, as in opening, transient porosity is generated (dilation) and by reconstituting bonds, porosity is closed (compaction) (Aslin et al., 2019). Deformation via ripplocations is an active deformation mechanism across all pressure and temperature conditions at which phyllosilicates are present, including at room temperature. At elevated temperatures, deformation via ripplocations becomes time-dependent, strain rate-sensitive and produces larger loops or ripples in the layered solid (Aslin et al., 2019; Barsoum, 2020).

Literature sources show there is little to no change in (*a*-*b*) values with temperature in the absence of pore fluid in dried clay-bearing fault gouges (Den Hartog et al., 2012; Morrow et al., 2000). Phyllosilicate minerals are more strongly affected by the presence of water than other silicate minerals because their surfaces are electrically charged and form hydrogen bonds with water molecules (Brady et al., 1996; Y. Han et al., 2020; Morrow et al., 2000). Frictional strength decreases following the introduction of water in frictional experiments (Morrow et al., 2000), hence the interaction between clay surfaces and water is important for rate and state friction. The decrease in (*a*-$\overline{b}$) to a minimum between 100 and 140°C for

kaolinite-quartz gouges occurs above the temperature window at which water held in kaolinite interlayers or between disordered particles is expelled (Y. Han et al., 2020; Horváth et al., 2003). A hypothesis is here proposed that the gradual removal of adsorbed water from kaolinite interlayers and surfaces within this temperature window leads to enhanced compaction of the gouge microstructure, as opposed to forming via pressure solution (Den Hartog & Spiers, 2013). Although the effect of stress on the loss of adsorbed water is not known, the heterogeneous distribution of stress within a gouge framework may contribute to the localisation of shear by removing adsorbed water preferentially from sites of anomalously high stress. Increasing localisation of shear and decreasing grain size within a gouge microstructure decreases the stability of slip (Bedford & Faulkner, 2021).

4.4. Conclusions:

The observation that mature faults, that appear ubiquitously clay-rich in nature, host significant seismicity is at odds with laboratory measurements of the frictional properties of clay minerals that are almost always velocity strengthening. In this work we have shown that clay-bearing fault gouges become less stable with increasing temperature up to 180°C. Fault gouges containing ≤50 wt% clay become velocity weakening and some slip unstably in our experiments at temperatures >100°C. Unstable slip is a consequence of increasing localisation of shear to form discrete shear zones within the fault gouges with increasing temperature. This systematic temperature dependence of frictional stability in clay-bearing fault gouges can explain the apparent disconnect between the laboratory and nature.

4.5. Methods:

The friction tests were conducted in a triaxial deformation apparatus in the Rock Deformation Laboratory at the University of Liverpool. The apparatus applied a confining pressure using silicon oil at pressures up to 250 MPa. A PVC (room temperature) or Viton (elevated temperatures) jacket isolated the sample from the confining fluid so that a pore pressure of up to 200 MPa could be independently imposed on the sample using deionised water. An axial load (σ_1) was applied to the sample through a motor-driven loading column with an internal force gauge that measured the axial force at a resolution greater than 0.05 kN.

In experiments at elevated temperatures, three external knuckle band heaters spaced along the length of the pressure vessel conducted heat through the vessel to the sample. The temperatures of the band heaters and the sample were monitored via external and internal thermocouples with to a resolution of 0.1°C. Calibration tests show the temperature varies across the length of the sample by <2˚C. To minimise the conduction of heat through the sample assembly to the force gauge, a cooling plate sat between the base of the pressure vessel and the loading column. The maximum temperature of 180°C in this study was a limit

not from the band heaters, but from jacketing, O-rings and direct shear spacers used in the sample assembly. In the experiments, the external furnace and cooling system were activated during the loading of confining and pore pressure to bring the sample to the target temperature ensuring that the target effective normal stress was not exceeded during the heating. Both the confining and pore pressure media were sensitive to the increase in temperature, and were only brought to the target pressures once the target temperature had been established.

Fault gouge samples were contained within the direct shear assembly for friction experiments. The direct shear sliders moved relative to each other to a maximum displacement of 6mm via the elastic deformation of two rubber spacers. Prior to an experiment, the 1.6 g of fault gouge sample was compacted in a uniaxial press at 50 MPa to improve the cohesion of the sample. The direct shear sliders housed connections to the control systems of the deformation apparatus, including the internal thermocouple and the pore pressure control. Porous 316 stainless steel disks within the direct shear sliders had a permeability of 10^{-12} m^2, which allowed the exchange of pore fluid between the sample and the servo-controlled pump.

The materials used to create the simulated fault gouges in this investigation were the kaolinite KGa-1b from the Clay Minerals Society (CMS) and the quartz powder Min-U-Sil 15 from the US Silica Company. Both KGa-1b and Min-U-Sil 15 had purities quoted at >99% (Vogt et al., 2002). The kaolinite and quartz powders had similar densities at 2.65g/cm^3 and fine mean grain sizes at <2 μm and <15 μm, respectively. To generate the simulated fault gouges, the powders were mixed via dry tumbling as the similar grain sizes and densities promote mixing over segregation. Kaolinite in the fault gouges was stepped in increments of 25 wt% to produce 3 intermediate mixtures that had been tumbled for a 3-hour period at 68 rpm in a 575 cm^3 container.

For the experiments in this study, the RSF parameters were calculated using the software RSFit3000 (Skarbek & Savage, 2019), which uses a non-linear least square fit on the experimental data. Fitting parameters in the program include the stiffness of the apparatus loading column.

In the analysis of microstructural samples, the techniques used to collect information on the samples in the SEM included Backscatter electron (BSE) imaging and energy dispersive X-Ray spectroscopy (EDS). BSE imaging provides information on the chemical composition of samples, based on the atomic number (z). EDS was used to confirm the minerals present based on their elemental composition. Both large area datasets and high-resolution images were acquired, spanning cm to sub-micron scales. All analyses were performed in a Zeiss GeminiSEM 450 in the Scanning Electron Microscopy Shared Research Facility at the University of Liverpool.

Acknowledgements:

We acknowledge financial support from a Natural Environment Research Council grant NE/V011804/1 to DRF and the NERC EAO DTP studentship to IRA at the University of Liverpool. Michael Allen provided essential technical support in the maintenance and development of the experimental apparatus. We gratefully acknowledge the Scanning Electron Microscopy Shared Research Facility for their technical support, training & assistance in this research.

4.6. Supporting Information:

Contents of section:

Introduction:

The information in this section covers the methodology of temperature controlled triaxial deformation experiments and the data collected concerning changes in rate and state friction (RSF) with increasing temperature for kaolinite-quartz gouges.

The frictional tests were conducted using a triaxial deformation apparatus that applies a confining pressure ($\sigma_2 = \sigma_3$) using silicon oil and the axial load (σ_1) is applied via a motor-driven axial piston. At the top of the axial loading column, the force gauge assembly houses an adapted Linear Variable Displacement Transducer (LVDT) with a spring-loaded long armature (Figure 4.6). The LVDT measures the elastic distortion of the axial column to produce a force measurement with a resolution better than 0.03 kN. This LVDT sits above the level of the dynamic variseal at the base of the pressure vessel (Figure 4.6), which removes the need for a seal friction correction in the measured data. A direct shear slider assembly was used to house the fault gouge samples during the velocity step tests. The direct shear configuration aligns the direction of shear with the direction of axial loading (σ_1), which maintains a constant normal stress throughout the experiment without needing to adjust the confining pressure, as is required in a sawcut configuration.

Experiments conducted at elevated temperatures were controlled using LabView software on the dedicated apparatus computer and a West P6100+ controller. A target working point (WP)

temperature was set in the LabView software that was compared to the temperature measured by the internal thermocouple (Figure 4.6). If there was a mismatch between the target WP and measured temperature, the controller sent power via solid state relays to the knuckle-band heaters spaced along the length of the pressure vessel. The magnitude of signals from the controller was adjusted using the proportional gain (P), integral gain (I) and derivative gain (D) to reduce any overshoot in the temperature control (e.g. P 4; I 15; D 5.5). Using these settings, the overshoot during heating was reduced to <2°C, even at the highest tested temperatures.

Further analysis of the RSF data in addition to that provided in the paper is included here. All error bars displayed in the graphs are the standard error of the mean. Both the direct effect (*a*) and the evolution effect (*b*) showed a dependence on temperature (Figure 4.7). In the kaolinite-quartz gouges, *a* decreased slightly from room temperature (~23°C) to 140°C and then increased at 180°C. The *b* values for the intermediate kaolinite-quartz mixtures had a stronger positive trend with increasing temperatures than the *a* values, for example the 75 wt% kaolinite gouge has a gradient of $4x10^{-6}$ °C^{-1} for *a* compared to $2x10^{-5}$ °C^{-1} for *b*. The end member gouges displayed different trends to the intermediate mixtures – 0 wt% kaolinite (100 wt% quartz) showed a drastic increase in both *a* and *b* with increasing temperature and the 100 wt% kaolinite gouge showed a decrease in both *a* and *b* with increasing temperature.

Figure 4.8 displays the change with increasing temperature in the critical slip distance (D_C) over which the friction evolves to a new steady state value following a velocity step change. D_C had a negative trend with increasing temperature, for example the 50 wt% kaolinite gouge had a D_C of 0.016 mm at room temperature (~23°C) that decreased to 0.002mm at 180°C. The dual effect of (*a*-*b*) decreasing and D_C decreasing with increasing temperature led to more unstable slip at higher temperatures in the kaolinite-quartz gouges (Figure 4.9). At room temperature, fault gouges that contained any amount of kaolinite deformed via stable slip. At higher temperatures, the velocity weakening (*a*-*b*) and the smaller D_C values are shown in the shear stress measurements as rapid shear stress drops following velocity step increases (Figure 4.9). The shear stress curves in Figure 4.9 have been corrected to remove any gradient of the steady state shear stress following the velocity step increase.

Figure 4.10 shows the montaged backscatter electron (BSE) micrographs of the deformed kaolinite-quartz gouges taken using a scanning electron microscope (SEM). Following a velocity-step test, samples of the deformed fault gouges were recovered from the direct shear assembly and preserved in epoxy resin. The gouges were cut to display the cross-sectional view of the samples parallel to the shear direction and perpendicular to the shear plane. Figure 4.10 specifically shows the montages of the samples chosen for microstructural analysis using the MatLab™ software FracPaQ (Healy et al., 2017). These samples were chosen for analysis

because they remained coherent following unloading of the gouges and the overprint of decompression fractures was relatively minor.

Figure 4.11 shows example energy dispersive spectroscopy (EDS) chemical maps of the 25 wt% kaolinite to 75 wt% quartz fault gouge sample that was deformed at 140°C. In EDS analysis, the absorption of an X-ray photon causes an outer-shell electron to be ejected with a signature energy peak. Elements have been indexed to their characteristic energy peaks so that the measured energy peaks in EDS can show the elemental composition of a sample. Figure 4.11B and C show the individual EDS maps of silicon and aluminium, which are used as proxies for quartz and kaolinite, respectively. The EDS analysis shows that there is no significant concentration of one mineral over another in the gouge shear bands.

Figure 4.12 shows the atomic structure of a kaolinite layer with the silica tetrahedral layer and the alumina octahedral layer (Brady et al., 1996; Y. Han et al., 2020). Kaolinite gains a surface charge from the adsorption of water and hydroxyls to unsaturated bonds, including on the basal silica plane, the alumina octahedral sheet and at exposed layer edges (Brady et al., 1996; Y. Han et al., 2020).

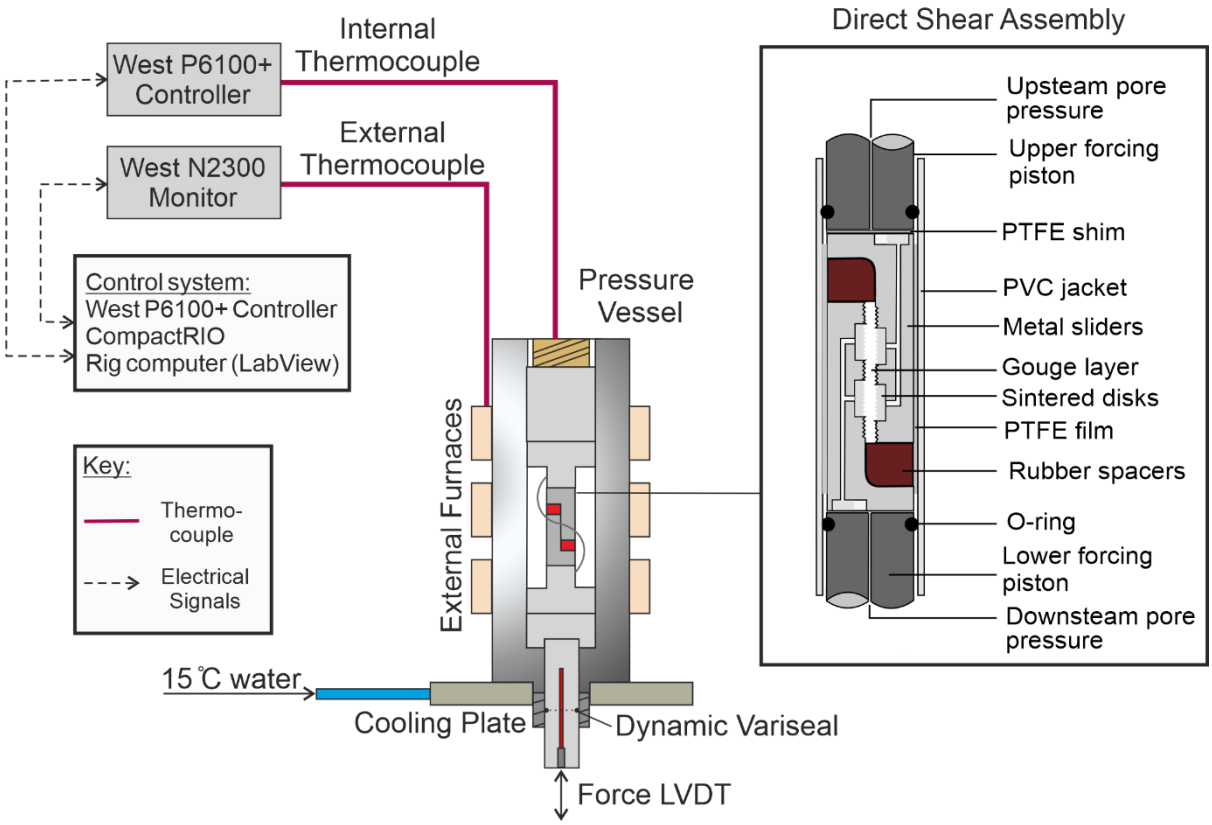

Figure 4.6: schematic diagram of the direct shear slider assembly and the temperature control system on the triaxial deformation apparatus in the University of Liverpool Rock Deformation Laboratory.

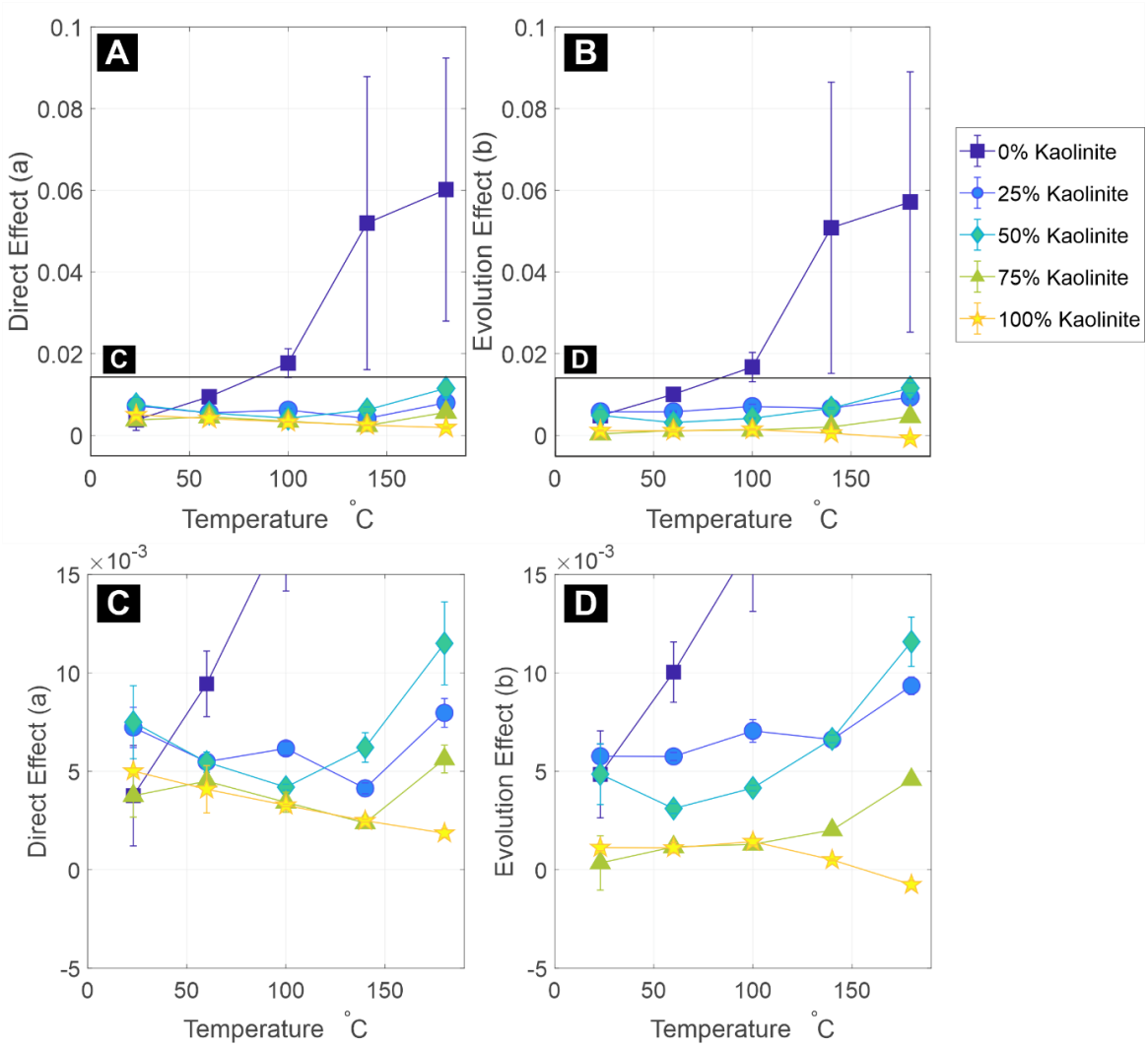

Figure 4.7: the direct effect (a, c) and the evolution effect (b,d) against temperature in the synthetic kaolinite-quartz fault gouges.

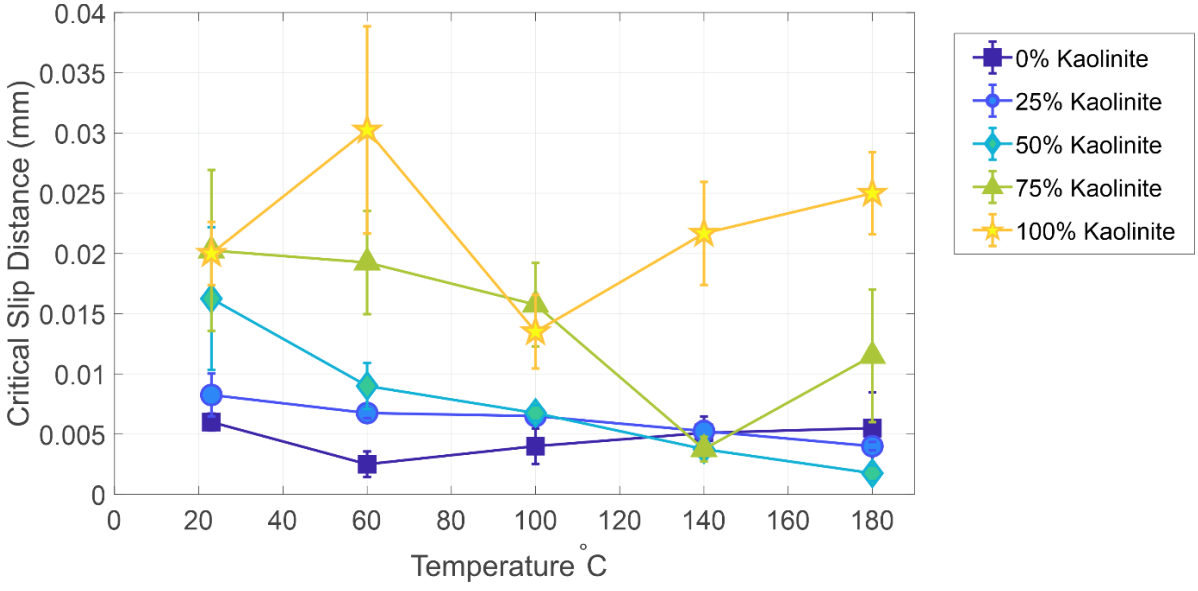

Figure 4.8: Average critical slip distance (D_C) in kaolinite-quartz fault gouges against increasing temperature conditions.

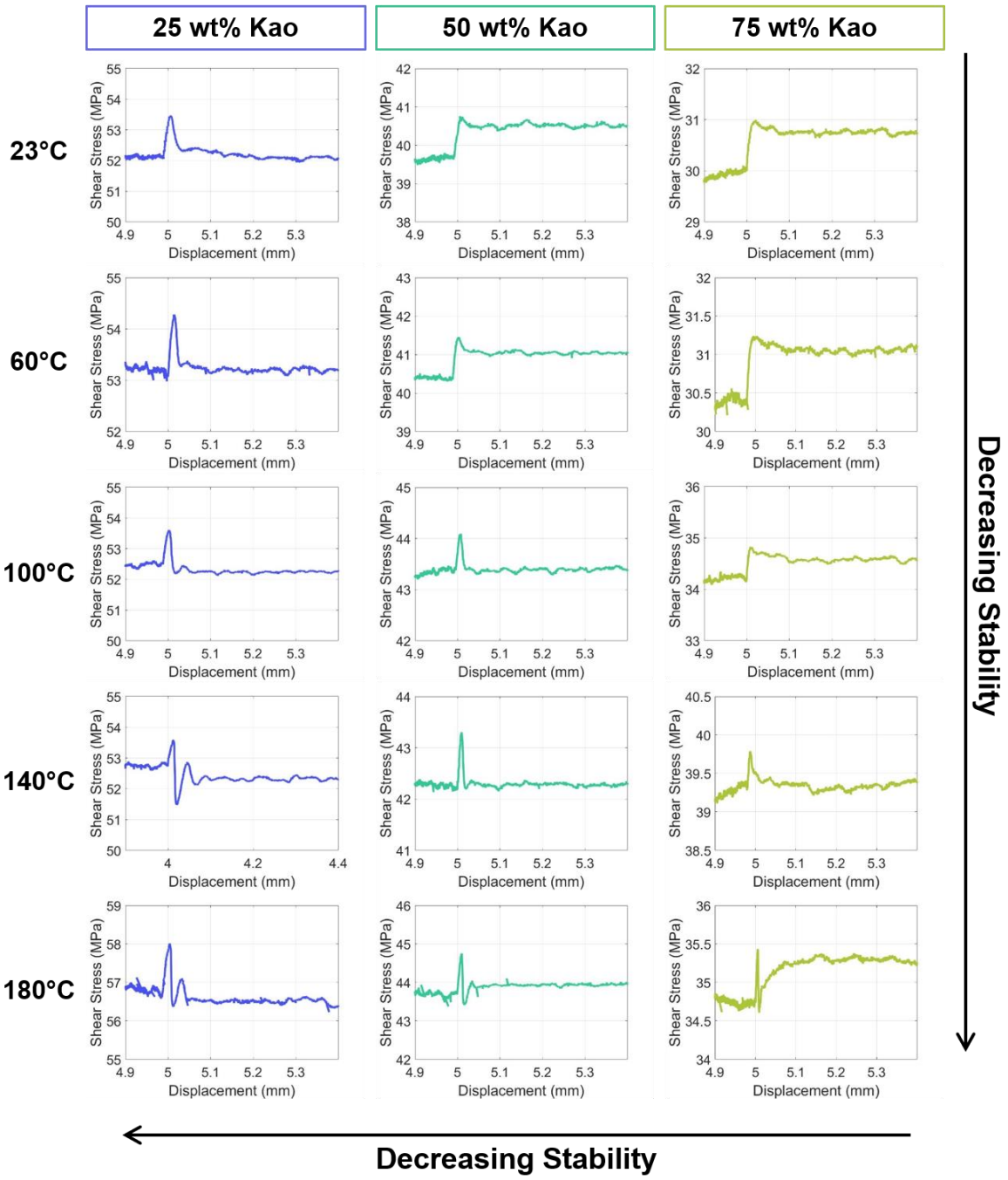

Figure 4.9: Shear stress responses to 10 fold velocity step increases in the 25, 50 and 75 wt% kaolinite-quartz fault gouges across all of the tested temperature conditions.

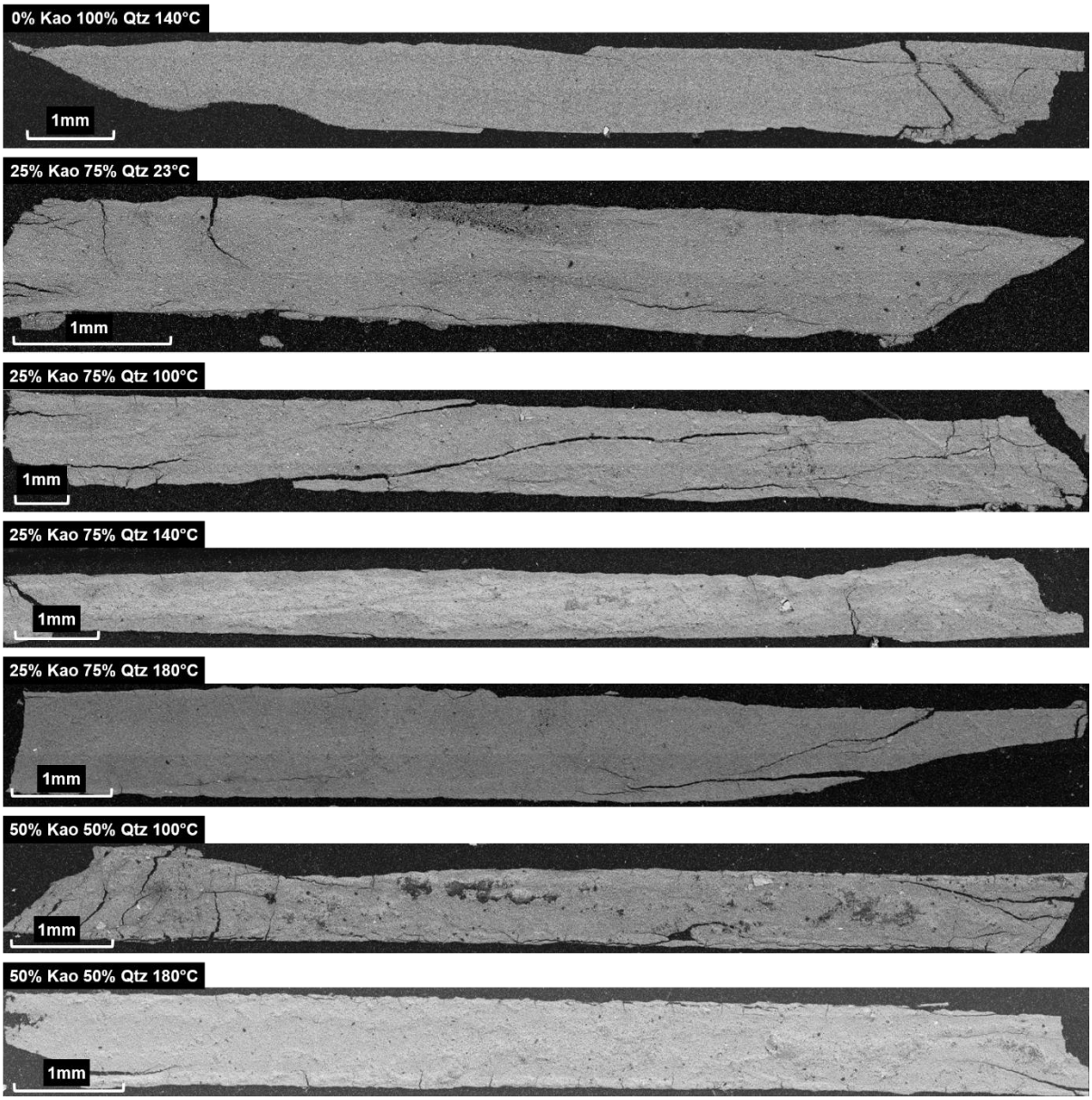

Figure 4.10: Montaged backscatter electron (BSE) micrographs of the deformed kaolinite-quartz fault gouges under scanning electron microscope (SEM), which were analysed using the fracture analysis software FracPaQ(Healy et al., 2017).

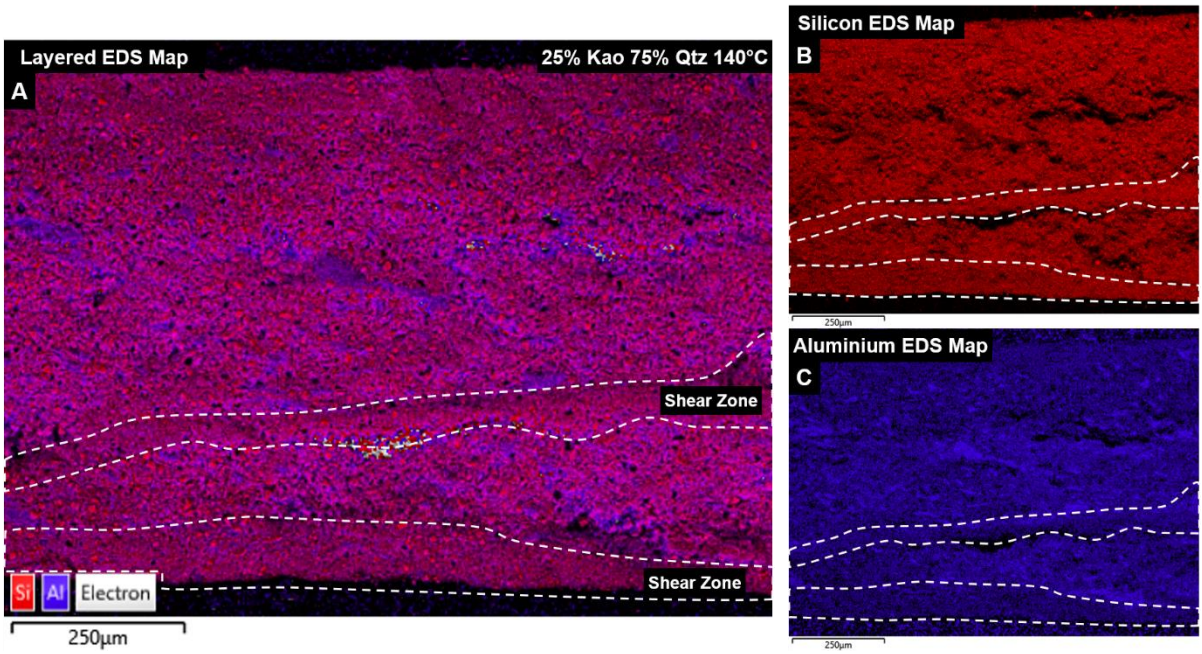

Figure 4.11: Energy dispersive spectroscopy (EDS) maps taken under a scanning electron microscope (SEM) of the 25 wt% kaolinite gouges deformed at 140°C, showing the layered map (A) of the silicon (B) and aluminium (C) maps.

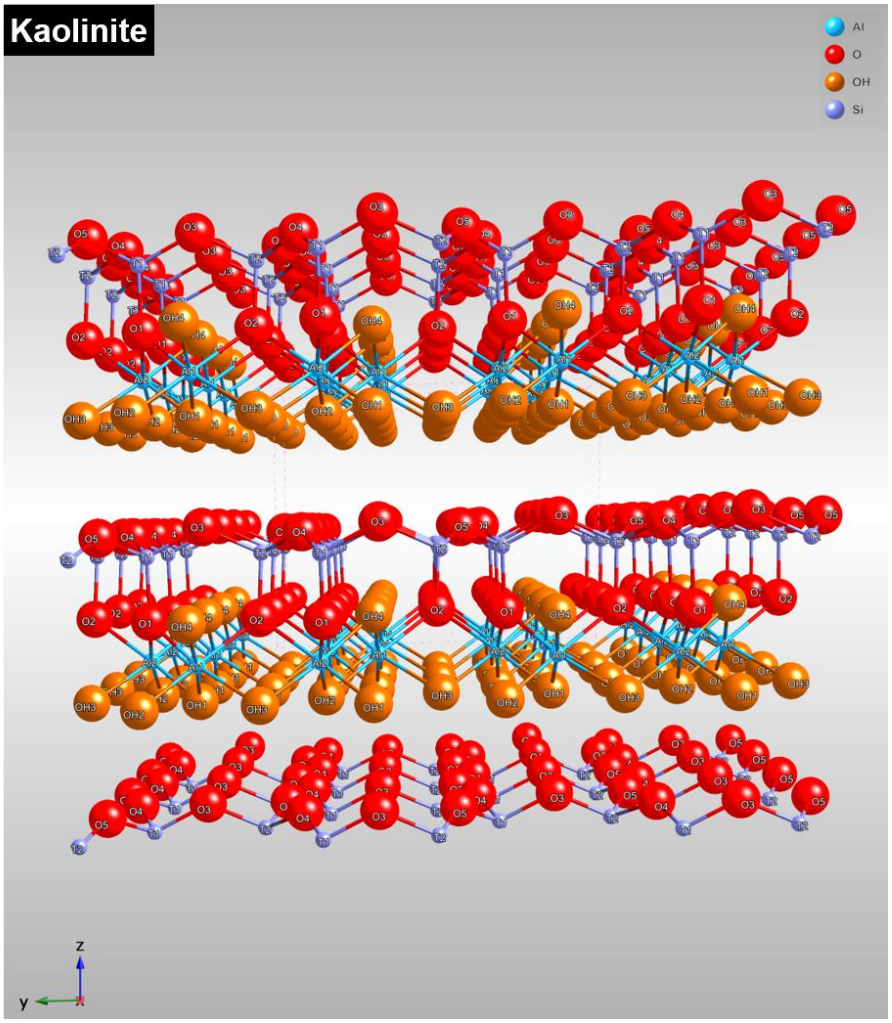

Figure 4.12: Schematic 3D atomic structure of kaolinite, showing the lack of interlayer cations that means that interlayer bonding is achieved through van der Waals forces and hydrogen bonding with interlayer water. Constituent atoms or ions: Al – light blue, O – red, OH – orange and Si – purple.

5. Strain accommodation in heterogeneous fault zones: the Carboneras Fault

5.1 Project Motivation:

The Carboneras Fault Zone (CFZ) is a left-lateral strike-slip fault in south-east Spain at the Africa-Iberia plate boundary. The exposed fault rocks incorporate the basement lithologies of mica schists, phyllites, dolomites and evaporites (Alonso-Chaves et al., 2004; Faulkner et al., 2003; Igbokwe et al., 2020; Keller et al., 1995; Rutter et al., 2012). On a large scale, the ~1km wide fault zone consists of high-strain fault strands of phyllosilicate-rich gouges surrounding lower-strain lenses of basement protolith. In addition to the several metre-wide strands of phyllosilicate-rich gouge that show distributed deformation across them, there are also highly localized fault zones hosted within more competent lithologies such as dolomitic horizons (Faulkner et al., 2003, 2008). This raises questions as to how strain compatibility is maintained when deformation transitions from highly localized to distributed within the fault zone.

Literature sources disagree as to whether the CFZ has hosted seismic slip during its history – the anastomosing phyllosilicate-rich fault strands would suggest aseismic creep behaviour dominated fault slip (Abad et al., 2017; Faulkner et al., 2003; Rutter et al., 2012; Solum & van der Pluijm, 2009), but historical earthquakes of magnitude (M_w) 5-6 have been assigned to the offshore portion of the CFZ (Echeverria et al., 2015; Gràcia et al., 2006). This potential for mixed-mode seismicity in a heterogeneous fault zone is the focus of this work.

Multiple approaches have been used by other researchers to investigate the deformation history of the CFZ, including: geological mapping (Faulkner et al., 2003; Rutter et al., 2012; Solum & van der Pluijm, 2009); chemical dating (Duggen et al., 2004; Rutter et al., 2014; Zeck et al., 1998); geodesy (Echeverria et al., 2015); and geophysical investigations such as seismic profiling (Gràcia et al., 2006) and ground penetrating radar (Reicherter & Reiss, 2001). However, there is a relative paucity of microstructural or frictional data from the fault rocks of the CFZ (Abad et al., 2017). This raises questions concerning the deformation mechanisms on the fault and if there is any evidence for the transfer of distributed deformation versus localised deformation in the CFZ.

Faulkner et al. (2003, 2008) proposed that the structure of the CFZ largely arose due to the combination of a low strength contrast between the fault gouges and the intact parent lithologies, and strain hardening of the fault gouge material. With accumulated strain on a non-planar fault, geometric asperities lock up fault gouge strands, so that it becomes energetically favourable to produce new faults within the intact parent lithology. In addition to the microstructural techniques used in this study, six samples of fault rock were tested in a triaxial

deformation apparatus to ascertain the frictional strength and rate and state frictional (RSF) behaviour of the materials in the CFZ.

Hence, the research questions that were formulated prior to the 2021 field season included:

- How does deformation in the CFZ transfer strain from a brittle-localising (dolomite) to a non-localising (phyllite) material?
    - How do the structures differ across the lithological boundaries between dolomite and phyllite?
    - How do the microstructures differ between the dolomites and phyllites?
    - Are there changes in the phyllite clay gouge microstructures or mineralogy in proximity to the dolomite fault blocks?
- Is there evidence of seismicity in the CFZ dolomite-hosted faults?
    - Pseudotachylytes – frictional melting (Di Toro et al., 2011)
    - Mirror surfaces (Fondriest et al., 2013; R. Han et al., 2010; Siman-Tov et al., 2013, 2015)
    - Pulverisation of quartz from seismic shock (Boullier et al., 2018; Mitchell et al., 2011; Ostermeijer et al., 2022; Rodríguez-Escudero et al., 2020)
    - Any crystal preferred orientations (CPO), foam textures, nanoparticles or evidence of viscous mechanisms (De Paola et al., 2015; Green et al., 2015)
    - Evidence of alteration (Han et al., 2007)
- What are the implications for mixed-mode seismic behaviour in heterogeneous shear zones?

5.2 Geological Background of the Carboneras Fault Zone:

5.2.1. Regional Setting:

The CFZ is set within the arcuate Alpine Orogenic belt of the western Mediterranean, which extends around the Alboran Sea from the Betic Cordillera of southern Spain, through Gibraltar to the Rif Mountains of Morocco (Comas et al., 1999; Lonergan & White, 1997; Marrone et al., 2021; Platt & Vissers, 1989; Vissers, 2012). The Betic Cordillera is an ENE-WSW-trending mountain belt that stretches over 600km along the south-eastern Spanish coastline from Valencia to Cadiz (Figure 5.1). Two belts with distinct characteristics, the External Betic Zone and Internal Betic Zone (or Alboran Domain), form the Betic Cordillera and are separated by thrust faults (Alonso-Chaves et al., 2004; Platt & Whitehouse, 1999; Vissers, 2012).

The External Betic Zone is dominated by folding and thrust sheet stacking of unmetamorphosed marine sediments, which is evidence of crustal thickening in the region due to the convergence of Africa and Iberia in the late Eocene (37-34 Ma) (Alonso-Chaves et al., 2004; Comas et al., 1999; Marrone et al., 2021; Rosenbaum et al., 2002; Sanz de

Galdeano, 2020). In comparison, the Internal Betic Zone is dominated by metamorphic rocks of Paleozoic and Mesozoic origin (Alonso-Chaves et al., 2004; Comas et al., 1999; Marrone et al., 2021; Platt & Whitehouse, 1999). Reconstructed PT-paths give peak metamorphic conditions of 1-1.2 GPa, which indicates maximum burial depths of 40-45 km (Bakker et al., 1989; Gomez-Pugnaire & Fernandez-Soler, 1987).

The step-wise decreases in metamorphic grade across tectonic discontinuities vertically up through the Internal Betic Zone is evidence of extension of the orogen through the excision of sections of the metamorphic sequence (Bakker et al., 1989; Gomez-Pugnaire & Fernandez-Soler, 1987; Lonergan & White, 1997; Martínez-Martínez et al., 2006; Platt & Vissers, 1989; Torres-Roldan, 1979). Extensional normal faulting juxtaposed lower grade metamorphic rocks (Alpujarride complex) above higher grade lithologies (Nevado-Filabride complex). While extension seems incongruous in a collisional setting, the Alboran Sea has been shown to be underlain by 13-20 km thick continental crust with a region of anomalously low velocity upper mantle (Booth-Rea et al., 2007; Comas et al., 1999; Platt & Vissers, 1989). Hence, the Betic-Rif mountain belt and Alboran Sea have been presented as an example of orogenic extensional collapse (Platt, 1982; Platt & Vissers, 1989; Vissers, 2012).

The Alboran Sea also hosts extensive volcanic deposits of calc-alkaline, potassic and basaltic chemistry that extend 500-600 km from Iberia to North Africa (Conticelli et al., 2009; Duggen et al., 2004, 2008; Rutter et al., 2014; Zeck et al., 1998). The Alboran Volcanic Province, dated between 15-6 Ma (Rutter et al., 2014; Zeck et al., 1998), is considered to have been active coeval with and postdating the extension and formation of the Alboran Sea (Duggen et al., 2004; Lonergan & White, 1997; Zeck et al., 1998).

The Alboran Sea and the Betic-Rif mountain chains mark the tectonic boundary between Iberia and Africa, but the diffuse nature of the boundary and the overprinting of compressional features with extensional structures has led to controversy over the formation of the Alboran Sea. Two lines of reasoning for the formation of the Alboran Sea dominate the literature: subducting slab-rollback (Lonergan & White, 1997; Rutter et al., 2014) and slab-detachment or lithospheric delamination (Martínez-Martínez et al., 2006; Platt & Vissers, 1989; Vissers, 2012; Zeck et al., 1998).

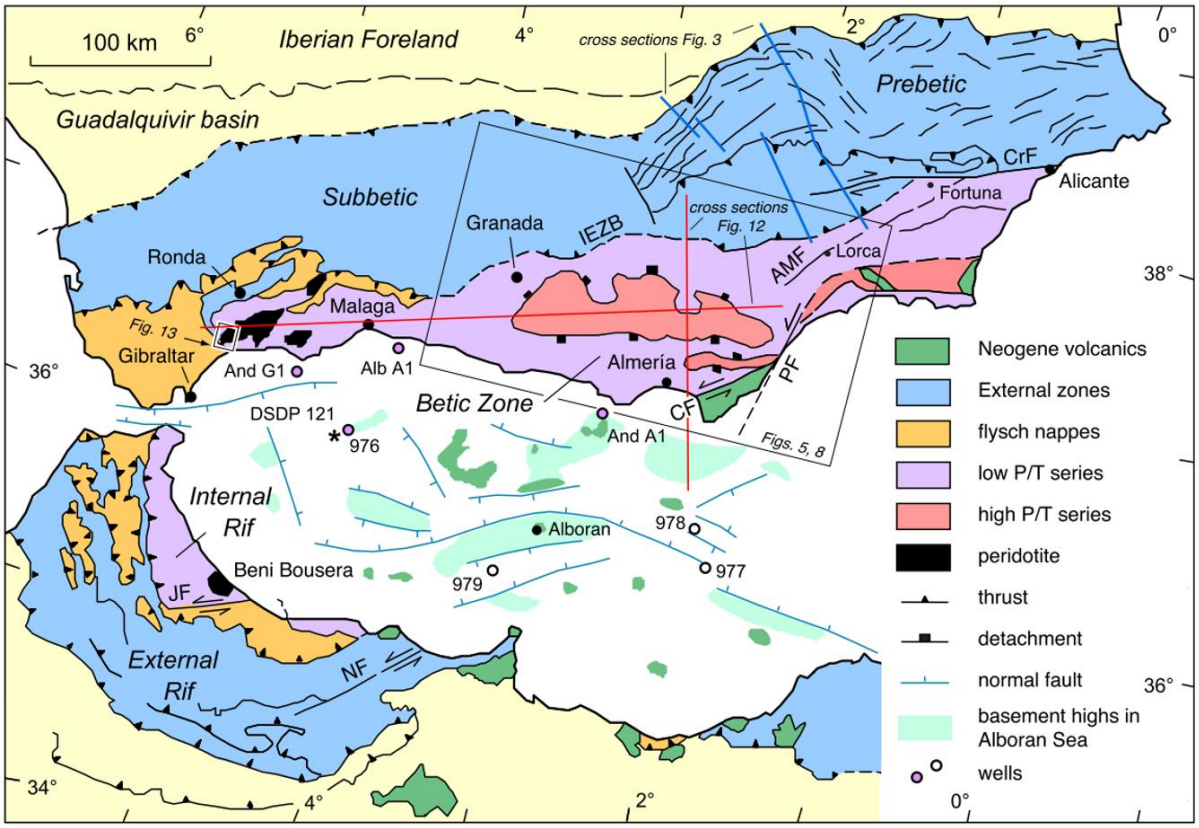

Figure 5.1: A sketch map of SE Spain and NW Africa showing the Betic-Rif mountain belts and the Alboran Sea, with the major fault zones and lithological complexes marked (modified after Vissers, 2012). Fault abbreviations are: AMF Alhama de Murcia Fault, CF Carboneras Fault, CrF Crevillente Fault, IEZB Internal External Zone boundary, JF Jehba Fault, NF Nekkor Fault, PF Palomares Fault.

Slab Rollback Model:

Prior to the Miocene, a north-south striking, eastwards-dipping subduction zone existed between Africa and Iberia (Lonergan & White, 1997). The subduction zone rolled back to the west, which caused the thickened lithosphere to extend rapidly to form the Alboran basin between 23-10 Ma (M.-A. Gutscher et al., 2002; M. A. Gutscher, 2012; Lonergan & White, 1997; Rutter et al., 2014). Impingement of the rollback on the passive margins of Iberia and Africa formed oblique thrusts and rotations in the External Betic Zone in the early Miocene.

Delamination or Slab Detachment Model:

In the latest Oligocene or earliest Miocene, removal of lithospheric mantle by mechanisms such as slab detachment (Zeck et al., 1998) or convective removal (Vissers, 2012) led to further uplift and then extensional collapse of the orogen. The extension and decompression of the crust and asthenospheric mantle caused partial melting to produce the Neogene volcanism in the Alboran Domain (Zeck et al., 1998). This has been linked with a regional thermal event recorded in the metamorphic rocks with peak temperatures of metamorphism

of 650-800°C dated between 23-19 Ma (Platt et al., 2003; Platt & Whitehouse, 1999; Vissers, 2012).

At the end of the Miocene, a large complex of strike-slip faults formed in the Internal Betic Zone due to the continuing convergence between Africa and Iberia (Alonso-Chaves et al., 2004; Martínez-Martínez et al., 2006; Sanz de Galdeano, 2020). This NNE-SSW trending, sinistral strike slip Eastern Betic Shear Zone (EBSZ) includes the Alhama de Murcia, Palomares and Carboneras faults (Sanz de Galdeano, 2020).

5.2.2. Lithologies of the Carboneras Fault Zone:

The following is an introduction to the tectonic complexes and lithologies in the area of El Saltador village in the Cabo de Gata-Nijar Natural Park of Almeria, Spain.

Nevado-Filabride Complex:

The Nevado-Filabride Complex comprises Ordovician graphitic mica schists, Permo-Triassic metamorphosed sandstones, carbonates and silicic meta-igneous rocks (Abad et al., 2017; Bakker et al., 1989; Faulkner et al., 2003; Gomez-Pugnaire & Fernandez-Soler, 1987; Kampschuur & Rondeel, 1975; Rutter et al., 2012). The elongate mountain belts of the Sierra Alhamilla, Sierra Nevada and Sierra de los Filabrides are formed predominantly by outcrops of the Nevado-Filabride metamorphic rocks (Vissers, 2012). Multiple phases of deformation are recorded in the metamorphosed lithologies, including an early greenschist-amphibolite grade (D_1) crenulation foliation that is overprinted by later (D_2) greenschist grade crenulations and foliations, which are axial planar to asymmetric folds (Bakker et al., 1989; Rutter et al., 2012; Vissers, 2012). Some exposures, including the Rambla del Cajon in this study, display locally elevated amphibolite facies conditions, as shown by the presence of migmatites and porphyroblasts of garnet, staurolite, andalusite and sillimanite (Bakker et al., 1989; Faulkner et al., 2003; Vissers, 2012). The Nevado-Filabride complex represents the lowest structural basement rocks through which the CFZ cuts and, outside of the CFZ, the contact to the overriding Alpujarride Complex is marked by a major detachment comprised of 100 m thick mylonites and breccias (Pedrera et al., 2010; Platt, 1982; Rutter et al., 2012; Vissers, 2012).

Alpujarride Complex:

The Alpujarride Complex forms the next level of tectonic basement for the CFZ and it includes Permo-Triassic aluminous phyllites, ferruginous quartzites, and Mid-to-Late Triassic dolomitized carbonates (Alonso-Chaves et al., 2004; Faulkner et al., 2003; Kampschuur & Rondeel, 1975; Platt et al., 2005; Rutter et al., 2012). White mica Ar-Ar dating of the lower greenschist facies metamorphism gives an age of 48-50 Ma in the Alpujarride phyllites, which is often taken as the timing of the early contractional, high P/T phase of the Alpine orogeny

(Alonso-Chaves et al., 2004; Platt et al., 2005; Sanz de Galdeano, 2020). A planar schistosity is associated with axial planes of folding with wavelengths of 10 to 100 m.

Triassic mesofractured dolomitic carbonates, sometimes interbedded with highly tectonised gypsum, form the topographic highs in the Sierra Alhamilla (Faulkner et al., 2003; Igbokwe et al., 2020; Rutter et al., 2012). Either prior to the activity of the CFZ or in the early stages of CFZ movement, the dolostones were pervasively fractured into centimetre- to decimetre-scale lithons of orthorhombic shape that indicate bulk non-plane strain (Igbokwe et al., 2020). The dolostone fracturing is overprinted by brecciation and then cataclasis attributed to the CFZ movements (Faulkner et al., 2003; Igbokwe et al., 2020).

Malaguide Complex:

The highest level of basement in the Betic Cordillera is the Malaguide Complex of unmetamorphosed sediments or low-grade meta-sediments, which mostly outcrop in the west of the Betic Cordillera north and east of Malaga, and in a narrow band along the Internal-External Zone Boundary (Alonso-Chaves et al., 2004; Egeler, 1964; Mäkel, 1985; Roep & Mac Gillavry, 1962; Vissers, 2012). The sedimentary sequence in the Malaguide Complex ranges from Ordovician phyllites, meta-greywackes and limestones to Palaeogene carbonates (Alonso-Chaves et al., 2004; Mäkel, 1985; Vissers, 2012). In the region of the CFZ, the Permo-Triassic red sandstones and siltstones and the Cretaceous to Palaeogene carbonate sequence of the Malaguide Complex outcrop to the south of the CFZ from the Rio Granatilla to the Playa la Manaca, as well as in the region north of El Llano de Don Antonio (Figure 5.2).

Neogene Sediments:

In the Sierra Alhamilla region of this study, the tectonic basement complexes are unconformably overlain by a sequence of Neogene, post-orogenic sediments. A non-conformity separates the metamorphic basement from the folded Saltador Formation, which is a sequence of Serravallian to Tortonian marine marls and sandstones (Fortuin & Krijgsman, 2003; Rutter et al., 2012; van de Poel, 1992). Another unconformable contact separates the Saltador Formation from the overlying Azagador Formation of beach sands and marls, which was deposited in the Tortonian to lower Messinian (Fortuin & Krijgsman, 2003; Rutter et al., 2012; van de Poel, 1992). A sequence of Messinian age formations comprised of marine marls (Abad Formation), gypsum deposits (Yesares Formation) and a mixture of clastic and marly sediments (Feos Formation) complete the Neogene succession in the study area (Fortuin & Krijgsman, 2003; Rutter et al., 2012; van de Poel, 1992).

Cabo de Gata Volcanic Series:

The Cabo de Gata Volcanic Series is exposed along the coast to the SE of the CFZ. It includes extrusive lavas, volcaniclastics and amphibole- and feldspar-phyric andesitic to dacitic rocks (Conticelli et al., 2009; Rutter et al., 2012, 2014; Zeck et al., 1998). An older volcanic group (18 – 11 Ma) of shoshonite to calc-alkaline chemistry are interpreted to have been deposited before the CFZ was active, during the regional uplift of the tectonic basement (Duggen et al., 2004; Mattei et al., 2014; Rutter et al., 2014; Zeck et al., 1998). The younger (11 – 6 Ma) volcanic groups range in chemistry from alkali-basalts to rhyolites (Duggen et al., 2004; Mattei et al., 2014; Rutter et al., 2014; Zeck et al., 1998). The CFZ is also intruded by a series of andesitic, NE-SW trending dykes (12.5 – 8.3 Ma) and by two elongate intrusions that are exposed on either side of the southern fault strand, which indicates that, during active volcanism, the CFZ acted as a magma conduit to the surface (Conticelli et al., 2009; Rutter et al., 2012, 2014; Zeck et al., 1998).

5.2.3. The Carboneras Fault Zone:

The onshore exposure of the CFZ extends 50 km in an ENE-WSW trend from south of Mojacar to Cabo de Gata, where the fault can be identified offshore for a distance of 100 km (García-Mayordomo et al., 2012; Gràcia et al., 2006; Rutter et al., 2012; Sanz de Galdeano, 2020). Pedrera et al. (2010) proposed that the CFZ initiated (at 12.5 Ma) at the base of a thinned crust, where partial melting processes had critically weakened the strength of the lithosphere, and the fault propagated to the surface. The flexure of the Moho boundary by 10-20° to the NNW beneath the CFZ (Pedrera et al., 2010) shows that the fault does cut through the full thickness of the crust (20-25 km) – hence, in the context of the regional geodynamic framework, the CFZ is considered as a transform fault (Echeverria et al., 2015; M. A. Gutscher, 2012; Means, 1989; Pedrera et al., 2010; Rutter et al., 2014). Gutscher (2012) proposed that the EBSZ, which includes the CFZ, acts as a stretching fault boundary (Means, 1989) for the back-arc extension in the Sierra Nevada and Sierra de los Filabrides. By assuming uniform stretching in the crust NW of the CFZ, the total offset of the fault can be loosely constrained to between a minimum of 15 km, needed to remove the volcanic deposits to the NW of the fault zone, and a maximum of 40 km (Rutter et al., 2014). The movement on the CFZ has not been purely strike-slip, but also included a transpressive component that initiated at 11.5 (±0.5) Ma, as shown by positive flower structures and the folding of Neogene sediments (Reicherter & Reiss, 2001; Rutter et al., 2014; Sanz de Galdeano, 2020). Using continuous and campaign GPS observations, Echevarria et al. (2015) measured the modern, left-lateral strike slip rate of the CFZ at 1.3 ±0.2 mm/yr along the N048° direction.

In the area close to El Saltador, the CFZ consists of two bounding faults (north and south) that enclose an area up to 1 km in width of anastomosing fault gouge strands with lenses of lower strain protolith (Faulkner et al., 2003). Displacement along the CFZ was accommodated in the high-strain fault gouge strands, which display sinistral R_1 Riedel shear arrays (Faulkner et al., 2003; Faulkner & Rutter, 2000; Rutter et al., 2012) Anomalously high-grade basement lithologies are exposed between the bounding faults, including: staurolite-, andalusite- and sillimanite-bearing schists; migmatite pods; and minor granitoids of 20 Ma age (Faulkner et al., 2003; Platt & Whitehouse, 1999; Rutter et al., 2014). The regional uplift in the Betic Cordillera means that the current exposure of basement cut by the CFZ was deformed at depths of up to 4 km (Faulkner et al., 2003).

Evidence from the literature is contradictory as to whether the CFZ is likely to have hosted seismic slip. The basement-derived fault gouges display evidence of deformation via creep processes such as pressure solution of embedded quartz clasts, frictional wear slickenlines on foliation surfaces, and the growth of authigenic clay minerals (Abad et al., 2017; Rutter et al., 2012). On the other hand, pulverised quartz clasts, which have been observed in the CFZ, have been proposed as evidence of seismic waves propagating through a body of rock (Ben-Zion & Shi, 2005; Faulkner et al., 2003; Mitchell et al., 2011). The quartz clasts in question are embedded within the fault gouges, are equidimensional in shape, and are intensely fractured down to sub-millimetric particle grain sizes (Faulkner et al., 2003; Rutter et al., 2012). Seismicity in southern Spain shows a wide spatial distribution with many low magnitude (M_w <5) earthquakes and tremors related to minor faults within the crustal blocks (Echeverria et al., 2015; García-Mayordomo et al., 2012; Gràcia et al., 2006; Rutter et al., 2014). Almeria has been affected by higher magnitude (M_w 5.8-6) historical earthquakes in 1522, 1658 and 1804 (García-Mayordomo et al., 2012; Gràcia et al., 2006) and the recent May 2011 M_w 5.1 earthquake on the Alhama de Murcia (AdM) fault caused significant damage to the town of Lorca (Masana et al., 2004; Ortuño et al., 2012). Reconstructions of the 1522 Almeria earthquake placed the epicentre close to the trace of the offshore segment of the CFZ, which prompted Gràcia et al. (2006) to suggest a predominance of aseismic fault creep on the CFZ that is perhaps interspersed with large, periodic seismic events.

5.3 Field Project Rationale:

The field site selected to study the differences in localised and distributed deformation in the CFZ was the Rambla del Cajon, situated 0.5 km to the east of the village of El Saltador Alto (Figure 5.2). This site was mapped in detail (Figure 5.3) at a scale of 1:3700 using the compass and pace technique by Faulkner et al. (2003, 2009 pers. comm.), which provided structural and spatial detail that was ideal for further targeted analysis. The Rambla is situated between the north and south bounding faults of the CFZ and includes the anomalously high

metamorphic grade graphitic mica schists of the Nevado-Filabride complex (Faulkner et al., 2003; Rutter et al., 2012). Individual fault gouge strands, both in the graphitic mica schists and in the Alpujarride phyllite and quartzite, can be traced for hundreds of metres. The Rambla del Cajon was also chosen for the presence of localised dolomite faults, the high degree of rock exposure available and the easy access it provided, at only 5 km from the town of Carboneras.

Figure 5.2: A satellite image (Google, 2023) of the town of Carboneras and the field site of the Rambla del Cajon in the Parque Natural del Cabo de Gata-Nijar.

In September 2021, 2 weeks of field work were conducted in the Rambla del Cajon. Due to travel restrictions caused by the Covid-19 pandemic in 2020 and 2021, the time available for field work was limited. Hence, the primary aim for the field work was the sample collection of both high-strain, clay-rich fault gouges and the low-strain parent lithologies. The majority of sample analysis could then proceed in a laboratory setting with fewer time constraints – microstructural analysis of the field samples was conducted using optical and scanning electron microscopy (SEM), chemical analysis utilised X-Ray Diffraction (XRD) and X-Ray Fluorescence (XRF) techniques, and frictional tests of the sample materials were conducted in the Rock Deformation Lab triaxial deformation apparatus.

The following results section separates the fault rocks according to the field classification of the collected samples. Table 5.1 summarises the classification scheme for fault rocks (Sibson,

1977) used in this study. All of the fault rocks that were collected using the copper tubes were incohesive and extremely fine grained and so were classified as fault gouges. Although further analysis using optical microscopes showed that some of the samples could be classified as fault breccias (Table 5.1), the samples are termed as fault gouges throughout this chapter to maintain continuity with the field observations. The fault rocks were also categorised by the inferred protolith lithologies, following the scheme of the geological mapping conducted by D.R. Faulkner in 2009 (Figure 5.3). These lithological categories include:

- Mica schist: derived from the Nevado-Filabride complex, graphitic mica pelitic schist and semi-pelitic schist;
- Phyllite and quartzite: derived from the Alpujarride complex, phyllites interbedded on the cm- to dm-scale with ferruginous quartzite;
- Dolomite: derived from the Alpujarride complex, mesofractured dolomites with minor evaporites.

One of the research aims for the field season focused on how strain was transferred from a brittle-localising to a non-localising material. Sample collection was focused along a single NE-SW-trending fault gouge strand that could be traced for over 600 m along the Rambla del Cajon (Figure 5.3). The fault strand juxtaposed faulted dolomite lithons with a ~5 m wide fault gouge zone in the phyllite-quartzite lithology. This made this fault strand ideal for investigating how the fault zone transferred strain from localising to non-localising material. The secondary faults (to the CFZ bounding faults, or Riedel Y shears) are referred to in this work according to the lithological contacts across the faults, as dolomite-dolomite, dolomite-gouge or as a fault gouge strand (gouge-gouge). The sampling of fault gouges focused on the dolomite-gouge fault contacts, in order to test for changes in the clay-bearing gouge microstructures or mineralogy due to the transfer of strain between the dolomite fault blocks and the fault gouges. The significant offset on the dolomite-gouge faults implied that the faults must continue into the surrounding gouges. Hence, the sampling strategy used in the field prioritised the collection of phyllite-derived gouge samples in close proximity to the dolomite lithons over the mica schist-derived gouge samples. Fault gouge samples that were collected from the field in copper tubes were cut for microstructural analysis with respect to the orientation of the dolomite-gouge fault planes. However, the results of the later microstructural observations indicate that the thin sections may not have been correctly oriented with respect to the shear direction in the fault gouges.

An additional transect across the width of a fault gouge strand was conducted at Locality 10 (Figure 5.4) to investigate the differences between the intact mica schist protolith and the mica schist-derived gouges. These samples were taken to test the model proposed in Faulkner et

al (2003) that the fault gouge strands evolved to be energetically less favourable to host slip than the intact parent lithology. Hence, the changes in chemical and mineralogical content between samples of mica schist-derived gouge and the intact protolith were investigated. In total, 50 samples of fault gouges and cohesive rocks were collected from eight localities. Table 5.2 lists the samples that were used in further laboratory-based analyses.

<table>
<tr><td></td><td colspan="2">Random fabric</td><td colspan="3">Foliated fabric</td></tr>
<tr><td>Incohesive</td><td colspan="2">Fault breccia
(>30% visible fragments)
Fault gouge
(<30% visible fragments)</td><td colspan="3">-</td></tr>
<tr><td rowspan="5">Cohesive</td><td>Glass or devitrified glass</td><td>Pseudotachylyte</td><td colspan="3">-</td></tr>
<tr><td rowspan="4">Tectonic reduction in grain size dominates grain growth by recrystallisation</td><td colspan="2">Crush breccia (fragments >5 mm)
Fine crush breccia (fragments 1-5 mm)
Crush microbreccia (fragments <1 mm)</td><td>0-10</td><td rowspan="4">Proportion of matrix (%)</td></tr>
<tr><td>Protocataclasite</td><td>Protomylonite</td><td>10-50</td></tr>
<tr><td>Cataclasite</td><td>Mylonite</td><td>50-90</td></tr>
<tr><td>Ultracataclasite</td><td>Ultramylonite</td><td>90-100</td></tr>
<tr><td>Grain growth pronounced</td><td>-</td><td colspan="3">Blastomylonite</td></tr>
</table>

Table 5.1: Classification of fault rocks (Sibson, 1977).

Figure 5.3: Digitised geological and geomorphological map along the La Rambla del Cajon conducted by Daniel Faulkner in October 2009.

La Rambla del Cajon Geological Map by Daniel Faulkner, 2009

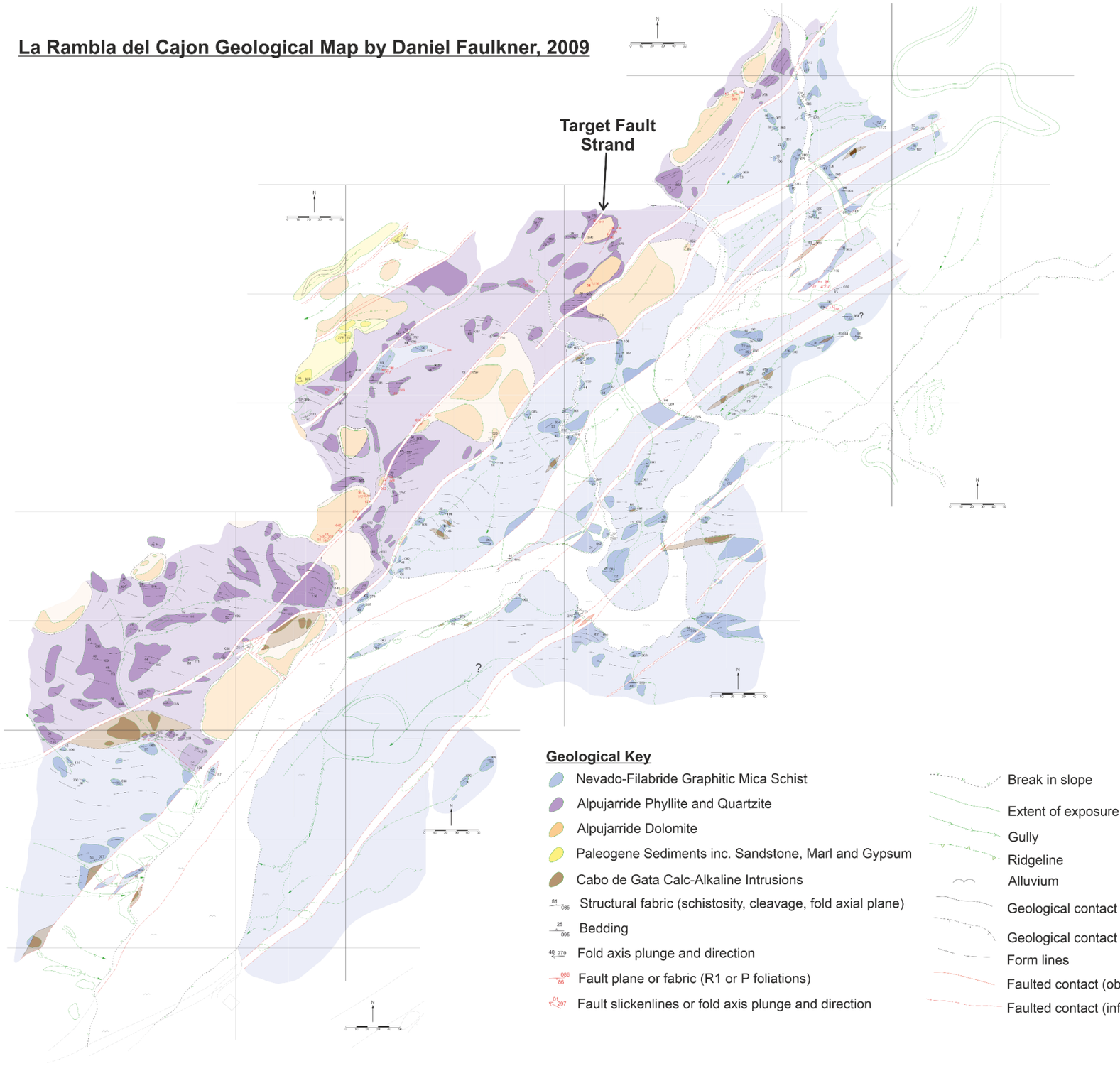

Geological Key

- Nevado-Filabride Graphitic Mica Schist
- Alpujarride Phyllite and Quartzite
- Alpujarride Dolomite
- Paleogene Sediments inc. Sandstone, Marl and Gypsum
- Cabo de Gata Calc-Alkaline Intrusions
- Structural fabric (schistosity, cleavage, fold axial plane)
- Bedding
- Fold axis plunge and direction
- Fault plane or fabric (R1 or P foliations)
- Fault slickenlines or fold axis plunge and direction

- Break in slope
- Extent of exposure
- Gully
- Ridgeline
- Alluvium
- Geological contact (observed)
- Geological contact (inferred)
- Form lines
- Faulted contact (observed)
- Faulted contact (inferred)

Sample Code	Orientation Mark	Latitude	Longitude	Locality Number	Lithology	Features	Chemical Analyses	Microscopy Analyses	Friction Analysis
CFIA02	09-276	37 1 45 N	-1 55 18 W	7	Mica schist gouge	Horizontal copper tube		✓	
CFIA04	02-133	37 1 45 N	-1 55 17 W	8	Mica schist gouge	Approx. 20m to the south east of samples 01 to 03, Horizontal copper tube		✓	
CFIA07	059/81SE	37 1 42 N	-1 55 21 W	8	Mica schist	Fault plane		✓	
CFIA08	n/a	37 1 41 N	-1 55 21 W	8	Mica schist gouge	XRD powdered sample	✓		✓
CFIA11	093/53 N	37 2 1 N	-1 55 3 W	3	Dolomite	Two sides of a cemented fault plane	✓		✓
CFIA13	01-145	37 2 1 N	-1 55 3 W	3	Phyllite Gouge	2.9m from fault plane, Horizontal copper tube	✓		
CFIA14	n/a	37 2 1 N	-1 55 3 W	3	Phyllite Gouge	20cm from fault plane, Vertical copper tube	✓		
CFIA15	23-143	37 2 1 N	-1 55 3 W	3	Phyllite Gouge	Contacting fault plane, Horizontal copper tube	✓		
CFIA16	n/a	37 2 1 N	-1 55 3 W	3	Phyllite Gouge	20cm from fault plane, Loose gouge	✓		✓
CFIA18	105/79 N	37 2 1 N	-1 55 3 W	6	Dolomite	Mirror surface	✓	✓	✓
CFIA20	n/a	37 1 53 N	-1 55 11 W	6	Phyllite Gouge	3m from Dolomite fault plane, Foliation orientation 094/50 N and 081/60 N		✓	
CFIA23	01-317	37 1 54 N	-1 55 11 W	6	Phyllite Gouge	<20cm from fault plane, Horizontal copper tube		✓	
CFIA24	12-283	37 1 54 N	-1 55 11 W	6	Phyllite Gouge	<20cm from fault plane, Horizontal copper tube		✓	
CFIA26	225/78 W	37 1 54 N	-1 55 11 W	5	Dolomite	Mirror surface, slickenlines 02 - 228		✓	
CFIA27	85-275 (B)	37 1 55 N	-1 55 10 W	5	Phyllite Gouge	1cm from fault, slickenlines on dolomite fault surface 12-207		✓	
CFIA28	n/a	37 1 55 N	-1 55 10 W	5	Phyllite Gouge	15cm from fault plane on trend 113 to CFIA27, Vertical copper tube		✓	

Sample Code	Orientation Mark	Latitude	Longitude	Locality Number	Lithology	Features	Chemical Analyses	Microscopy Analyses	Friction Analysis
CFIA30	76-321	37 1 55 N	-1 55 10 W	5	Phyllite Gouge	1cm from fault, 7cm from CFIA27 on trend 025	✓	✓	
CFIA31	04-131	37 1 55 N	-1 55 10 W	5	Phyllite Gouge	10cm from fault, Horizontal copper tube	✓	✓	
CFIA32	n/a	37 1 55 N	-1 55 10 W	5	Phyllite Gouge	<20cm from fault plane, Loose gouge	✓		✓
CFIA33	225/85 N	37 1 55 N	-1 55 10 W	5	Dolomite	Mirror surface		✓	
CFIA35	01-264	37 1 48 N	-1 55 5 W	10	Mica schist gouge	6m from western edge of fault gouge strand on bearing 108, Horizontal copper tube	✓		
CFIA37	05-304	37 1 48 N	-1 55 4 W	10	Mica schist gouge	7m from samples CFIA35 and 36 along bearing 104, Horizontal copper tube	✓		
CFIA42	021/73 SE	37 1 49 N	-1 55 4 W	10	Mica schist	Western edge of fault gouge strand, Many tight and small (<5cm wavelength) folds, high grade schist	✓		✓
CFIA44	041/86 SE	37 1 48 N	-1 55 3 W	10	Mica schist	Eastern edge of fault gouge strand	✓		
CFIA45	08-323	37 2 2 N	-1 55 1 W	12	Phyllite Gouge	11m SSE of dolomite exposure, Horizontal copper tube		✓	
CFIA49	86-032	37 2 2 N	-1 55 2 W	12	Phyllite Gouge	Gouge in the gouge strand on the NW fault strand from cairn map 1, Vertical copper tube		✓	

Table 5.2: Summary of samples collected from the CFZ and the subsequent laboratory-based analyses that were conducted.

5.4 Results:

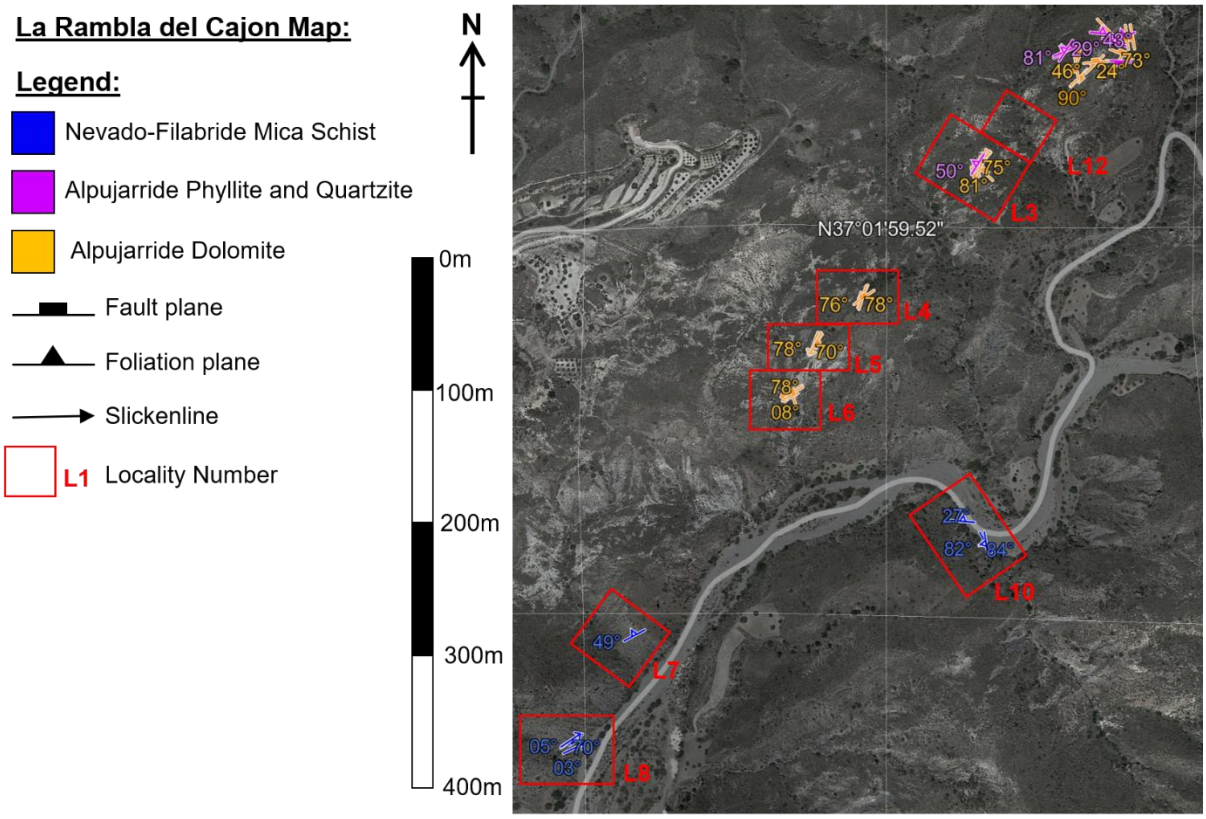

Figure 5.4: A georeferenced map containing the structural data that was collected using the FieldMove Clino application in La Rambla del Cajon.

5.4.1. Field Observations:

There was a clear distinction between exposures of the intact mica schists and the mica schist-derived fault gouges. The fault gouge strands were highly weathered to form gullies covered in a loose soil, whereas the intact mica schist exposures were cohesive and stood proud from the level of the Rambla. The structures of the intact mica schist varied between different fault blocks, such as at Locality 10, where to the NW of a fault strand the mica schist was pervasively folded in cm- to dm-scale Z-folds that were wholly absent to the SE of the fault. Foliation, as defined by a schistose fabric and quartz mineralisation in the intact mica schists, varied in strike from 040-090° or 150-180° between fault blocks (Figure 5.5). The mica schist-derived fault gouges were extremely friable, ranged in colour from black, dark grey to green, and clast sizes ranged from cm-scale relict grains to fine powders (Figure 5.6). The pulverised quartz clasts, previously described by Rutter et al. (2012), were observed as brilliant white, cm-scale quartz clasts formed of extremely fine-grained powder that were embedded within the mica schist-derived gouges.

Unlike the mica schist, it was extremely difficult to distinguish exposures of intact phyllite from the phyllite-derived fault gouges. All of the exposures of phyllite-quartzite in the Rambla del

Cajon were covered by a loose weathered soil (Figure 5.7). Colour changes from blue-grey to yellow weathering products showed the exposure pattern of phyllite and quartzite, respectively. The phyllite and quartzite were juxtaposed at the cm- to dm-scale, so the two lithologies were not distinguished at the map-scale. The sharp transitions between gouge types, identified as Y-shears by Faulkner et al. (2003), were targeted for sampling (e.g. CFIA23). Once the weathered top soil was removed for sampling, the phyllite-quartzite derived gouges were highly friable and intact lithons contained foliation on the mm-cm scale with orientations of 045-090° (Figure 5.5).

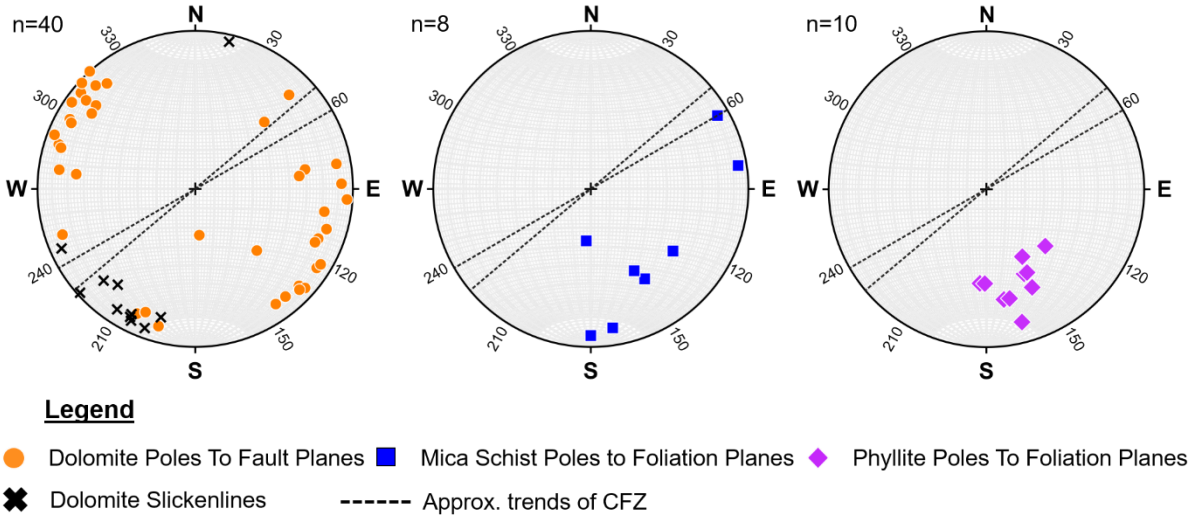

Figure 5.5: Stereonets of the fault planes in the dolomite lithons and the foliation planes in the mica schist and phyllite lithologies in the CFZ.

Dolomite exposures along the Rambla del Cajon topped the hills, formed 5-10 m high cliffs and stood proud from the fault gouges due to their greater resistance to weathering (Figure 5.7). The dolomite was composed of angular carbonate clasts of mm to dm-scale that were reconstituted by a carbonate cement (Figure 5.8). The pervasive fracturing of the dolomite predates or occurred at the onset of movement of the CFZ, as the fracturing was overprinted by later faulting. Faults occurred both at dolomite-dolomite contacts and as dolomite-gouge contacts. While some fault surfaces were dulled by weathering, others were highly polished, even reflective in visible light. Several of the fault surfaces were sealed or cemented by apparent iron-oxide mineralisation (e.g. CFIA11), which presented as opaque, metallic black material between dolomite-dolomite fault planes or as an orange discolouration on weathered dolomite-gouge fault planes. In the field, a hypothesis was formed that the iron oxide mineralisation along dolomite fault planes was caused by fluid flow along the fault network and the signature of the fluid flow may be affected by distance from the localised faults.

Slickenlines on the fault surfaces indicated a predominance of strike slip movement (Figure 5.5). The majority of dolomite-gouge fault contacts were oriented parallel or close to the trend

of the CFZ bounding faults at 030-050° and had dip angles close to the vertical. Many of the dolomite-dolomite fault surfaces were oriented at a higher angle to the boundary faults, at 100-130°. This suggests that the faults bounding the dolomite fault blocks represented R_1 shears, which accommodated greater displacement than the subsidiary R_2 faults fully contained within the dolomite fault blocks (Figure 5.9).

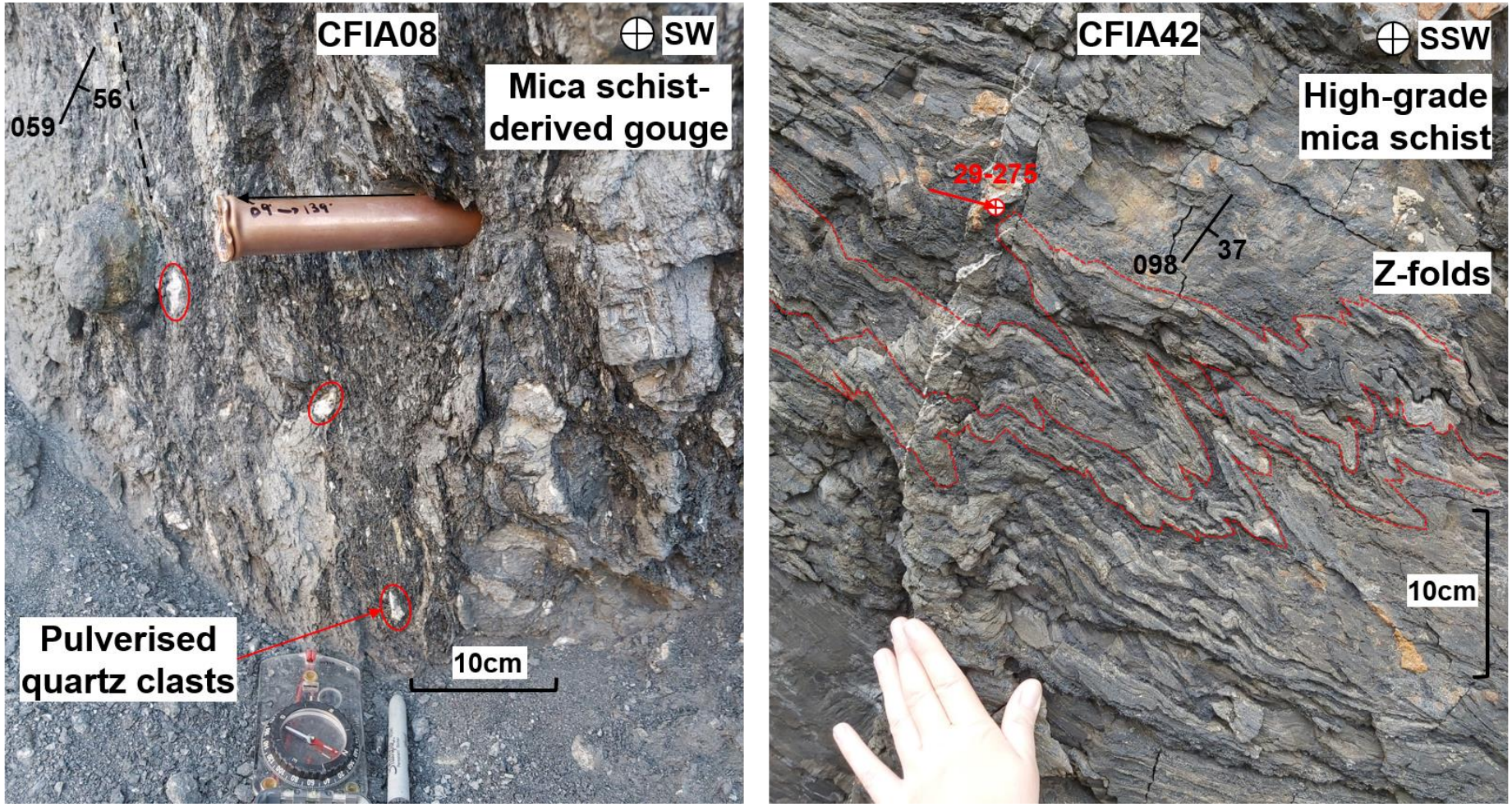

Figure 5.6: Photos of the Nevado-Filabride mica schist-derived fault gouge (left) from Locality 8 and the intact mica schist (right) that shows pervasive folding of the schistose fabric and quartz layering at Locality 10.

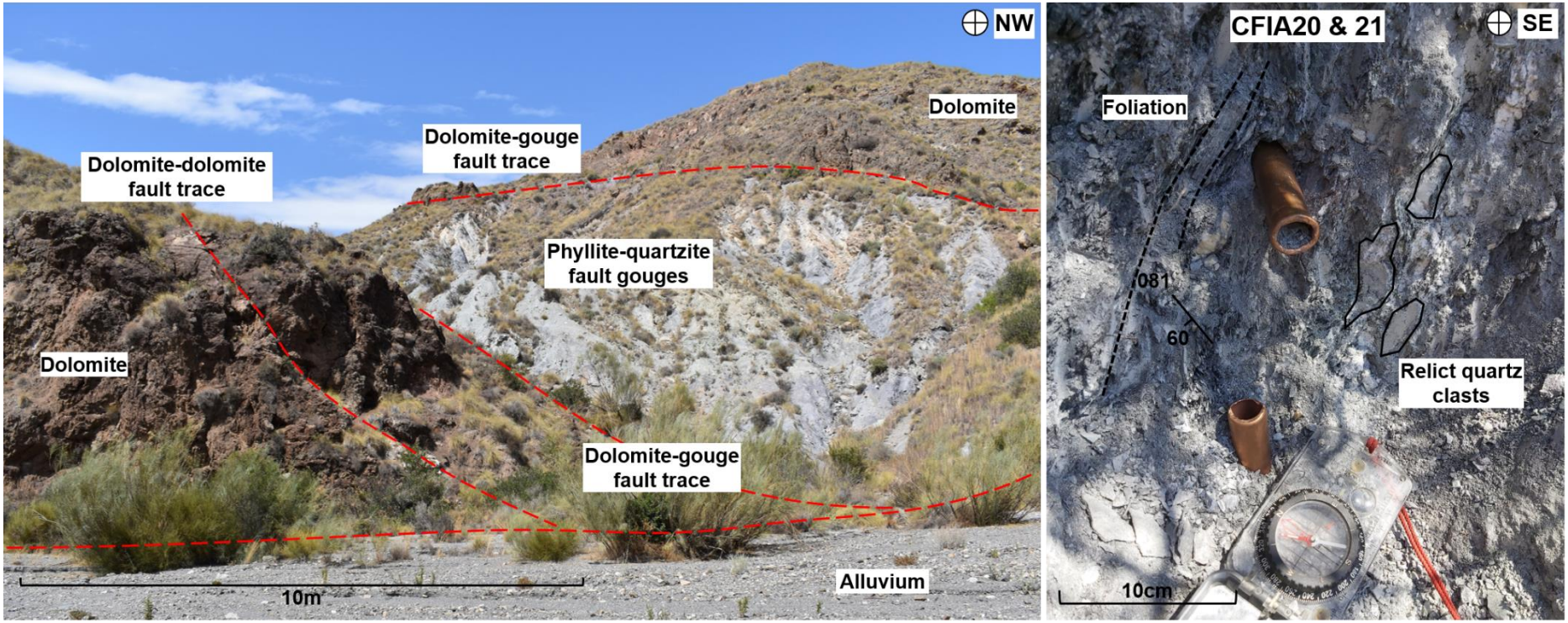

Figure 5.7: A photo that shows the pattern of the dolomite and phyllite-quartzite exposures and fault traces (left) and a photo showing the texture of the phyllite-derived fault gouges (right) at Locality 6.

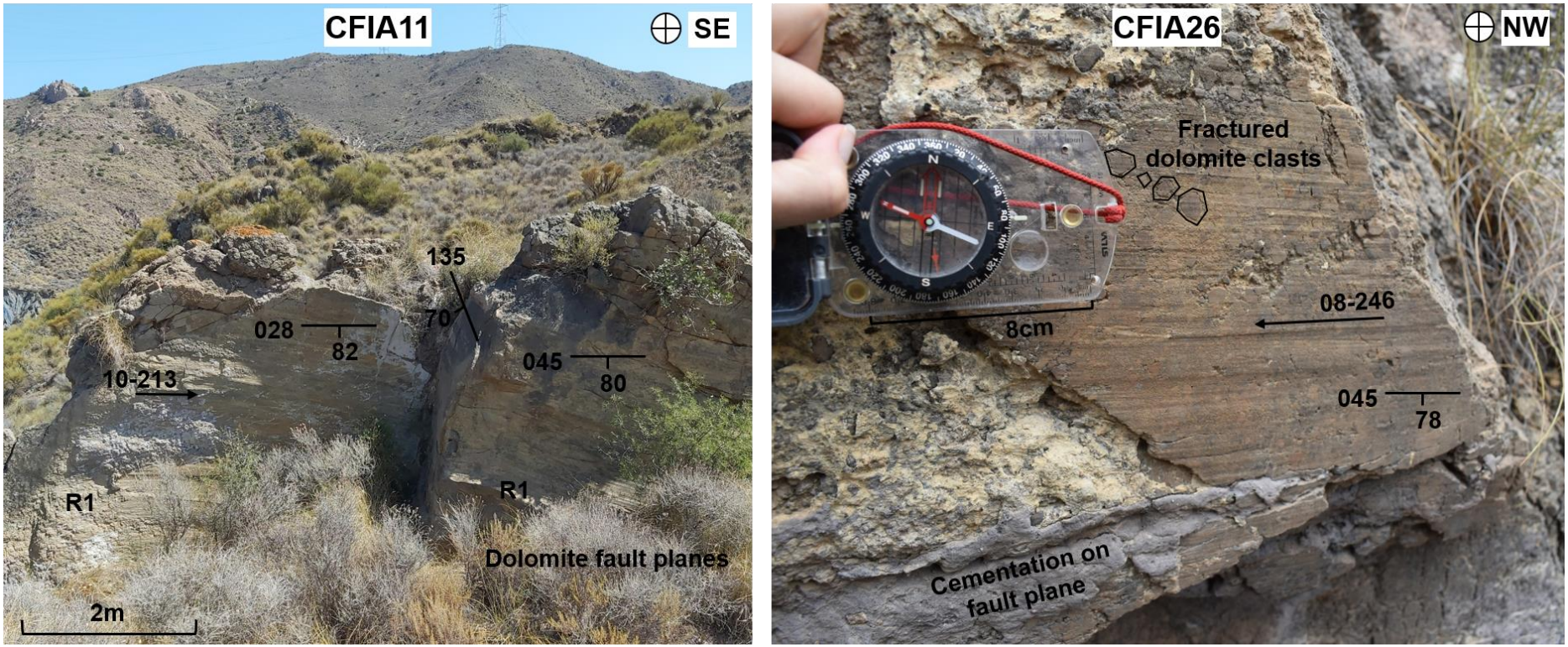

Figure 5.8: A photo of cross-cutting fault planes in an exposure of dolomite (left) at Locality 3 and a photo of a highly polished, 'mirror' fault plane (right) with slickenlines on the dolomite at Locality 6.

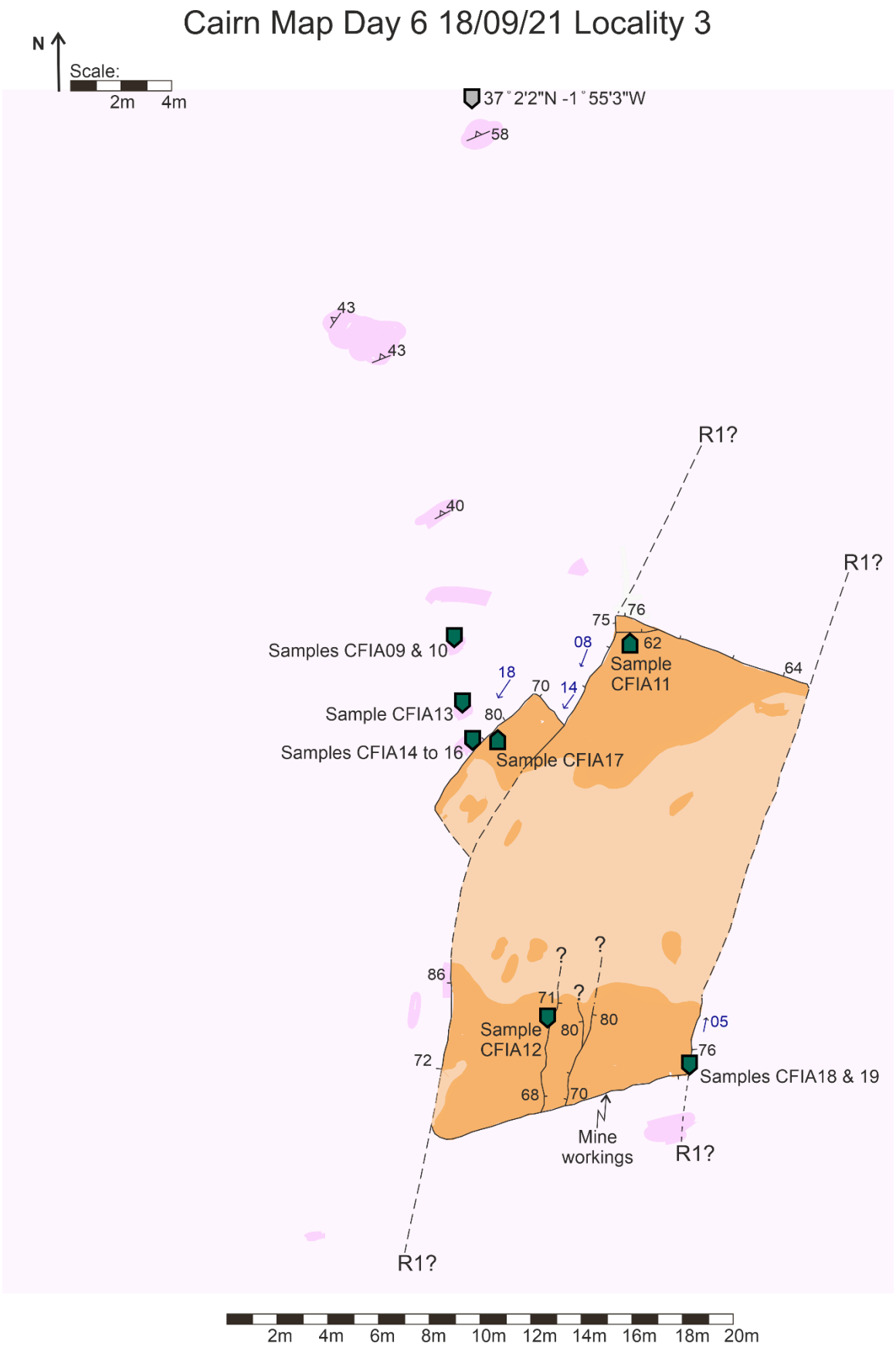

Figure 5.9: Digitised cairn map of the lithologies and fault orientations at Locality 3. Lithological colour labelling follows the scheme in Figure 5.3.

5.4.2. Chemical results:

The fault gouges of the CFZ have been well characterised from field observations, but few studies have applied XRF and XRD techniques to classify or quantify the gouge components (Abad et al., 2017; Faulkner et al., 2003; Rutter et al., 2012). Of interest to this study was the change in chemistry between the intact parent lithologies and the fault gouges. Hence, samples of mica schist were collected from a transect across a fault gouge strand at locality 10 (Figure 5.10). The intact mica schist samples of CFIA42 and 44 were composed of quite different mineral assemblages - CFIA42 was a phyllosilicate-rich mica schist compared to CFIA44, which contained a higher proportion of quartz and plagioclase feldspar (Table 5.3). Faulkner et al. (2003) identified increases in metamorphic grade of the Nevado-Filabride schists across fault gouge strands in the Rambla del Cajon, such as at locality 10 (Figure 5.10). The phyllosilicate-rich sample CFIA42, with its tightly folded quartz mineral layers, had a mineral assemblage typical of greenschist facies conditions. CFIA44 was the only sample tested to contain biotite, when field observations suggested that biotite was a common constituent of the fault rocks. This suggested that biotite in the other samples had been replaced by other phyllosilicates, such as chlorite, which can appear almost black in hand specimen. The mica schist-derived fault gouges from locality 10 (CFIA35 and 37) differed from the intact mica schists in that they contained higher proportions of quartz and a minor component of calcite. CFIA08 (Figure 5.6) was collected from a different fault gouge strand 400 m to the southwest of locality 10 and it was the only sample to contain any gypsum or halite. These would have been derived from evaporite deposits, such as the mid-Messinian (6 Ma) Yesares Formation.

Abad et al. (2016) previously published XRF data that compared the composition of the parent Nevado-Filabride mica schist and the associated CFZ gouge from the Rambla de la Granatilla outcrop near Sopalmo (Figure 5.11B). The authors concluded that the fault gouges were enriched in SiO_2 and depleted in Al_2O_3 relative to the parent lithology (Abad et al., 2016). The data collected in this study shows that there may be more variation in the chemical composition of the parent mica schist, as sample CFIA44 had an anomalously high proportion of SiO_2 compared to all other mica schist-derived samples (Figure 5.11B). There are a limited number of XRF measurements of the mica schists, even in combination with the data from Abad et al. (2016), which may not be sufficient to capture the full chemical variety in a heterogeneous rock type such as a schist. The XRF results also implied that the plagioclase in CFIA44 was andesine, due to the ratios of Na_2O to CaO given in Table 5.4.

Most of the Alpujarride phyllite-derived fault gouges had similar mineral assemblages that were dominated by quartz and muscovite/illite (Table 5.3). Chlorite and paragonite were detected in the bulk powder analysis for all of the phyllite-derived fault gouges. Yet, the exact

clay mineral assemblages varied between the samples, as shown by the additional oriented clay analysis (Table 5.3), which detected smectite in CFIA16, 31 and 32. The only major anomaly in the Alpujarride-derived fault gouges was sample CFIA13, which was taken from a bright yellow fault gouge that was identified in the field as having derived from a quartzite. The quantitative XRD analysis confirmed that CFIA13 had a significantly higher quartz content (81%) than all other measured fault gouges. All of the phyllite- and quartzite-derived fault gouges contained evidence of iron-oxide mineralisation, from the presence of either hematite (Fe_2O_3) or the weathering product goethite (FeO(OH)). The phyllite-derived fault gouges also contained ankerite, an iron or manganese-rich variation of dolomite, that was likely derived from the local Alpujarride dolomites.

XRD analysis was conducted on the bulk rock powder for the dolomite samples CFIA11 and 18 to provide the mineralogy in preparation for the friction experiments, and it showed that these samples were almost entirely composed of dolomite with only a minor quartz component (2%). The XRF results showed that the dolomite samples CFIA11 and 18 contained only a small proportion of Fe_2O_3 (Table 5.4), and it is likely that the iron oxide content was derived from the mineralisation that was observed on the fault surfaces. In contrast, the fault gouges contained a consistent 5 to 7 mass% Fe_2O_3, except for the quartzite-derived fault gouge CFIA13. The iron oxide mineralisation along dolomite fault planes observed in the field prompted a hypothesis that the mineralisation was caused by fluid flow along the fault network and, thus, the degree of mineralisation would vary with distance from the localised faults. However, the consistency of the Fe_2O_3 values at varying distances from the localised faults obtained using XRF makes this hypothesis unlikely to be true.

	Mica schist gouge			Mica schist		Quartzite	Phyllite gouge					Dolomite	
Bulk XRD	**CFIA08**	**CFIA35**	**CFIA37**	**CFIA42**	**CFIA44**	**CFIA13**	**CFIA15**	**CFIA16**	**CFIA30**	**CFIA31**	**CFIA32**	**CFIA11**	**CFIA18**
Quartz	38	53	62	34	55	81	45	37	43	28	29	2	2
Plagioclase	4	-	-	-	8	-	-	-	-	-	-	-	-
K-feldspar	1	-	-	1	-	1	2	2	4	3	3	-	-
Calcite	-	2	2	-	-	-	-	-	-	-	-	-	-
Dolomite	-	-	-	-	-	-	-	-	-	-	-	98	98
Ankerite	-	-	-	-	-	-	2	4	2	3	3	-	-
Hematite	-	-	-	-	-	1	2	3	4	3	2	-	-
Goethite	-	-	-	-	-	2	-	-	-	-	-	-	-
Gypsum	1	-	-	-	-	-	-	-	-	-	-	-	-
Halite	2	-	-	-	-	-	-	-	-	-	-	-	-
Biotite/phlogopite	-	-	-	-	7	-	-	-	-	-	-	-	-
Muscovite/illite	37	37	27	58	25	11	40	40	34	47	48	-	-
Paragonite	-	-	-	-	-	5	5	7	9	8	9	-	-
Chlorite	13	5	7	5	3	-	2	5	4	6	4	-	-
Kaolinite	3	2	2	1	2	-	-	1	-	1	2	-	-
Smectite (approx)	-	-	-	2	-	-	-	-	-	-	-	-	-
Oriented clay analysis													
Biotite/phlogopite	-	-	-	-	-	-	-	-	-	-	-		
Muscovite/illite	74	84	77	88	71	84	81	73	69	70	73		
Paragonite	-	-	-	-	-	16	14	18	21	21	18		
Chlorite	18	12	18	5	9	-	5	5	7	6	5		
Kaolinite	1	4	5	7	20	-	-	1	3	2	2		
Smectite (approx)	7	-	-	-	-	-	-	4	-	1	2		

Table 5.3: Mineral compositions collected using bulk powder XRD and oriented clay analysis of a clay separate from rock samples from the CFZ.

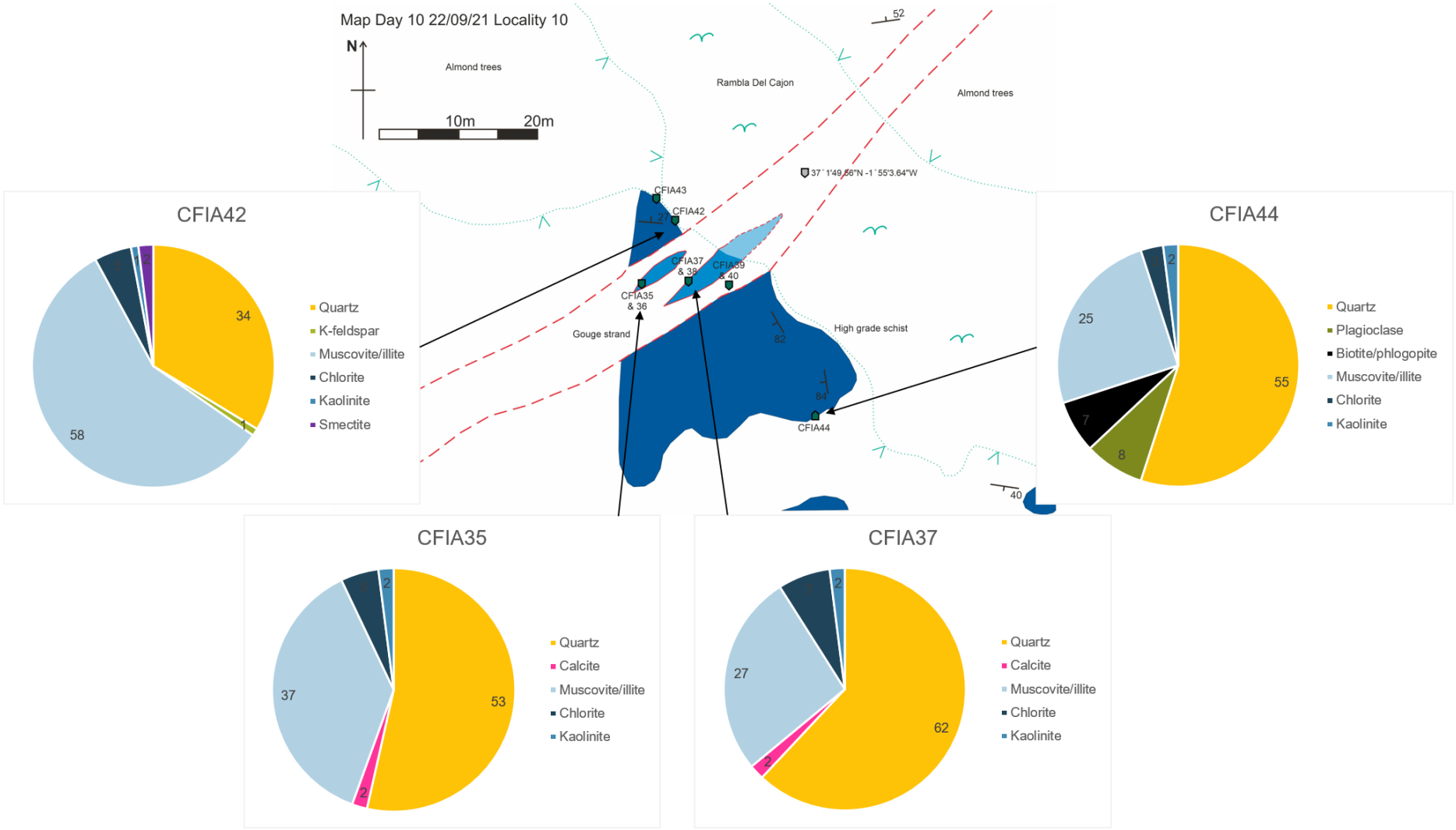

Figure 5.10: Digitised cairn map showing the changes in mineralogy from intact mica schists (CFIA42 & 44) to mica schist-derived gouges (CFIA35 & 37) across a fault gouge strand at locality 10 in the Rambla del Cajon. Lithological colour labelling follows the scheme in Figure 5.3.

		Na_2O	MgO	Al_2O_3	SiO_2	P_2O_5	SO_3	Cl	K_2O	CaO	TiO_2	V_2O_5	Cr_2O_3	MnO	Fe_2O_3	Co_2O_3	NiO	CuO	ZnO	Ga_2O_3	As_2O_3	Rb_2O	SrO	Y_2O_3	ZrO_2	Nb_2O_5	BaO	PbO	Balance
		mass%	mass%	mass%	mass%	mass%	mass%	mass%	mass%	mass%	mass%	mass%	mass%	mass%	mass%	mass%	mass%	mass%	mass%	mass%	mass%	mass%	mass%	mass%	mass%	mass%	mass%	mass%	mass%
Mica schist gouge	CFIA08	1.236	1.881	19.512	44.575	0.143	0.864	1.499	3.809	0.991	0.885	-	0.027	0.075	7.276	-	0.021	-	0.029	-	0.006	0.019	0.011	0.005	0.036	-	0.057	-	17.044
	CFIA35	0.615	1.710	16.750	46.786	0.146	0.067	0.427	3.481	1.782	0.766	-	0.030	0.088	6.282	0.010	0.051	0.299	0.016	-	0.013	0.017	0.008	0.004	0.031	0.003	0.073	-	20.547
	CFIA37	0.755	1.514	14.990	45.739	0.155	0.174	0.619	2.962	1.832	0.643	-	0.026	0.094	5.240	-	0.047	0.345	0.027	-	0.006	0.017	0.006	0.002	0.025	-	-	-	24.784
Mica schist	CFIA42	0.701	1.489	19.709	55.933	0.170	0.013	0.005	4.278	0.429	0.895	0.015	0.032	0.071	7.482	-	0.057	-	0.017	-	-	0.019	0.009	0.005	0.036	0.004	0.086	-	8.548
	CFIA44	1.409	1.193	11.000	69.844	0.113	-	0.006	2.282	0.764	0.712	-	0.031	0.058	3.996	-	0.056	-	0.009	-	-	0.011	0.009	0.004	0.046	-	0.055	-	8.403
Phyllite gouge	CFIA16	1.096	2.677	21.441	48.092	0.123	0.081	0.099	3.595	3.559	0.836	-	0.029	0.113	7.375	-	0.020	-	0.012	-	0.007	0.023	0.026	0.004	0.026	-	0.066	-	10.701
	CFIA32	1.404	3.016	22.962	49.264	0.134	0.046	0.063	3.652	2.990	0.905	-	0.029	0.075	7.553	-	0.026	0.006	0.012	0.006	0.044	0.022	0.031	0.004	0.026	0.004	-	-	7.727
	CFIA15	0.866	1.846	17.546	44.012	0.099	0.175	0.262	3.580	1.546	0.690	-	0.030	0.044	5.007	-	0.046	0.595	0.010	-	0.006	0.023	0.030	0.004	0.020	-	0.294	-	23.270
	CFIA30	1.594	2.907	19.729	43.398	0.088	0.069	0.104	2.770	3.002	0.782	-	0.026	0.059	6.680	0.012	0.033	0.125	0.012	-	0.004	0.019	0.033	0.003	0.023	-	0.070	-	18.458
	CFIA31	1.073	3.243	19.225	46.809	0.129	0.028	0.042	3.041	3.157	0.764	-	0.032	0.096	7.328	-	0.028	0.041	0.015	-	0.009	0.018	0.029	0.002	0.020	-	-	-	14.929

		Na_2O	MgO	Al_2O_3	SiO_2	P_2O_5	SO_3	Cl	K_2O	CaO	TiO_2	V_2O_5	Cr_2O_3	MnO	Fe_2O_3	Co_2O_3	NiO	CuO	ZnO	Ga_2O_3	As_2O_3	Rb_2O	SrO	Y_2O_3	ZrO_2	Nb_2O_5	BaO	PbO	Balance
		mass%	mass%	mass%	mass%	mass%	mass%	mass%	mass%	mass%	mass%	mass%	mass%	mass%	mass%	mass%	mass%	mass%	mass%	mass%	mass%	mass%	mass%	mass%	mass%	mass%	mass%	mass%	mass%
Quartzite gouge	CFI A13	0.298	0.467	8.963	60.098	0.040	0.473	0.296	2.045	0.112	0.345	-	0.023	0.111	3.869	-	0.075	0.208	0.005	-	-	0.012	0.090	0.001	0.018	-	0.605	0.009	21.837
Dolomite	CFI A11		17.465	0.494	1.016	0.047	0.037	0.032	0.09	30.722				0.189	1.713								0.007						48.189
	CFI A18		17.44	0.399	0.904	0.03	0.028	0.011	0.083	30.548				0.045	0.682		0.013						0.012						49.806

Table 5.4: Chemical compositions collected using XRF on geo-pellets of powdered rock samples from the CFZ.

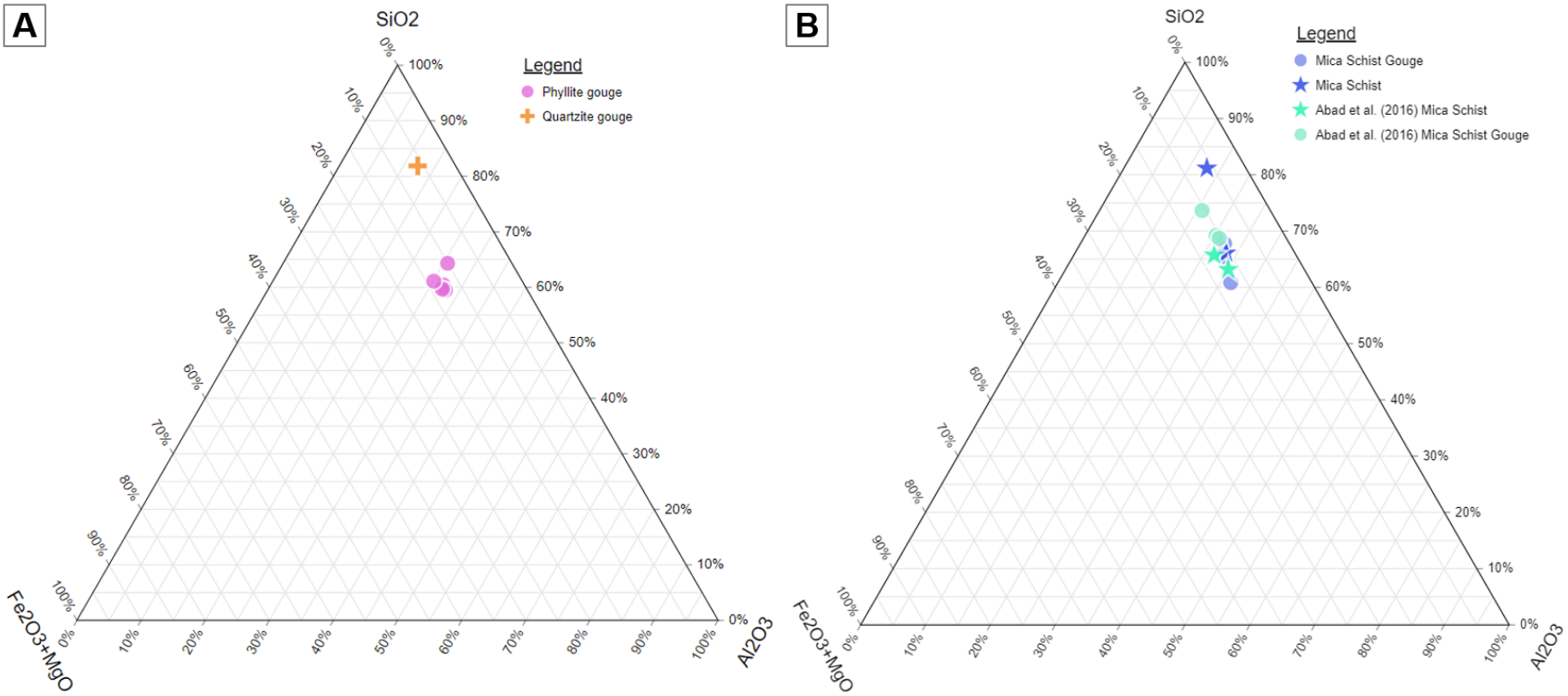

Figure 5.11: Ternary plots showing the changes in XRF measured SiO_2, Al_2O_3 and Fe_2O_3+MgO content from: (A) samples of phyllite- and quartzite-derived fault gouges; and (B) samples of protolith mica schist and mica schist-derived gouge, including literature XRF data from Abad et al. (2016).

5.4.3. Microscopy results:

Mica Schist (Nevado-Filabride):

The mica schist gouge samples, CFIA02 and 04, both contained coarse-grained (>0.5 mm) relict lithic clasts and extremely fine-grained (≤20 μm) fault gouge (Figure 5.12). Relict mica schist clasts had a maximum grain size of 6 mm and retained evidence of the original penetrative schistose fabric. The earlier fabric was defined by the preferred orientation of the phyllosilicate minerals (mus, chl & bio) and mineral banding of quartz-rich and mica-rich bands (Figure 5.12 A). Quartz grains in the relict lithic clasts contained subgrains and sweeping or undulose extinction, which are evidence of intracrystalline plastic deformation. The orientation of this fabric could not be correlated between relict clasts due to the rotation of grains in the later brittle deformation episodes. In CFIA04, the lithic clasts contained several crystals of a metamorphic aluminosilicate mineral, identified as andalusite (Figure 5.13) that had been partially or entirely replaced by sericite micas.

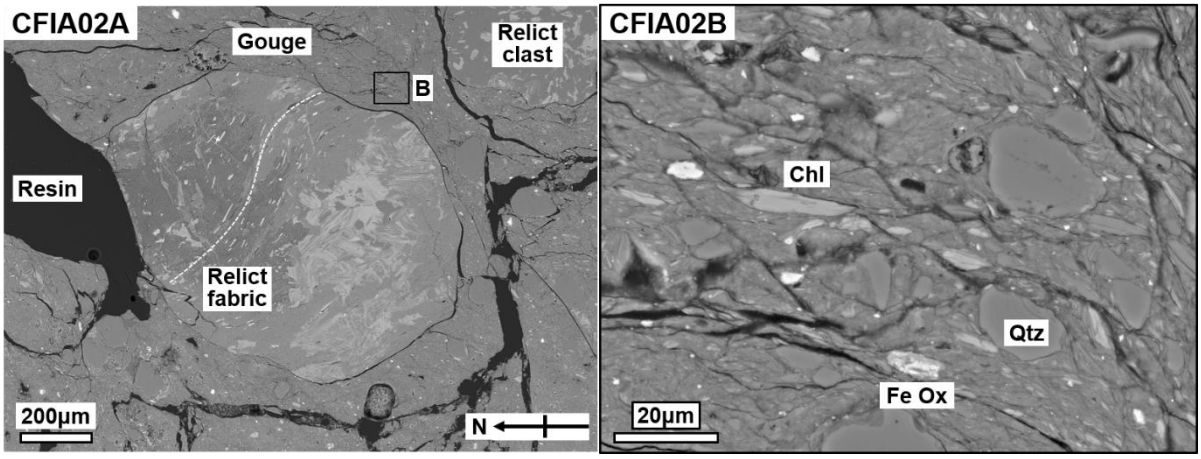

Figure 5.12: BSEM images of mica schist-derived fault gouge sample CFIA02 showing the contrast in textures between a relict lithic clast (A) and the extremely fine-grained fault gouge (B).

Although both mica schist gouge samples were collected several metres from the dolomite faults in the Rambla del Cajon, the samples contained differing proportions of fault gouge. The relative proportion of fault gouge (grain size <30 μm) to lithic clasts (or fault breccia) was estimated using stitched compilation images of the entire thin section. Regions of fault gouge were outlined and the area of these regions were compared to the total thin section area to provide an estimated fault gouge proportion. CFIA02 contained only ~10% fault gouge whereas CFIA04 had a high proportion (>70 %) of fault gouge to lithic clasts. The fault gouges derived from the mica schists presented as black in colour under the optical microscope, due to the extremely fine grain size of the majority of grains at <10 μm. EDS maps of the fault gouge showed that the fault gouge was dominated by phyllosilicate minerals, including muscovite and chlorite, along with well-rounded quartz grains and minor iron-oxides, titanium-oxides and carbonate material.

In CFIA02, a network of fractures (Figure 5.14A), with at least 3 distinct orientations extended for >5 cm through the gouge sample. When in situ, the earliest identified fracture set had orientations of NW-SE and is marked by anomalously high proportions of chlorite and iron-oxide mineralisation. Two sets of later, overprinting shear fractures were oriented NNW-SSE and NE-SW, with this last set showing left lateral offsets of ~1 mm. Chlorite was often associated with biotite, which appeared to have been highly altered (Figure 5.14A). The chlorite appeared to be stained by the iron oxide mineralisation, which made it difficult to identify any biotite in the thin sections (Figure 5.14A), but there were examples in CFIA02 of chlorite grains that were interlayered with biotite (Figure 5.14C). This suggests that chlorite formed from the hydration reaction of biotite and that the fracture networks acted as fluid pathways for hydrothermal fluids.

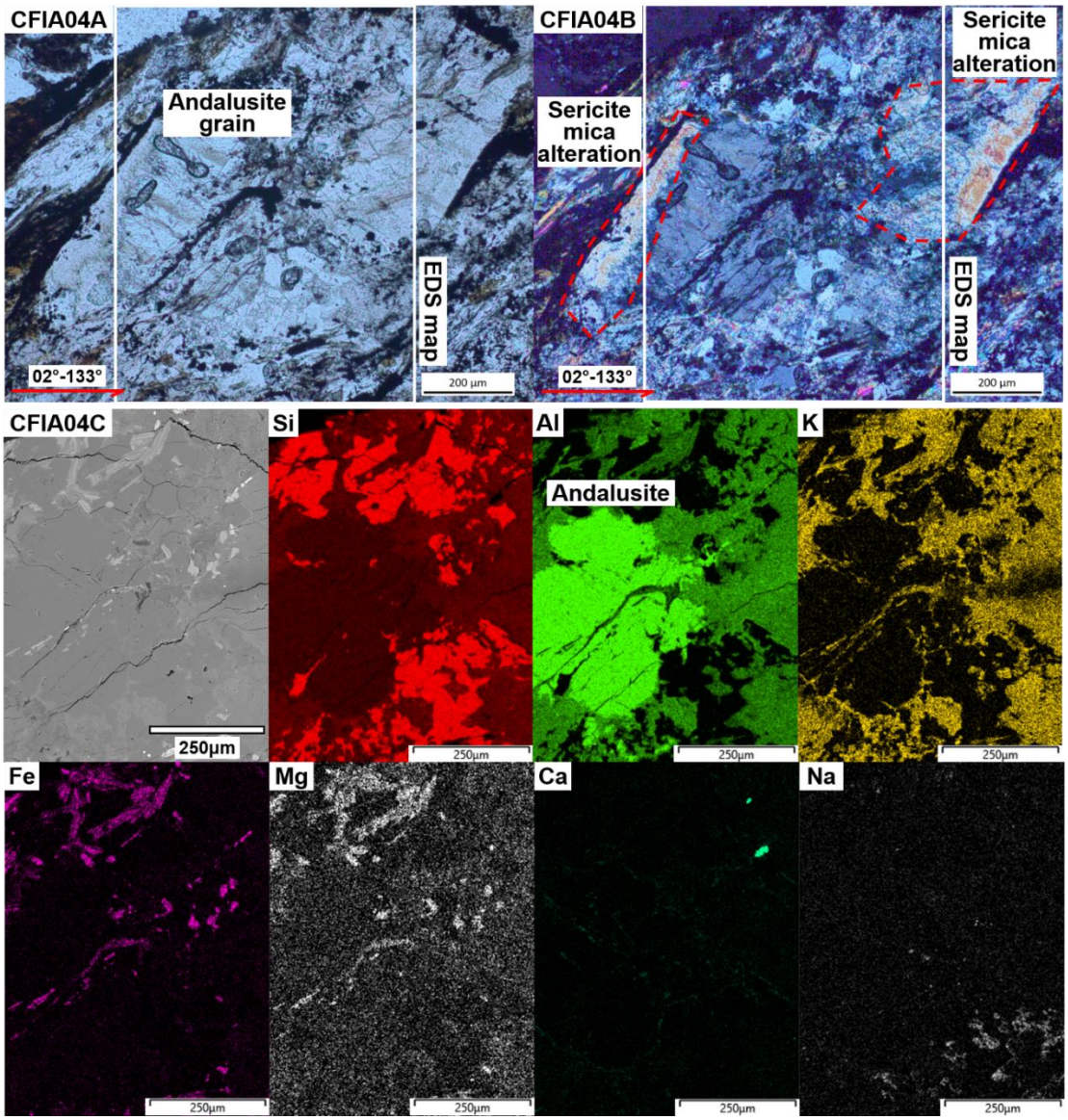

Figure 5.13: Mica-schist-derived fault gouge sample CFIA04: (A) plane polarised optical image and (B) cross polarised optical image of partially altered aluminosilicate mineral in a relict grain of mica schist; (C) BSEM image of the aluminosilicate mineral as the basis for EDS analysis (Si, Al, K, Fe, Mg, Ca and Na).

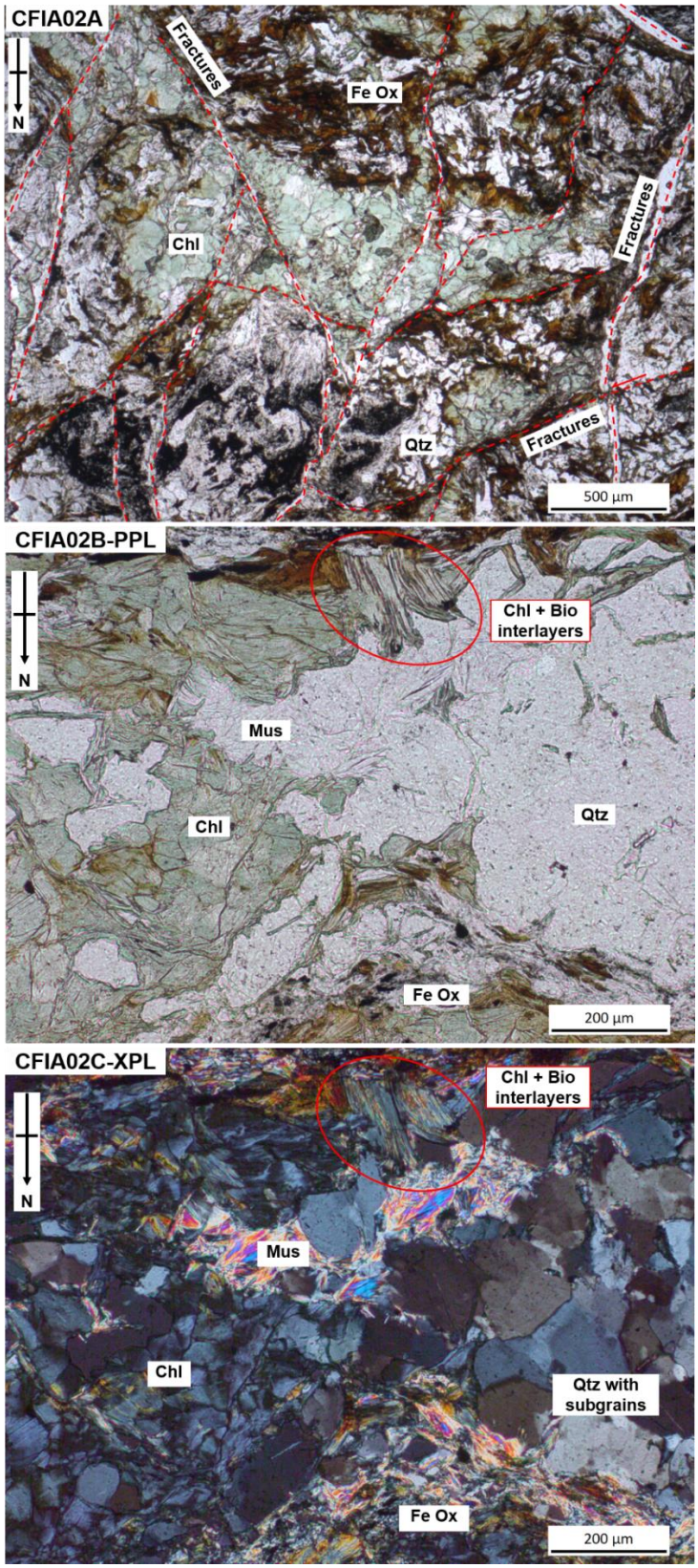

Figure 5.14: Mica-schist-derived fault gouge sample CFIA02: (A) plane polarised optical image showing the concentration of chlorite and iron oxide mineralisation in proximity to the network of fractures; (B) plane polarised optical image of the interlaying of chlorite with biotite, which is evidence of the hydration of biotite to chlorite; and (C) cross polarised optical image of the chlorite and quartz, including the characteristic berlin-blue interference colour of chlorite and subgrains in quartz, which are evidence of intracrystalline deformation .

Phyllite (Alpujarride):

The phyllite- and quartzite-derived fault gouges were collected with the aim of identifying spatial changes in proximity to the localised dolomite faults. For example, a 10 cm by 20 cm grid of samples was collected at Locality 5 (Figure 5.15). Relict lithic clasts of phyllite are most apparent in the samples CFIA23, 28, and 31 (Figure 5.16). The penetrative schistose fabric was defined by the preferred orientation of phyllosilicate minerals, namely muscovite, and chlorite (from altered biotite). A mineralogical layering of quartz-rich bands and phyllosilicate-rich bands was sometimes present, ranging from 5 μm to 200 μm in thickness. In the relict phyllite grains, EDS maps (e.g. Figure 5.16) show that the mineralogical layering consists of Mg- and Fe-rich layers that are depleted in K and Al, and vice versa. The Mg- and Fe-rich layers in EDS likely represent chlorite-rich mineralogical layers and the K- and Al-rich, with minor Na, layers represent muscovite with minor paragonite (Figure 5.16). In samples CFIA23, 28 and 31, the relict phyllite clasts also displayed a symmetric, zonal crenulation cleavage texture (Figure 5.16). Other relict lithic clasts in the phyllite- and quartzite-derived fault gouge samples included brecciated quartz veins (CFIA20) and carbonate clasts (CFIA30).

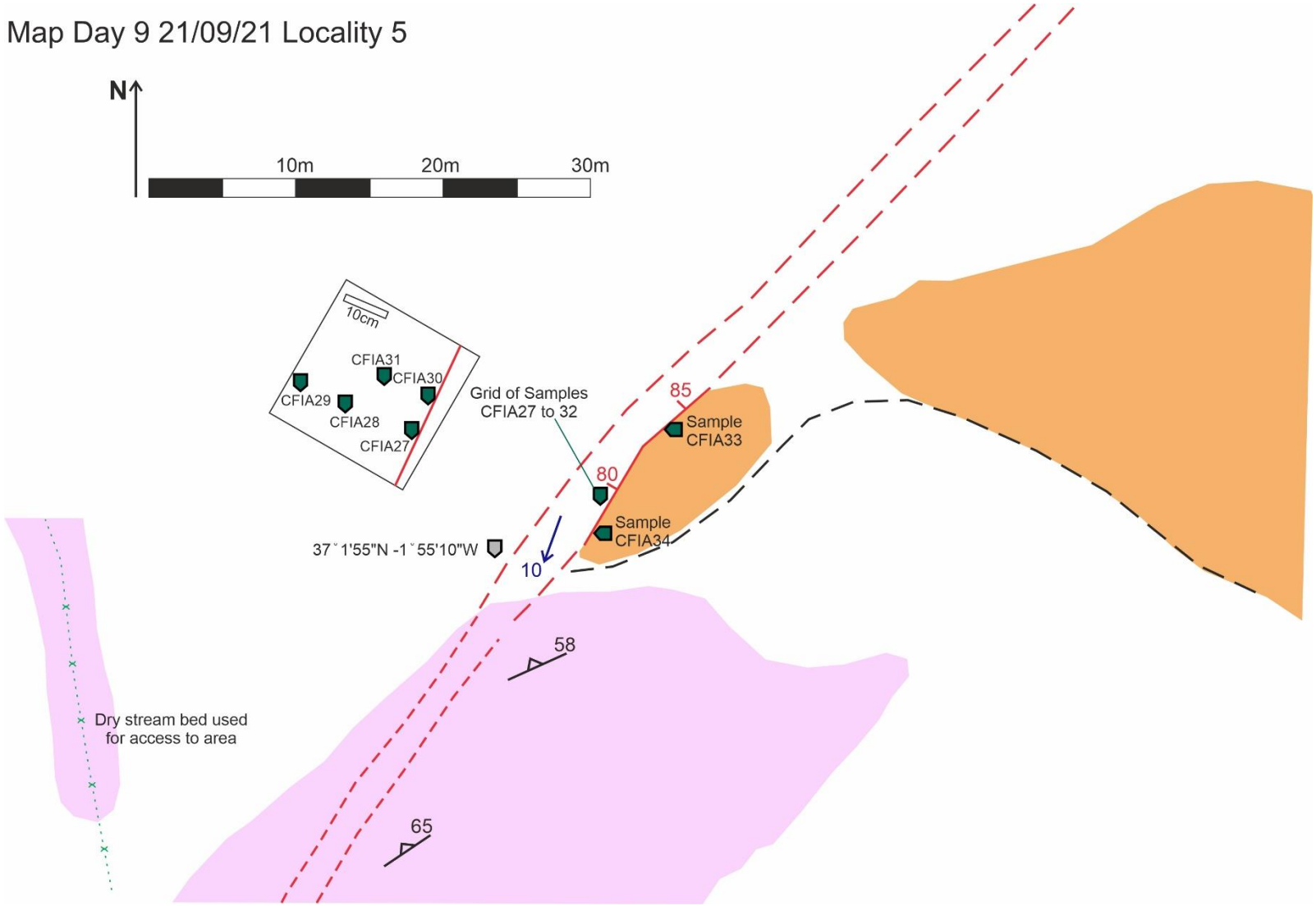

Figure 5.15: Digitised cairn map of locality 5 in the Rambla del Cajon that shows the spatial distribution of fault gouge samples in the phyllite-quartzite gouge relative to the dolomite fault plane.

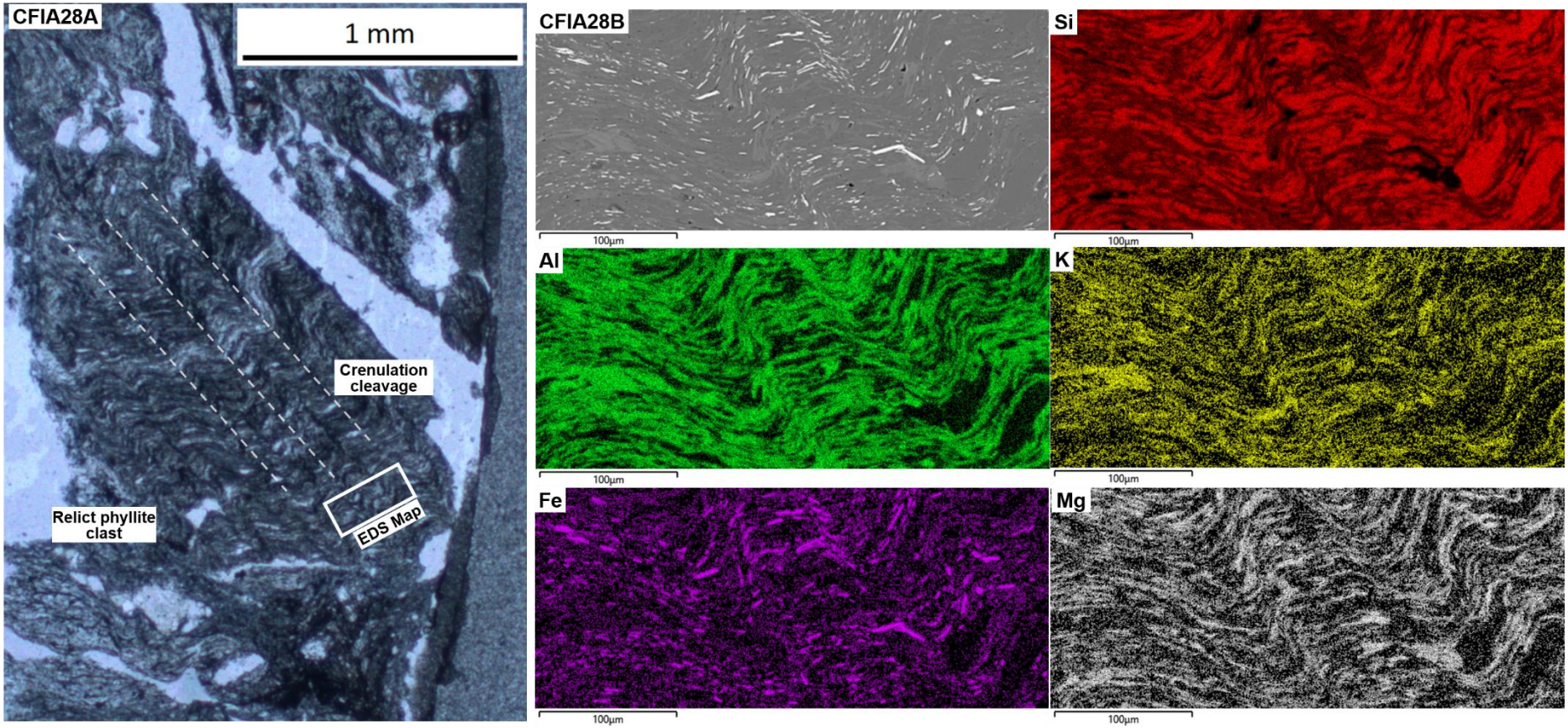

Figure 5.16: Phyllite-derived fault gouge sample CFIA28: (A) plane polarised optical image of a relict phyllite clast with crenulation cleavage defined by the orientation of phyllosilicate minerals; (B) BSEM image of the phyllite with crenulation cleavage as the basis for EDS analysis (Si, Al, K, Fe and Mg).

Sample CFIA20 was a good example of the contrasts between the relict lithic clast types and the fault gouge. The sample, shown in Figure 5.17, could be split into 3 distinct domains: (1) a brecciated quartz vein; (2) a fault gouge strand; and (3) brecciated phyllite. The fault gouge strand separated the quartz and phyllite domains and it had a width ranging from 200 μm to 1 mm. The quartz vein clasts ranged in size from <10 μm to 5 mm, the largest of which contained elongate subgrains and displayed sweeping undulose extinction. This internal viscous deformation of the quartz vein was overprinted by extensive fracturing to form highly angular quartz clasts and zones of grain comminution. The internal distortions of the quartz clasts could be a relic of earlier viscous deformation during the greenschist-grade metamorphism associated with the Alpine Orogeny.

The phyllite clasts had mineralogical banding formed of fine-grained (~20 μm) quartz, with microstructures typical of dynamic recrystallisation by sub-grain rotation, and strongly aligned phyllosilicate minerals. This earlier microstructural fabric is overprinted by pervasive intra- and intergranular brittle fracturing that formed angular clasts of 100 μm to 1 mm. CFIA20 is an example of a sample that was classified as a 'fault gouge' from field observations but, according to the microstructural observations, the sample would be described as a fault breccia (Table 5.1).

The fault gouge strand (domain 2) in CFIA20 was representative of the fault gouges observed in most of the phyllite- and quartzite-derived fault gouges. Clast sizes in the fault gouges were predominantly <20 μm, with a component of ~5% well-rounded quartz or lithic clasts of ≤40 μm clast size. EDS maps showed that the gouge chemistry was dominated by phyllosilicates rich in Al and K, with minor Fe and Mg (Figure 5.17), likely representing muscovite, and possibly illite. Less abundant modal chlorite is highlighted by the distribution of Mg and, to a lesser extent, Fe (Figure 5.17). The fault gouges also contained (2-5%) iron oxides and rare (<0.5%) calcium phosphate clasts. CFIA20 showed that localisation of deformation in the fault strands was occurring across multiple scales – the sample was collected from a fault gouge strand ~10 m wide that was identified from field observations, but it also contained a localised <1 mm width band of fault gouge between lower strain material.

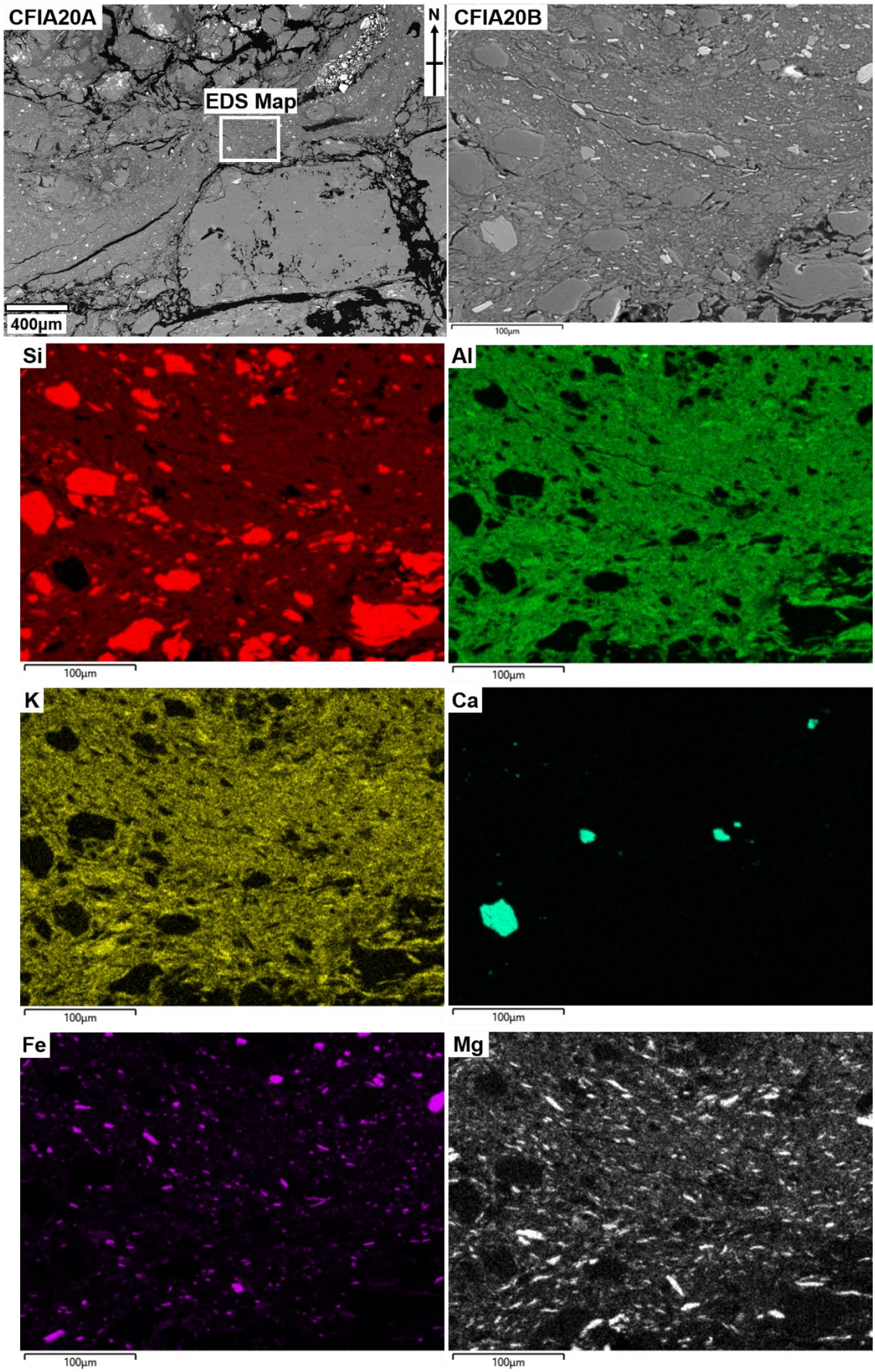

Figure 5.17: BSEM image of a fault gouge strand and fractured lithic clasts in sample CFIA20 (A); zoomed in view of the fault gouge texture (B) as the basis for an EDS map (Si, Al, K, Ca, Fe, Mg).

Phyllite-derived fault gouge sample CFIA27 was collected in direct contact with a dolomite fault plane (Figure 5.15) and in it several unexpected microstructural features were observed. This sample could also be separated into 3 separate domains: (1) fault gouge dominated by carbonate grains; (2) a dark iron-oxide-rich band; and (3) phyllosilicate-rich fault gouge with large (sub-mm) relict grains of quartz.

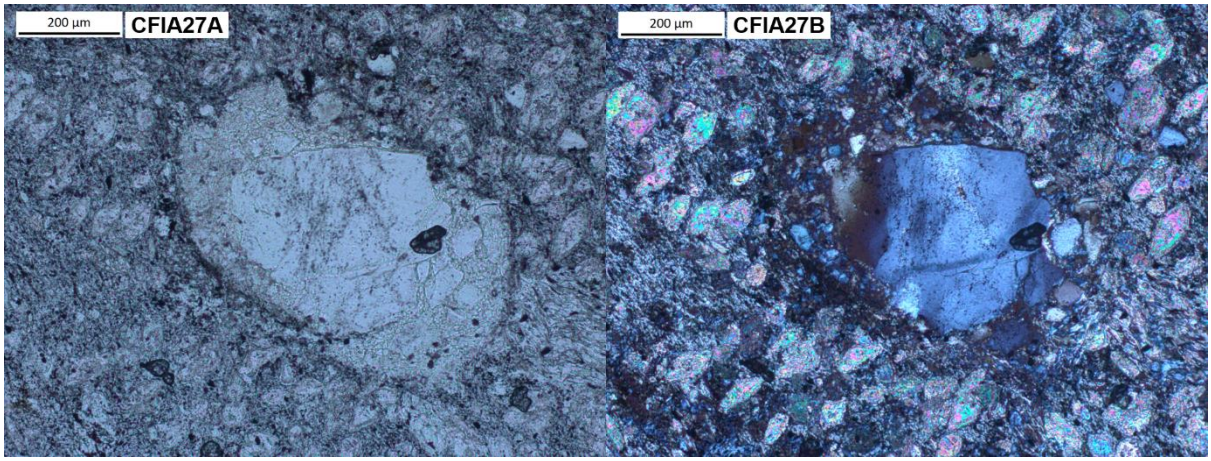

Figure 5.18: Phyllite-derived fault gouge sample CFIA27: (A) plane polarised optical image showing the central clast and rim texture of a pulverised quartz clast in the fault gouge; and (B) crossed polarised optical image that highlights the presence of carbonate fossils in the fault gouge and the sweeping undulose extinction in the central quartz clast.

In region 1 (Figure 5.18), embedded fully within the fault gouge material are carbonate clasts that accounted for 40 % of this region and several relict quartz grains of 400 to 800 µm size. The carbonate clasts were of a consistent size at 50-100 µm with elliptical shapes (Figure 5.19) and were characterised by a core surrounded by a thin rim. This carbonate material contained gaps around the rim of the clast and often contained voids in the centre of the grain. These features could be fractures formed during deformation, but could also be relics of original fossil features (see text below). The majority of carbonate clasts were fully enveloped by fault gouge, but several examples showed straightened and embayed carbonate-carbonate grain boundaries, which is evidence of dissolution (Figure 5.19A). EDS maps in region 1 (Figure 5.19), showed that the carbonate material was calcite with a slightly Mg-enriched rim (~1% to ~3%) that corresponded with the clast rims. These clasts were identified as foraminifera test fossils, likely from the family of Miliolida. EBSD maps in region 1 showed that the fossil structure had been fully replaced by secondary calcite, and recrystallised to a single crystal orientation in each fossil, which may explain the lack of chambers in the tests. It was unexpected that fossils would be preserved as fairly intact relict clasts in the fault gouge – the foraminifera would have been derived from one of the Neogene sedimentary units as more competent clasts that were removed from a weaker cement or matrix. Miliolida occur in a range of marine settings including brackish, coastal and benthic environments. A potential

source of the foraminifera tests may be the Azagador Formation, which has been reported to contain benthic foraminifera (Sänchez-Almazo et al., 2001; van de Poel, 1992).

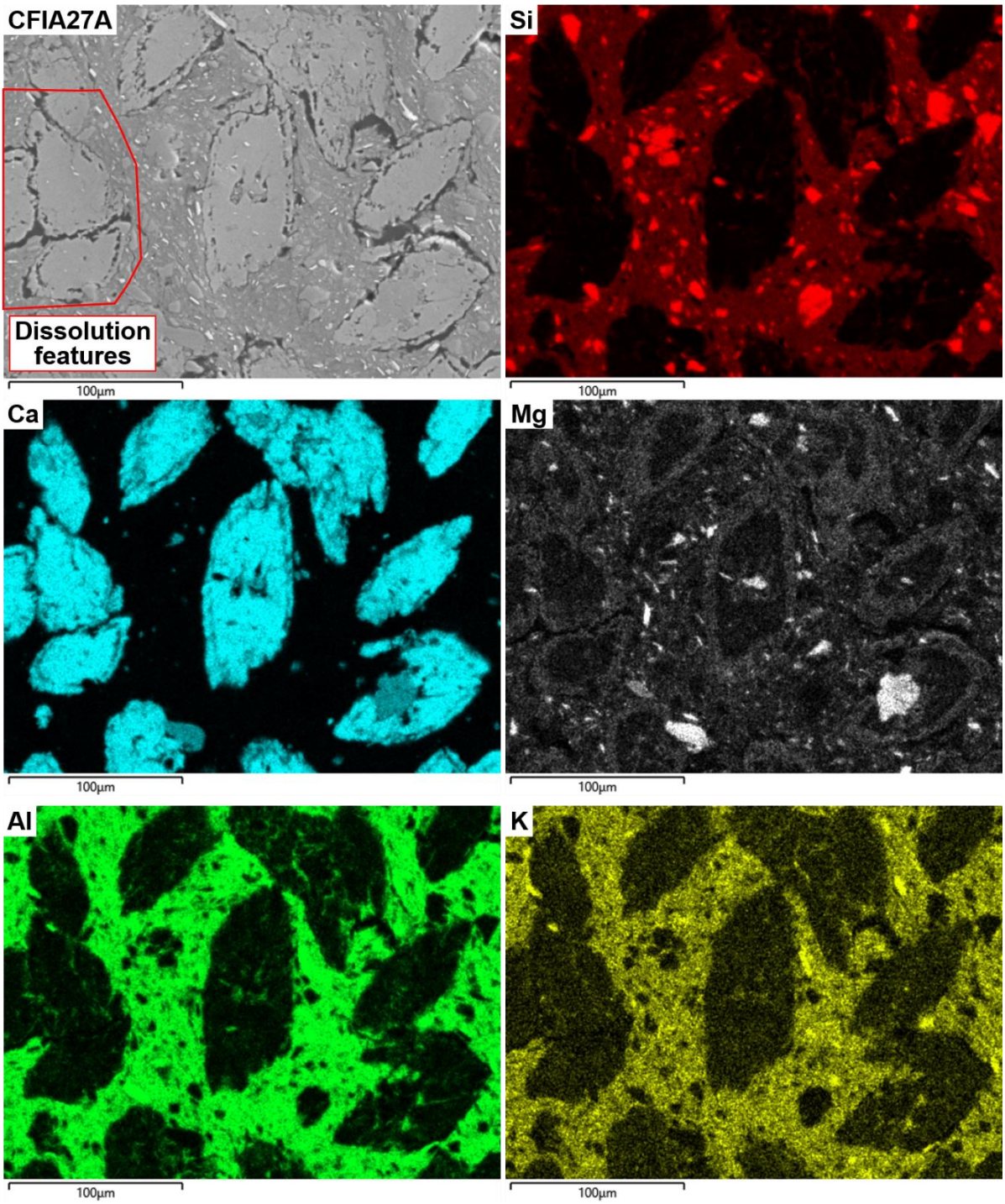

Figure 5.19: BSEM image (A) and EDS maps of the Foraminifera fossils embedded in fault gouge in sample CFIA27 (Si, Ca, Mg, Al & K). The red box highlights straightened and embayed grain contacts that represent areas of dissolution of the fossils.

In region 1 of CFIA27, there were also several relict quartz grains that had a central clast (optically a single crystal) and an outer quartz rim formed by angular quartz fragments (Figure 5.18). The central quartz clast, in Figure 5.20, showed sweeping undulose extinction and

subgrains on the scale of 50-200 μm size. In contrast, the rim of the quartz clast was characterised by a large grain size range, from quartz nanoparticles to clasts of 100 μm diameter (Figure 5.20). EDS maps of the central quartz clast, rim and the fault gouge matrix (Figure 5.20) showed that the rim was formed of only quartz material and had not incorporated any of the phyllosilicate-rich fault gouge. This texture potentially represented a pulverised quartz clast (PQC): a clast that has been pervasively fragmented without any shear strain, but the original fabrics are still recognisable (Aben et al., 2016; Doan & Gary, 2009; Rodríguez-Escudero et al., 2020; Rowe & Griffith, 2015). Rodriguez-Escudero et al. (2020) identified similar potential PQC in the Nevado-Filabride-derived fault rocks in the Alhama de Murcia fault, 80 km north of the CFZ. The analysis of the microstructures of the potential PQC from the Alhama de Murcia fault was limited to FracPaq analysis of fractures in the clast rim. This is not enough evidence to derive the formation mechanisms of a PQC. Hence, EBSD experiments were conducted on the potential PQC in the phyllite-derived sample CFIA27.

During EBSD data collection, both the central quartz clast and rim indexed well as a quartz phase. This is illustrated in the phase maps generated from the EBSD experiment (Figure 5.21) and it confirms the earlier mineralogy observations from the EDS maps – the rim of fine-grained (average 14.5 μm) quartz clasts is clearly distinct from the fault gouge. The crystal orientation maps, the All Euler (AE) map (Figure 5.22) and the inverse pole figure (IPF) map with colouring referenced to the Y-axis (Figure 5.23), were the most important outcome of the EBSD experiment. Both the AE and IPF maps are necessary to understand crystal orientations – AE maps show the absolute crystal orientations but small orientation changes can relate to drastic colour changes. The changes in colouring scheme are more intuitive for IPF maps, but as IPF map colouration is based on a chosen orientation axis (X, Y or Z) it can fail to capture rotations around that axis.

It would be expected that a PQC would show similar orientations across the related pulverised clasts, as there would have been no shear strain in its formation. The clast in CFIA27 does not show a crystallographic relationship between the central quartz clast and the fragments in the pulverised rim. This is evidenced in the pole figures in Figure 5.24. In Figure 5.24A, the central quartz clast crystallographic axes and poles to prism faces show elongated clusters, thus demonstrating that the single quartz crystal is intensely twinned by Dauphine twinning (in red in Figure 5.23), and that it is also characterised by large internal distortions. Figure 5.23 confirms that distortion is both distributed (e.g. smooth change in shades of green) and organised into irregular sub-grain boundaries and sub-grain walls (yellow, green and blue lines). In contrast, Figure 5.24B and C show that quartz fragments in the rim have a randomly distributed crystallographic orientation and do not display a crystallographic relationship with the central quartz clast.

PQC have been used as indicators of seismic slip (Mitchell et al., 2011; Ostermeijer et al., 2022; Rodríguez-Escudero et al., 2020). In terms of seismic slip, PQC are inferred to form due to the propagation of seismic waves through a fault rock, which drastically reduces the effective normal stress and causes rapid expansion and contraction, resulting in pulverisation of the clast in-situ, devoid of shear strain or large rotations. The EBSD data collected in this study (Figure 5.24) do not show an idealised rotation-free PQC formed in-situ. However, a PQC may undergo partial pulverisation in the rim only, and subsequent rotation due to shear strain would cause the misorientation of clasts in the rim. The PQC would also be expected to form an overall sigmoidal clast geometry that seems to be absent in sample CFIA27. This may be due to the orientation of the thin section, which was cut at an orientation respective to the dolomite fault planes in contact with sample CFIA27. The clasts in the rim of a PQC that had undergone later shear strain would show rounded grain shapes, due to deformation by grain rolling, rotation and wear. The roundness of the quartz rim clasts in the potential PQC in CFIA27 were measured using the EBSD data and the analysis software AZtecCrystal (Figure 5.25). A roundness of 1 represents perfectly spherical clast shapes, so the average roundness of 0.8 in the quartz rim clasts (Figure 5.25) indicates that the quartz rim clasts are highly rounded – this supports the hypothesis that the misorientation between the central quartz clast and the quartz rim clasts resulted from a shear strain overprint.

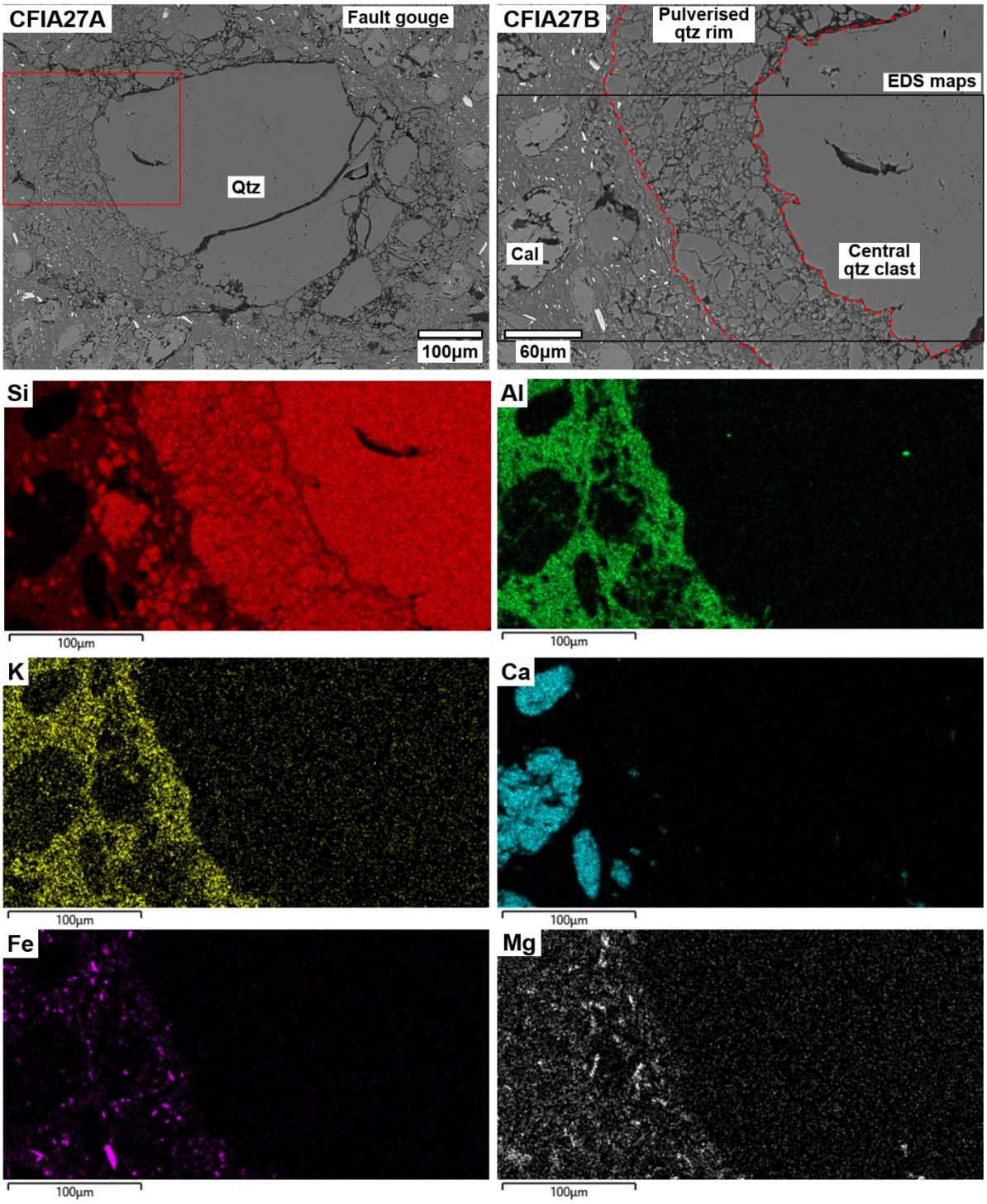

Figure 5.20: BSEM images showing the whole of a pulverised quartz grain in sample CFIA27 (A) and the detail of the pulverised quartz rim around the central quartz clast (B): EDS maps of the pulverised quartz grain in sample CFIA27 (Si, Al, K, Ca, Fe & Mg).

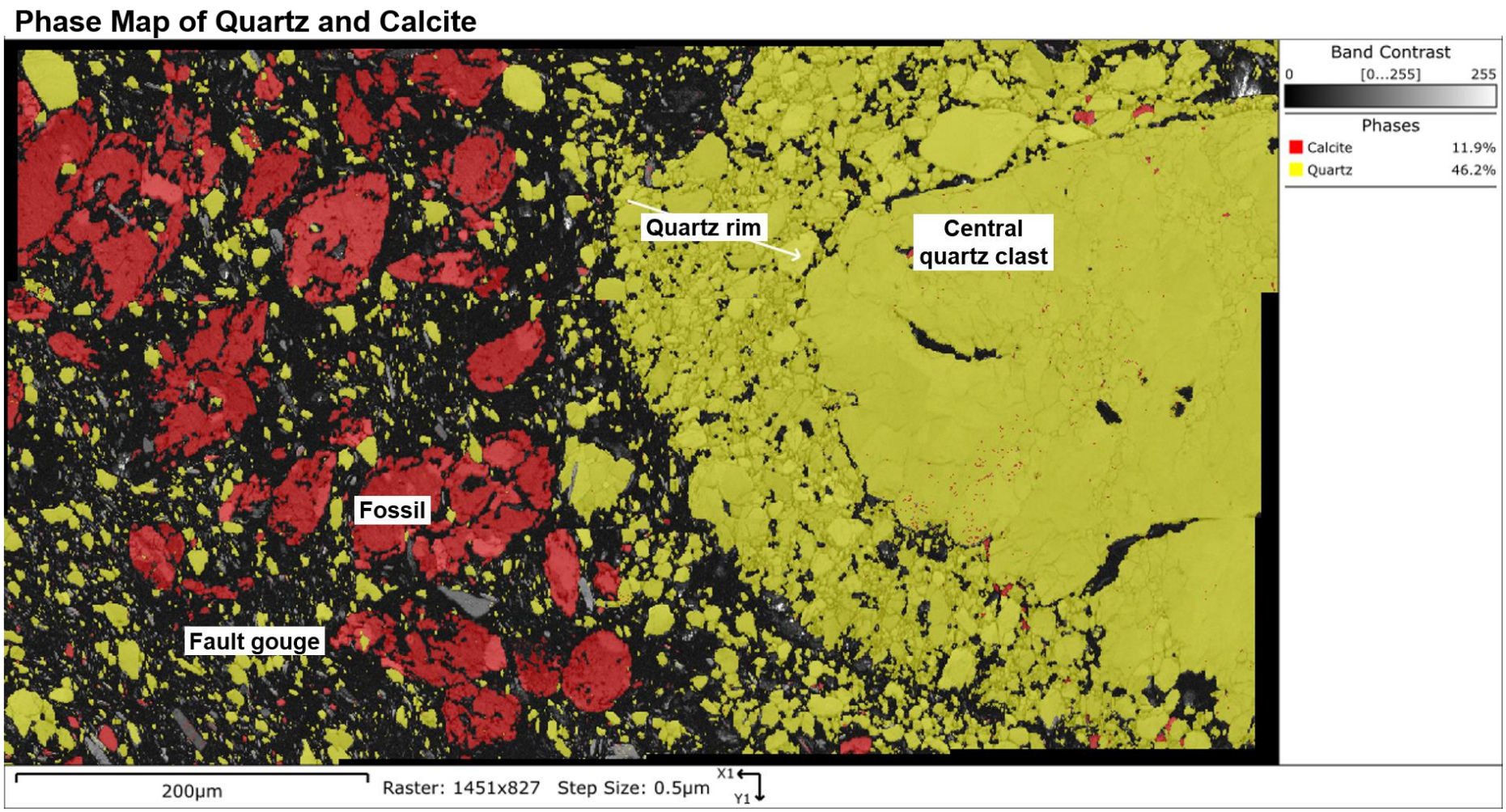

Figure 5.21: EBSD phase map of quartz and calcite in the fault gouge, fossils and quartz clast in region 1 of sample CFIA27.

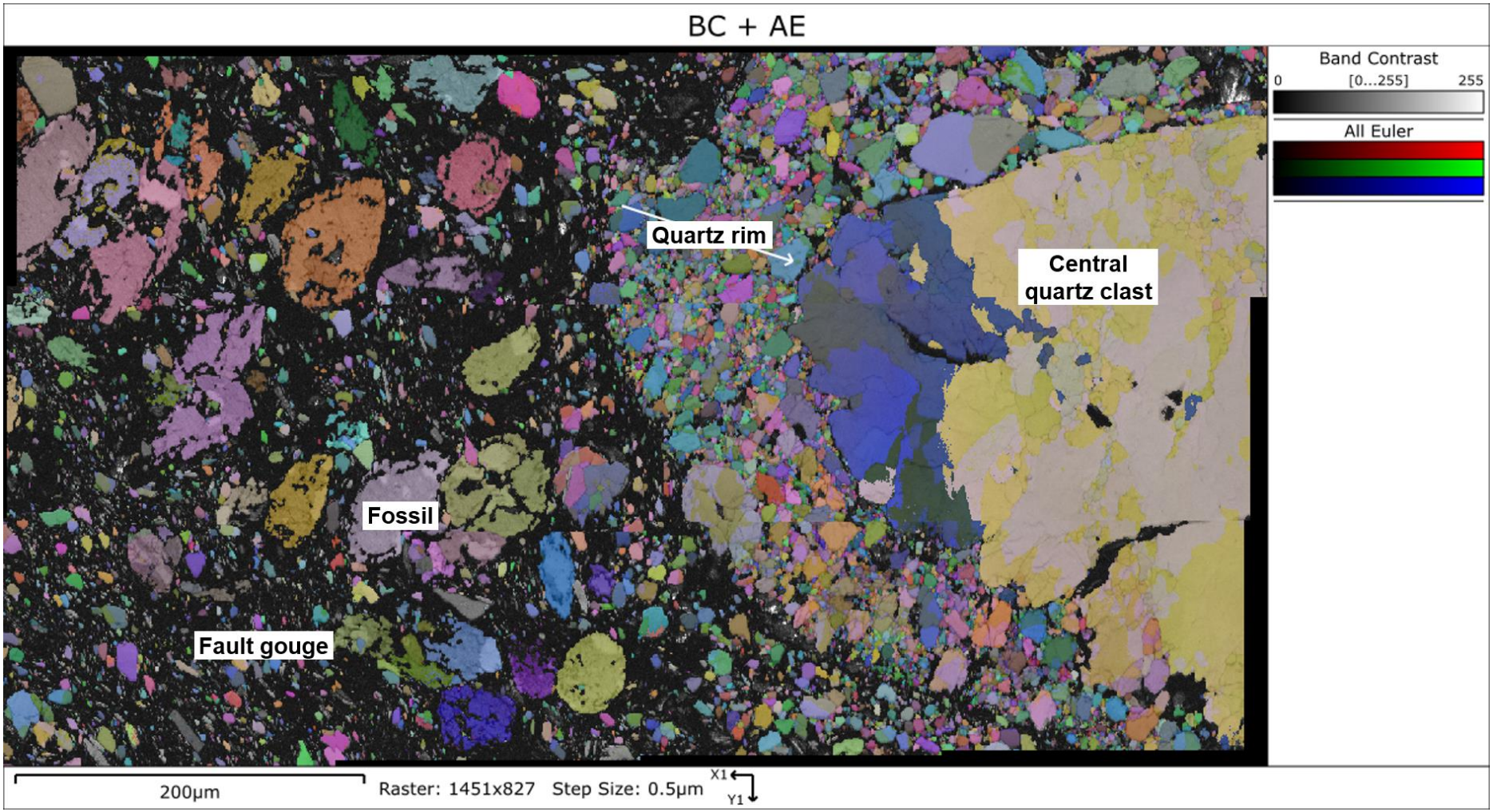

Figure 5.22: EBSD band contrast (BC) and All Euler (AE) map of the fault gouge, fossils and quartz clast in region 1 of sample CFIA27.

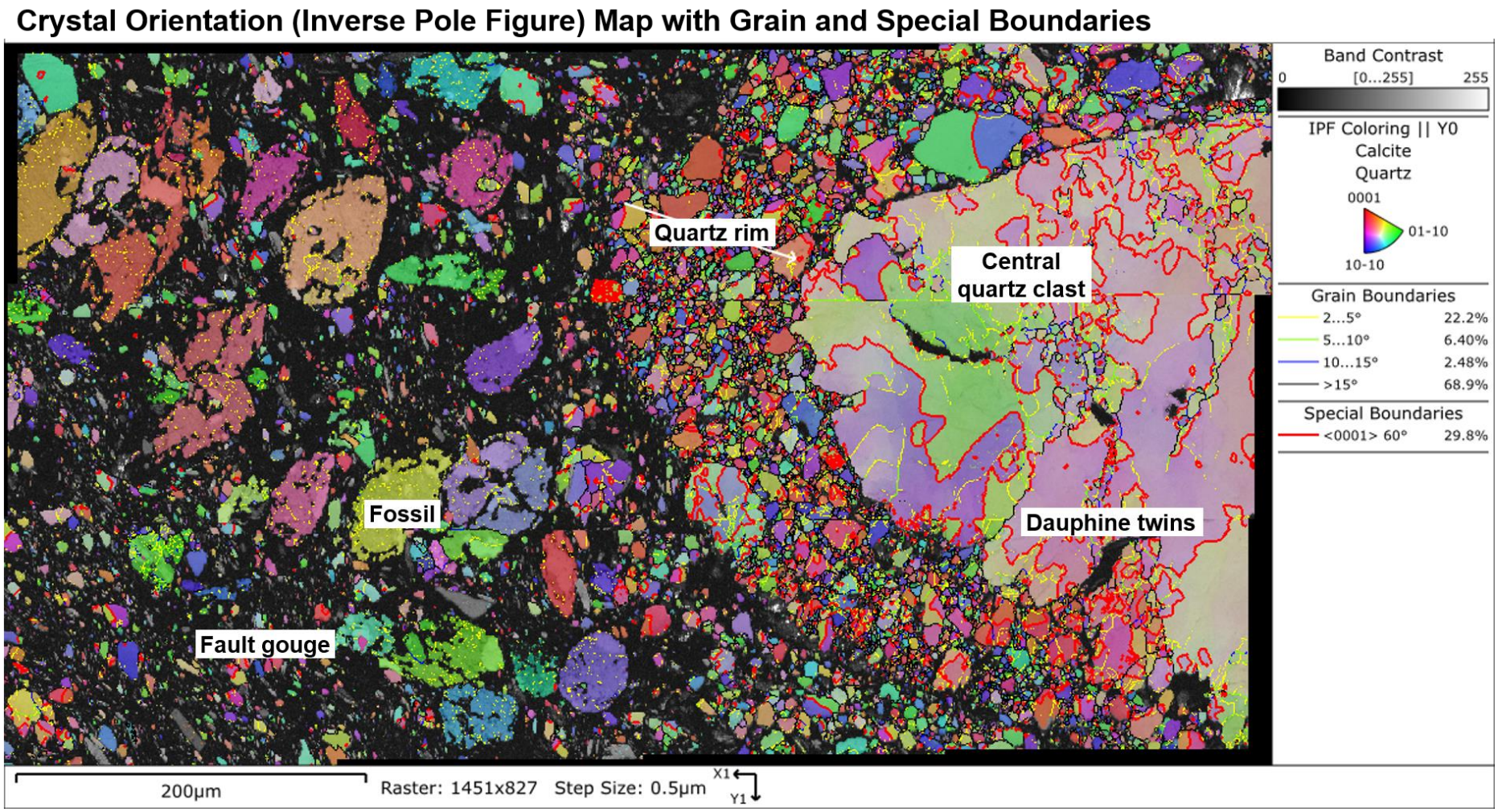

Figure 5.23: EBSD crystal orientation map (Y axis) using inverse pole figure (IPF) colouring in region 1 of sample CFIA27. Grain boundaries are marked according to the degree of crystal misorientation including special boundaries, for Dauphiné twin boundaries, that form in quartz by a 60° rotation around the c axis.

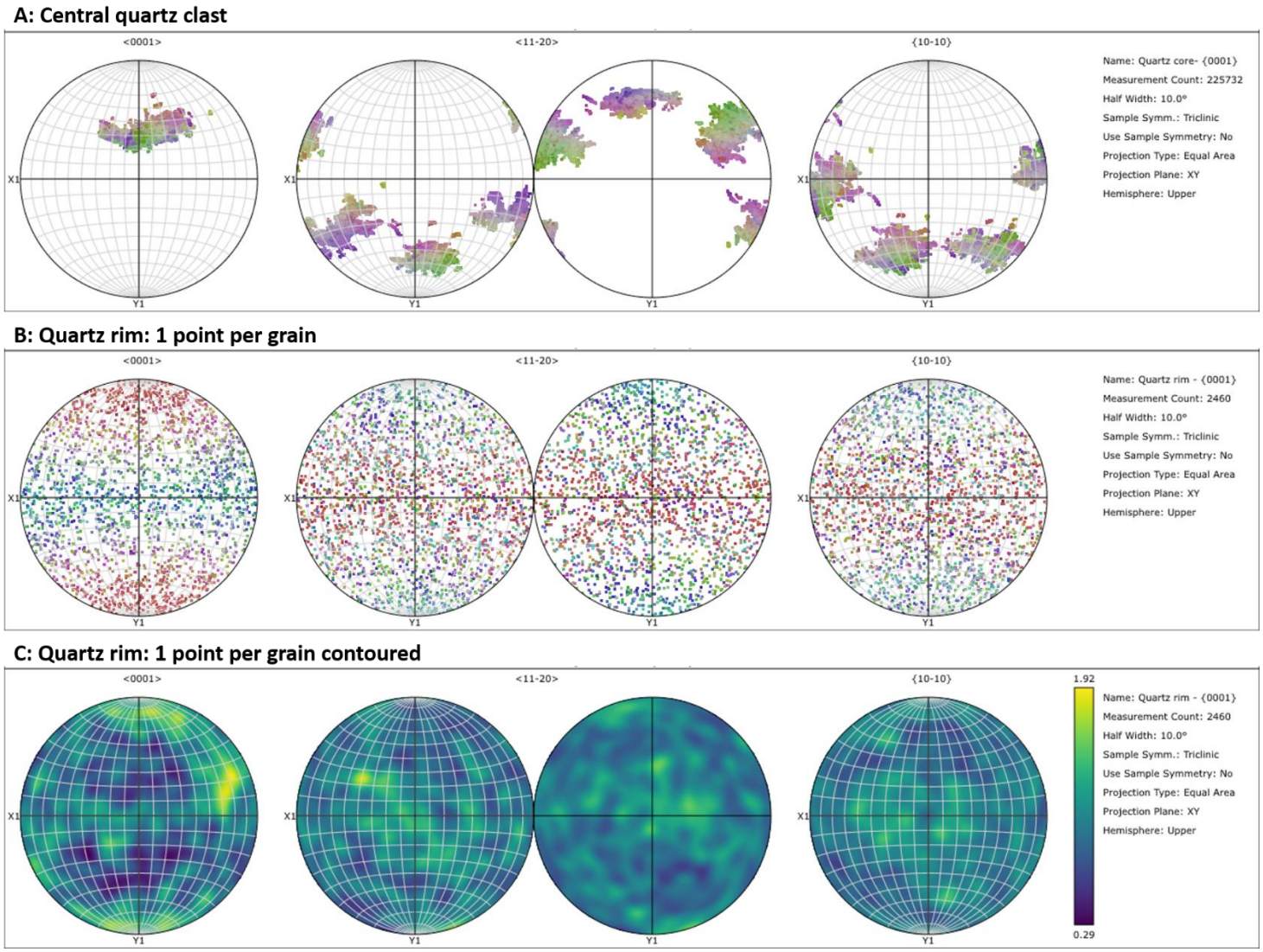

Figure 5.24: EBSD pole figures for the (A) central quartz clast and the (B and C) quartz clast rim in region 1 of sample CFIA27. The quartz rim contains data for 1 point per grain, to reduce the skew of data towards larger clast orientations over smaller clast orientations.

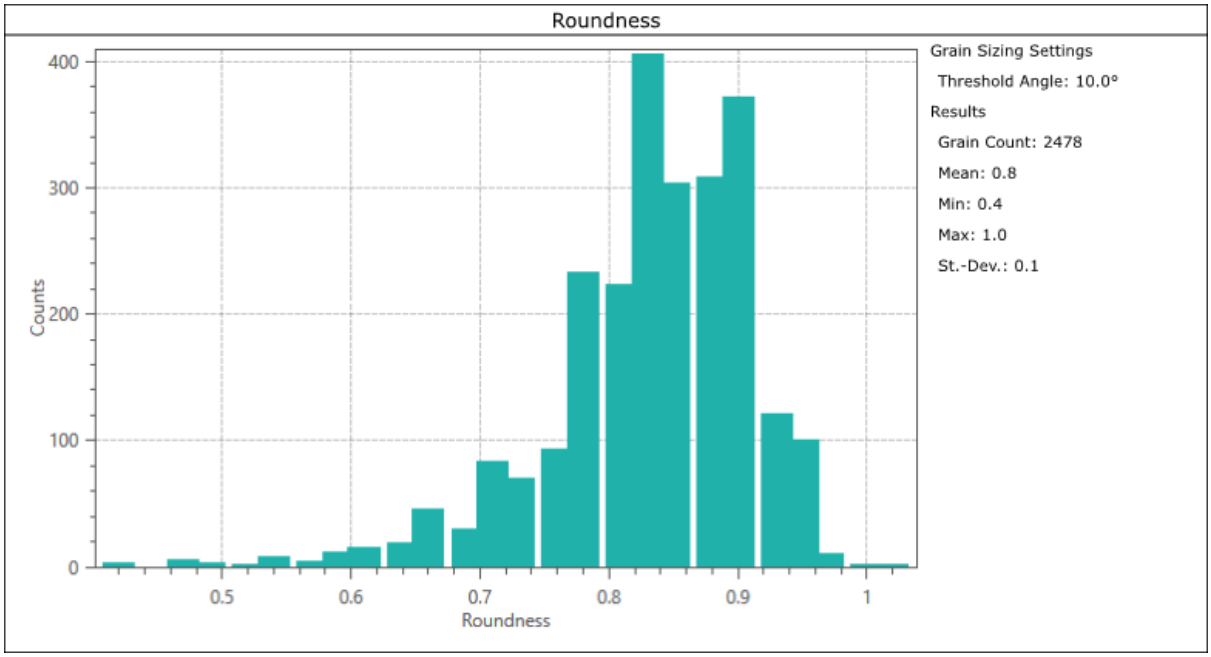

Figure 5.25: EBSD-obtained roundness graph of the quartz clasts in the rim of the potential PQC in region 1 of sample CFIA27.

Dolomite (Alpujarride):

In the field, the dolomite fault planes clearly showed reflective 'mirror' surfaces, but quantification of surface roughness was not possible at this scale of observation. Hence, the 'mirror' dolomite fault surfaces that were sampled in the Rambla del Cajon were studied using a Keyence VHX Digital Microscope. The digital microscope was used to capture high-zoom optical images, optical shadow effect images and surface roughness measurements of the fault planes (Figure 5.26). To obtain surface roughness measurements, transects were measured both parallel and perpendicular to the slickenlines on the fault surfaces (Figure 5.27). The Keyence software applied a correction to account for any tilt of the sample surface. Surface roughness is a scale-dependent parameter, so the measurements reported here were obtained at the same scale of view (200x magnification). In addition, the sample that contained a cemented fault plane (CFIA11) was cut at an orientation perpendicular to the fault plane to study the structure of the fault and associated damage zone.

The dolomite fault planes overprinted the earlier brecciation and cementation – clasts of relatively intact dolomite ranged in size from 50 µm to 500 µm and were set within a yellow-orange carbonate cement (Figure 5.26). These dolomite clasts were crystalline, rounded to sub-angular, randomly oriented and contained intragranular fractures. All of the fault surfaces showed evidence of iron-oxide mineralisation that infilled the pore spaces, including in fractures (Figure 5.26A). The more weathered fault surface of CFIA18 had a saccharine texture and higher porosity, whereas the fault plane surfaces of CFIA26 and 33 appeared more crystalline and polished. Individual slickenlines could be traced for several centimetres across multiple dolomite clasts and the sample fault surface, such as in Figure 5.27, but the slickenlines and reflective 'mirror' surfaces were clearest on the intact dolomite clasts.

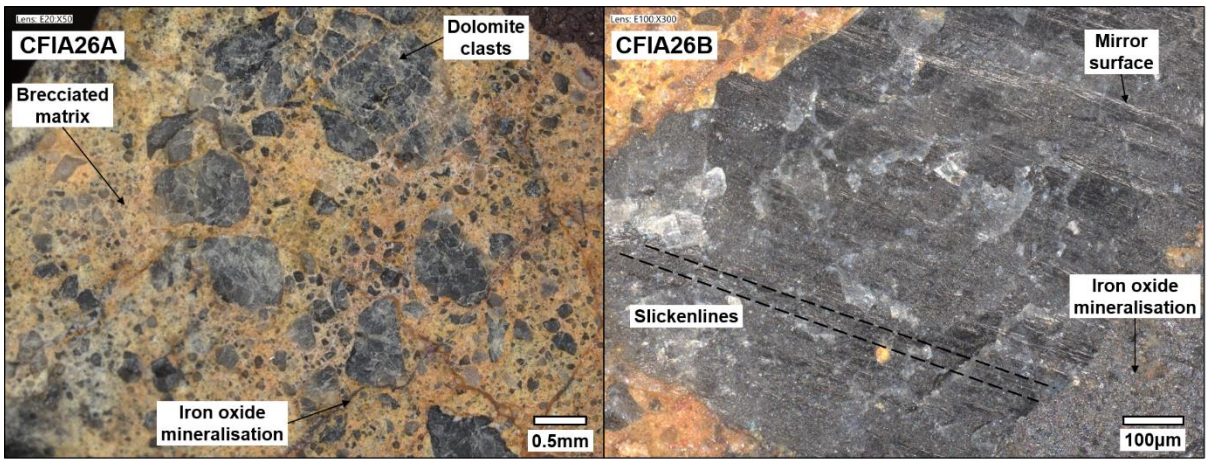

Figure 5.26: Zoom microscope optical images of dolomite fault plane surfaces from sample CFIA26 at 20x zoom (A) and 160x zoom (B).

Surface topography and roughness measurements showed that the greatest changes in fault surface topography occurred at clast boundaries, fractures and sites of iron oxide mineralisation (Figure 5.27). Amplitudes of the slickenlines, as measured through perpendicular topographic profiles, ranged between 2 µm and 9 µm. The arithmetic mean roughness *Ra* is the average surface roughness over a measured length and is calculated by:

$$Ra = \frac{1}{L}\int_0^L |z(x)|dx) \qquad \text{Eq. 5.1}$$

Where *L* is sample length, *z* is absolute height and *x* is a coordinate along the sample profile. For the profiles measured perpendicular to and parallel to slickenlines, the *Ra* values were 3.03 µm and 2.65 µm, respectively.

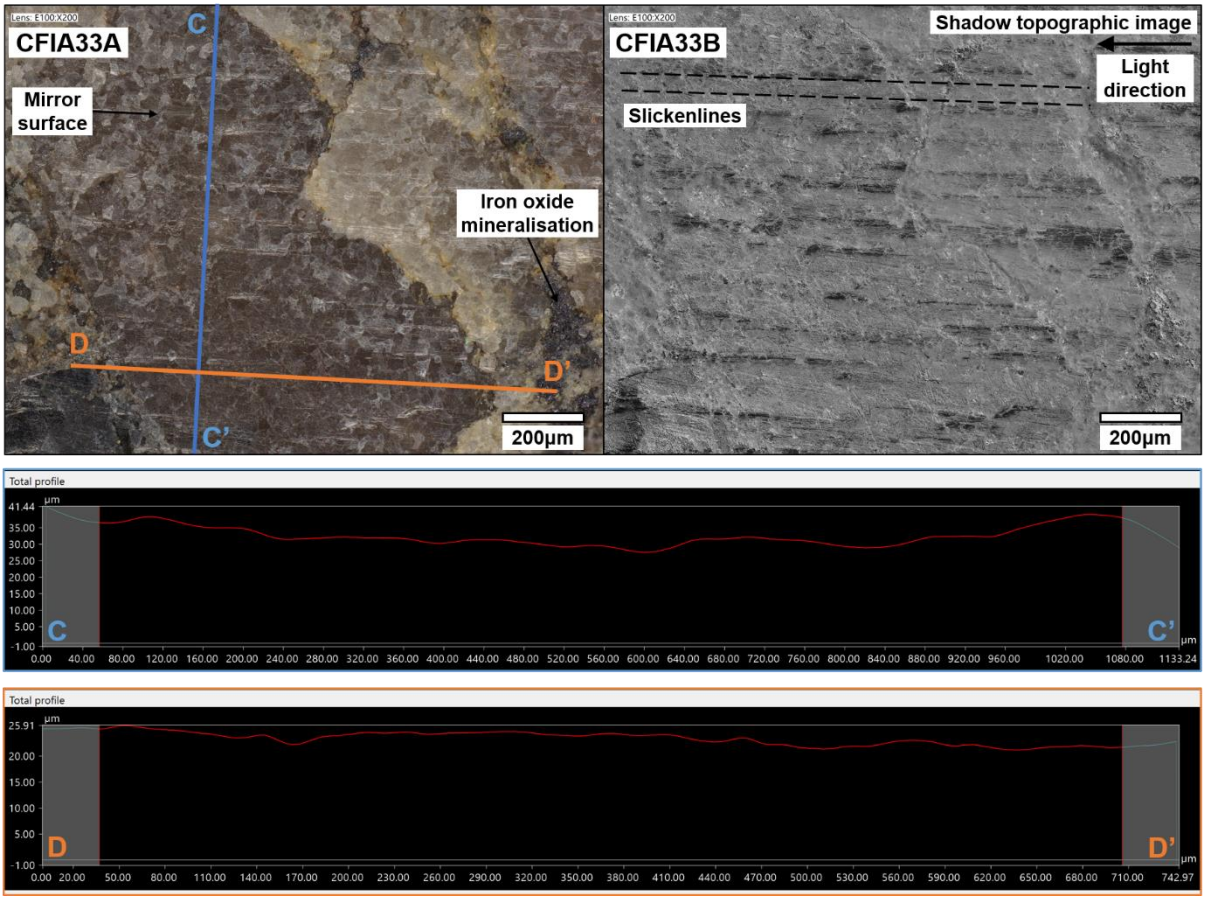

Figure 5.27: Zoom microscope optical image (A) of sample CFIA33 dolomite fault surface at 200x zoom; an optical shadow effect image (B) that highlights the surface topography of the fault plane at 100x zoom; measured topographic profiles perpendicular to slickenline orientation (C) and parallel to slickenline direction (D) – the y-axes of the profiles are exaggerated by 3.4x the scale of the horizontal axes.

Sample CFIA11 contained a subsidiary dolomite-dolomite fault (093/53 N) collected from Locality 3 (Figure 5.8). The fault plane was cemented by iron oxide mineralisation, which is confirmed by the elevated Fe_2O_3 compared to the dolomite in sample CFIA18 (see XRF measurements in Table 5.4). The cross-sectional view of CFIA11 revealed striking bands of

colour in a narrow (1.5 cm to 4 cm wide) damage zone on either side of the fault plane (Figure 5.28). An inner yellow band of up to 1 cm in width occurred in contact with the fault plane, which contained dolomite clasts that were predominantly < 1 mm in diameter. Several dolomite clasts were truncated by the fault plane and the offset of the fault must be greater than the scale of the sample (20 cm), as the clasts could not be correlated across the fault (Figure 5.28). An outer band of pink-coloured material of up to 2.5 cm in width contained a greater range of clast sizes, with a maximum clast size of 1.5 cm. At the margins of the sample, the dolomite was pervasively fractured with intergranular fractures up to 3 cm in length (Figure 5.28). The highly angular dolomite clasts and pervasive fracturing mean that the dolomite 2-4 cm from the fault plane would be classed as a clast-supported breccia (Table 5.1).

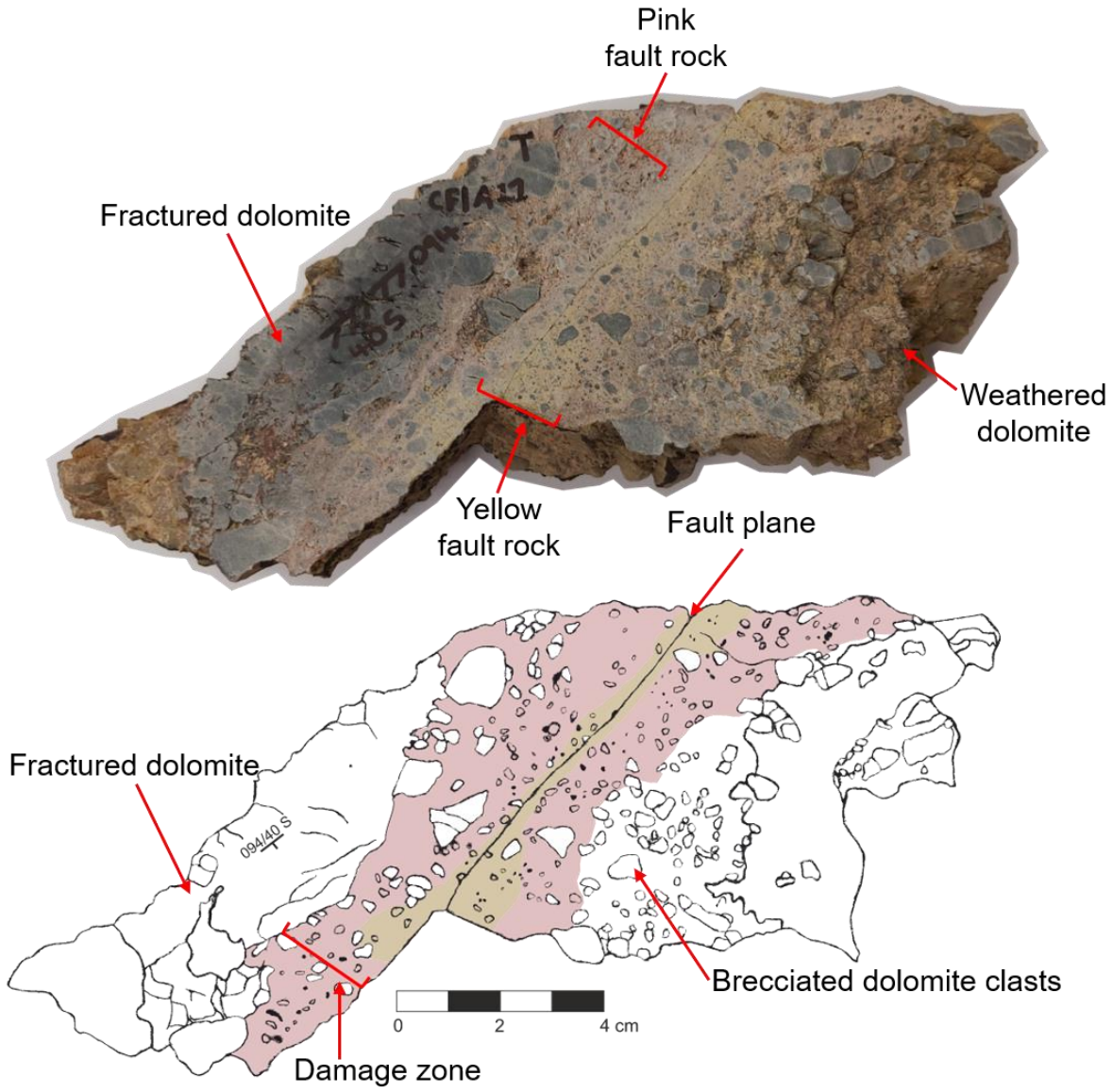

Figure 5.28: Photo and accompanying sketch of a cross sectional view of CFIA11, showing a cemented fault plane and the associated damage zone in the dolomite lithology.

5.4.4. *Frictional experiments:*

In the friction experiments, 2.5 g of the crushed fault materials were placed in a direct shear slider assembly to produce a 1 mm thick layer after an initial compaction load of 50MPa. The samples were hydrostatically loaded to 100 MPa confining pressure and 40 MPa pore fluid pressure (60 MPa effective pressure) to simulate conditions at 4 km depth, which is in line with depth estimates for the current CFZ exposures in the late Miocene (Faulkner et al., 2003; Rutter et al., 2012, 2014). Velocity step experiments were used to test the frictional properties of the fault samples in order to retrieve the material RSF parameters (*a*, *b*, and D_C). An initial run-in phase at an imposed 0.3 µm/s displacement rate ran for 3 mm of displacement to guarantee that all samples had undergone frictional yield. After the run-in phase, the imposed displacement rate was stepped between 3.0 µm/s and 0.3 µm/s for a total of 9 velocity steps. Each velocity step ran for a displacement of 0.5 mm to ensure that a new steady state frictional strength had been established – a necessary condition of RSF data processing.

Out of the 6 materials that were tested, the two dolomite samples had the highest frictional strengths (Figure 5.29). CFIA11 and 18 had Byerlee frictional strengths at the initial velocity step of 0.65, which evolved to ~0.7 with increasing strain (Byerlee, 1978). There was a significant strength contrast between the dolomite samples and the fault gouge samples – all of the fault gouges displayed similar frictional strengths of ~0.4, regardless of the parent lithologies. The mica schist sample CFIA42 had a smaller strength contrast to the fault gouges than the dolomite, as it displayed an initial strength at the onset of the velocity step phase of 0.55 that evolved via a strain weakening trend to 0.5 at the maximum displacement.

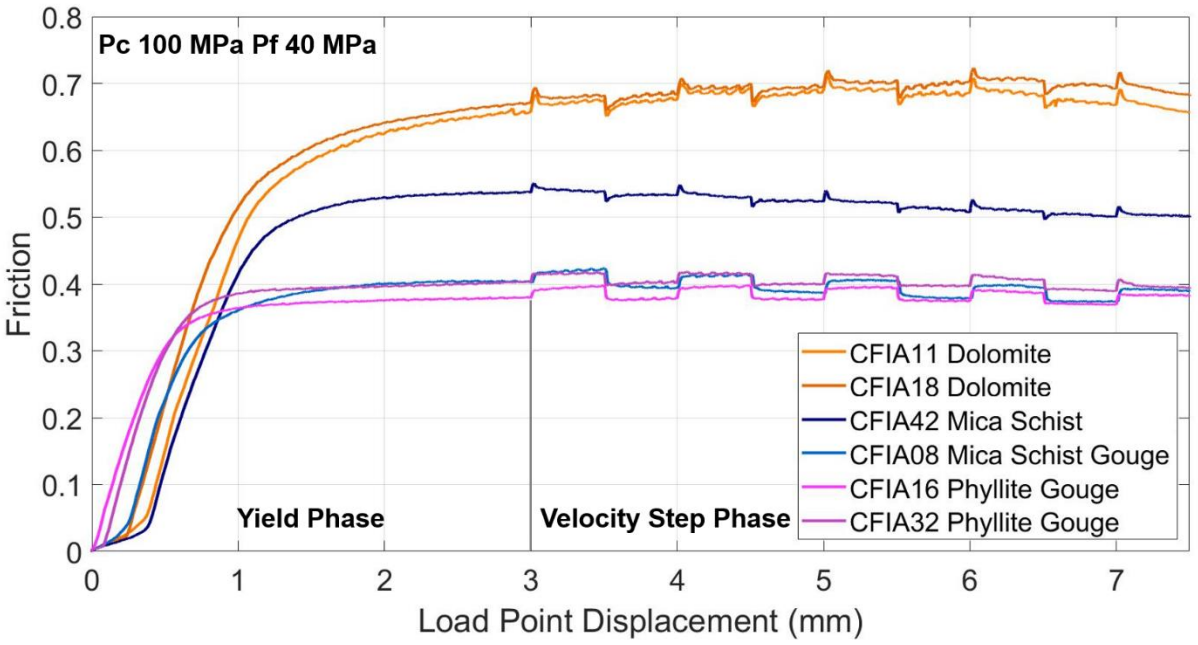

Figure 5.29: Friction curves from the velocity step triaxial deformation experiments on gouge and rock samples from the CFZ.

All of the tested fault materials were velocity strengthening with positive RSF (*a-b*) parameters (Figure 5.30), as calculated from 10x slip velocity step changes using both the aging (Ruina, 1983) and slip law (Dieterich, 1979). The fault gouges returned the most velocity strengthening (*a-b*) parameters, whereas the least velocity strengthening material was the intact mica schist. The tests for the field study were conducted at room temperature (20-23°C) due to time constraints – it is recommended that further experiments on such samples be conducted at temperatures typical to depths of 4 km (~100°C).

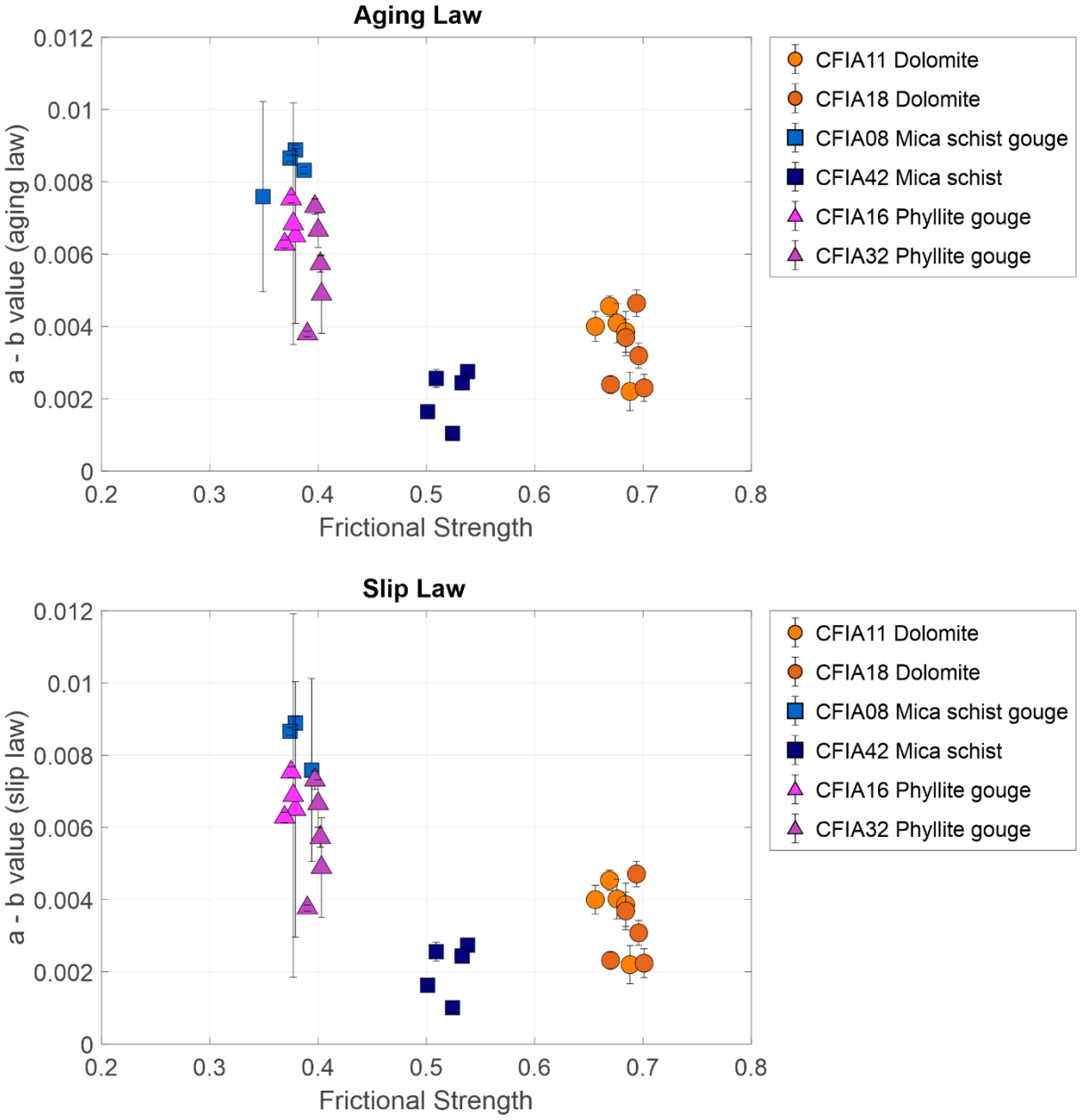

Figure 5.30: RSF parameter (a-b) calculated using both the aging and slip laws from a 10x velocity-step increase against the frictional strength of the tested CFZ fault rocks.

5.5 Discussion:

How do fault zones transfer strain between brittle-localising and non-localising material?

Prior to the September 2021 field season, the aim of the field work was to test the microstructural and chemical changes in the fault gouges with distance from the dolomite faults. This approach assumed that the dolomite-dolomite faults accommodated strain that would be transferred to the adjacent fault gouges (Figure 5.31). The dolomite fault blocks appeared to 'float' in the CFZ fault gouge strands, with the striated 'mirror' fault planes aligned in the orientation of R_1 riedel shears to the overall trend of the CFZ. Subsidiary dolomite-dolomite faults were also closely aligned to the R_2, X and P riedel shear orientations (Figure 5.32). This stage of faulting clearly overprints the background low strain deformation (Igbokwe et al., 2020). The frictional results of this study revealed a large strength contrast of 0.3-0.35 between the dolomite and all of the fault gouges (Figure 5.29).

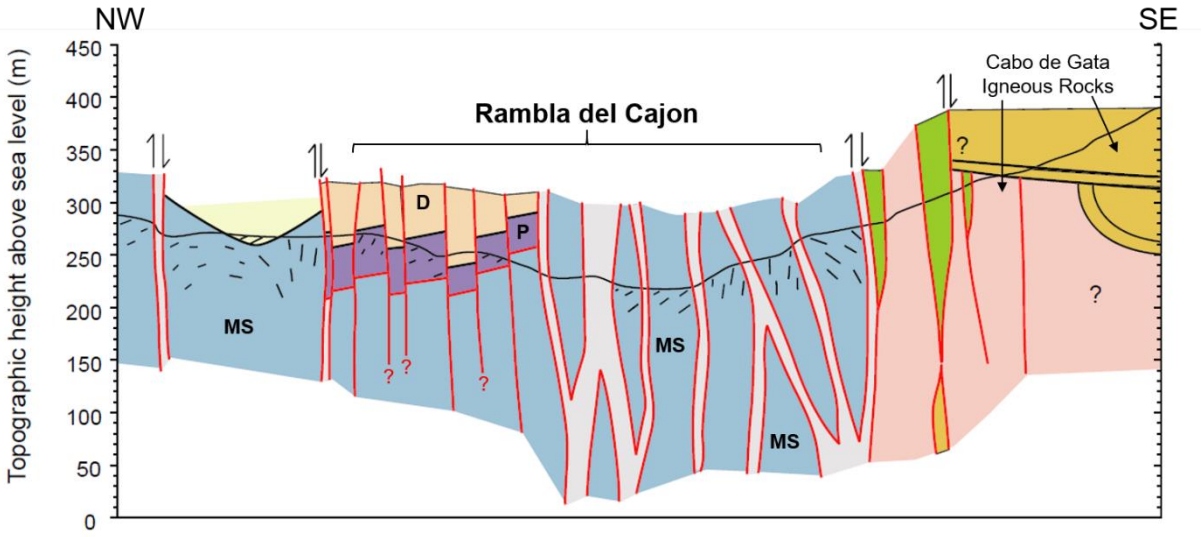

Figure 5.31: Schematic cross section across the Rambla del Cajon (modified after Faulkner et al., 2003). Key rock types: MS – mica schist (blue), P – phyllite (purple) and D – dolomite (orange).

Sample CFIA11, with its cemented fault plane, gave an example of a cross section through a dolomite-dolomite fault and the associated damage zone. The brightly coloured bands of fault breccia in the damage zones on either side of the cemented fault plane suggested that fault-related alteration had taken place. The XRD chemical analysis of the dolomite fault samples CFIA11 and 18 did not reveal any mineralogical differences between the two samples. In contrast, the XRF analysis was able to measure the subtle changes to the chemistry of CFIA11 compared to CFIA18 – Fe_2O_3 and MnO, from the fault plane mineralisation, and Al_2O_3 and SiO_2 were enriched in CFIA11. This strongly suggests that pore fluids were percolating through fault and fracture networks in the dolomite lithons. The scale of this damage zone, at 4-5 cm width, indicated that the offset on this dolomite-dolomite fault is on the scale of ~10-20

cm as a minimum estimate (Mayolle et al., 2019). This strengthened the interpretation of the dolomite-dolomite faults as being subsidiary faults (R_2, X, or P riedel shears) to the dolomite-gouge, NNE-SSW trending (R_1 shear) faults. The XRD chemical analysis was conducted as a bulk rock analysis of crushed rock chips from CFIA11 and 18, which may have masked more subtle changes in chemistry. Further analysis of these samples could include SEM chemical mapping using EDS in a transect across the cemented fault plane in CFIA11. Sample blocks of CFIA11 were prepared for this purpose, but time and budget constraints meant that this analysis has not yet been conducted.

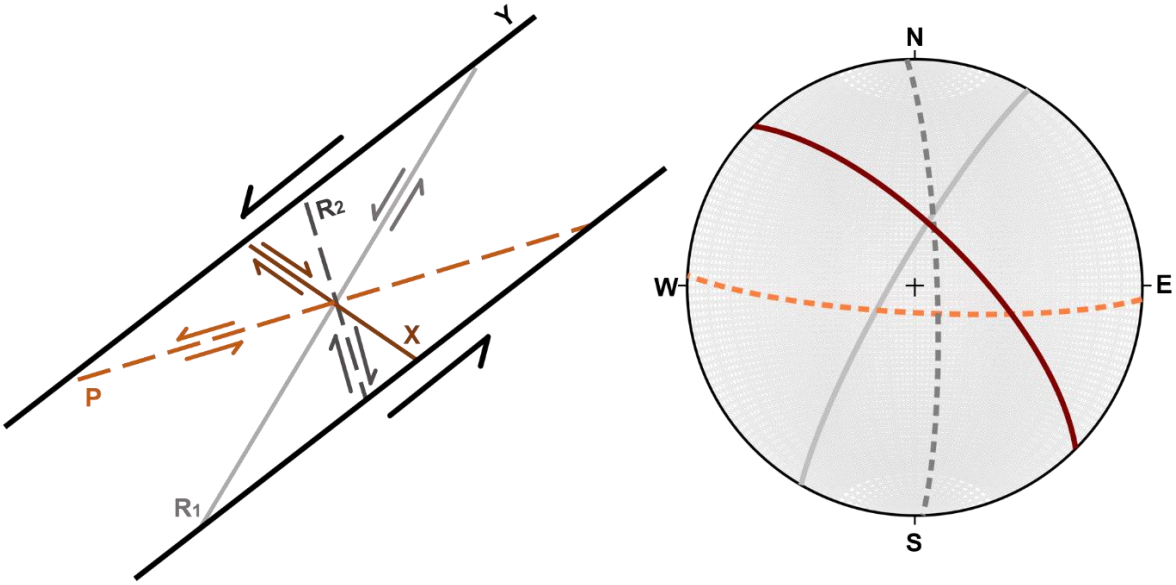

Figure 5.32: A schematic diagram of the orientation of Riedel shears in the CFZ with a stereonet of the measured fault plane orientations in the dolomite, coloured according to the shear type.

The complexity and heterogeneity of the fault gouge samples at the microstructural scale was underestimated during the field work phase – the heterogeneity of the fault gouge samples overprinted the potential influence of the proximity to the dolomite faults. Several spatial relationships were tested, such as the proportion of gouge to relict lithic fragments in a sample, but no significant trends were identified. Samples CFIA27 and 30 were collected in direct contact with the dolomite fault surfaces and were formed almost entirely of fault gouge (70-90%). In contrast, CFIA23 and 24, also located in contact with dolomite faults, were formed of brecciated lithic clasts with a lower proportion of fault gouge (20-40%). Iron oxide mineralisation on the dolomite fault planes suggested that the fault and fracture networks had hosted hydrothermal fluids, so the spatial variation in Fe with respect to the dolomite fault planes was tested. No link was found between the iron content (XRF measured Fe_2O_3 and EDS measured Fe) of the fault gouges and the distance from the fault plane – Fe proportions ranged between 2-8 mass % across all of the measured phyllite-derived fault gouges. It was not possible, therefore, to resolve the transfer of strain between the localising and non-

localising materials in the CFZ, although the deformation of both types of material were described using detailed microstructural and chemical analyses.

Is there evidence of seismicity from the fault rocks in the CFZ?

Potential evidence of seismicity was identified in this study – fault mirror surfaces on the dolomite fault planes (Fondriest et al., 2013; R. Han et al., 2010; Siman-Tov et al., 2013) and pulverisation of quartz clasts from seismic shock (Mitchell et al., 2011; Rodríguez-Escudero et al., 2020). Fault mirrors are used as evidence of slip at seismic velocities based on the dynamic weakening that has been observed with seismic slip rates (>0.1 m/s) on carbonate fault materials (R. Han et al., 2010; Siman-Tov et al., 2013, 2015; S. A. F. Smith et al., 2013; Tisato et al., 2012). Drastic dynamic fault weakening is thought to occur via thermal decomposition of the carbonate material (R. Han et al., 2007; S. A. F. Smith et al., 2013) or via powder lubrication following the formation of a carbonate nanoparticle (<1 μm) layer on the fault surface (R. Han et al., 2011; Tisato et al., 2012). Some experiments conducted at sub-seismic slip rates (0.1-10 μm/s) have also shown the formation of fault mirror surfaces in carbonate fault materials (Verberne et al., 2014, 2019), which calls into question the validity of fault mirrors as seismic slip indicators.

The fault mirror surfaces in this study were observed on the dolomite-gouge faulted contacts, but the possibility of the gouge polishing the dolomite surface is impeded by the significant strength contrast between the two materials. A more plausible scenario for the formation of the fault mirrors would be their formation in an early phase of faulting within the dolomites in the CFZ. Attempts were made in this study to quantify the roughness of apparent fault mirror surfaces in the Alpujarride dolomite. Siman-Tov et al. (2013) used a quantitative classification threshold for fault mirrors of:

$$A < \frac{\lambda}{16 \cos \theta} \qquad \text{Eq. 5.1}$$

Where A is the mean roughness amplitude, θ is the angle of incident light and λ is the light wavelength (Siman-Tov et al., 2013). If a surface is observed at $0° < \theta < 70°$ under visible light (λ = 550 nm) and appears glossy at lateral scales < 550 nm then A < 100nm and it is classed as a fault mirror (Siman-Tov et al., 2013). The average roughness values parallel to the slickenline directions on the glossy dolomite fault surfaces (2.65 μm) were measured at lateral scales of 1000 μm, rather than at the nanometre-scale. While the dolomite fault surfaces are here termed as 'fault mirrors', further assessment using an SEM would be required to test the dolomite samples according to the classification of Siman-Tov et al. (2013). It is not possible to interpret the presence of fault mirrors in the dolomites as evidence of seismic slip due to the disagreement on the conditions for the formation of fault mirrors at either seismic slip rates

(R. Han et al., 2010; Siman-Tov et al., 2013, 2015; S. A. F. Smith et al., 2013) or at sub-seismic slip rates (Verberne et al., 2014, 2019) in the scientific literature.

Pulverised quartz clasts (PQC) in the CFZ fault gouges had previously been identified from field observations (Faulkner et al., 2003; Rutter et al., 2012, 2014) and have also been recorded in Nevado-Filabride mica schist-derived gouges from the Alhama de Murcia (AdM) fault (Rodríguez-Escudero et al., 2020). The AdM fault is another left-lateral strike-slip fault in the EBSZ, north of the CFZ and Palomares fault, that accommodates the relative plate motion on the Iberian-African margin (Masana et al., 2004; Ortuño et al., 2012). Rodríguez-Escudero et al. (2020) did not conduct microstructural investigations beyond the FracPaQ analysis of fracture orientations in the PQC rim, yet the authors attributed the formation of the PQC to seismic activity. Unlike the CFZ, the AdM fault is known to host seismic slip, as shown by the May 2011 M_w 5.1 earthquake that caused significant damage to the town of Lorca (Masana et al., 2004; Ortuño et al., 2012). PQC form due to local stresses that are anomalously high in the quartz clasts so that the sudden release of confining pressure due to the propagation of seismic waves causes rapid expansion and pulverisation. Rodríguez-Escudero et al. (2010) observed sigma-type geometry of PQC rim clasts, which migrated to pressure shadows by frictional sliding around the edge of the central quartz clast (Figure 5.33).

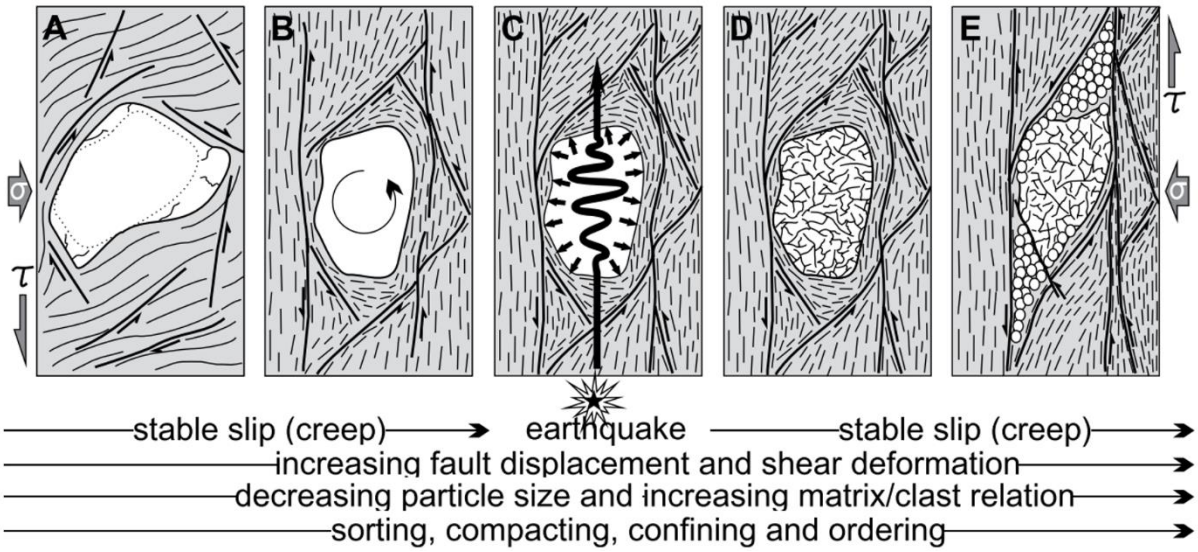

Figure 5.33: The schematic model for the formation of pulverised quartz clasts (PQC) from seismic shock (Rodríguez-Escudero et al., 2020): (A) incorporation of relict lithic clasts into fault gouge; (B) competent quartz clasts remain isolated in progressively fragmented and comminuted fault gouge; (C) local stresses are anomalously high in the quartz clasts so that the sudden release of confining pressure due to the propagation of seismic waves causes rapid expansion and pulverisation; (D) particles from clast edges start to migrate to pressure shadows by frictional sliding; (E) resulting sigma-type geometry of PQC.

In this study, fracture analysis alone was not considered adequate evidence for seismic slip on the CFZ, so the investigation of PQC was taken further by conducting EBSD experiments

on the PQC in CFIA27. Two surprising outcomes came from these experiments: (1) there was no orientation relationship between the central and rim quartz clasts; and (2) the central quartz clast contained pervasive dauphiné twinning. The conceptual model for PQC is that they form without shear strain so the rim quartz clasts would be expected to bear orientations similar to the central quartz clast (in fact there would be no core or rim). The random orientations of the rim quartz clasts may have resulted from high rotations associated with shear strain and the migration of the rim quartz clasts through frictional sliding towards pressure shadows at the margins of the PQC (Figure 5.33E). This sigmoidal clast geometry is absent in CFIA27, however, which would be expected in an overprint with fault creep processes. The possibility that the central quartz clast was simply embedded within a quartz-rich gouge region was considered, but this appeared unlikely. The EBSD and EDS analysis showed that the grain sizes in the quartz rim were comparable to the quartz clasts in the gouge and the high roundness (average 0.8) of the quartz rim grains suggest that a later shear strain phase has affected the PQC. It is possible that the orientation of the thin section of CFIA27 does not capture the full geometry of the PQC and that a different orientation would reveal a sigma-type geometry as in Figure 5.33.

Dauphiné twinning is a 60° rotation around the c-axis in quartz crystals that reverses the positive and negative crystal rhombs (Menegon et al., 2011; Wenk et al., 2006, 2007, 2011). At room temperatures, Dauphiné twinning initiates at 500 MPa differential stress, but the twinning mechanism has been found to be temperature sensitive – at 500°C Dauphiné twinning commences at 50-200 MPa differential stress (Wenk et al., 2006, 2007, 2011). Dauphiné twins are often used as evidence of a temperature transition between alpha (*α*) and beta (*β*) quartz at ~570°C, but there is evidence linking the formation of Dauphiné twins to seismic shock. The compressive strength of quartz is 1-1.5 GPa, whilst the tensile and shear strength are orders of magnitude lower at 30-50 MPa (Griggs et al., 1960; Kimberley et al., 2010). Local stresses in rigid quartz grains within a gouge matrix can far exceed the average applied stresses. Brecciated and fragmented quartz clasts must have experienced local stresses greater than the strength of quartz to cause failure, which is also sufficient to initiate Dauphiné twinning (Wenk et al., 2011).

Dauphiné twins were observed in pseudotachylyte-related quartz grains from mylonitic material in Santa Rosa, California, although this texture was absent in the local viscously deformed metamorphic rocks (Wenk et al., 2011). In drilled cores from SAFOD that crossed the principal slip zone, fragmented and Dauphiné twinned quartz clasts were also observed (Wenk et al., 2011). The close association of Dauphiné twinned quartz with pseudotachylyte, widely considered as the most reliable evidence of seismic slip (Di Toro et al., 2011), is highly suggestive that seismic stress led to the formation of the Dauphiné twins. Dauphiné twinning

has also been observed in quartz clasts from cores of granodiorite ~50 m from the Nojima fault in Japan, which hosted the 1995 Kobe Mw 7.2 earthquake (Boullier et al., 2018).

Though the presence of Dauphiné twinning in PQC in the CFZ gouges is compelling, further research is needed to confirm whether seismic slip occurred on the CFZ. The parent material of greenschist grade (300-400°C) Alpujarride phyllites and amphibolite grade (500-700°C) Nevado-Filabride mica schists would need to be analysed to confirm the presence or absence of Dauphiné twinning in quartz. Further microstructural analyses of PQCs in the CFZ would include: EBSD analysis of PQC in sample CFIA31 and CFIA27; and thin sectioning of sample CFIA27 orthogonal to the shear plane and parallel to the shear direction perpendicular in the gouge strand (as opposed to the dolomite fault plane) in Figure 5.23 to test for possible migration of PQC rim quartz clasts to pressure shadows.

What was the effect of chemical alteration due to hydrothermal activity on the CFZ?

The lack of biotite detected in the chemical analyses of this study was unexpected, as field descriptions of the Nevado-Filabride mica schists identified biotite as a major component of the rock type (Faulkner et al., 2003; Rutter et al., 2012, 2014). In addition, the prevalence of the Na-rich mica paragonite in the phyllite-derived fault gouges was not expected as paragonite is usually associated with blueschist grade (200-500°C and >0.6 GPa) metamorphism.

The microscopic analysis revealed that both the mica schist and phyllite material contained significant proportions of chlorite, with examples of chlorite and biotite coexisting in mineral assemblages. Chloritization occurs at temperatures up to 400°C and the composition of the resulting chlorite is affected by the in-situ pressure and temperature conditions, as well as the bulk rock and hydrothermal fluid conditions (Eggleton & Banfield, 1985; Jiménez-Millán et al., 2015; Yuguchi et al., 2015). The process of chloritization of biotite involves either:

- The influx of metallic ions (Al^{3+}, Fe^{2+}, Mn^{2+} and Mg^{2+}) from the hydrothermal fluid into the octahedral sheet of biotite, which causes an associated small volume decrease (6-20 %) from the original biotite (Eggleton & Banfield, 1985; Yuguchi et al., 2015);
- Or the replacement of the interlayer (K^{+} or Na^{+}) ions with a brucite-type layer that causes an outflow of metallic ions into the hydrothermal fluid and a large (27-63 %) volume decrease (Fiebig & Hoefs, 2002; Xiao et al., 2020; Yuguchi et al., 2015).

Chlorite alteration can be accompanied by breakdown products including titanite, Ti-oxide, epidote and dolomite (Eggleton & Banfield, 1985; Xiao et al., 2020; Yuguchi et al., 2015). The chlorite alteration that is widespread in the fault samples is evidence of a hydrothermal system that was active in the CFZ. Later overprinting stages of mineralisation included the

precipitation of iron-rich minerals (hematite and goethite) along fracture and fault networks in all of the rock types investigated, and quartz and dolomite vein material that had been fragmented and incorporated into the CFZ fault gouges. The timing of this hydrothermal mineralisation must have initiated prior to the majority of movement on the CFZ as the lithic clasts were altered to include chlorite, iron oxide minerals and vein deposits prior to their incorporation in the fault gouges. The field observations in the Rambla del Cajon categorised the mica schists as low strain protolith material, but the lack of biotite and prevalence of chlorite calls into question how much resemblance this low strain material has to the true protolith.

Evidence of widespread mineralisation has been recorded in the region surrounding the CFZ, including at the Palai-Islica hydrothermal deposit near Carboneras and the Rambla de la Granatilla near Sopalmo (García-Romero et al., 2006; Jiménez-Millán et al., 2015; Ruano et al., 2000). The Palai-Islica gold-bearing hydrothermal deposit is hosted within the Cabo de Gata volcanic group. While Palai-Islica is not located directly on the CFZ, it does contain evidence of widespread chloritization at temperatures of 120°C to 400°C (Ruano et al., 2000). Similarly, a study on the palygorksite fault seals in the CFZ south of the field site in this study indicated a hydrothermal origin for the palygorskite, which is stable at temperatures of <220°C to 275°C (García-Romero et al., 2006).

Jiménez-Millan et al (2015) studied the effect of the hydrothermal system along the CFZ on the phyllosilicate assemblages in the fault gouges – significant increases in the amounts of Mg, Fe, H_2O, Zn and As in the fault rocks were attributed to the hydrothermal alteration of quartz-rich rocks by base-metal fluids related to volcanic activity. Mg-rich chlorite in the CFZ fault gouges is indicative of a mixed origin of hydrothermal fluids, of both volcanic and meteoric origin (Jiménez-Millán et al., 2015). The eruption of the Cabo de Gata volcanic group commenced at 18.5 Ma, with an associated phase of hydrothermal alteration of the basement lithologies at temperatures of ~100-400°C, prior to the inferred initiation of movement on the CFZ at 12.5 Ma (Duggen et al., 2004; Mattei et al., 2014; Pedrera et al., 2010; Rutter et al., 2014; Zeck et al., 1998). Phyllosilicate alteration products are weaker than the intact parent silicate minerals, therefore sites of extensive hydrothermal alteration would contain mechanically weak, but stable velocity strengthening material. Hence, it is possible that the hydrothermal alteration of the basement lithologies prior to initiation of strike slip faulting contributed to the formation of the fault structure of the CFZ (Jiménez-Millán et al., 2015).

What are the implications for the slip modes in the CFZ?

Faulkner et al. (2003, 2008) proposed a model to explain the unusual structure and the potential fault slip modes of the CFZ. In this model, the fault gouge strands in the CFZ underwent strain hardening, and geometric irregularities lead to frictional lock-up of the fault

strands. Thus, the formation of new fault strands was energetically favourable over continued slip in established fault gouge strands. Lenses of relatively intact basement rock were incorporated into the fault gouge strands by the formation of new, overprinting fault strands. This model requires that the fault gouges and host rocks have similar mechanical strengths. The fault gouges were found to have a large frictional strength contrast with the dolomites in this study, but the contrast between the fault gouges and the mica schist was far lower (0.1-0.15). The mica schist parent material, when subjected to velocity-step tests, showed a strain weakening trend and the lowest RSF (*a*-*b*) values of any tested material. This presents the possibility that, upon fault strand initiation, the mica schist lithology would have been the most likely to host seismic slip. With ongoing slip, the development of fault gouge through grain size reduction and mineral alterations changed the mechanical properties of the mica schist material to be frictionally weak and strongly velocity strengthening. As all of the experiments were conducted on crushed powders, this difference in strength between the mica schist and gouge fault material was a mineralogically controlled, not a texturally controlled, difference. Pre-existing fabrics with a strong anisotropy, such as the schistosity in the phyllites and mica schists, can significantly weaken a lithology's mechanical strength. The fault gouges velocity strengthening responses in the velocity step experiments confirm the expected strain hardening behaviour necessary in the Faulkner et al. (2003) CFZ formation model. The lower strength contrast between the strain hardening fault gouge strands and the mica schist favours fault strand initiation in the mica-schist basement lithology.

It is difficult to combine the interpretations of the geological and geophysical data from the CFZ into one cohesive slip model because the literature sources have drawn opposing conclusions. Geological evidence, including the mineralogy of the fault rocks and the fault zone structure, point to aseismic slip as the dominant slip behaviour on the CFZ (Faulkner et al., 2003; Rutter et al., 2012, 2014). Various geophysical techniques have been applied to the CFZ to investigate the potential for seismic slip, including seismic profiling (Gràcia et al., 2006), ground penetrating radar (Reicherter & Reiss, 2001) and geodesy mapping (Echeverria et al., 2015). The only historical seismicity that has been loosely ascribed to slip on the CFZ was the 1522 Almeria M_w 5 earthquake (Echeverria et al., 2015; García-Mayordomo et al., 2012; Gràcia et al., 2006; Moreno, 2011). Several of these studies reference the trench wall mapping by Moreno (2011) in the CFZ that identified a record of seismic slip events from colluvial wedges dating back to 130 ka. Colluvial wedges have been shown to be poor indicators of paleoseismicity due to complex sediment transport processes including debris facies formation, erosion and sediment reworking (Gray et al., 2022). The estimate of a 70 km long surface rupture along the CFZ creating a M_w 7.2 earthquake (Gràcia et al., 2006) would carry more weight if it were supported by reliable evidence of large magnitude paleoseismicity on

the CFZ. Other fault zones that host both seismic and aseismic slip, such as the LVF in Taiwan (Den Hartog et al., 2021; Thomas, Avouac, Champenois, et al., 2014), contain both locked, unstably sliding and aseismic creeping fault segments. Earthquake nucleation on a locked, velocity weakening fault segment can propagate and rupture a normally creeping, velocity strengthening fault segment, depending on the dynamic weakening mechanisms that can be activated on the respective fault segments (Lambert et al., 2021; Lapusta et al., 2000; Noda & Lapusta, 2013; Thomas, Avouac, Champenois, et al., 2014). There is currently no confirmed evidence of seismic slip in the lithologies within the CFZ, but if the dolomite-dolomite faults did host seismic slip, as is suggested in Faulkner et al. (2003, 2008), the estimates of the magnitude of the earthquakes that would be produced are small at M_w < 4 (Wells & Coppersmith, 1994).

Throughout the samples collected from the CFZ, there was evidence that the dominant deformation mechanism was aseismic fault creep. The strongly velocity strengthening RSF (*a*-*b*) values (0.004-0.009) in the fault gouges would lead to the arrest of seismic ruptures and would preclude earthquake nucleation. Also, the field evidence of the structure of the CFZ, with the broad distribution of slip in the fault gouge strands and the 1 km wide fault core, are not indicative of seismic slip. Although the occurrence of seismic slip on the CFZ has not been confirmed in this study, the presence of PQC embedded in the fault gouges warrants further analysis to investigate the potential for intermittent seismic slip on the predominantly aseismic CFZ.

5.6 Conclusions:

Despite the wealth of data collected in this study, a comprehensive model of the deformation history of the CFZ is not yet possible. Suggestions for further avenues of study are included in Chapter 6. The conclusions of this study include:

- It was not possible to discern the transfer of strain from a brittle-localising (dolomite) to a non-localising (gouge) material, due to the heterogeneity of the fault samples;
- Fault rocks in the CFZ have undergone extensive hydrothermal alteration of biotite to chlorite;
- All of the tested fault materials were velocity strengthening at room temperature, with a large frictional strength contrast between the dolomites and the fault gouges;
- The fault gouges included pulverised quartz clasts containing Dauphiné twins that can form due to seismic shock (Boullier et al., 2018; Mitchell et al., 2011; Wenk et al., 2011);
- Deformation on the CFZ was dominated by aseismic fault creep, but it may have hosted intermittent seismic slip during its history.

6. Conclusions and Further Work

In this chapter, the main findings of the individual studies that were presented in Chapters 3, 4 and 5 are summarised. Outlines of suggestions for further research that have developed from the outcomes of this research are then discussed.

6.1 Summary of results:

In Chapter 3, a series of velocity-step deformation experiments were conducted on synthetic quartz-kaolinite fault gouges to investigate the effect of clay content on the pore volume changes during slip in fault gouges. Granular fault materials were known to dilate in response to increases in sliding velocity but, thus far, dilatancy has been measured predominantly in clay-poor materials (Lockner & Byerlee, 1994; Mair & Marone, 1999; Rathbun & Marone, 2013; Samuelson et al., 2009). Clay minerals are common in mature fault cores and have low frictional strengths. In previous experiments, even small proportions of clay minerals were shown to affect the frictional properties of a fault (Rutter et al., 2013). Hence, these experiments aimed to document in detail the impact of changing the proportion of clay in fault gouges on their frictional behaviour and dilatancy. In this work, a suite of triaxial deformation experiments were conducted at effective normal stresses of 60 MPa, 25 MPa and 10 MPa to simulate hydrostatic to overpressured pore pressure conditions. Samples were initially run at an axial loading rate of 0.3 µm/s for a displacement of 2 mm to bring the sample past yield to where the shear strength of the sample reached steady state. Following the initial yield phase, the sliding velocity was stepped between 0.3 µm/s and 3.0 µm/s for every 0.5 mm of load point displacement to a maximum of 5.5 mm. The rate and state friction (RSF) stability parameter (*a*-*b*) was calculated from the frictional response to the velocity step changes.

The Chapter 3 experimental results include that:

- All of the quartz-kaolinite gouges experienced dilation in response to an increase in slip velocity and compaction in response to a decrease in slip velocity;
- The scale of dilatancy in response to velocity-step changes was affected by the gouge kaolinite content but not by the effective stress conditions. Peak dilation did not occur in the pure quartz gouges, but rather in gouges containing 10 to 40 wt% kaolinite;
- Increasing kaolinite content in the synthetic gouges decreased the gouge frictional strength and increased (*a*-*b*) to promote stable sliding rather than unstable, earthquake slip;
- Increasing effective normal stress increased the likelihood of nucleation of unstable slip by decreasing the rate and state friction parameter (*a*-*b*);
- A transition occurred at ~40 wt% kaolinite from strong, unstably sliding quartz-dominated gouges to weak but stably sliding kaolinite-dominated gouges.

The increase in dilation in clay-bearing fault gouges compared to quartz-only gouges was inferred to be due to changes in gouge microstructure. The transition between quartz- and kaolinite-dominated frictional behaviour occurs at ~40 wt% kaolinite because the clay particles fill the available pore space and the quartz grains become isolated. Dilatancy increases with the addition of small proportions of kaolinite (10-40 wt%) due to the clay particles interrupting the quartz grain comminution. Dilation increases with the width of the active shear zone – quartz-only gouges form extremely narrow shear zones, but the addition of small proportions of kaolinite broadens the width of the active shear zones. Dilatancy in clay-rich regions of faults would increase the capacity of the fault to arrest seismic ruptures.

In Chapter 4, the aim of the study was to investigate the effect of increasing experimental temperature conditions on the frictional stability of the full range of clay proportions (0 to 100 wt%) in fault gouges. This was to address the discrepancy between the typical frictionally stable slip produced in clay-bearing fault rock deformation experiments and observations of unstable seismic slip on natural, clay-bearing faults. The proportion of kaolinite to quartz powder was stepped in 25 wt% increments to produce five synthetic fault gouge mixtures. In addition to room temperature experiments (~23°C), experimental temperature conditions were controlled at 60°C, 100°C, 140°C and 180°C (+/- 0.4°C) using external band heaters. A confining pressure of 150 MPa and a pore fluid pressure (using deionized water as the pore fluid) of 60 MPa simulated the conditions typical of 6-7 km depth with a hydrostatic pressure gradient. As in Chapter 3, the experiments included an initial yield phase of 2 mm displacement at a velocity of 0.3 μm/s. Following this, the sliding velocity was stepped between 3.0 μm/s and 0.3 μm/s for every 0.5 mm of slip until the maximum displacement of 5.5 mm was reached.

The Chapter 4 experimental results included that:

- The frictional stability of clay-bearing fault gouges decreased systematically with elevated temperatures so that gouges containing ≤50 wt% kaolinite displayed unstable slip at temperatures between 100°C and 180°C;
- At temperatures between 100°C and 180°C, kaolinite-bearing fault gouges showed conditionally-unstable slip, so that an imposed velocity-step increase caused stick-slip events;
- Increasing experimental temperature conditions led to the development of longer and broader shear zones in the gouge microstructure, compared to room temperature tests;
- With increasing experimental temperature conditions, the frictional strength and dilatancy of kaolinite-bearing fault gouges increased;

- The quartz-only fault gouge had the opposite relationship with increasing temperature to the kaolinite-bearing fault gouges – with increasing temperature, the frictional strength decreased and the stability of slip increased for the quartz-only gouges.

The observed decrease in (*a*-*b*) to a minimum between 100 and 140°C for kaolinite-quartz gouges occurs above the temperature window at which water is expelled from kaolinite interlayers or between disordered particles. Hence, the removal of adsorbed water from kaolinite interlayers and surfaces within this temperature window leads to enhanced compaction of the gouge microstructure. Shear was accommodated via stable creep until a velocity step increase was imposed, which induced unstable slip. This is similar to a propagating slip patch impinging on a clay-rich, water-saturated fault segment in nature. If earthquake models discount the potential for seismic slip on clay-bearing fault segments, the seismic hazard could be underestimated.

In Chapter 5, the focus of the study in the Carboneras Fault Zone (CFZ) was on the accommodation of strain in brittle-localising and non-localising materials and the potential consequences for mixed-mode seismicity in a heterogeneous fault zone. Prior to this study, there was a relative paucity of microstructural data from the fault rocks and gouges of the CFZ (Abad et al., 2017; Rutter et al., 1986). There is disagreement between literature sources as to whether the CFZ has hosted seismic slip – the broad, anastomosing, phyllosilicate-rich fault core suggests that the CFZ accommodated offset via aseismic creep (Abad et al., 2017; Faulkner et al., 2003; Rutter et al., 2012; Solum & van der Pluijm, 2009), but geophysical studies have assigned historical earthquakes of magnitude 5-6 to the offshore portion of the CFZ (Echeverria et al., 2015; Gràcia et al., 2006; Moreno, 2011).

The Chapter 5 results included that:

- The transfer of strain from a brittle-localising (dolomite) to a non-localising (gouge) material was overprinted by the heterogeneity of the fault sample microstructures;
- Fault gouges in the CFZ contain phyllosilicate minerals such as illite/muscovite, chlorite, paragonite, kaolinite and smectites at proportions between 16-63 %;
- Microstructures in the fault gouges were dominated by aseismic fault creep textures;
- All of the fault materials were velocity strengthening in frictional velocity-step tests at room temperature, with a large strength contrast between the dolomites and the fault gouges;
- The dolomite fault planes included apparent fault ‘mirror’ surfaces that can form due to seismic (or possibly aseismic) slip;
- The fault gouges included pulverised quartz clasts containing Dauphiné twins that can form due to seismic slip, but the quartz clasts in the rim and the central quartz clast did not have the expected relationship of crystal orientation.

The results of Chapter 5 indicated that the mica schist protolith lithology had a lower strength contrast with the significantly weaker fault gouges than the dolomite lithology. This concurs with the model proposed by Faulkner et al. (2003, 2008) on the formation of the broad anastomosing structure of the CFZ. The pulverised quartz clasts in the fault gouges are suggestive, but not concrete evidence, of seismic slip. Deformation on the CFZ would have been dominated by aseismic fault creep in the phyllosilicate-rich fault gouges, but the CFZ may have hosted intermittent seismic slip during its history.

At the start of this thesis, a number of specific aims were proposed to guide the analysis of the deformation behaviours of phyllosilicate minerals (Section 1.2). The high-resolution pore volumometer on the triaxial apparatus and the methodology for high temperature experiments on clay-bearing fault gouges were developed to reduce the gap between natural and rock mechanics experimental conditions. The methodology for producing simulated fault gouges that vary the clay content between 0% and 100% enabled the detailed measurement of the systematic changes in the frictional behaviour of fault materials by clay content. These are important contributions to the equipment capabilities and experimental methods that can be applied in ongoing research into pore fluid pressure evolution in faults, the influence of temperature on frictional sliding and phyllosilicate mechanical behaviour in the Rock Deformation Laboratory in the University of Liverpool.

This thesis aimed to investigate the potential mechanisms that could drive slow slip earthquakes, including dilatant hardening, low effective stress conditions, conditionally stable frictional properties and heterogeneous fault structures and lithologies. Dilation was observed in clay-bearing fault gouges, which would decrease the capacity of faults to accelerate to fast earthquake slip rates. Conditionally stable slip behaviour, in which stable, aseismic slip could become unstable due to an imposed external factor (e.g. velocity step), was observed in clay-bearing fault gouges at elevated temperatures typical of the brittle crust. Thus, this thesis adds to the scientific understanding of the micromechanical processes that govern slow slip earthquakes, especially in clay-rich materials.

6.2 Further work:

The following suggestions for further research are attributed to the specific research projects in this thesis using the notation: (1) the dilatancy of clay-bearing fault gouges; (2) the effect of temperature on clay-bearing fault gouges; and (3) the slip behaviour of the Carboneras Fault Zone.

What is the effect of pre-compaction load on the frictional behaviour of quartz-clay fault gouges? (1)

In response to reviewers concerns about the pre-compaction loading on submission of the dilatancy manuscript, an initial 6 tests were conducted in the Rock Deformation Lab in Liverpool to test the effect of pre-compaction load on the frictional and volume change behaviour of quartz-kaolinite gouges. In the earlier method, the preparation of the fault gouges included loading the sample in the direct shear slider jig to improve cohesion of the sample. This pre-compaction load was originally set at 50 MPa, which exceeded the effective normal stresses (σ_n^{eff}) of 10 MPa and 25 MPa in the dilatancy study. The revised methodology prepared the fault gouges to pre-compaction loads of 10 MPa, so that the σ_n^{eff} would not be exceeded.

The review tests showed that the frictional strength, dilatancy and compaction (ε) were not significantly altered by reducing the pre-compaction load. In contrast, the rate and state friction (RSF) stability parameter (a-b) and the shear enhanced compaction were significantly different in the tests conducted at 10 MPa and 25 MPa σ_n^{eff}. There was no change in any results for the 60 MPa σ_n^{eff} tests. As a result of these initial findings, all of the tests conducted at 10 MPa σ_n^{eff} and 6 of the tests at 25 MPa σ_n^{eff} were repeated using the new sample preparation method.

The 17 review tests confirmed that the initial method of loading the fault gouges above the σ_n^{eff} had affected the frictional strength at low kaolinite contents (Figure 6.1A), the (a-b) values (Figure 6.1B), and the shear enhanced compaction (Figure 6.2C) of the quartz-kaolinite gouges. The increase in shear enhanced compaction caused by the decreased pre-compaction load was expected. The pre-compaction load of 50 MPa was originally developed to create a dense, cohesive gouge microstructure – by reducing the pre-compaction load to 10 MPa, the microstructure had a higher starting porosity so that shear enhanced compaction during tests was also increased (Figure 6.2).

At 10 MPa pre-compaction load, the tests conducted at 10 MPa σ_n^{eff} had (a-b) values 2 to 3 times greater than the tests using the original method (Figure 6.1B). The end member gouge of 0 wt% kaolinite (100 wt% quartz) also showed a drastic change from velocity weakening to velocity strengthening behaviour. This effect of pre-compaction load on rate and state friction

behaviour was unexpected and should be further pursued, if only to inform future rock mechanics experiment methodology.

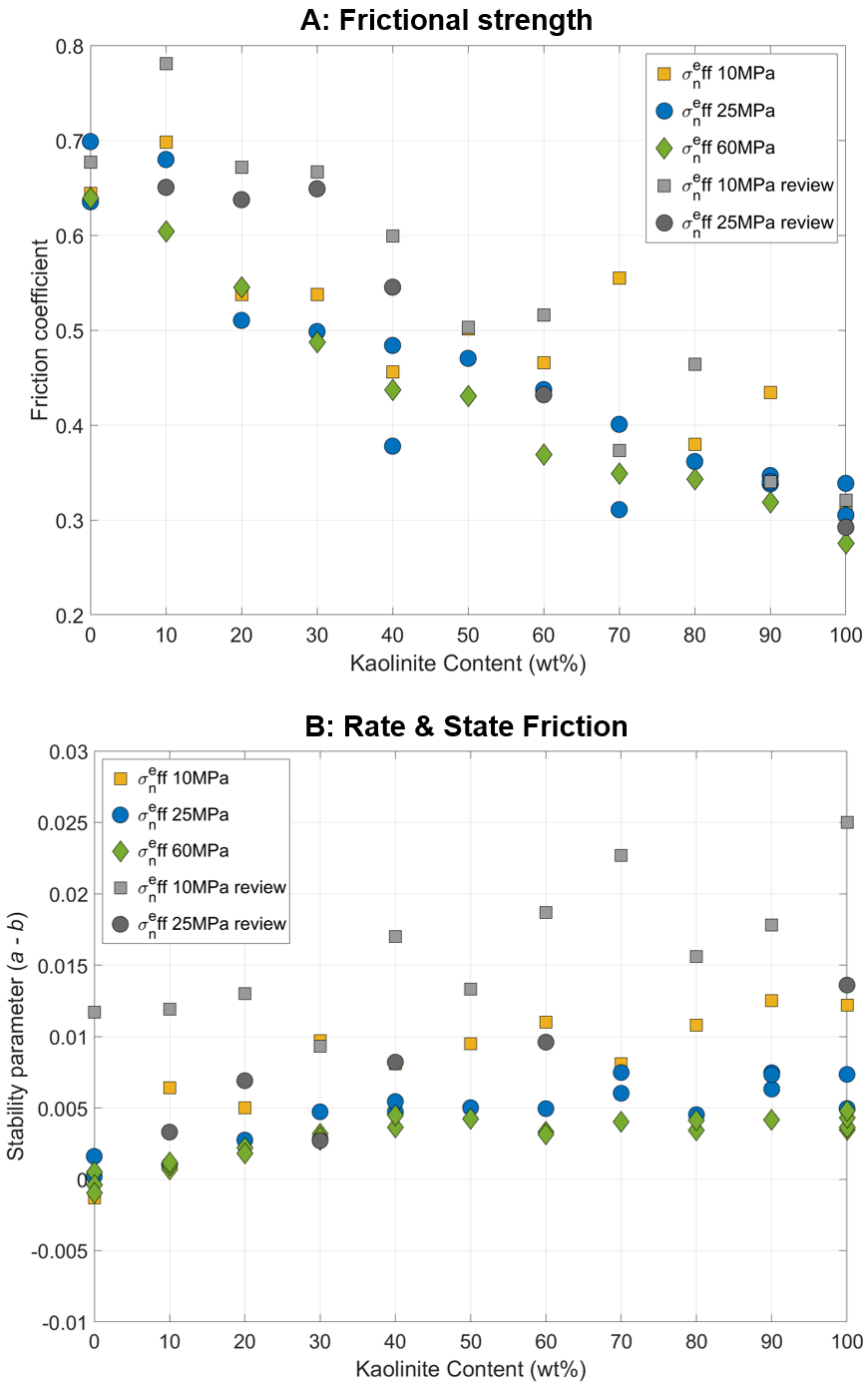

Figure 6.1: Average values for (A) frictional strength and (B) stability parameter (a-b) from 10x velocity step increases by gouge kaolinite content. Coloured data was pre-compacted at 50 MPa and monochrome data was pre-compacted at 10 MPa.

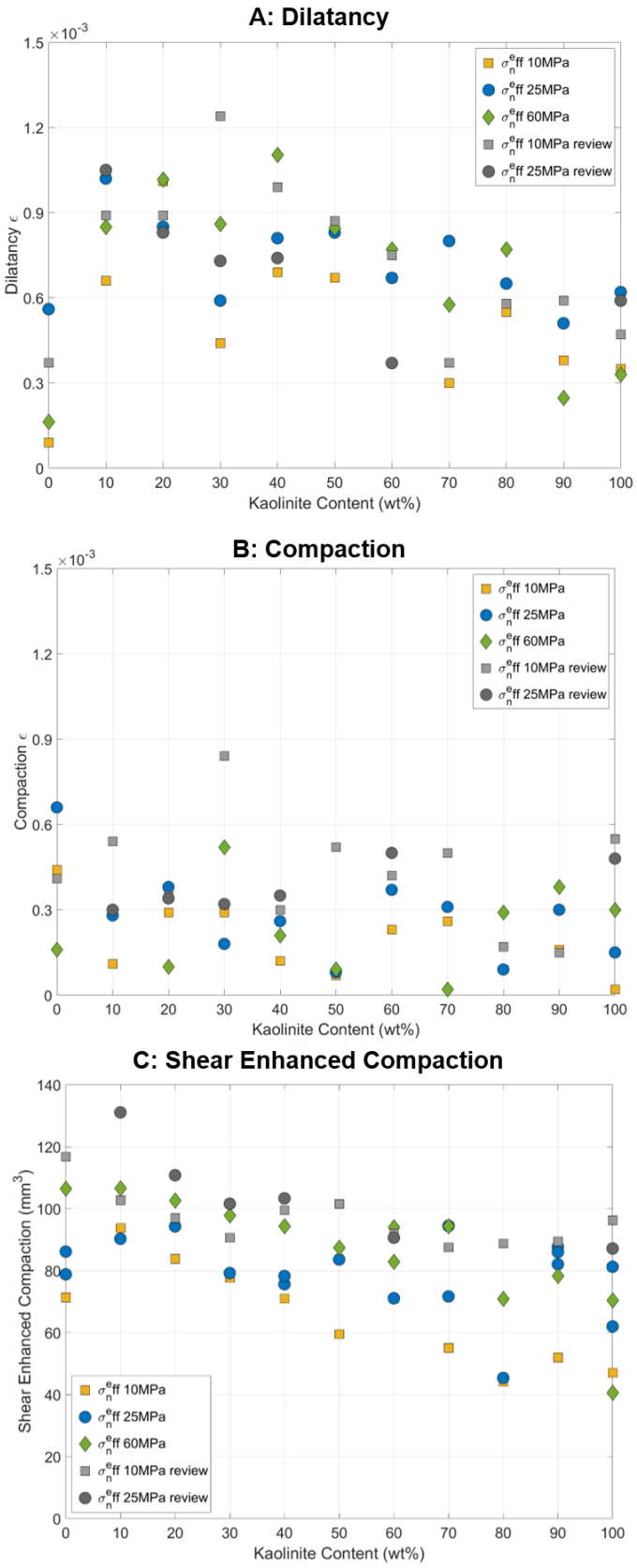

Figure 6.2: Average values for (A) normalised dilation and (B) normalised compaction from 10x velocity step increases and (C) the total shear enhanced compaction in a test by gouge kaolinite content. Pre-compaction load was 50 MPa for coloured data and 10 MPa for monochrome data.

Does dilatancy occur in other phyllosilicate mineral-quartz fault gouges? (1)

The study in Chapter 3 used kaolinite as a proxy for other non-swelling phyllosilicate minerals. Kaolinite is a 1:1 dioctahedral phyllosilicate, similar to lizardite and chrysotile, and the water-saturated shear stress at yield for kaolinite is similar to chlorite, illite and lizardite (Behnsen & Faulkner, 2012). However, very few measurements of dilatancy following slip velocity increases in phyllosilicate-bearing materials have been published (Rathbun & Marone, 2013; Zhang et al., 2020). Smectite is the only other clay that has measured dilatancy data across the full range of clay contents (Figure 6.3) from Zhang et al. (2020). The normalised dilatancy coefficients from Zhang et al. (2020) correspond closely with the data from Chapter 3, even though smectites are 2:1 tri- or di-octahedral swelling clays.

The experimental procedure that was developed in Chapter 3 to measure the dilatancy of clay-quartz fault gouges could easily be applied to different phyllosilicate minerals. Common phyllosilicate minerals that occur in fault gouges include muscovite, chlorite, illite and smectites. The main requirement of the testing procedure is that the permeability of the fault gouge material must be sufficient to equilibrate pore pressure between the sample and the control pump within a velocity step. Although Zhang et al. (2020) have conducted measurements of dilatancy in smectite-bearing fault gouges, the experimental procedure was conducted in a double direct shear biaxial loading frame, so the experiments did not include any pore pressure as the apparatus was not fully confined. Hence, smectite-bearing fault gouges should be tested using the experimental procedure developed in Chapter 3 to test the difference in dilatancy behaviour between swelling and non-swelling clays in the presence of pore fluid. Different groups of phyllosilicate minerals could be investigated to measure if there are variations in dilatancy between trioctahedral and dioctahedral, or 1:1 and 2:1 layered phyllosilicate minerals.

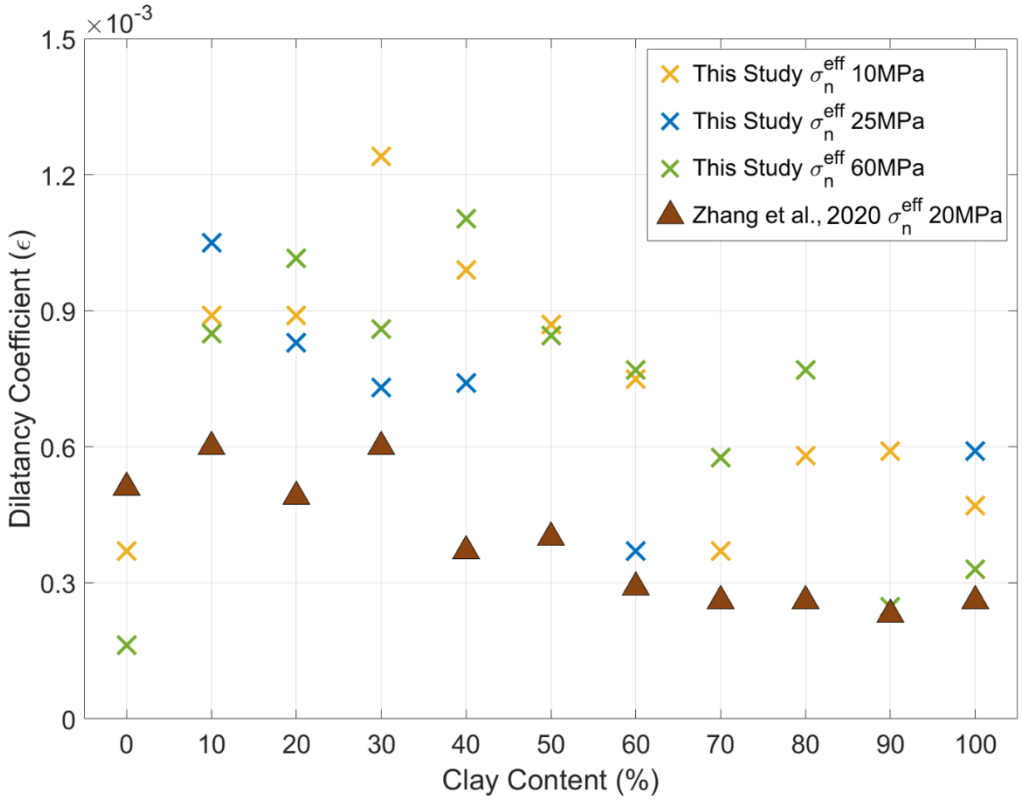

Figure 6.3: Average normalised dilatancy (ε) of clay-quartz fault gouges following a slip velocity increase. Dilatancy is normalised to sample volume and velocity step increases.

How does temperature affect the frictional behaviour of kaolinite-quartz gouges between 0-25 wt% clay? (2)

Vastly different frictional behaviours at elevated temperatures were observed in the 0 wt% kaolinite (100 wt% quartz) and 25 wt% kaolinite (75 wt% quartz) fault gouges in Chapter 4. The 0 wt% kaolinite gouge showed unstable stick slip behaviour at room temperature, but at elevated temperatures the slip switched to stable strain weakening behaviour (Figure 6.4). Increasing temperatures had the opposite effect on the 25 wt% kaolinite gouge, which switched from stable sliding at room temperature to conditionally unstable behaviour at elevated temperatures (Figure 6.4). This drastic change in behaviour between 0 and 25 wt% kaolinite indicates that the addition of only small proportions of clay to a fault gouge have the greatest impact on the frictional behaviour at elevated temperatures.

Hence, a suite of experiments should investigate the change in frictional behaviour between 0 wt% and 25 wt% kaolinite at elevated temperatures. Kaolinite-quartz mixtures of 5, 10, 15 and 20 wt% kaolinite should be prepared using the tumbling methodology described in Chapter 2. Triaxial velocity-step tests should be conducted at the same temperature conditions (~23°C, 60°C, 100°C, 140°C & 180°C) as those already completed in Chapter 4, to allow comparison with the data already collected for the 0 wt% and 25 wt% kaolinite fault gouges.

From this suite of 20 experiments, the fault gouge material should be recovered following the velocity-step tests and preserved for microstructural analysis using a SEM. The change in the frictional behaviour of the gouges between 0 wt% and 25 wt% kaolinite must correspond with a change in microstructure – the 25 wt% kaolinite gouges accommodated shear via diffuse shear zones at room temperatures that, at elevated temperatures, switched to localised Riedel Y- and R_1 shears. Few 0 wt% kaolinite sheared samples from the study in Chapter 4 could be recovered from the direct shear slider assembly due to their extreme fragility – hence, the study of the microstructures of gouges of 5-20 wt% kaolinite would significantly improve our understanding of the change in deformation mechanisms causing the different frictional behaviours observed in Figure 6.4.

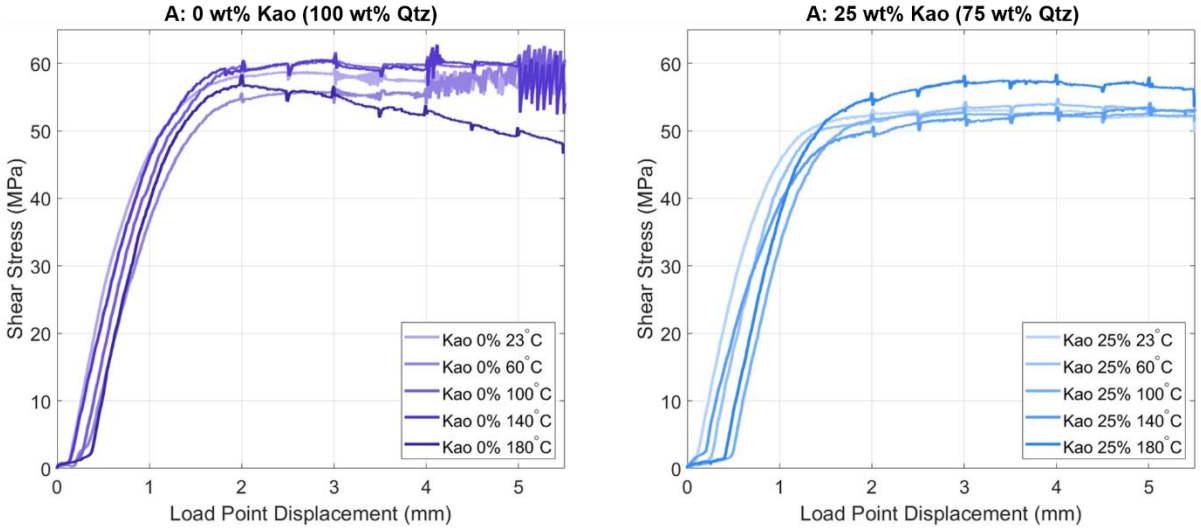

Figure 6.4: Shear stress curves against load point displacement for (A) 0 wt% kaolinite (100 wt% quartz) fault gouges and (B) 25 wt% kaolinite (75 wt% quartz) fault gouges.

How does temperature affect the rate and state friction of kaolinite-quartz gouges beyond 200°C? (2)

The suite of experiments in Chapter 4 that investigated the effect of temperature on the frictional behaviour of kaolinite-quartz fault gouges was limited to a maximum temperature of 200°C. The materials used in the direct shear sliders, such as the silicon spacers, begin to degrade above this maximum temperature. Several authors, including Boulton et al. (2014) and Den Hartog et al. (2013), conducted friction tests on clay-bearing materials up to 350˚C (Figure 6.5). The minimum of (*a*-*b*) that occurred at 140˚C in the kaolinite-quartz gouges in Chapter 4 was followed by an increase in (*a*-*b*) at 180˚C, which suggests that there would be further evolution of (*a*-*b*) above temperatures of 200˚C.

Adjustments are currently underway on one of the hydrostatic apparatus in the Rock Deformation Lab to modify it into a triaxial apparatus using argon gas as the compressive

medium. Argon gas as a confining medium would be suitable for experiments at temperatures beyond the operating temperatures of the silicon oil (maximum of 250-310°C). The external chromalux band furnaces could be applied to this new triaxial apparatus or a newly developed internal furnace could be used within the pressure vessel to heat the sample assembly. To conduct experiments exceeding the 200°C temperature limit of the silicon spacers, an alternative elastic or visco-elastic spacer material would be required.

Kaolinite is stable up to temperatures of 450°C, so the suggested experimental procedure would be to test kaolinite-quartz mixtures at the same proportions (0, 25, 50, 75 & 100 wt%) as in Chapter 4. The temperatures would be stepped in similar increments at 200°C, 240°C, 280°C, and 320°C to conduct a total of 20 experiments.

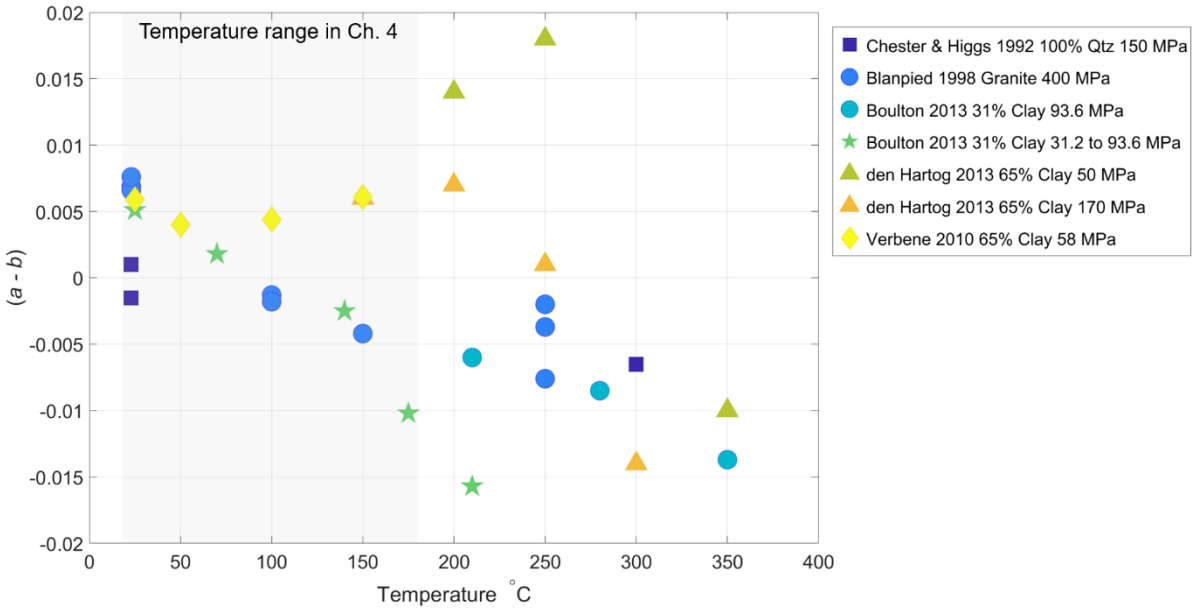

Figure 6.5: The effect of temperature upon the stability parameter (a-b) of different materials and lithologies from literature sources. The grey box denotes the temperature range studied in Chapter 4.

How does temperature affect the frictional behaviour of different phyllosilicate minerals in phyllosilicate-quartz fault gouges? (2)

As with the further work suggested for dilatancy measurements, the effect of temperature on phyllosilicate minerals other than kaolinite should be pursued. In Figure 6.5, the literature published data on a variety of materials at elevated temperatures are shown. In the majority of these experimental studies, a single composition of fault gouge was taken to several temperature conditions (Boulton et al., 2014; Den Hartog & Spiers, 2013; Verberne et al., 2010). The value of the experimental procedure in Chapter 4 is that the effect of temperature on the frictional stability of phyllosilicate-bearing fault gouges is tested across the compositional range of clay contents. The new suite of experiments could use illite or smectite

clays, as these are both common in natural fault gouges and are stable at elevated temperatures – illite is stable up to 950°C and smectites are stable up to 500°C. Different clay minerals lose the bound surface water across characteristic temperature ranges, for example illite expels surface water between 110-140°C and smectites lose surface water between 100-200°C. This would test whether the hypothesis developed in Chapter 4, that the minimum (*a-b*) values occur between 100-140°C due to the loss of surface water from kaolinite and the formation of a denser microstructure, can be applied to other clay minerals.

What frictional behaviour do CFZ gouges show at temperatures typical of the depths at which the current exposure of the CFZ was deformed at? (2, 3)

The investigation in Chapter 4 showed that the temperature conditions of fault slip affects the stability of slip in clay-bearing fault gouges. The frictional experiments in Chapter 5 on the clay-bearing CFZ gouges were conducted at room temperature, but it is estimated from the regional uplift in the Betic Cordillera that the current exposure of basement cut by the CFZ was deformed at depths of up to 4 km (Faulkner et al., 2003). Assuming a geothermal gradient of 20-25°C/km, the CFZ fault gouges would have been deformed at 100-120°C. These temperatures correspond with the minimum (*a-b*) stability measured in kaolinite-quartz gouges at up to 50 wt% kaolinite. From the XRD measurements in Chapter 5, the CFZ gouge phyllosilicate contents are known to range from 16-63 wt%. There are sufficient amounts of the sampled CFZ gouges that were prepared for frictional testing to allow repeats of the velocity-step tests at temperatures of 100°C.

Are the pulverised quartz clasts (PQC) in the CFZ fault gouges evidence of seismic slip? (3)

The analysis of a potential pulverised quartz clast (PQC) in Chapter 5 produced contradictory results. The central quartz grain was surrounded by a rim of extremely fine grained comminuted quartz grains (Figure 6.6). From EBSD analysis, the rim clasts and central quartz clast were shown to have no relationship of crystal orientation and the central quartz clast displayed pervasive Dauphiné twinning. The lack of an orientation relationship suggests that the quartz rim did not originate from the same parent clast as the central quartz clast, as would occur with a PQC. In contrast, the pervasive Dauphiné twinning in the central quartz clast could have been created by seismogenic shock (Wenk et al., 2011). This issue rates further microstructural analysis, as it may reveal whether the CFZ hosted seismic slip.

Only one large scale EBSD experiment mapped a section of the PQC in CFIA27 (Figure 6.6), due to the time constraints of access to the SEM. Further work on sample CFIA27 should include completing an EBSD experiment map of the entire PQC. Another sample that contained several potential PQC that should be analysed using EBSD was CFIA31, which is another phyllite-derived sample that was collected in close proximity to a dolomite fault plane.

Rodriguez-Escudero et al. (2020) identified similar PQC textures in fault gouges of the Alhama de Murcia fault (AdMF). The AdMF PQC often had winged sigma-type geometries, which was evidence of a shear strain overprint. This texture may explain the different orientations of the central and rim quartz clasts in the PQC observed in CFIA27, but the thin section plane of view may have been incorrect to capture this texture. Another thin section at an orientation oblique to the original should be prepared to investigate whether there is a shear strain overprint on the PQC.

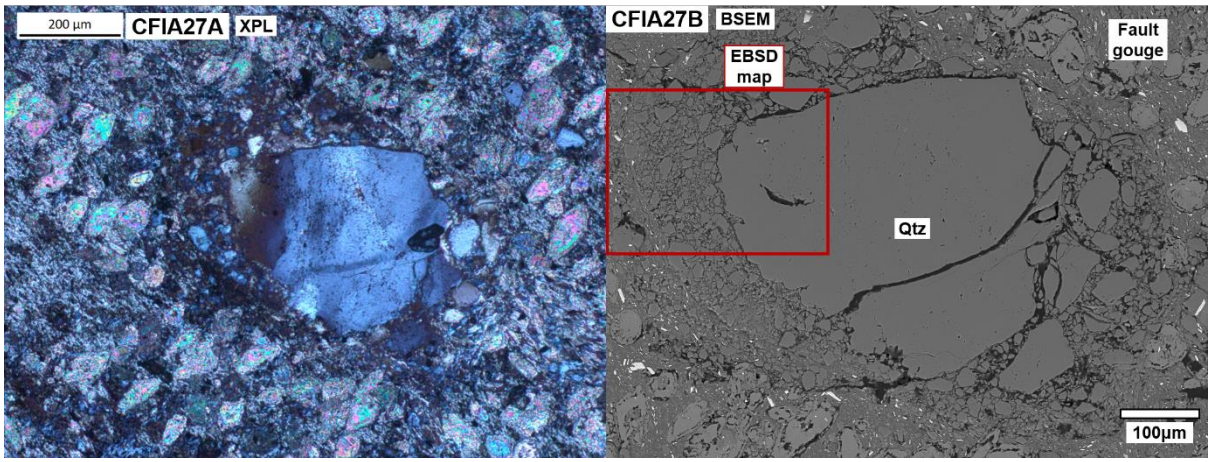

Figure 6.6: Phyllite-derived gouge sample CFIA27 shown in (A) a crossed-polars optical microscope image with the potential PQC embedded in fault gouge and (B) a back-scatter electron image of the potential PQC. The red box covers the area that has already been mapped using EBSD.

7. References

Abad, I., Jiménez-Millán, J., Schleicher, A. M., & van der Pluijm, B. A. (2017). Mineral characterization, clay quantification and Ar–Ar dating of faulted schists in the Carboneras and Palomares Faults (Betic Cordillera, SE Spain). *European Journal of Mineralogy*, *29*(1), 17–34. https://doi.org/10.1127/ejm/2017/0029-2580

Aben, F. M., Doan, M. L., Mitchell, T. M., Toussaint, R., Reuschlé, T., Fondriest, M., Gratier, J. P., & Renard, F. (2016). Dynamic fracturing by successive coseismic loadings leads to pulverization in active fault zones. *Journal of Geophysical Research: Solid Earth*, *121*(4), 2338–2360. https://doi.org/10.1002/2015JB012542

Aharonov, E., & Scholz, C. H. (2018). A Physics-Based Rock Friction Constitutive Law: Steady State Friction. *Journal of Geophysical Research: Solid Earth*, *123*(2), 1591–1614. https://doi.org/10.1002/2016JB013829

Alonso-Chaves, F., Soto, J. I., Orozco, M., Kilias, A. A., & Tranos, M. D. (2004). TECTONIC EVOLUTION OF THE BETIC CORDILLERA: AN OVERVIEW. *Bulletin of the Geological Society of Greece*, *36*(4), 1598. https://doi.org/10.12681/bgsg.16563

Ampuero, J. P., & Rubin, A. M. (2008). Earthquake nucleation on rate and state faults - Aging and slip laws. *Journal of Geophysical Research: Solid Earth*, *113*(1), 1–21. https://doi.org/10.1029/2007JB005082

Arrhenius, S. (1889). Über die Dissociationswärme und den Einfluss der Temperatur auf den Dissociationsgrad der Elektrolyte. *Zeitschrift Für Physikalische Chemie*, *4U*(1), 96–116. https://doi.org/doi:10.1515/zpch-1889-0408

Aslin, J., Mariani, E., Dawson, K., & Barsoum, M. W. (2019). Ripplocations provide a new mechanism for the deformation of phyllosilicates in the lithosphere. *Nature Communications*, *10*(1). https://doi.org/10.1038/s41467-019-08587-2

Audet, P., Bostock, M. G., Christensen, N. I., & Peacock, S. M. (2009). Seismic evidence for overpressured subducted oceanic crust and megathrust fault sealing. *Nature*, *457*(7225), 76–78. https://doi.org/10.1038/nature07650

Bakker, H. E., Jong, K. DE, Helmers, H., & Biermann, C. (1989). The geodynamic evolution of the Internal Zone of the Betic Cordilleras (south-east Spain): a model based on structural analysis and geothermobarometry. *Journal of Metamorphic Geology*, *7*(3), 359–381. https://doi.org/10.1111/j.1525-1314.1989.tb00603.x

Barsoum, M. W. (2020). Ripplocations: A Progress Report. *Frontiers in Materials*, *7*(May), 1–17. https://doi.org/10.3389/fmats.2020.00146

Bedford, J. D., & Faulkner, D. R. (2021). The Role of Grain Size and Effective Normal Stress on Localization and the Frictional Stability of Simulated Quartz Gouge. *Geophysical Research Letters*, *48*(7). https://doi.org/10.1029/2020GL092023

Behnsen, J., & Faulkner, D. R. (2011). Water and argon permeability of phyllosilicate powders under medium to high pressure. *Journal of Geophysical Research: Solid Earth*, *116*(12), 1–13. https://doi.org/10.1029/2011JB008600

Behnsen, J., & Faulkner, D. R. (2012). The effect of mineralogy and effective normal stress on frictional strength of sheet silicates. *Journal of Structural Geology*, *42*, 49–61. https://doi.org/10.1016/j.jsg.2012.06.015

Ben-Zion, Y., Rice, J. R., & Dmowska, R. (1993). Interaction of the San Andreas Fault creeping segment with adjacent great rupture zones and earthquake recurrence at Parkfield. *Journal of Geophysical Research*, *98*(B2), 2135–2144. https://doi.org/10.1029/92JB02154

Ben-Zion, Y., & Shi, Z. (2005). Dynamic rupture on a material interface with spontaneous generation of plastic strain in the bulk. *Earth and Planetary Science Letters*, *236*(1–2), 486–496. https://doi.org/10.1016/j.epsl.2005.03.025

Bergaya, F., Jaber, M., & Lambert, J. F. (2011). Clays and Clay Minerals. In *Rubber-Clay Nanocomposites: Science, Technology, and Applications* (1st ed., pp. 3–44). John Wiley & Sons, Inc. https://doi.org/10.2136/sssaj1956.03615995002000020037x

Bernabé, Y., Mok, U., & Evans, B. (2006). A note on the oscillating flow method for measuring rock permeability. *International Journal of Rock Mechanics and Mining Sciences*, *43*(2), 311–316. https://doi.org/10.1016/j.ijrmms.2005.04.013

Berryman, K. R., Cochran, U. A., Clark, K. J., Biasi, G. P., Langridge, R. M., & Villamor, P. (2012). Major Earthquakes Occur Regularly on an Isolated Plate Boundary Fault. *Science*, *336*(6089), 1690–1693. https://doi.org/10.1126/science.1221329

Bhattacharya, P., Rubin, A. M., & Beeler, N. M. (2017). Does fault strengthening in laboratory rock friction experiments really depend primarily upon time and not slip? *Journal of Geophysical Research: Solid Earth*, *122*(8), 6389–6430. https://doi.org/10.1002/2017JB013936

Blanpied, M. L., Lockner, D. A., & Byedee, J. D. (1995). Frictional slip of granite at hydrothermal conditions. In *JOURNAL OF GEOPHYSICAL RESEARCH* (Vol. 100, Issue B7).

Blanpied, M. L., Marone, C. J., Lockner, D. A., Byerlee, J. D., & King, D. P. (1998). Quantitative measure of the variation in fault rheology due to fluid-rock interactions. *Journal of Geophysical Research*, *103*(B5), 9691–9712.

Bleloch, A. L., Howie, A., & Milne, R. H. (1989). *High Resolution Secondary Electron Imaging and Spectroscopy*. *31*, 99–110.

Booth-Rea, G., Ranero, C. R., Grevemeyer, I., & Martínez-Martínez, J. M. (2007). Crustal types and tertiary tectonic evolution of the Alborán sea, western Mediterranean. *Geochemistry, Geophysics, Geosystems*, *8*(10). https://doi.org/10.1029/2007GC001639

Boullier, A. M., Robach, O., Ildefonse, B., Barou, F., Mainprice, D., Ohtani, T., & Fujimoto, K. (2018). High stresses stored in fault zones: Example of the Nojima fault (Japan). *Solid Earth*, *9*(2), 505–529. https://doi.org/10.5194/se-9-505-2018

Boulton, C., Moore, D. E., Lockner, D. A., Toy, V. G., Townend, J., & Sutherland, R. (2014). Frictional properties of exhumed fault gouges in DFDP-1 cores, Alpine Fault, New Zealand. *Geophysical Research Letters*, *41*(2), 356–362. https://doi.org/10.1002/2013GL058236

Brady, P. V, Cygan, R. T., & Nagy, K. L. (1996). Molecular Controls on Kaolinite Surface Charge. *JOURNAL OF COLLOID AND INTERFACE SCIENCE*, *183*, 356–364.

Brantut, N. (2020). Dilatancy-induced fluid pressure drop during dynamic rupture: Direct experimental evidence and consequences for earthquake dynamics. *Earth and Planetary Science Letters*, *538*, 116179. https://doi.org/10.1016/j.epsl.2020.116179

Brigatti, M. F., Galan, E., & Theng, B. K. G. (2006). Structures and Mineralogy of Clay Minerals. In *Developments in Clay Science* (Vol. 1, pp. 19–86). Elsevier Ltd. https://doi.org/10.1016/S1572-4352(05)01002-0

Brindley, G. W., & Bradley, W. F. (1951). *The X-ray identification and crystal structures of clay minerals*. Mineralogical Society, Clay Minerals Group.

Brown, G. (1982). *Crystal structures of clay minerals and their X-ray identification* (Vol. 5). The Mineralogical Society of Great Britain and Ireland.

Brown, K. M., Kopf, A., Underwood, M. B., & Weinberger, J. L. (2003). Compositional and fluid pressure controls on the state of stress on the Nankai subduction thrust: A weak plate boundary. *Earth and Planetary Science Letters*, *214*(3–4), 589–603. https://doi.org/10.1016/S0012-821X(03)00388-1

Byerlee, J. (1978). Friction of Rocks. *Pageoph*, *116*.

Candela, T., Renard, F., Klinger, Y., Mair, K., Schmittbuhl, J., & Brodsky, E. E. (2012). Roughness of fault surfaces over nine decades of length scales. *Journal of Geophysical Research: Solid Earth*, *117*(8). https://doi.org/10.1029/2011JB009041

Chakraborty, A. K. (2014). *Phase Transformation of Kaolinite Clay*. https://doi.org/10.1007/978-81-322-1154-9

Chen, K. H., Rau, R. J., & Hu, J. C. (2009). Variability of repeating earthquake behavior along the Longitudinal Valley fault zone of eastern Taiwan. *Journal of Geophysical Research: Solid Earth*, *114*(5). https://doi.org/10.1029/2007JB005518

Chen, L., Xu, J., & Chen, J. (2015). Applications of scanning electron microscopy in earth sciences. *Science China Earth Sciences*, *58*(10), 1768–1778. https://doi.org/10.1007/s11430-015-5172-9

Chester, F. M., Evans, J. P., & Biegel, R. L. (1993). Internal structure and weakening mechanisms of the San Andreas Fault. *Journal of Geophysical Research*, *98*(B1), 771–

786. https://doi.org/10.1029/92JB01866

Chester, F. M., & Higgs, N. G. (1992). Multimechanism friction constitutive model for ultrafine quartz gouge at hypocentral conditions. *Journal of Geophysical Research*, *97*(B2), 1859–1870. https://doi.org/10.1029/91JB02349

Chester, F. M., & Logan, J. M. (1986). Implications for Mechanical Properties of Brittle Faults from Observations of the Punchbowl Fault Zone, California. *PAGEOPH*, *124*(2).

Chester, F. M., & Logan, J. M. (1987). Composite planar fabric of gouge from the Punchbowl Fault, California. *Journal of Structural Geology*, *9*(5–6). https://doi.org/10.1016/0191-8141(87)90147-7

Chester, F. M., Mori, J., Eguchi, N., & Toczko, S. (2013). Expedition 343/343T summary. *Proceedings of the Integrated Ocean Drilling Program*, *343*. https://doi.org/10.2204/iodp.proc.343343t.101.2013

Chester, F. M., Rowe, C., Ujiie, K., Kirkpatrick, J., Regalla, C., Remitti, F., Moore, J. C., & Toy, V. (2013). *Structure and Composition of the Plate-Boundary Slip Zone for the 2011 Tohoku-Oki Earthquake*. *December*, 1208–1211.

Chester, M., & Chester, J. S. (2000). Stress and deformation along wavy frictional faults. *Journal of Geophysical Research*, *105*(B10), 23,421-23430.

Chung, F. H. (1974). Quantitative interpretation of X-ray diffraction patterns of mixtures. I. Matrix-flushing method for quantitative multicomponent analysis. *Journal of Applied Crystallography*, *7*(6), 519–525. https://doi.org/10.1107/s0021889874010375

Ciston, J., Brown, H. G., D'Alfonso, A. J., Koirala, P., Ophus, C., Lin, Y., Suzuki, Y., Inada, H., Zhu, Y., Allen, L. J., & Marks, L. D. (2015). Surface determination through atomically resolved secondary-electron imaging. *Nature Communications*, *6*. https://doi.org/10.1038/ncomms8358

Collettini, C., Niemeijer, A., Viti, C., Smith, S. A. F., & Marone, C. (2011). Fault structure, frictional properties and mixed-mode fault slip behavior. *Earth and Planetary Science Letters*, *311*(3–4), 316–327. https://doi.org/10.1016/j.epsl.2011.09.020

Comas, M. C., Platt, J. P., Soto, J. I., & Watts, A. B. (1999). The origin and tectonic history of the Alboran Basin: Insights from Leg 161 results. *Proceedings of the Ocean Drilling Program: Scientific Results*, *161*, 555–580. https://doi.org/10.2973/odp.proc.sr.161.262.1999

Conticelli, S., Guarnieri, L., Farinelli, A., Mattei, M., Avanzinelli, R., Bianchini, G., Boari, E., Tommasini, S., Tiepolo, M., Prelević, D., & Venturelli, G. (2009). Trace elements and Sr-Nd-Pb isotopes of K-rich, shoshonitic, and calc-alkaline magmatism of the Western Mediterranean Region: Genesis of ultrapotassic to calc-alkaline magmatic associations in a post-collisional geodynamic setting. *Lithos*, *107*(1–2), 68–92. https://doi.org/10.1016/j.lithos.2008.07.016

Crawford, B. R., Faulkner, D. R., & Rutter, E. H. (2008). Strength, porosity, and permeability development during hydrostatic and shear loading of synthetic quartz-clay fault gouge. *Journal of Geophysical Research: Solid Earth*, *113*(3), 1–14. https://doi.org/10.1029/2006JB004634

Dal Zilio, L., Lapusta, N., & Avouac, J. P. (2020). Unraveling Scaling Properties of Slow-Slip Events. *Geophysical Research Letters*, *47*(10). https://doi.org/10.1029/2020GL087477

De Paola, N., Holdsworth, R. E., Viti, C., Collettini, C., & Bullock, R. (2015). Can grain size sensitive flow lubricate faults during the initial stages of earthquake propagation? *Earth and Planetary Science Letters*, *431*, 48–58. https://doi.org/10.1016/j.epsl.2015.09.002

Deer, W. A., Howie, R. A., & Zussman, J. (2013). *An Introduction to the Rock-Forming Minerals* (3rd ed.). Mineralogical Society of Great Britain and Ireland. https://doi.org/10.1180/DHZ

Den Hartog, S. A. M., Niemeijer, A. R., & Spiers, C. J. (2012). New constraints on megathrust slip stability under subduction zone P-T conditions. *Earth and Planetary Science Letters*, *353–354*, 240–252. https://doi.org/10.1016/j.epsl.2012.08.022

Den Hartog, S. A. M., & Spiers, C. J. (2013). Influence of subduction zone conditions and gouge composition on frictional slip stability of megathrust faults. *Tectonophysics*, *600*, 75–90. https://doi.org/10.1016/j.tecto.2012.11.006

Den Hartog, S. A. M., Thomas, M. Y., & Faulkner, D. R. (2021). How do Laboratory Friction Parameters Compare With Observed Fault Slip and Geodetically Derived Friction Parameters? Insights From the Longitudinal Valley Fault, Taiwan. *Journal of Geophysical Research: Solid Earth*, *126*(10). https://doi.org/10.1029/2021JB022390

Di Toro, G., Han, R., Hirose, T., De Paola, N., Nielsen, S., Mizoguchi, K., Ferri, F., Cocco, M., & Shimamoto, T. (2011). Fault lubrication during earthquakes. *Nature*, *471*(7339), 494–499. https://doi.org/10.1038/nature09838

Dieterich, J. H. (1979). Modeling of rock friction 1. Experimental results and constitutive equations. *Journal of Geophysical Research: Solid Earth*, *84*(B5), 2161–2168. https://doi.org/10.1029/JB084iB05p02161

Dieterich, J. H. (1992). Earthquake nucleation on faults with rate-and state-dependent strength. *Tectonophysics*, *211*(1–4), 115–134. https://doi.org/10.1016/0040-1951(92)90055-B

Dieterich, J. H., & Kilgore, B. D. (1996). Imaging surface contacts: Power law contact distributions and contact stresses in quartz, calcite, glass and acrylic plastic. *Tectonophysics*, *256*(1-4 SPEC. ISS.), 219–239. https://doi.org/10.1016/0040-1951(95)00165-4

Dieterich, J. H., & Smith, D. E. (2009). Nonplanar Faults: Mechanics of Slip and Off-fault Damage. *Pure and Applied Geophysics*, *166*, 1799–1815.

https://doi.org/10.1007/s00024-009-0517-y

Doan, M. L., & Gary, G. (2009). Rock pulverization at high strain rate near the SanAndreas fault. *Nature Geoscience*, *2*(10), 709–712. https://doi.org/10.1038/ngeo640

Duggen, S., Hoernle, K., Klügel, A., Geldmacher, J., Thirlwall, M., Hauff, F., Lowry, D., & Oates, N. (2008). Geochemical zonation of the Miocene Alborán Basin volcanism (westernmost Mediterranean): Geodynamic implications. *Contributions to Mineralogy and Petrology*, *156*(5), 577–593. https://doi.org/10.1007/s00410-008-0302-4

Duggen, S., Hoernle, K., van den Bogaard, P., & Harris, C. (2004). Magmatic evolution of the Alboran region: The role of subduction in forming the western Mediterranean and causing the Messinian Salinity Crisis. *Earth and Planetary Science Letters*, *218*(1–2), 91–108. https://doi.org/10.1016/S0012-821X(03)00632-0

Dusevich, V. M., Purk, J. H., & Eick, J. D. (2010). Choosing the Right Accelerating Voltage for SEM (An Introduction for Beginners). *Microscopy Today*, 48–52. https://doi.org/10.1017/S1551929509991192

Echeverria, A., Khazaradze, G., Asensio, E., & Masana, E. (2015). Geodetic evidence for continuing tectonic activity of the Carboneras fault (SE Spain). *Tectonophysics*, *663*, 302–309. https://doi.org/10.1016/j.tecto.2015.08.009

Egeler, C. G. (1964). On the tectonics of the eastern Betic Cordilleras (SE Spain). *Geologische Rundschau*, *53*(1), 260–269. https://doi.org/10.1007/BF02040750

Eggleton, A., & Banfield, F. (1985). The alteration of granitic biotite to chlorite. *American Mineralogist*, *70*, 902–910. http://www.minsocam.org/msa/collectors_corner/amtoc/toc1985.htm

Fagereng, Å., & Sibson, R. H. (2010). Mélange rheology and seismic style. *Geology*, *38*(8), 751–754. https://doi.org/10.1130/G30868.1

Fang, Z., & Dunham, E. M. (2013). Additional shear resistance from fault roughness and stress levels on geometrically complex faults. *Journal of Geophysical Research: Solid Earth*, *118*(7), 3642–3654. https://doi.org/10.1002/jgrb.50262

Faulkner, D. R., & Armitage, P. J. (2013). The effect of tectonic environment on permeability development around faults and in the brittle crust. *Earth and Planetary Science Letters*, *375*, 71–77. https://doi.org/10.1016/j.epsl.2013.05.006

Faulkner, D. R., Jackson, C. A. L., Lunn, R. J., Schlische, R. W., Shipton, Z. K., Wibberley, C. A. J., & Withjack, M. O. (2010). A review of recent developments concerning the structure, mechanics and fluid flow properties of fault zones. *Journal of Structural Geology*, *32*(11), 1557–1575. https://doi.org/10.1016/j.jsg.2010.06.009

Faulkner, D. R., Lewis, A. C., & Rutter, E. H. (2003). On the internal structure and mechanics of large strike-slip fault zones: Field observations of the Carboneras fault in southeastern Spain. *Tectonophysics*, *367*(3–4), 235–251. https://doi.org/10.1016/S0040-

1951(03)00134-3

Faulkner, D. R., Mitchell, T. M., Rutter, E. H., & Cembrano, J. (2008). On the structure and mechanical properties of large strike-slip faults. *Geological Society Special Publication*, *299*, 139–150. https://doi.org/10.1144/SP299.9

Faulkner, D. R., & Rutter, E. H. (1998). The gas permeability of clay-bearing fault gouge at 20 degrees C. *Geological Society Special Publication*, *147*, 147–156.

Faulkner, D. R., & Rutter, E. H. (2000). Comparisons of water and argon permeability in natural clay-bearing fault gouge under high pressure at 20°C. *Journal of Geophysical Research: Solid Earth*, *105*(B7), 16415–16426. https://doi.org/10.1029/2000jb900134

Faulkner, D. R., Sanchez-Roa, C., Boulton, C., & den Hartog, S. A. M. (2018). Pore Fluid Pressure Development in Compacting Fault Gouge in Theory, Experiments, and Nature. *Journal of Geophysical Research: Solid Earth*, *123*(1), 226–241. https://doi.org/10.1002/2017JB015130

Ferdowsi, B., & Rubin, A. M. (2020). A Granular Physics-Based View of Fault Friction Experiments. *Journal of Geophysical Research: Solid Earth*, *125*(6), 1–32. https://doi.org/10.1029/2019JB019016

Fiebig, J., & Hoefs, J. (2002). Hydrothermal alteration of biotite and plagioclase as inferred from intragranular oxygen isotope- and cation-distribution patterns. *European Journal of Mineralogy*, *14*(1), 49–60. https://doi.org/10.1127/0935-1221/02/0014-0049

Fischer, G. J., & Paterson, M. S. (1992). Measurement of Permeability and Storage Capacity in Rocks During Deformation at High Temperature and Pressure. In *International Geophysics* (Vol. 51, Issue C). https://doi.org/10.1016/S0074-6142(08)62824-7

Fondriest, M., Smith, S. A. F., Candela, T., Nielsen, S. B., Mair, K., & Toro, G. Di. (2013). Mirror-like faults and power dissipation during earthquakes. *Geology*, *41*(11), 1175–1178. https://doi.org/10.1130/G34641.1

Fortuin, A. R., & Krijgsman, W. (2003). The Messinian of the Nijar Basin (SE Spain): Sedimentation, depositional environments and paleogeographic evolution. *Sedimentary Geology*, *160*(1–3), 213–242. https://doi.org/10.1016/S0037-0738(02)00377-9

Frank, W. B., & Brodsky, E. E. (2019). Daily measurement of slow slip from low-frequency earthquakes is consistent with ordinary earthquake scaling. *Science Advances*, *5*(10), 1–7. https://doi.org/10.1126/sciadv.aaw9386

Frank, W. B., Shapiro, N. M., Husker, A. L., Kostoglodov, V., Bhat, H. S., & Campillo, M. (2015). Along-fault pore-pressure evolution during a slow-slip event in Guerrero, Mexico. *Earth and Planetary Science Letters*, *413*, 135–143. https://doi.org/10.1016/j.epsl.2014.12.051

French, M. E., & Chester, J. S. (2018). Localized Slip and Associated Fluidized Structures Record Seismic Slip in Clay-Rich Fault Gouge. *Journal of Geophysical Research: Solid*

Earth, *123*(10), 8568–8588. https://doi.org/10.1029/2018JB016053

Fulton, P., Brodsky, E., Kano, Y., Mori, J., Chester, F., Ishikawa, T., Harris, R., Lin, W., Eguchi, N., & Toczko, S. (2013). Low Coseismic Friction on the Tohoku-Oki Fault Determined from Temperature Measurements. *Science*, *21107005*(December), 1214–1217.

García-Mayordomo, J., Insua-Arévalo, J. M., Martínez-Díaz, J. J., Jiménez-Díaz, A., Martín-Banda, R., Martín-Alfageme, S., Álvarez-Gómez, J. A., Rodríguez-Peces, M., Pérez-López, R., Rodríguez-Pascua, M. A., Masana, E., Perea, H., Martín-González, F., Giner-Robles, J., Nemser, E. S., Cabral, J., Sanz de Galdeano, C., Peláez, J. A., García-Tortosa, F. J., … Linares, R. (2012). The Quaternary Active Faults Database of Iberia (QAFI v.2.0). *Journal of Iberian Geology*, *38*(1), 285–302. https://doi.org/10.5209/rev_JIGE.2012.v38.n1.39219

García-Romero, E., Suárez, M., Oyarzun, R., López-García, J. A., & Regueiro, M. (2006). Fault-hosted palygorskite from the Serrata de Níjar deformation zone (SE Spain). *Clays and Clay Minerals*, *54*(3), 324–332. https://doi.org/10.1346/CCMN.2006.0540304

Giorgetti, C., Carpenter, B. M., & Collettini, C. (2015). Frictional behavior of talc-calcite mixtures. *Journal of Geophysical Research: Solid Earth*, *120*(9), 6614–6633. https://doi.org/10.1002/2015JB011970

Goebel, T. H. W., Candela, T., Sammis, C. G., Becker, T. W., Dresen, G., & Schorlemmer, D. (2013). Seismic event distributions and off-fault damage during frictional sliding of saw-cut surfaces with pre-defined roughness. In *Geophysical Journal International* (Vol. 196, Issue 1, pp. 612–625). https://doi.org/10.1093/gji/ggt401

Goebel, T. H. W., Kwiatek, G., Becker, T. W., Brodsky, E. E., & Dresen, G. (2017). What allows seismic events to grow big?: Insights from b-value and fault roughness analysis in laboratory stick-slip experiments. *Geology*, *45*(9), 815–818. https://doi.org/10.1130/G39147.1

Gomez-Pugnaire, M. T., & Fernandez-Soler, J. M. (1987). Contributions to Mineralogy and Petrology High-pressure metamorphism in metabasites from the Betie Cordilleras (S.E. Spain) and its evolution during the Alpine orogeny. In *Contrib Mineral Petrol* (Vol. 95).

Google. (2023). *Carboneras*. Google Maps. https://goo.gl/maps/jgMRibD78UK4T1mb9

Gràcia, E., Pallàs, R., Soto, J. I., Comas, M., Moreno, X., Masana, E., Santanach, P., Diez, S., García, M., Dañobeitia, J., Bartolomé, R., Farrán, M., Gómez, M., Alpiste, M. J. R., Lastras, G., Wilmott, V., Perea, H., Blondel, P., Gómez, O., … Roque, C. (2006). Active faulting offshore SE Spain (Alboran Sea): Implications for earthquake hazard assessment in the Southern Iberian Margin. *Earth and Planetary Science Letters*, *241*(3–4), 734–749. https://doi.org/10.1016/j.epsl.2005.11.009

Gray, H., DuRoss, C., Nicovich, S., & Gold, R. (2022). Luminescence sediment tracing reveals the complex dynamics of colluvial wedge formation. *Science Advances*, *8*(22), 1–12.

https://doi.org/10.1126/sciadv.abo0747

Green, H. W., Shi, F., Bozhilov, K., Xia, G., & Reches, Z. (2015). Phase transformation and nanometric flow cause extreme weakening during fault slip. *Nature Geoscience*, *8*(6), 448–489. https://doi.org/10.1038/NGEO2436

Griggs, D. T., Turner, F. J., & Heard, H. C. (1960). Chapter 4: Deformation of Rocks at 500° to 800° C. In D. Griggs & J. Handin (Eds.), *Rock Deformation (A Symposium)* (Vol. 79, p. 0). Geological Society of America. https://doi.org/10.1130/MEM79-p39

Gutenberg, B., & Richter, C. F. (1944). Frequency of earthquakes in California. *Bulletin of the Seismological Society of America*, *34*, 185–188. https://doi.org/10.1038/156371a0

Gutscher, M.-A., Malod, J., Rehault, J.-P., Contrucci, I., Klingelhoefer, F., & Spakman, W. (2002). Evidence for active subduction beneath Gibraltar. In *Geology*. http://pubs.geoscienceworld.org/gsa/geology/article-pdf/30/12/1071/3522962/i0091-7613-30-12-1071.pdf

Gutscher, M. A. (2012). Subduction beneath Gibraltar? Recent studies provide answers. *Eos*, *93*(13), 133–134. https://doi.org/10.1029/2012EO130001

Han, R., Hirose, T., & Shimamoto, T. (2010). Strong velocity weakening and powder lubrication of simulated carbonate faults at seismic slip rates. *Journal of Geophysical Research: Solid Earth*, *115*(B3), 3412. https://doi.org/10.1029/2008JB006136

Han, R., Hirose, T., Shimamoto, T., Lee, Y., & Ando, J. I. (2011). Granular nanoparticles lubricate faults during seismic slip. *Geology*, *39*(6), 599–602. https://doi.org/10.1130/G31842.1

Han, R., Shimamoto, T., Hirose, T., Ree, J.-H., & Ando, J. (2007). Ultralow Friction of Carbonate Faults Caused by Thermal Decomposition. *Science*, *316*(May), 878–881.

Han, S., Löhr, S. C., Abbott, A. N., Baldermann, A., Farkaš, J., McMahon, W., Milliken, K. L., Rafiei, M., Wheeler, C., & Owen, M. (2022). Earth system science applications of next-generation SEM-EDS automated mineral mapping. *Frontiers in Earth Science*, *10*(November), 1–22. https://doi.org/10.3389/feart.2022.956912

Han, Y., Yan, Z., Jin, L., Liao, J., & Feng, G. (2020). In situstudy on interactions between hydroxyl groups in kaolinite and re-adsorption water. *RSC Advances*, *10*(29), 16949–16958. https://doi.org/10.1039/d0ra01905d

Healy, D., Rizzo, R. E., Cornwell, D. G., Farrell, N. J. C., Watkins, H., Timms, N. E., Gomez-Rivas, E., & Smith, M. (2017). FracPaQ: A MATLAB™ toolbox for the quantification of fracture patterns. *Journal of Structural Geology*, *95*, 1–16. https://doi.org/10.1016/j.jsg.2016.12.003

Heimisson, E. R., Rudnicki, J., & Lapusta, N. (2021). Dilatancy and Compaction of a Rate-and-State Fault in a Poroelastic Medium: Linearized Stability Analysis. *Journal of Geophysical Research: Solid Earth*, *126*(8), 1–28. https://doi.org/10.1029/2021JB022071

Hendricks, S. B. (1942). Lattice Structure of Clay Minerals and Some Properties of Clays. *The Journal of Geology*, *50*(3), 276–290. https://doi.org/10.1086/625051

Hey, M. H. (1954). A new review of the chlorites. *Mineralogical Magazine and Journal of the Mineralogical Society*, *30*(224), 277–292. https://doi.org/10.1180/minmag.1954.030.224.01

Hillers, G., Ben-Zion, Y., & Mai, P. M. (2006). Seismicity on a fault controlled by rate- and state-dependent friction with spatial variations of the critical slip distance. *Journal of Geophysical Research: Solid Earth*, *111*(1). https://doi.org/10.1029/2005JB003859

Hillier, S. (2000). Accurate quantitative analysis of clay and other minerals in sandstones by XRD: comparison of a Rietveld and a reference intensity ratio (RIR) method and the importance of sample preparation. *Clay Minerals*, *35*(1), 291–302. https://doi.org/10.1180/000985500546666

Horváth, E., Frost, R. L., Makó, É., Kristóf, J., & Cseh, T. (2003). Thermal treatment of mechanochemically activated kaolinite. *Thermochimica Acta*, *404*(1–2), 227–234. https://doi.org/10.1016/S0040-6031(03)00184-9

Humphreys, F. J. (2004). Reconstruction of grains and subgrains from electron backscatter diffraction maps. *Journal of Microscopy*, *213*(3), 247–256. https://doi.org/10.1111/j.0022-2720.2004.01297.x

Hüpers, A., & Kopf, A. J. (2009). The thermal influence on the consolidation state of underthrust sediments from the Nankai margin and its implications for excess pore pressure. *Earth and Planetary Science Letters*, *286*(1–2), 324–332. https://doi.org/10.1016/j.epsl.2009.05.047

Ide, S., Beroza, G. C., Shelly, D. R., & Uchide, T. (2007). A scaling law for slow earthquakes. *Nature*, *447*(7140), 76–79. https://doi.org/10.1038/nature05780

Igbokwe, O. A., Mueller, M., Bertotti, G., Timothy, J. J., Abah, O., & Immenhauser, A. (2020). Morphology and topology of dolostone lithons in the regional Carboneras Fault Zone, Southern Spain. *Journal of Structural Geology*, *137*. https://doi.org/10.1016/j.jsg.2020.104073

Ikari, M. J. (2019). Laboratory slow slip events in natural geological materials. *Geophysical Journal International*, *218*(1), 354–387. https://doi.org/10.1093/gji/ggz143

Ikari, M. J., Ito, Y., Ujiie, K., & Kopf, A. J. (2015). Spectrum of slip behaviour in Tohoku fault zone samples at plate tectonic slip rates. *Nature Geoscience*, *8*(11), 870–874. https://doi.org/10.1038/ngeo2547

Ikari, M. J., Marone, C., & Saffer, D. M. (2011). On the relation between fault strength and frictional stability. *Geology*, *39*(1), 83–86. https://doi.org/10.1130/G31416.1

Ikari, M. J., Marone, C., Saffer, D. M., & Kopf, A. J. (2013). Slip weakening as a mechanism for slow earthquakes. *Nature Geoscience*, *6*(6), 468–472.

https://doi.org/10.1038/ngeo1818

Ikari, M. J., Saffer, D. M., & Marone, C. (2007). Effect of hydration state on the frictional properties of montmorillonite-based fault gouge. *Journal of Geophysical Research: Solid Earth*, *112*(6), 1–12. https://doi.org/10.1029/2006JB004748

Ikari, M. J., Saffer, D. M., & Marone, C. (2009a). Frictional and hydrologic properties of clay-rich fault gouge. *Journal of Geophysical Research: Solid Earth*, *114*(5), 1–18. https://doi.org/10.1029/2008JB006089

Ikari, M. J., Saffer, D. M., & Marone, C. (2009b). Frictional and hydrologic properties of clay-rich fault gouge. *Journal of Geophysical Research: Solid Earth*, *114*(5). https://doi.org/10.1029/2008JB006089

Ikari, M. J., Wallace, L. M., Rabinowitz, H. S., Savage, H. M., Hamling, I. J., & Kopf, A. J. (2020). Observations of Laboratory and Natural Slow Slip Events: Hikurangi Subduction Zone, New Zealand. *Geochemistry, Geophysics, Geosystems*, *21*(2). https://doi.org/10.1029/2019GC008717

Im, K., Saffer, D., Marone, C., & Avouac, J. P. (2020). Slip-rate-dependent friction as a universal mechanism for slow slip events. *Nature Geoscience*, *13*(October). https://doi.org/10.1038/s41561-020-0627-9

Ishikawa, T., Hirono, T., Matsuta, N., Kawamoto, K., Fujimoto, K., Kameda, J., Nishio, Y., Maekawa, Y., & Honda, G. (2014). Geochemical and mineralogical characteristics of fault gouge in the Median Tectonic Line, Japan: Evidence for earthquake slip. *Earth, Planets and Space*, *66*(1). https://doi.org/10.1186/1880-5981-66-36

Ito, Y., Hino, R., Kido, M., Fujimoto, H., Osada, Y., Inazu, D., Ohta, Y., Iinuma, T., Ohzono, M., Miura, S., Mishina, M., Suzuki, K., Tsuji, T., & Ashi, J. (2013). Episodic slow slip events in the Japan subduction zone before the 2011 Tohoku-Oki earthquake. *Tectonophysics*, *600*, 14–26. https://doi.org/10.1016/j.tecto.2012.08.022

Jefferies, S. P., Holdsworth, R. E., Wibberley, C. A. J., Shimamoto, T., Spiers, C. J., Niemeijer, A. R., & Lloyd, G. E. (2006). The nature and importance of phyllonite development in crustal-scale fault cores: An example from the Median Tectonic Line, Japan. *Journal of Structural Geology*, *28*(2), 220–235. https://doi.org/10.1016/j.jsg.2005.10.008

Jiménez-Millán, J., Abad, I., Hernández-Puentes, P., & Jiménez-Espinosa, R. (2015). Influence of phyllosilicates and fluid–rock interaction on the deformation style and mechanical behaviour of quartz-rich rocks in the Carboneras and Palomares fault areas (SE Spain). *Clay Minerals*, *50*(5), 619–638. https://doi.org/10.1180/claymin.2015.050.5.06

Kacher, J., Landon, C., Adams, B. L., & Fullwood, D. (2009). Bragg's Law diffraction simulations for electron backscatter diffraction analysis. *Ultramicroscopy*, *109*(9), 1148–1156. https://doi.org/10.1016/j.ultramic.2009.04.007

Kampschuur, W., & Rondeel, H. E. (1975). *THE ORIGIN OF THE BETIC OROGEN, SOUTHERN SPAIN* (Vol. 27).

Kanamori, H., & Anderson, D. (1975). Theoretical Basis Of Some Empirical Relations In Seismology. *Bulletin of the Seismological Society of America*, *65*(5), 1073–1095.

Kato, A., & Nakagawa, S. (2014). Multiple slow-slip events during a foreshock sequence of the 2014 Iquique, Chile Mw 8.1 earthquake. *Geophysical Research Letters*, *41*, 5420–5427. https://doi.org/10.1002/2014GL061138.Received

Kato, N., & Tullis, E. (2001). A composite rate- and state-dependent law for rock friction. *Geophysical R*, *28*(6), 1103–1106.

Keller, J. V. A., Hall, S. H., Dart, C. J., & McClay, K. R. (1995). The geometry and evolution of a transpressional strike-slip system: the Carboneras fault, SE Spain. *Journal of the Geological Society, London*, *152*, 339–351.

Kimberley, J., Ramesh, K. T., & Barnouin, O. S. (2010). Visualization of the failure of quartz under quasi-static and dynamic compression. *Journal of Geophysical Research: Solid Earth*, *115*(8), 1–13. https://doi.org/10.1029/2009JB007006

King, G. (1983). The accommodation of large strains in the upper lithosphere of the earth and other solids by self-similar fault systems: the geometrical origin of b-Value. *Pure and Applied Geophysics PAGEOPH*, *121*(5–6), 761–815. https://doi.org/10.1007/BF02590182

Kodaira, S., Iidaka, T., Kato, A., Park, J. O., Iwasaki, T., & Kaneda, Y. (2004). High pore fluid pressure may cause silent slip in the Nankai Trough. *Science*, *304*(5675), 1295–1298. https://doi.org/10.1126/science.1096535

Kranz, R. L., Saltzman, J. S., & Blacic, J. D. (1990). Hydraulic diffusivity measurements on laboratory rock samples using an oscillating pore pressure method. *International Journal of Rock Mechanics and Mining Sciences And*, *27*(5), 345–352. https://doi.org/10.1016/0148-9062(90)92709-N

Kuo, L. W., Song, S. R., Yeh, E. C., & Chen, H. F. (2009). Clay mineral anomalies in the fault zone of the Chelungpu fault, Taiwan, and their implications. *Geophysical Research Letters*, *36*(18). https://doi.org/10.1029/2009GL039269

Kushima, A., Qian, X., Zhao, P., Zhang, S., & Li, J. (2015). Ripplocations in van der Waals layers. *Nano Letters*, *15*(2), 1302–1308. https://doi.org/10.1021/nl5045082

Lambert, V., Lapusta, N., & Faulkner, D. (2021). Scale Dependence of Earthquake Rupture Prestress in Models With Enhanced Weakening: Implications for Event Statistics and Inferences of Fault Stress. *Journal of Geophysical Research: Solid Earth*, *126*(10). https://doi.org/10.1029/2021JB021886

Lapusta, N., Rice, J. R., Ben-Zion, Y., & Zheng, G. (2000). Elastodynamic analysis for slow tectonic loading with spontaneous rupture episodes on faults with rate- and state-

dependent friction. *Journal of Geophysical Research: Solid Earth*, *105*(B10), 23765–23789. https://doi.org/10.1029/2000jb900250

Leclère, H., Faulkner, D., Wheeler, J., & Mariani, E. (2016). Permeability control on transient slip weakening during gypsum dehydration: Implications for earthquakes in subduction zones. *Earth and Planetary Science Letters*, *442*, 1–12. https://doi.org/10.1016/j.epsl.2016.02.015

Lee, J. C., Angelier, J., Chu, H. T., Yu, S. B., & Hu, J. C. (1998). Plate-boundary strain partitioning along the sinistral collision suture of the Philippine and Eurasian plates: Analysis of geodetic data and geological observation in southeastern Taiwan. *Tectonics*, *17*(6), 859–871. https://doi.org/10.1029/98TC02205

Leeman, J. R., Marone, C., & Saffer, D. M. (2018). Frictional Mechanics of Slow Earthquakes. *Journal of Geophysical Research: Solid Earth*, *123*(9), 7931–7949. https://doi.org/10.1029/2018JB015768

Leeman, J. R., Saffer, D. M., Scuderi, M. M., & Marone, C. (2016). Laboratory observations of slow earthquakes and the spectrum of tectonic fault slip modes. *Nature Communications*, *7*, 1–6. https://doi.org/10.1016/0360-3016(81)90183-8

Li, Q., Tullis, T. E., Goldsby, D., & Carpick, R. W. (2011). Frictional ageing from interfacial bonding and the origins of rate and state friction. *Nature*, *480*(7376), 233–236. https://doi.org/10.1038/nature10589

Liu, Y. (2013). Numerical simulations on megathrust rupture stabilized under strong dilatancy strengthening in slow slip region. *Geophysical Research Letters*, *40*(7), 1311–1316. https://doi.org/10.1002/grl.50298

Lloyd, G. E. (1987). Atomic number and crystallographic contrast images with the SEM: a review of backscattered electron techniques. *Mineralogical Magazine*, *51*(359), 3–19. https://doi.org/10.1180/minmag.1987.051.359.02

Lockner, D. A., & Byerlee, J. D. (1994). Dilatancy in hydraulically isolated faults and the suppression of instability. *Geophysical Research Letters*, *21*(22), 2353–2356.

Logan, J. M., & Rauenzahn, K. A. (1987). Frictional dependence of gouge mixtures of quartz and montmorillonite on velocity, composition and fabric. *Tectonophysics*, *144*(1–3), 87–108. https://doi.org/10.1016/0040-1951(87)90010-2

Logan, J., & Rauenzahn, K. A. (1987). Frictional dependence of gouge mixtures of quartz and montmorillonite on velocity, composition and fabric. *Tectonophysics*, *144*, 87–108.

Lonergan, L., & White, N. (1997). Origin of the Betic-Rif mountain belt. *Tectonics*, *16*(3), 504–522. https://doi.org/10.1029/96TC03937

Lupini, J. F., Skinner, A. E., & Vaughan, P. R. (1981). The drained residual strength of cohesive soils. *Geotechnique*, *31*(2), 181–213.

Mair, K., & Marone, C. (1999). Friction of simulated fault gouge for a wide range of velocities

and normal stresses. *Journal of Geophysical Research*, *104*(1), 28899–28914.

Mäkel, G. H. (1985). *The geology of the Malaguide Complex and its bearing on the geodynamic evolution of the Betic-Rif Orogen (Southern Spain and Northern Morocco)*. GUA.

Manighetti, I., Campillo, M., Bouley, S., & Cotton, F. (2007). Earthquake scaling, fault segmentation, and structural maturity. *Earth and Planetary Science Letters*, *253*(3–4), 429–438. https://doi.org/10.1016/j.epsl.2006.11.004

Mariani, E., Brodie, K. H., & Rutter, E. H. (2006). Experimental deformation of muscovite shear zones at high temperatures under hydrothermal conditions and the strength of phyllosilicate-bearing faults in nature. *Journal of Structural Geology*, *28*(9), 1569–1587. https://doi.org/10.1016/j.jsg.2006.06.009

Mariani, E., Mecklenburgh, J., Wheeler, J., Prior, D. J., & Heidelbach, F. (2009). Microstructure evolution and recrystallization during creep of MgO single crystals. *Acta Materialia*, *57*(6), 1886–1898. https://doi.org/10.1016/j.actamat.2008.12.029

Marion, D., Nur, A., Yin, H., & Han, D. (1992). Compressional velocity and porosity in sand-clay mixtures. *Geophysics*, *57*(4), 554–563.

Marrone, S., Monié, P., Rossetti, F., Aldega, L., Bouybaouene, M., Charpentier, D., Lucci, F., Phillips, D., Theye, T., & Zaghloul, M. N. (2021). Timing of Alpine Orogeny and Postorogenic Extension in the Alboran Domain, Inner Rif Chain, Morocco. *Tectonics*, *40*(7). https://doi.org/10.1029/2021TC006707

Martínez-Martínez, J. M., Booth-Rea, G., Azañón, J. M., & Torcal, F. (2006). Active transfer fault zone linking a segmented extensional system (Betics, southern Spain): Insight into heterogeneous extension driven by edge delamination. *Tectonophysics*, *422*(1–4), 159–173. https://doi.org/10.1016/j.tecto.2006.06.001

Masana, E., Martínez-Díaz, J. J., Hernández-Enrile, J. L., & Santanach, P. (2004). The Alhama de Murcia fault (SE Spain), a seismogenic fault in a diffuse plate boundary: Seismotectonic implications for the Ibero-Magrebian region. *Journal of Geophysical Research: Solid Earth*, *109*(B1), 1–17. https://doi.org/10.1029/2002jb002359

Mattei, M., Riggs, N. R., Giordano, G., Guarnieri, L., Cifelli, F., Soriano, C. C., Jicha, B., Jasim, A., Marchionni, S., Franciosi, L., Tommasini, S., Porreca, M., & Conticelli, S. (2014). Geochronology, geochemistry and geodynamics of the Cabo de Gata volcanic zone, Southeastern Spain. *Italian Journal of Geosciences*, *133*(3), 341–361. https://doi.org/10.3301/IJG.2014.44

Mayolle, S., Soliva, R., Caniven, Y., Wibberley, C., Ballas, G., Milesi, G., & Dominguez, S. (2019). Scaling of fault damage zones in carbonate rocks. *Journal of Structural Geology*, *124*, 35–50. https://doi.org/10.1016/j.jsg.2019.03.007

Mead, W. J. (1925). The Geologic Role of Dilatancy. *The Journal of Geology*, *33*(7), 685–698.

https://doi.org/10.1086/623241

Means, W. D. (1989). Stretching faults. *Geology*, *17*, 893–896. http://pubs.geoscienceworld.org/gsa/geology/article-pdf/17/10/893/3510949/i0091-7613-17-10-893.pdf

Meike, A. (1989). In situ deformation of micas: a high-voltage electron-microscope study. *American Mineralogist*, *74*(7–8), 780–796.

Menegon, L., Piazolo, S., & Pennacchioni, G. (2011). The effect of Dauphiné twinning on plastic strain in quartz. *Contributions to Mineralogy and Petrology*, *161*(4), 635–652. https://doi.org/10.1007/s00410-010-0554-7

Michel, S., Gualandi, A., & Avouac, J. P. (2019). Similar scaling laws for earthquakes and Cascadia slow-slip events. *Nature*, *574*(7779), 522–526. https://doi.org/10.1038/s41586-019-1673-6

Mitchell, T. M., Ben-Zion, Y., & Shimamoto, T. (2011). Pulverized fault rocks and damage asymmetry along the Arima-Takatsuki Tectonic Line, Japan. *Earth and Planetary Science Letters*, *308*(3–4), 284–297. https://doi.org/10.1016/j.epsl.2011.04.023

Mitchell, T. M., & Faulkner, D. R. (2008). Experimental measurements of permeability evolution during triaxial compression of initially intact crystalline rocks and implications for fluid flow in fault zones. *Journal of Geophysical Research: Solid Earth*, *113*(11), 1–16. https://doi.org/10.1029/2008JB005588

Miyazaki, S., McGuire, J. J., & Segall, P. (2011). Seismic and aseismic fault slip before and during the 2011 off the Pacific coast of Tohoku Earthquake. *Earth, Planets and Space*, *63*(7), 637–642. https://doi.org/10.5047/eps.2011.07.001

Moore, D. E., & Lockner, D. A. (2011a). Frictional strengths of talc-serpentine and talc-quartz mixtures. *Journal of Geophysical Research: Solid Earth*, *116*(1), 1–17. https://doi.org/10.1029/2010JB007881

Moore, D. E., & Lockner, D. A. (2011b). Frictional strengths of talc-serpentine and talc-quartz mixtures. *Journal of Geophysical Research: Solid Earth*, *116*(1). https://doi.org/10.1029/2010JB007881

Moreno, M. X. (2011). *Neotectonic and Paleoseismic Onshore-Offshore integrated study of the Carboneras Fault (Eastern Betics , SE Iberia)*. University of Barcelona.

Morrow, C. A., & Byerlee, J. D. (1989). Experimental studies of compaction and dilatancy during frictional sliding on faults containing gouge. *Journal of Structural Geology*, *11*(7), 815–825. https://doi.org/10.1016/0191-8141(89)90100-4

Morrow, C. A., Moore, D. E., & Lockner, D. A. (2000). The effect of mineral bond strength and adsorbed water on fault gouge frictional strength. *Geophysical Research Letters*, *27*(6), 815–818. https://doi.org/10.1029/1999GL008401

Morrow, C. A., Moore, D. E., & Lockner, D. A. (2017). Frictional strength of wet and dry

montmorillonite. *Journal of Geophysical Research: Solid Earth*, *122*(5), 3392–3409. https://doi.org/10.1002/2016JB013658

Morrow, C. A., Shi, L. Q., & Byerlee, J. D. (1984). Permeability of fault gouge under confining pressure and shear stress. *Journal of Geophysical Research*, *89*(B5), 3193–3200. https://doi.org/10.1029/JB089iB05p03193

Murray, H. H. (2006). Structure and Composition of the Clay Minerals and their Physical and Chemical Properties. In *Developments in Clay Science* (pp. 7–31). https://doi.org/10.1016/S1572-4352(06)02002-2

Murray, J., & Langbein, J. (2006). Slip on the San Andreas fault at Parkfield, California, over two earthquake cycles, and the implications for seismic hazard. *Bulletin of the Seismological Society of America*, *96*(4 B). https://doi.org/10.1785/0120050820

Nickel Development Institute. (2015). High-Temperature Characteristics Of Stainless Steels. In *A Designers' Handbook Series* (Vol. 9004).

Niemeijer, A. R., & Spiers, C. J. (2007). A microphysical model for strong velocity weakening in phyllosilicate-bearing fault gouges. *Journal of Geophysical Research: Solid Earth*, *112*(10). https://doi.org/10.1029/2007JB005008

Noda, H., & Lapusta, N. (2013). Stable creeping fault segments can become destructive as a result of dynamic weakening. *Nature*, *493*(7433), 518–521. https://doi.org/10.1038/nature11703

Noda, H., & Shimamoto, T. (2009). Constitutive properties of clayey fault gouge from the Hanaore fault zone, southwest Japan. *Journal of Geophysical Research: Solid Earth*, *114*(4), 1–29. https://doi.org/10.1029/2008JB005683

Obara, K., & Kato, A. (2016). Connecting slow earthquakes to huge earthquakes. *Science (New York, N.Y.)*, *353*(6296), 253–257. https://doi.org/10.1126/science.aaf1512

Okamoto, A. S., Verberne, B. A., Niemeijer, A. R., Takahashi, M., Shimizu, I., Ueda, T., & Spiers, C. J. (2019). Frictional Properties of Simulated Chlorite Gouge at Hydrothermal Conditions: Implications for Subduction Megathrusts. *Journal of Geophysical Research: Solid Earth*, *124*(5), 4545–4565. https://doi.org/10.1029/2018JB017205

Ortuño, M., Masana, E., García-Meléndez, E., Martínez-Díaz, J., Štěpančíková, P., Cunha, P. P., Sohbati, R., Canora, C., Buylaert, J. P., & Murray, A. S. (2012). An exceptionally long paleoseismic record of a slow-moving fault: The Alhama de Murcia fault (Eastern Betic shear zone, Spain). *Bulletin of the Geological Society of America*, *124*(9–10), 1474–1494. https://doi.org/10.1130/B30558.1

Ostermeijer, G. A., Aben, F. M., Mitchell, T. M., Rockwell, T. K., Rempe, M., & Farrington, K. (2022). Evolution of co-seismic off-fault damage towards pulverisation. *Earth and Planetary Science Letters*, *579*. https://doi.org/10.1016/j.epsl.2021.117353

Ougier-Simonin, A., & Zhu, W. (2013). Effects of pore fluid pressure on slip behaviors: An

experimental study. *Geophysical Research Letters*, *40*(11), 2619–2624. https://doi.org/10.1002/grl.50543

Patria, A., Kimura, H., Kitade, Y., & Tsutsumi, H. (2022). Right-lateral offset associated with the most recent earthquake on the Ikeda fault of the Median Tectonic Line, southwest Japan, revealed by ground-penetrating radar profiling. *Progress in Earth and Planetary Science*, *9*(1). https://doi.org/10.1186/s40645-022-00466-7

Pedrera, A., Mancilla, F. D. L., Ruiz-Constán, A., Galindo-Zaldívar, J., Morales, J., Arzate, J., Marín-Lechado, C., Ruano, P., Buontempo, L., Anahnah, F., & Stich, D. (2010). Crustal-scale transcurrent fault development in a weak-layered crust from an integrated geophysical research: Carboneras Fault Zone, eastern Betic Cordillera, Spain. *Geochemistry, Geophysics, Geosystems*, *11*(12). https://doi.org/10.1029/2010GC003274

Peng, Z., & Gomberg, J. (2010). An integrated perspective of the continuum between earthquakes and slow-slip phenomena. *Nature Geoscience*, *3*(9), 599–607. https://doi.org/10.1038/ngeo940

Platt, J. P. (1982). Emplacement of a fold-nappe, Betic orogen, southern Spain. *Geology*, *10*(2), 97–102. https://doi.org/10.1130/0091-7613(1982)10<97:EOAFBO>2.0.CO;2

Platt, J. P., Kelley, S. P., Carter, A., & Orozco, M. (2005). Timing of tectonic events in the Alpujárride Complex, Betic Cordillera, southern Spain. *Journal of the Geological Society*, *162*(3), 451–462. https://doi.org/10.1144/0016-764903-039

Platt, J. P., & Vissers, R. L. M. (1989). Extensional collapse of thickened continental lithosphere: A working hypothesis for the Alboran Sea and Gibraltar arc. *Geology*, *17*, 540–543. http://pubs.geoscienceworld.org/gsa/geology/article-pdf/17/6/540/3511457/i0091-7613-17-6-540.pdf

Platt, J. P., & Whitehouse, M. J. (1999). Early Miocene high-temperature metamorphism and rapid exhumation in the Betic Cordillera (Spain): evidence from U-Pb zircon ages. In *Earth and Planetary Science Letters* (Vol. 171). www.elsevier.com/locate/epsl

Platt, J. P., Whitehouse, M. J., Kelley, S. P., Carter, A., & Hollick, L. (2003). Simultaneous extensional exhumation across the Alboran Basin: Implications for the causes of late orogenic extension. *Geology*, *31*(3), 251–254. www.geosociety.org/pubs/ft2003.htm.

Prior, D. J., Boyle, A. P., Brenker, F., Cheadle, M. C., Austin, D., Lopez, G., Peruzzo, L., Potts, G. J., Reddy, S., Spiess, R., Timms, N. E., Trimby, P., Wheeler, J., & Zetterström, L. (1999). The application of electron backscatter diffraction and orientation contrast imaging in the SEM to textural problems in rocks. *American Mineralogist*, *84*(11–12), 1741–1759. https://doi.org/10.2138/am-1999-11-1204

Prior, D. J., Mariani, E., & Wheeler, J. (2009). EBSD in Materials Science: Applications, Common Practice, and Challenges. In A. J. Schwartz, M. Kumar, B. L. Adams, & D. P.

Field (Eds.), *Electron Backscatter Diffraction in Materials Science* (2nd ed., pp. 345–360). Springer Science and Business Media. http://dx.doi.org/10.1016/j.actamat.2012

Proctor, B., Lockner, D. A., Kilgore, B. D., Mitchell, T. M., & Beeler, N. M. (2020). Direct Evidence for Fluid Pressure, Dilatancy, and Compaction Affecting Slip in Isolated Faults. *Geophysical Research Letters*, *47*(16). https://doi.org/10.1029/2019gl086767

Pruett, R. J., & Webb, H. L. (1993). Sampling and analysis of Kga-1B well-crystallized kaolin source clay. *Clays and Clay Minerals*, *41*(4), 514–519. https://doi.org/10.1346/CCMN.1993.0410411

Rathbun, A. P., & Marone, C. (2010). Effect of strain localization on frictional behavior of sheared granular materials. *Journal of Geophysical Research*, *115*(B1), 1–16. https://doi.org/10.1029/2009jb006466

Rathbun, A. P., & Marone, C. (2013). Symmetry and the critical slip distance in rate and state friction laws. *Journal of Geophysical Research: Solid Earth*, *118*(7), 3728–3741. https://doi.org/10.1002/jgrb.50224

Reicherter, K. R., & Reiss, S. (2001). The carboneras fault zone (Southeastern Spain) revisited with ground penetrating radar - Quaternary structural styles from high-resolution images. *Geologie En Mijnbouw/Netherlands Journal of Geosciences*, *80*(3–4), 129–138. https://doi.org/10.1017/s0016774600023799

Reinen, L. A., & Weeks, J. D. (1993). Determination of rock friction constitutive parameters using an iterative least squares inversion method. *Journal of Geophysical Research*, *98*(B9). https://doi.org/10.1029/93jb00780

Remitti, F., Smith, S. A. F., Mittempergher, S., Gualtieri, A. F., & Di Toro, G. (2015). Frictional properties of fault zone gouges from the J-FAST drilling project (Mw 9.0 2011 Tohoku-Oki earthquake). *Geophysical Research Letters*, *42*(8), 2691–2699. https://doi.org/10.1002/2015GL063507

Reynolds, O. (1885). On the dilatancy of media composed of rigid particles in contact. With experimental illustrations. *The London, Edinburgh, and Dublin Philosophical Magazine and Journal of Science*, *20*(127), 469–481.

Rice, J. R. (2006). Heating and weakening of faults during earthquake slip. *Journal of Geophysical Research: Solid Earth*, *111*(5), 1–29. https://doi.org/10.1029/2005JB004006

Rodríguez-Escudero, E., Martínez-Díaz, J. J., Giner-Robles, J. L., Tsige, M., & Cuevas-Rodríguez, J. (2020). Pulverized quartz clasts in gouge of the alhama de murcia fault (Spain): Evidence for coseismic clast pulverization in a matrix deformed by frictional sliding. *Geology*, *48*(3), 283–287. https://doi.org/10.1130/G47007.1

Roep, T. B., & Mac Gillavry, H. J. (1962). *Preliminary note on the presence of distinct tectonic units in the Betic of Málaga of the Vélez Rubio region (SE Spain)*. Verlag nicht ermittelbar.

Rosenbaum, G., Lister, G. S., & Duboz, C. (2002). Reconstruction of the tectonic evolution of

the western Mediterranean since the Oligocene. *Journal of the Virtual Explorer*, *8*. https://doi.org/10.3809/jvirtex.2002.00053

Rowe, C. D., & Griffith, W. A. (2015). Do faults preserve a record of seismic slip: A second opinion. In *Journal of Structural Geology* (Vol. 78, pp. 1–26). Elsevier Ltd. https://doi.org/10.1016/j.jsg.2015.06.006

Ruano, S. M., Rosua, F. J. C., Hach-Ali, P. F., Chacon, F. D. L. F., & Lopez, E. C. (2000). Epithermal Cu-Au mineralization in the Palai-Islica deposit, Almeria, southeastern Spain: Fluid-inclusion evidence for mixing of fluids as a guide to gold mineralization. *Canadian Mineralogist*, *38*(3), 553–565. https://doi.org/10.2113/gscanmin.38.3.553

Rubin, A. M. (2008). Episodic slow slip events and rate-and-state friction. *Journal of Geophysical Research: Solid Earth*, *113*(11), 1–18. https://doi.org/10.1029/2008JB005642

Rudnicki, J. W., & Chen, C. H. (1988). Stabilization of rapid frictional slip on a weakening fault by dilatant hardening. *Journal of Geophysical Research*, *93*(B5), 4745–4757. https://doi.org/10.1029/JB093iB05p04745

Ruggieri, R., Scuderi, M. M., Trippetta, F., Tinti, E., Brignoli, M., Mantica, S., Petroselli, S., Osculati, L., Volontè, G., & Collettini, C. (2021). The role of shale content and pore-water saturation on frictional properties of simulated carbonate faults. *Tectonophysics*, *807*. https://doi.org/10.1016/j.tecto.2021.228811

Ruina, A. (1983). Slip instability and state variable friction laws. *Journal of Geophysical Research*, *88*(B12), 10359–10370. https://doi.org/10.1029/JB088iB12p10359

Rutter, E. H., Burgess, R., & Faulkner, D. R. (2014). Constraints on the movement history of the carboneras fault zone (SE Spain) from stratigraphy and 40Ar-39Ar dating of neogene volcanic rocks. *Geological Society Special Publication*, *394*(1), 79–99. https://doi.org/10.1144/SP394.5

Rutter, E. H., Faulkner, D. R., & Burgess, R. (2012). Structure and geological history of the Carboneras Fault Zone, SE Spain: Part of a stretching transform fault system. *Journal of Structural Geology*, *45*, 68–71. https://doi.org/10.1016/j.jsg.2012.08.009

Rutter, E. H., Hackston, A. J., Yeatman, E., Brodie, K. H., Mecklenburgh, J., & May, S. E. (2013). Reduction of friction on geological faults by weak-phase smearing. *Journal of Structural Geology*, *51*, 52–60. https://doi.org/10.1016/j.jsg.2013.03.008

Rutter, E. H., Maddock, R. H., Hall, S. H., & White, S. H. (1986). Comparative microstructures of natural and experimentally produced clay-bearing fault gouges. *Pure and Applied Geophysics PAGEOPH*, *124*(1–2), 3–30. https://doi.org/10.1007/BF00875717

Saffer, D. M., & Marone, C. (2003). Comparison of smectite- and illite-rich gouge frictional properties: Application to the updip limit of the seismogenic zone along subduction megathrusts. *Earth and Planetary Science Letters*, *215*(1–2), 219–235.

https://doi.org/10.1016/S0012-821X(03)00424-2

Saffer, D. M., & Wallace, L. M. (2015). The frictional, hydrologic, metamorphic and thermal habitat of shallow slow earthquakes. *Nature Geoscience*, *8*(8), 594–600. https://doi.org/10.1038/ngeo2490

Samuelson, J., Elsworth, D., & Marone, C. (2009). Shear-induced dilatancy of fluid-saturated faults: Experiment and theory. *Journal of Geophysical Research: Solid Earth*, *114*(12), 1–15. https://doi.org/10.1029/2008JB006273

Sänchez-Almazo, I. M., Spiro, B., Braga, J. C., & Martin, J. M. (2001). Constraints of stable isotope signatures on the depositional palaeoenvironments of upper Miocene reef and temperate carbonates in the Sorbas Basin, SE Spain. *Palaeogeography, Palaeoclimatology, Palaeoecology*, *175*, 153–172. www.elsevier.com/locate/palaeo

Sánchez-Roa, C., Jiménez-Millán, J., Abad, I., Faulkner, D. R., Nieto, F., & García-Tortosa, F. J. (2016). Fibrous clay mineral authigenesis induced by fluid-rock interaction in the Galera fault zone (Betic Cordillera, SE Spain) and its influence on fault gouge frictional properties. *Applied Clay Science*, *134*, 275–288. https://doi.org/10.1016/j.clay.2016.06.023

Sanz de Galdeano, C. (2020). Main faults of the betic cordillera. *Boletin Geologico y Minero*, *131*(3), 373–385. https://doi.org/10.21701/BOLGEOMIN.131.3.003

Schleicher, A. M., van der Pluijm, B. A., & Warr, L. N. (2010). Nanocoatings of clay and creep of the San Andreas fault at Parkfield, California. *Geology*, *38*(7), 667–670. https://doi.org/10.1130/G31091.1

Scholz, C. H. (1968). Experimental study of the fracturing process in brittle rock. *Journal of Geophysical Research*, *73*(4), 1447–1454. https://doi.org/10.1029/jb073i004p01447

Scholz, C. H. (2019). *The Mechanics of Earthquakes and Faulting* (3rd ed.). Cambridge University Press. https://doi.org/10.1017/9781316681473

Schulz, B., Sandmann, D., & Gilbricht, S. (2020). SEM-based automated mineralogy and its application in geo-and material sciences. *Minerals*, *10*(11), 1–26. https://doi.org/10.3390/min10111004

Segall, P., & Rice, J. R. (1995). Dilatancy, compaction, and slip instability of a fluid-infiltrated fault. *Journal of Geophysical Research*, *100*, 155–171.

Segall, P., Rubin, A. M., Bradley, A. M., & Rice, J. R. (2010). Dilatant strengthening as a mechanism for slow slip events. *Journal of Geophysical Research: Solid Earth*, *115*(12), 1–37. https://doi.org/10.1029/2010JB007449

Sibson, R. H. (1977). Fault rocks and fault mechanisms. *Journal of the Geological Society*, *133*(3), 191–213. https://doi.org/10.1144/gsjgs.133.3.0191

Sibson, R. H. (1994). An Assessment of Field Evidence for ' Byerlee ' Friction applicable to natural fault systems and govern their strength throughout the. *PAGEOPH*, *142*(3).

Siman-Tov, S., Aharonov, E., Boneh, Y., & Reches, Z. (2015). Fault mirrors along carbonate faults: Formation and destruction during shear experiments. *Earth and Planetary Science Letters*, *430*, 367–376. https://doi.org/10.1016/j.epsl.2015.08.031

Siman-Tov, S., Aharonov, E., Sagy, A., & Emmanuel, S. (2013). Nanograins form carbonate fault mirrors. *Geology*, *41*(6), 703–706. https://doi.org/10.1130/G34087.1

Skarbek, R. M., & Savage, H. M. (2019). RSFit3000: A MATLAB GUI-based program for determining rate and state frictional parameters from experimental data. *Geosphere*, *15*(5), 1665–1676. https://doi.org/10.1130/GES02122.1

Smith, S. A. F., Di Toro, G., Kim, S., Ree, J. H., Nielsen, S., Billi, A., & Spiess, R. (2013). Coseismic recrystallization during shallow earthquake slip. *Geology*, *41*(1), 63–66. https://doi.org/10.1130/G33588.1

Smith, J. V, & Yoder, H. S. (1956). Experimental and theoretical studies of the mica polymorphs. *Mineralogical Magazine and Journal of the Mineralogical Society*, *31*(234), 209–235. https://doi.org/10.1180/minmag.1956.031.234.03

Solum, J. G., Hickman, S. H., Lockner, D. A., Moore, D. E., Van Der Pluijm, B. A., Schleicher, A. M., & Evans, J. P. (2006). Mineralogical characterization of protolith and fault rocks from the SAFOD Main Hole. *Geophysical Research Letters*, *33*(21). https://doi.org/10.1029/2006GL027285

Solum, J. G., & van der Pluijm, B. A. (2009). Quantification of fabrics in clay gouge from the Carboneras fault, Spain and implications for fault behavior. *Tectonophysics*, *475*(3–4), 554–562. https://doi.org/10.1016/j.tecto.2009.07.006

Starkey, H. C., Blackmon, P. D., & Hauff, P. L. (1984). The Routine Mineralogical Analysis Of Clay-Bearing Samples. *Geological Society of America Bulletin*, *1563*.

Sugiyama, Y. (1992). Neotectonics of the forearc zone and the Setouchi Province in southwest Japan. *Chishitsugaku Ronshū*, *40*, 219–233.

Takagi, R., Uchida, N., & Obara, K. (2019). Along-Strike Variation and Migration of Long-Term Slow Slip Events in the Western Nankai Subduction Zone, Japan. *Journal of Geophysical Research: Solid Earth*, *124*(4), 3853–3880. https://doi.org/10.1029/2018JB016738

Takahashi, M., Mizoguchi, K., Kitamura, K., & Masuda, K. (2007). Effects of clay content on the frictional strength and fluid transport property of faults. *Journal of Geophysical Research: Solid Earth*, *112*(8). https://doi.org/10.1029/2006JB004678

Tarling, M. S., Smith, S. A. F., Scott, J. M., Rooney, J. S., Viti, C., & Gordon, K. C. (2019). The internal structure and composition of a plate-boundary-scale serpentinite shear zone: The Livingstone Fault, New Zealand. *Solid Earth*, *10*(4), 1025–1047. https://doi.org/10.5194/se-10-1025-2019

Tembe, S., Lockner, D. A., & Wong, T. F. (2010a). Effect of clay content and mineralogy on frictional sliding behavior of simulated gouges: Binary and ternary mixtures of quartz,

illite, and montmorillonite. *Journal of Geophysical Research: Solid Earth*, *115*(3), 1–22. https://doi.org/10.1029/2009JB006383

Tembe, S., Lockner, D. A., & Wong, T. F. (2010b). Effect of clay content and mineralogy on frictional sliding behavior of simulated gouges: Binary and ternary mixtures of quartz, illite, and montmorillonite. *Journal of Geophysical Research: Solid Earth*, *115*(3). https://doi.org/10.1029/2009JB006383

Tesei, T., Collettini, C., Barchi, M. R., Carpenter, B. M., & Di Stefano, G. (2014). Heterogeneous strength and fault zone complexity of carbonate-bearing thrusts with possible implications for seismicity. *Earth and Planetary Science Letters*, *408*, 307–318. https://doi.org/10.1016/j.epsl.2014.10.021

Thomas, M. Y., Avouac, J. P., Champenois, J., Lee, J. C., & Kuo, L. C. (2014). Spatiotemporal evolution of seismic and aseismic slip on the Longitudinal Valley Fault, Taiwan. *Journal of Geophysical Research: Solid Earth*, *119*(6), 5114–5139. https://doi.org/10.1002/2013JB010603

Thomas, M. Y., Avouac, J. P., Gratier, J. P., & Lee, J. C. (2014). Lithological control on the deformation mechanism and the mode of fault slip on the Longitudinal Valley Fault, Taiwan. *Tectonophysics*, *632*(C), 48–63. https://doi.org/10.1016/j.tecto.2014.05.038

Tisato, N., Di Toro, G., De Rossi, N., Quaresimin, M., & Candela, T. (2012). Experimental investigation of flash weakening in limestone. *Journal of Structural Geology*, *38*, 183–199. https://doi.org/10.1016/j.jsg.2011.11.017

Torres-Roldan, R. L. (1979). The tectonic subdivision of the Betic Zone (Betic Cordilleras, southern Spain); its significance and one possible geotectonic scenario for the westernmost Alpine Belt. *American Journal of Science*, *279*(1), 19–51.

Toy, V. G., Boulton, C. J., Sutherland, R., Townend, J., Norris, R. J., Little, T. A., Prior, D. J., Mariani, E., Faulkner, D., Menzies, C. D., Scott, H., & Carpenter, B. M. (2015). Fault rock lithologies and architecture of the central Alpine fault, New Zealand, revealed by DFDP-1 drilling. *Lithosphere*, *7*(2), 155–173. https://doi.org/10.1130/L395.1

Ujiie, K., Tanaka, H., Saito, T., Tsutsumi, A., Mori, J., & Toczko, S. (2013). Low Coseismic Shear Stress on the Tohoku-Oki Megathrust Determined from Laboratory Experiments. *Science*, *342*(December), 1211–1214.

van de Poel, H. M. (1992). Foraminiferal biostratigraphy and palaeoenvironments of the Miocene-Pliocene Carboneras-Nijar Basin (SE Spain). *Scripta Geol.*, *102*, 1–32.

van den Ende, M. P. A., Chen, J., Ampuero, J. P., & Niemeijer, A. R. (2018). A comparison between rate-and-state friction and microphysical models, based on numerical simulations of fault slip. *Tectonophysics*, *733*, 273–295. https://doi.org/10.1016/j.tecto.2017.11.040

Verberne, B. A., He, C., & Spiers, C. J. (2010). Frictional properties of sedimentary rocks and

natural fault gouge from the Longmen Shan fault zone, Sichuan, China. *Bulletin of the Seismological Society of America*, *100*(5 B), 2767–2790. https://doi.org/10.1785/0120090287

Verberne, B. A., Plümper, O., & Spiers, C. J. (2019). Nanocrystalline principal slip zones and their role in controlling crustal fault rheology. *Minerals*, *9*(6), 1–25. https://doi.org/10.3390/min9060328

Verberne, B. A., Spiers, C. J., Niemeijer, A. R., De Bresser, J. H. P., De Winter, D. A. M., & Plümper, O. (2014). Frictional Properties and Microstructure of Calcite-Rich Fault Gouges Sheared at Sub-Seismic Sliding Velocities. *Pure and Applied Geophysics*, *171*(10), 2617–2640. https://doi.org/10.1007/s00024-013-0760-0

Vissers, R. L. M. (2012). André Dumont medallist lecture 2011 Extension in a convergent tectonic setting: a lithospheric view on the Alboran system of SW Europe. *Geologica Belgica*, *15*(1–2), 53–72.

Vogt, C., Lauterjung, J., & Fischer, R. X. (2002). Investigation of the clay fraction (<2 µm) of the clay minerals society reference clays. *Clays and Clay Minerals*, *50*(3), 388–400. https://doi.org/10.1346/000986002760833765

von Terzhagi, K. (1936). The shearing resistance of saturated soils and the angle between the planes of shear. *First Int. Conf. Soil Mech.*, *1*, 54–56.

Voss, N., Dixon, T. H., Liu, Z., Malservisi, R., Protti, M., & Schwartz, S. (2018). Do slow slip events trigger large and great megathrust earthquakes? *Science Advances*, *4*(10), 1–6. https://doi.org/10.1126/sciadv.aat8472

Wallace, L. M., Bartlow, N., Hamling, I., & Fry, B. (2014). Quake clamps down on slow slip. *Geophysical Research Letters*, *41*(24), 8840–8846. https://doi.org/10.1002/2014GL062367

Wallace, L. M., Kaneko, Y., Hreinsdóttir, S., Hamling, I., Peng, Z., Bartlow, N., D'Anastasio, E., & Fry, B. (2017). Large-scale dynamic triggering of shallow slow slip enhanced by overlying sedimentary wedge. *Nature Geoscience*, *10*(10), 765–770. https://doi.org/10.1038/ngeo3021

Wallis, D., Hansen, L. N., Britton, T. B., & Wilkinson, A. J. (2019). High-Angular Resolution Electron Backscatter Diffraction as a New Tool for Mapping Lattice Distortion in Geological Minerals. *Journal of Geophysical Research: Solid Earth*, *124*(7), 6337–6358. https://doi.org/10.1029/2019JB017867

Wells, D. L., & Coppersmith, K. J. (1994). New empirical relationships among magnitude, rupture length, rupture width, rupture area, and surface displacement. *Bulletin - Seismological Society of America*, *84*(4), 974–1002.

Wenk, H. R., Bortolotti, M., Barton, N., Oliver, E., & Brown, D. (2007). Dauphiné twinning and texture memory in polycrystalline quartz. Part 2: In situ neutron diffraction compression

experiments. *Physics and Chemistry of Minerals*, *34*(9), 599–607. https://doi.org/10.1007/s00269-007-0174-6

Wenk, H. R., Janssen, C., Kenkmann, T., & Dresen, G. (2011). Mechanical twinning in quartz: Shock experiments, impact, pseudotachylites and fault breccias. *Tectonophysics*, *510*(1–2), 69–79. https://doi.org/10.1016/j.tecto.2011.06.016

Wenk, H. R., Rybacki, E., Dresen, G., Lonardelli, I., Barton, N., Franz, H., & Gonzalez, G. (2006). Dauphiné twinning and texture memory in polycrystalline quartz. Part 1: Experimental deformation of novaculite. *Physics and Chemistry of Minerals*, *33*(10), 667–676. https://doi.org/10.1007/s00269-006-0115-9

Wheeler, J., Mariani, E., Piazolo, S., Prior, D. J., Trimby, P. J., & Drury, M. R. (2012). The Weighted Burgers Vector: A quantity for constraining dislocation densities and types using electron backscatter diffraction on 2D sections through crystalline materials. *Materials Science Forum*, *715–716*(May 2008), 732–736. https://doi.org/10.4028/www.scientific.net/MSF.715-716.732

Wibberley, C. A. J., & Shimamoto, T. (2003a). Internal structure and permeability of major strike-slip fault zones: the Median Tectonic Line in Mie Prefecture, Southwest Japan. *Journal of Structural Geology*, *25*, 59–78. www.elsevier.com/locate/jsg

Wibberley, C. A. J., & Shimamoto, T. (2003b). Internal structure and permeability of major strike-slip fault zones. *Journal of Structural Geology*, *25*, 59–78.

Williams, J. C. (1968). The mixing of dry powders. *Powder Technology*, *2*(1), 13–20. https://doi.org/10.1016/0032-5910(68)80028-2

Winkelmann, A., & Nolze, G. (2015). Chirality determination of quartz crystals using electron backscatter diffraction. *Ultramicroscopy*, *149*, 58–63. https://doi.org/10.1016/j.ultramic.2014.11.013

Wu, W. J., Kuo, L. W., Ku, C. S., Chiang, C. Y., Sheu, H. S., Aprilniadi, T. D., & Dong, J. J. (2020). Mixed-Mode Formation of Amorphous Materials in the Creeping Zone of the Chihshang Fault, Taiwan, and Implications for Deformation Style. *Journal of Geophysical Research: Solid Earth*, *125*(6). https://doi.org/10.1029/2020JB019862

Wu, Y., & Chen, X. (2014). The scale-dependent slip pattern for a uniform fault model obeying the rate- and state-dependent friction law. *Journal of Geophysical Research: Solid Earth*, *119*(6), 4890–4906. https://doi.org/10.1002/2013JB010779

Wu, Y. M., Chen, Y. G., Shin, T. C., Kuochen, H., Hou, C. S., Hu, J. C., Chang, C. H., Wu, C. F., & Teng, T. L. (2006). Coseismic versus interseismic ground deformations, fault rupture inversion and segmentation revealed by 2003 Mw 6.8 Chengkung earthquake in eastern Taiwan. *Geophysical Research Letters*, *33*(2). https://doi.org/10.1029/2005GL024711

Xiao, B., Chen, H., Hollings, P., Zhang, Y., Feng, Y., & Chen, X. (2020). Chlorite alteration in

porphyry Cu systems: New insights from mineralogy and mineral chemistry. *Applied Clay Science*, *190*(March), 105585. https://doi.org/10.1016/j.clay.2020.105585

Yuguchi, T., Sasao, E., Ishibashi, M., & Nishiyama, T. (2015). Hydrothermal chloritization processes from biotite in the Toki granite, Central Japan: Temporal variations of of the compositions of hydrothermal fluids associated with chloritization. *American Mineralogist*, *100*(5–6), 1134–1152. https://doi.org/10.2138/am-2015-5126

Zeck, H., Kristensen, A., & Williams, I. (1998). Post-collisional volcanism in a sinking slab setting-crustal anatectic origin of pyroxene-andesite magma, Caldear Volcanic Group, Neogene Alboran volcanic province, southeastern Spain´H. In *Lithos* (Vol. 45).

Zhang, F., An, M., Zhang, L., Fang, Y., & Elsworth, D. (2020). Effect of mineralogy on friction-dilation relationships for simulated faults: Implications for permeability evolution in caprock faults. *Geoscience Frontiers*, *11*(2), 439–450. https://doi.org/10.1016/j.gsf.2019.05.014

Zilio, L. D., & Ampuero, J. (2023). Earthquake doublet in Turkey and Syria. *Communications Earth and Environment*, *February*, 2–5. https://doi.org/10.1038/s43247-023-00747-z

Zoback, M., Hickman, S., & Ellsworth, W. (2011). Scientific drilling into the San Andreas fault zone - An overview of SAFOD's first five years. *Scientific Drilling*, *1*, 14–28. https://doi.org/10.2204/iodp.sd.11.02.2011